

박사학위논문
Ph.D. Dissertation

테라헤르츠 전자기파를 활용한 광물의 격자 진동과
슬릿 내부 물질의 편광 의존성에 관한 연구

Lattice vibrations of mineral and polarization dependence of
material in a slit using terahertz waves

2016

한대훈 (韓大勳 Han, Daehoon)

한국과학기술원

Korea Advanced Institute of Science and Technology

박사학위논문

테라헤르츠 전자기파를 활용한 광물의 격자 진동과
슬릿 내부 물질의 편광 의존성에 관한 연구

2016

한대훈

한국과학기술원

물리학과

테라헤르츠 전자기파를 활용한 광물의 격자 진동과 슬릿 내부 물질의 편광 의존성에 관한 연구

한 대 훈

위 논문은 한국과학기술원 박사학위논문으로
학위논문 심사위원회의 심사를 통과하였음

2016년 5월 27일

심사위원장 안 재 욱 (인)

심 사 위 원 강 명 수 (인)

심 사 위 원 공 홍 진 (인)

심 사 위 원 박 재 현 (인)

심 사 위 원 양 찬 호 (인)

Lattice vibrations of mineral and polarization dependence of material in a slit using terahertz waves

Daehoon Han

Advisor: Jaewook Ahn

A dissertation submitted to the faculty of
Korea Advanced Institute of Science and Technology in
partial fulfillment of the requirements for the degree of
Doctor of Philosophy in Physics

Daejeon, Korea
May 27, 2016

Approved by

Jaewook Ahn
Professor of Physics

The study was conducted in accordance with Code of Research Ethics¹.

¹ Declaration of Ethical Conduct in Research: I, as a graduate student of Korea Advanced Institute of Science and Technology, hereby declare that I have not committed any act that may damage the credibility of my research. This includes, but is not limited to, falsification, thesis written by someone else, distortion of research findings, and plagiarism. I confirm that my thesis contains honest conclusions based on my own careful research under the guidance of my thesis advisor.

DPH
20107148

한대훈. 테라헤르츠 전자기파를 활용한 광물의 격자 진동과 슬릿 내부 물질의 편광 의존성에 관한 연구. 물리학과 . 2016년. 193+v 쪽. 지도교수: 안재욱. (영문 논문)

Daehoon Han. Lattice vibrations of mineral and polarization dependence of material in a slit using terahertz waves. Department of Physics . 2016. 193+v pages. Advisor: Jaewook Ahn. (Text in English)

초 록

이 논문에서 우리는 테라헤르츠 시 분해 분광을 활용한 광물의 광학 계수와 파장 이하 금속 슬릿 속에 속박된 물질의 편광 의존성에 관한 연구를 다루었다. 우리는 측정된 실험결과로부터 백운석이 테라헤르츠 광학 렌즈로써 사용될 수 있다는 것을 알 수 있었다. 또한, 세라피나이트 보석 광물이 0.96 테라헤르츠에서 격자 진동 상태를 가지고 있으며, 이 상태는 Kurosawa 공식으로 분석되었다. 또한, 슬릿 내부에 있는 젯산에서의 흡수가 사라지는 것을 실험적으로 관측함으로써 베테 회절 이론에 의해 예상된 특이한 현상을 확인할 수 있었다.

핵심 낱 말 테라헤르츠 시분해 분광, 세라피나이트, 격자 진동, 베테 회절 이론, 테라헤르츠 백운석 렌즈

Abstract

Terahertz time-domain spectroscopy was used to probe the optical constants of natural mineral compounds and the polarization dependence of material confined in a sub-wavelength metal slit. The experimental results show that dolomite is a promising candidate as THz optical element material and seraphinite exhibits lattice vibrations at 0.96 THz whose mode is analyzed by the Kurosawa formula. The abnormal behavior predicted by Bethe's diffraction theory is also experimentally observed from the vanishing in absorption from α -lactose in the slit.

Keywords Terahertz time-domain spectroscopy (THz-TDS), seraphinite, lattice vibrations, Bethe diffraction theory, THz dolomite lens

Contents

Contents	i
List of Tables	iv
List of Figures	v
Chapter 1. Introduction	1
Chapter 2. Experimental methods	3
2.1 Terahertz Time Domain Spectroscopy (THz-TDS)	3
2.2 Advantage of THz-TDS	6
2.3 THz generation using the Photoconductive antenna	7
2.3.1 Radiation by an accelerated electric point charge	8
2.3.2 Radiation induced by the nonlinear polarization	9
2.4 Other THz generation methods	13
2.4.1 Optical Rectification	13
2.4.2 Air plasma	16
2.5 THz detection method: Electro optic detection	17
2.5.1 Introduction	17
2.5.2 The Pockels effect and the Kerr effect	18
2.5.3 The index ellipsoid in the electro-optic medium	21
2.5.4 THz detection process using the Jones matrix	28
2.5.5 Calculation of the phase retardation Γ_{THz}	29
2.5.6 Electro-optic detection : Probing the index ellipsoid induced from elliptically polarized probe beams	32
2.5.7 Electro-optic detection : Probing the index ellipsoid induced from linear polarized probe beam	37
2.6 Spectral components from time-domain THz waveform	39
2.7 Summary	40
Chapter 3. Data analysis	42
3.1 Extraction of the complex refractive index	42
3.1.1 Optical constants for an optically thick sample with low absorption	44
3.1.2 Optical constants of two identical samples with different thicknesses	45
3.1.3 Numerical calculation: The fixed-point iteration method	46

3.1.4	Examples: optical constants of dolomite stone and Teflon	48
3.2	Dynamic range in TDS transmission spectroscopy	49
3.3	Dielectric constant and complex refractive index	50
Chapter 4.	THz spectroscopy of natural mineral compounds	51
4.1	THz spectroscopy of natural stones and its application	51
4.1.1	Introduction	51
4.1.2	Measurement of optical constants of natural stones	52
4.1.3	Lens fabrication using dolomite	55
4.1.4	Results and Discussion	58
4.1.5	Conclusion	60
4.1.6	Appendix	60
4.2	Lattice vibrations of natural seraphinite gemstone	64
4.2.1	Introduction	64
4.2.2	Experimental procedure	66
4.2.3	Results	66
4.2.4	Discussion	73
4.2.5	Conclusion	76
4.2.6	Appendix	77
Chapter 5.	THz spectroscopy of the polarization dependence of the resonant material confined in a sub-wavelength slit	79
5.1	Introduction	79
5.2	Experimental description	80
5.3	Theoretical background	81
5.3.1	Boundary conditions by Bethe	81
5.3.2	Bethe's diffraction theory by a small hole	86
5.3.3	Diffraction by a sub-wavelength slit	109
5.4	Results and discussion	117
5.5	Conclusion	120
Chapter 6.	Conclusion	121
Appendix		122
Chapter A.	Supplements	123
A.1	The physical units in THz frequency range	123
A.2	No Pockels effect in the centro-symmetric crystals	124
A.3	Estimating the peak intensity of the laser beam	124

A.3.1	Beam radius at the focus	124
A.3.2	Peak intensity (power) at the focus	125
A.3.3	Estimating the electric field strength and the peak in- tensity	126
A.4	Estimating the THz electric field strength	129
A.5	Radiated electric field by the nonlinear source in the far-field .	131
A.6	Generation and detection behavior from zinc-blende crystals with various cut orientation	136
A.6.1	THz generation via optical rectification	136
A.6.2	THz detection via the Pockels effect	141
A.7	EO detection by probing the index ellipse induced from linear polarized probe beam	147
A.8	Finding the optic axis on (110) ZnTe in the presence of THz field	147
A.9	THz pulse train shown in the measured THz field	150
A.10	Why the directionality of light becomes better for higher fre- quency light?	151
A.10.1	Fraunhofer diffraction in the rectangular aperture	151
A.10.2	Fraunhofer diffraction in the circular aperture	152
A.11	Different intensity of optical beam with 45° pol. by two optical components	155
Chapter B.	Experiment equipment	157
B.1	Lock-in amplifier	157
B.2	Laser system	157
Chapter C.	Useful mathematical formulas	158
	Bibliography	182
	Acknowledgments in Korean	191
	Curriculum Vitae in Korean	192

List of Tables

2.1	Typical physical units in the THz range	3
2.2	The existent electro-optic effect for each crystal symmetry.	19
4.1	Refractive indices n , extinction coefficients α (cm^{-1}) and thicknesses (mm) of the investigated natural stones at 0.5 THz.	54
4.2	Mineral concentration of the investigated stones.	56
4.3	Refractive indices n and extinction coefficients α (cm^{-1}) of dolomite and typical lens materials at 0.5 THz.	57
4.4	The characteristics of the strong absorption line of \perp -cut seraphinite at 0.96 THz.	69
4.5	Cartesian components corresponding to subscript m [104].	77
A.1	Transmitted intensities from an optical beam with 45° polarization through different optical elements. $R(\varphi)$ is the rotation matrix defined in Eq. (2.120).	155
C.1	Vector derivatives in each coordinate system.	161

List of Figures

2.1	THz waves are phase measurable ultra-broadband light with frequency range from 0.1 to 10 THz.	3
2.2	A schematic diagram of a conventional THz-TDS system. PCA : Photoconductive antenna, WP : Wollaston prism, QWP : quarter-wave plate.	4
2.3	A variety of THz generation methods. (a) Photoconductive antenna. (b) Optical rectification in nonlinear medium. (c) Plasma induced from intense laser pulses. A silicon (Si) substrate or a Teflon substrate is widely used as a low-pass filter.	5
2.4	(a) Measured THz time domain signal through THz-TDS. (b) Frequency domain spectrum after applying the Fourier transformation to time domain data. (c) Phase information is also obtained simultaneously. Blue and red indicate phase and phase after applying unwrap function, respectively.	5
2.5	(a) The radiation power as a function of the solid angle for the velocity term $\beta \ll 1$ and $\beta \rightarrow 1$. (b) THz waves emitted from accelerated free carriers induced from PCA are radiated in the forward or backward direction of the PCA since the velocity of the accelerated free carriers is much smaller than the speed of light c , which is the same when $\beta \ll 1$	7
2.6	Calculated photocurrent (gray line) in the PCA and the electric field amplitude of the THz radiation (blue line) as a function of time. The red line indicates a temporal shape of the laser pulses. All the lines were normalized for the sake of clarity [2].	10
2.7	(a) The installed PCA. The generated THz waves from the PCA are vertically polarized. (b) Photo of an enlarged PCA. (c) The antenna structure of the PCA (BATOP optoelectronics).	11
2.8	A simple physical picture of difference-frequency generation [7]	13
2.9	The coherence length of ZnTe as a function of THz frequency for given optical frequencies (wavelength).	15
2.10	The energy-level diagram of the four-wave mixing [7, 10, 20].	16
2.11	The schemes of electro-optic (EO) detection. A detailed description of EO detection can be found in section 2.5.	17
2.12	Geometry of the (110) ZnTe crystal represented as a THz sensor. A ZnTe has a (110) plane. The THz beam and probe beam counterpropagates through (110) ZnTe. α and φ are angles of the polarization of the THz beam and the polarization of the probe beam, respectively [21]. Here, the principal axes of the crystal and the lab frame are denoted as (x, y, z) and (x^*, y^*, z^*) , respectively.	27
2.13	The electro-optic detection using a quarter-wave plate and a Wollaston prism.	33
2.14	Schematic diagram of a typical setup for free-space EO detection. The polarization of the probe beam does not changed without THz waves. The polarization of the probe, however, is changed by birefringence in ZnTe induced by THz waves. By sweeping in time-domain using time-delay, the whole THz waveform can be measured. QWP and WP indicate a quarter-wave plate and a Wollaston prism, respectively.	36

2.15	The electro-optic detection using crossed polarizers.	37
2.16	Simple schematic representation by Fourier transformation.	39
2.17	The THz-TDS setup of in a linear configuration. There are two ways to co-propagate the THz waves and probe beam to ZnTe. One is to use an ITO wafer to reflect THz waves. The other is to use a Pellicle beam splitter or silicon substrate to reflect the probe beam. The PCA is biased by using a step function signal generated from a 65 kHz function generator with 30 V dc voltages (TOELLNER TOE 7704). The Lock-in amplifier was used to record the photo currents from the two photodiodes (or one photodiode). The reference signal of the Lock-in amplifier was locked to a step function signal provided by the 65 kHz function generator.	40
2.18	The constructed THz-TDS using (a) 4 Teflon lenses and (b) 4 parabolic mirrors, respectively. (c) The whole THz-TDS setup is purged with dry air to reduce the absorption by water vapor in the THz frequency range. (d) Enlarged sample section of THz-TDS in a linear configuration. (e) THz-TDS setup purged with acylic box.	41
3.1	The reflected rays are represented with the tilted angles for sake of clarity. E_i , E_{t_i} , and E_r are the initial wave, the successive transmitted waves, and the reference wave, respectively. By designating medium 1 as air and medium 2 as the sample, the transmission and reflection Fresnel coefficients are represented as t_{12} and r_{12} , respectively. The transmission of transmitted waves through the sample is determined at point P	42
3.2	The diagram of transmitted waves through two identical samples with different thickness. The relative transmission of transmitted waves through two samples is determined at point P	45
3.3	(a) Measured time-domain THz waveforms with and without a sample. The THz waves through a sample are time-delayed from the reference peak as much as Δt . Note that there is an earlier pulse than the main THz signal near 55 ps, which comes from the reflected optical probe beam. (b) Amplitude spectrums and (c) phase information of reference and sample THz signals after Fourier transformation. Here the sample is dolomite stone with a thickness of 8.31 mm.	48
3.4	The extracted refractive index (red solid line) and the extinction coefficient (black dotted line) of (a) dolomite and (b) Teflon.	49
3.5	The dynamic range of (a) dolomite and (b) Teflon measured by the transmission THz-TDS. The gray and red shaded areas represent the $\alpha_{\max}(\omega)$ and $\alpha(\omega)$ of each sample, respectively. The measurement ranges for (a) and (b) are valid for frequencies below 1 THz and 1.5 THz by comparing the two curves, respectively.	49
4.1	Measured refractive indices and extinction coefficients of stones in the frequency range from 0.2 to 1.2 THz corresponds to wavelengths between 1500 μm to 250 μm . Solid lines and dashed lines represent the extracted refractive indices and extinction coefficients of investigated stones, respectively.	53
4.2	a) Quartz weight % with respect to refractive index at 0.5 THz. (b) The extinction coefficient with respect to the refractive index. Each dotted lines represents a guide to the particle sizes of the rocks [62].	55

4.3	(a) Specification of the fabricated dolomite lens. f = effective focal length, f_b = back focal length, t_c = center thickness, t_e = edge thickness, R = radius curvature. (b) Photo of the fabricated dolomite lens.	57
4.4	(a) Schematic of our linear configuration THz-TDS setup using two THz lenses; a Teflon lens and the fabricated dolomite lens. Overall intensity profiles were measured by moving the lens with an XYZ translation stage. (b) Image of the THz-TDS setup corresponding to the boxed area of (a). The THz field was focused on to ZnTe by the fabricated dolomite lens. ITO playing a role as a dichroic polarization beam splitter reflects the THz field and transmits the probe beam. (c) A temporal THz amplitude signal measured at the focal point and the corresponding amplitude spectrum after Fourier transformation.	58
4.5	(a) Beam profile measurement geometry, where W_0 in Eq. (5) is the diameter of the collimated beam. (b) Extracted diameters (FWHM) of the focused THz field at various wavelengths obtained by numerical fitting of the amplitude profile to the Bessel function. (c) Transmission amplitudes with respect to frequency. All the amplitudes were divided by the amplitude of the THz signal measured without the fabricated dolomite lens. The colorbar indicates the magnitude of the signal with respect to the THz signal measured without the dolomite lens. The lines (solid line) fitted by the Bessel function plotted in the horizontal and vertical directions across the THz amplitude profile (open circle) are indicated in the figures (Normalized amplitude vs. position with respect to frequency).	59
4.6	(a) The spherical aberration formed by a single spherical surface [11,64]. (b) The spherical aberration formed by a plano-convex lens. (c) Reduction of aberration by turning the lens [11].	61
4.7	Atomic structure of seraphinite. The atomic position parameters are from Ref. [81]. The unit cell parameters are $a = 5.350(3)$, $b = 9.267(5)$, $c = 14.27(1)$, and $\gamma (\angle(a, c)) = 96.35(5)^\circ$	65
4.8	(a) Schematic representation of bulk seraphinite. The \perp -cut and \parallel -cut seraphinite samples are prepared as illustrated in (a). We assumed that the sample plane of each seraphinite is approximately corresponding to crystal axes as shown in (b)	66
4.9	(a) Measured electric-field amplitudes of a THz pulse at the azimuthal angle of 120° transmitted through the \perp -cut (blue solid line) and \parallel -cut (red dash-dot line) seraphinite sample, respectively, compared with the reference signal (black dotted line). The time delay Δt between the main peaks of the two signals corresponds to the differential index Δn between the sample ($n_g = 3.0$) and air ($n_a = 1$) times the the thickness ($d = 0.96$ mm) divided by c . (b) Polarization-dependent THz waveforms measured by varying the azimuthal angle of the \perp -cut and \parallel -cut seraphinites with respect to linearly-polarized incident THz waves. The THz waveforms are normalized for the sake of comparison.	67
4.10	(a, c) The index of refraction $n(\omega, \theta)$ for $\theta \in \{0, \dots, 360\}$ and (b, d) the extinction coefficient $\alpha(\omega, \theta)$ for $\theta \in \{0, \dots, 360\}$ of \perp -cut and \parallel -cut seraphinites measured as a function of the azimuthal angle (θ) with respect to the THz polarization direction, respectively; (a) $n_\perp(\omega, 120^\circ)$ and $n_\perp(\omega, 300^\circ)$, (b) $\alpha_\perp(\omega, 120^\circ)$ and $\alpha_\perp(\omega, 300^\circ)$. The strong absorption mode is measured at 0.96 THz. (c, d) $n_\parallel(\omega, \theta)$ and $\alpha_\parallel(\omega, \theta)$ at $\theta = 20^\circ, 60^\circ$, and 120° . (e) The strong absorption mode of \perp -cut seraphinite. When the extinction coefficient at azimuthal angle of $\theta = 120^\circ$ of \perp -cut seraphinite was fitted to two Lorentzian functions, the 0.96 THz absorption peak has a linewidth of 0.12 THz (FWHM).	68

4.11	(Color online) (a) The principle coordinates. (b) The sample coordinates of the \perp -cut sample. (c) The sample coordinates of the the \parallel -cut sample. (d) The lab-frame coordinates are transformed from the principle or sample coordinates via M , where θ_j and ϕ_j represent the polar angle and the azimuthal angle between the j -th dipole moment (red arrow) and the z' -axis. The crystal surface is represented by dark gray color in each figure.	70
4.12	(Color online) The effective susceptibility χ_{eff} of the \parallel -cut seraphinite is extracted by Eq. (4.32). $\chi_{\text{eff}}(0.96 \text{ THz})$ for B_u mode (blue) is fitted to Eq. (4.45). $\chi_{\text{eff}}(0.8 \text{ THz})$ and $\chi_{\text{eff}}(1.20 \text{ THz})$ corresponding to A_u modes (red) are fitted to Eq. (4.71) represented by the red solid line.	73
4.13	(Color online) The Phonon-polariton dispersion of the experimental results of \perp -cut seraphinite measured at an azimuthal angle of 120° . The dispersion relation and the experimental data are indicated with a red solid line and closed circles, respectively. The dispersion relation and the measured data are plotted with respect to the real parts of Eq. (4.57) and Eq. (4.59), respectively. The Kurosawa formula is represented with a blue dotted line, which is also computed using the real part of Eq. (4.57) in the case of no damping.	75
5.1	(a) Schematic experimental setup. The sub-wavelength-scale slits were located at the focus of the THz wave. Inset shows the polarization angle defined with respect to the slit direction. The wedge-shaped slits are consists of identical single slits with a width of d and a length of L . The polarization of the electric field and magnetic field are parallel to the slit direction for $\theta = 0$ and $\theta = \pi/2$, respectively, where the slit direction is along the slit length of L . (b) The geometry of the fabricated wedge-shaped pair of slits in the side and front views. The slits are fabricated in copper film deposited on a silicon substrate. (c) A reference slit and a sample slit obtained by using a compound of α -lactose and water. A rectangular hole with $10 \text{ mm} \times 20 \text{ mm}$ was used to estimate the thickness of spread lactose.	80
5.2	(a), (b) Red dotted rectangular boxes represent the boundary section for the boundary condition. Tangential and normal components are in the direction of x and z , respectively.	82
5.3	Schematic representations for the scattered field ($\mathbf{E}_1, \mathbf{H}_1$) and the diffracted field ($\mathbf{E}_2, \mathbf{H}_2$) propagating in (a) the normal direction, (b) the inclined direction and (c) the overall direction (upper half-plane) from the origin $z = 0$	84
5.4	(a) The magnetic surface charge density η_m over the hole. (b) Representation for the integral in Eq. (5.101).	94
5.5	Representation of integration in Eq. (5.159). α is an angle defined as $\angle(\hat{r}, \hat{z}'')$ and δ is an angle defined as $\angle(\hat{r}', \hat{r}'')$	102
5.6	Representations for integration in (a) Eq. (5.171b) and (b) Eq. (5.182b). α is an angle defined as $\angle(\hat{r}, \hat{z}'')$ and δ is an angle defined as $\angle(\hat{r}', \mathbf{H}_0)$. A unit vector \hat{m} is parallel to the constant H field vector \mathbf{H}_0	105
5.7	The magnetic surface charge density η over the slit.	110
5.8	The Gaussian cylinder in the slit.	111
5.9	Schematic geometry including a Gaussian sphere with a Gaussian surface (S) on the edge of the slit when $\mathbf{E}_0 \perp \mathbf{L}$	115

5.10	Average field amplitude of the measured transmitted THz waves at 0.53 THz through the reference slit with respect to the relative slit thickness of d for \parallel -case (black, closed circles) and \perp -case (gray, closed rectangles). Inset shows average field amplitude in near-field zone for \parallel -case (black, open circles) and \perp -case (gray, open rectangles) confirmed by the FDTD simulation. All the red and black solid lines represent fitting curves described by Eqs. (5.227) and (5.256), respectively. Note that measured average field amplitudes are normalized by a factor with the limitation for the \perp -case.	118
5.11	The extracted absorbances calculated by Eq. (5.259) for (a) the \parallel -case and (c) the \perp -case as a function of the relative slit width. Corresponding computed absorbances calculated by Eq. (5.260) for (b) the \parallel -case (d) for the \perp -case. Absorbance at 0.53 THz (e) at $d=16.5$ mm or (f) at $d=4$ mm. Absorbances at 1.2 THz and 1.37 THz (g) at $d=16.5$ mm and (h) at $d=8$ mm. All the measured data are plotted with closed circles (black) for the \parallel -case and open rectangles (gray) for the \perp -case. The fitting curves obtained by Eq. (5.260) are represented as red solid lines for the \parallel -case and black dashed lines for the \perp -case.	119
A.1	The spot size w (blue) of a Gaussian beam as a function of propagation direction of z	124
A.2	A Gaussian pulse and a square pulse as a function of time t . FWHM of the Gaussian pulse $ E(t) $ and square pulse are represented by blue letter and red letters, respectively.	126
A.3	THz field strength measurement setup in case of probing (a) the elliptically polarized probe beam and (b) the linearly polarized probe beam. The polarizer denoted by P has a slow axis oriented at 90° with respect to the former polarizer (not seen this figure). The experimental components should be the same as THz-TDS except for applying not THz waves but AC bias voltage to the EO material using function generator.	130
A.4	The described EO responsiveness measured frequency range.	131
A.5	Lab coordinates and crystallographic coordinates in case of (a) (110) ZnTe (b) (100) ZnTe.	139
A.6	The angular dependence of the radiated THz field with respect to the azimuthal angle θ of (110) ZnTe crystal.	140
A.7	Geometry of the (110) ZnTe crystal as a THz sensor. x , y and z are the principal axes of the ZnTe crystal, where the z -axis is parallel to $[001]$ of the crystal. α and φ are angles of the polarization of the THz beam and the polarization of the probe beam with respect to the z -axis $[001]$, respectively.	143
A.8	Geometry of (110) ZnTe crystal as a THz sensor. x , y and z are the principal axes of the ZnTe crystal and z -axis is parallel to $[001]$ of the crystal. α and φ are angles of the polarization of the THz beam and the probe beam with respect to the z -axis $[001]$, respectively.	146
A.9	Intersection of the normal surface of a biaxial crystal in xz plane. θ is the angle between the optic axis and k_z	148
A.10	Schematic diagram of measuring THz waveform using a probe pulse. (a) The optical probe beam is reflected by some optical elements. (b) When THz waveform is measured by the probe beam by varying the time-delay between the THz signal and the probe beam in a range depicted by a gray color, the THz waveform is measured as a shape with an earlier THz pulse illustrated in (c).	150
A.11	Graph of a function of $f(x)$	154
C.1	Trigonometric functions.	166

C.2 Triangle	167
C.3 Hyberbolic functions.	171
C.4 (a) A contour $C = C_1 + C_2$ on the complex plane $z = x + iy$. (b) There is singular pole at $z = 0$ in a contour C_3	180

Chapter 1. Introduction

Terahertz frequency waves refer to electromagnetic waves in the far-infrared (IR) frequency region ranging from 0.1 THz (0.33 cm^{-1}) to 10 THz (330 cm^{-1}) between microwave and far-infrared electromagnetic waves [1–4]. In the far-infrared frequency range, many physical phenomena occur due to material excitations resulting from magnons, plasmons, and phonons which are interesting topics in condensed matter physics [2–4]. Researchers studying in the field of atomic and molecular physics were anticipating to investigate the molecular rotation, vibration, and other modes in the same frequency range [2–4]. A half-century ago, it was recognized in the field of spectroscopy that probing the spectral features of material in the far-infrared frequency below 3 THz (100 cm^{-1}) was a challenging task due to the lack of coherent THz sources and techniques for measuring them [4,5]. Blackbody radiation from an incandescent light bulb was a commonly used light source to obtain low frequency waves although the light intensity was weak [4,5]. Detectors such as the bolometer or the pyroelectric detector had poor signal-to-noise ratios in the aforementioned frequency range so that researchers had to develop brighter far-IR sources and detectors with high sensitivity [4].

Thanks to the nonlinear optics, the wave mixing by the difference frequency generation (DFG) method was considered as a way to induce new frequencies covering the far-IR frequency range [1–7]. Advanced laser systems made it possible to generate and measure the coherent THz radiation [4]. The DFG process for short pulses is their optical rectification in which a pico-second (ps) rectified field with a shape of a single-cycle pulse can be generated by a femto-second (fs) Ti:sapphire mode-lock pulsed laser [1–4]. The THz waves can also be generated through the time-varying transient photocurrents excited by fs optical pulses in a photoconductive antenna [1–4]. The temporal shapes of the THz waves can be directly measured by a co-propagating optical pulse acting as an optical gate, where the linear electro-optic effect otherwise referred to as the inverse of optical rectification is used [1–4]. THz time-domain spectroscopy (THz-TDS) represents an integrated spectroscopic system comprised of experimental components related to the generation and detection of THz waves. The generation and detection of THz waves and THz-TDS are described in Chapter 2 in detail.

Direct field measurement carried out by electro-optic sampling allows us to simultaneously obtain the phase information as well as the amplitude of the transmitted or reflected waves from a sample without resorting to the Kramers-Kronig relationship [1,2]. Spectral information on the measured THz waveforms is simply computed by applying Fourier transformation to the time-domain THz waveforms with and without the sample. The index of refraction and the extinction coefficient are obtained by comparing the spectral transmission and the theoretical transfer function. If the measured time-window is sufficiently longer than the duration of the main THz waveform, several echo signals appear in the time-domain data caused by the multiple internal reflections described by the Fabry-Pérot effect. Thus, the numerical method to extract the material parameter given by the complex refractive index (\tilde{n}) should be considered for use. In Chapter 3, the material parameter extractions for an optically thick sample as well as two identical samples were explained. The dynamic range in THz-TDS was also discussed. All the extractions are described only in the context of the transmission-type spectroscopy.

Chapter 4 describes the spectroscopic results of materials in the THz frequency range from 0.1 THz to 2 THz. As mentioned above, THz-TDS played an important role in investigating new properties and phenomena of materials in the THz frequency range. In our lab, we found out that natural stones

are transparent in the measured frequency range, where dolomite stone in particular had a uniform refractive index of 2.7 and a slightly low absorption in the measured frequency range. The feasibility of a THz lens fabricated with dolomite was also demonstrated by beam profile measurement which showed good agreement with the Fraunhofer diffraction theory. Similarly, we found for the first time that seraphinite gemstone with a monoclinic crystal system had terahertz frequency lattice vibrations at 0.96 THz. This was proven by the phonon-polariton dispersion relation showing excellent agreement with theoretical expectations based on Kurosawa formula with damping terms. It is worth to note that the high quality factor of this mode is comparable to the well-known absorption mode at 0.53 THz in a α -lactose monohydrate. Furthermore, we demonstrated that isotropic and anisotropic behaviors in seraphinite can be described by linear and high-order polarization terms. We hope that THz spectroscopy may become useful for the identification and characterization of various natural stones such as gemstones.

Chapter 5 describes the polarization dependence of material confined in a sub-wavelength metal slit in which the experiments were conducted by THz-TDS. The diffracted field through a slit can be explained by Kirchhoff's diffraction theory provided that the slit width is large compared to the wavelength of the incident field. Although Kirchhoff's theory fails in the sub-wavelength region, where the slit width is sufficiently small compared to the wavelength, we may induce from the waveguide theory that the electric field perpendicular to the slit direction can propagate through the slit due to the low cutoff frequency. Whereas the electric field parallel to the slit direction, however, is difficult to propagate owing to the same analogy. Compared to the electric field, the magnetic field perpendicular or parallel to the slit direction is always considered as constant over the slit. This is because the boundary conditions obtained by Bethe's first-order approximation are not influenced by the shape and size of the aperture. Thus, only the E field inside the slit exhibits a strong polarization dependence. Using α -lactose monohydrate having a strong absorption line at 0.53 THz, we investigated the temporal and spectral amplitude changes of transmitted THz waves within a slit with respect to the slit width. Experimental result revealed that the spectral response of the material was strongly coupled with the polarization state of the THz wave and that the material did not interact with the THz wave in the limit of an extreme sub-wavelength-sized slit.

The conclusions made throughout this dissertation will be summarized in Chapter 6.

Chapter 2. Experimental methods

2.1 Terahertz Time Domain Spectroscopy (THz-TDS)

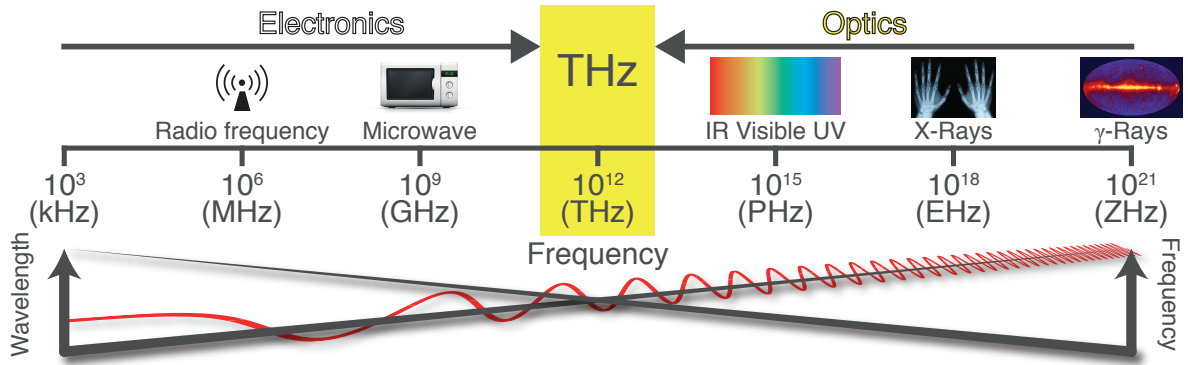


Figure 2.1: THz waves are phase measurable ultra-broadband light with frequency range from 0.1 to 10 THz.

Terahertz (THz) waves, also called as THz field, T-rays, THz radiation or submillimeter radiation, are a kind of electromagnetic waves with frequencies ranging from 0.1 THz to 10 THz (or sometimes 100 THz), which lie between microwave and far infrared rays (FIR) as shown in Fig. 2.1. Physical parameters corresponding to 1 THz have a relation given by

$$1 \text{ THz} \Leftrightarrow 300 \mu\text{m} \Leftrightarrow 33 \text{ cm}^{-1} \Leftrightarrow 4.1 \text{ meV}, \quad (2.1)$$

which is explained in section A.1. Typical physical units in the THz range are summarized in Table 2.1.

Terahertz time domain spectroscopy (THz-TDS) is a spectroscopic method widely used in a variety of scientific and industrial fields due to its specific properties. A conventional THz-TDS in a transmission configuration is shown in Fig. 2.2. To understand the mechanism of THz-TDS, one needs to know about the femtosecond (fs) pulsed laser, methods on THz generation and detection methods for the generated THz wave. Each topic is further discussed in chapter 2.

Although many scientists have been conducting research on THz sources, there does not exist a THz source with a high signal to noise ratio (SNR) that can scan the entire frequency range from 0.1 THz to 10 THz (or 100 THz). There are, however, alternatives that can overcome this situation. One may use a laser or an accelerator to generate THz waves. An accelerator, which is comprised of a variety of components, consists of two primary components: a linear accelerator system and an undulator system.

Frequency (THz)	Wavelength (μm)	Wavenumber (cm^{-1})	Energy (meV)
0.1	3000		
0.5	600		
1.0	300	33	4.1
2.0	150		

Table 2.1: Typical physical units in the THz range

A free electron laser (FEL) is generally known as the unit of a linear accelerator and undulator. THz waves are generated from the linear accelerator system by coherent transition radiation (CTR) [8, 9]. Other THz generation techniques using the accelerator are not treated here. If we do not use an accelerator, then there is no alternative but to use a laser system.

There are several methods to generate THz waves using a table-top laser system. A femtosecond (fs) Ti:Sapphire pulsed laser with a repetition rate of 80 MHz or an amplifier system with a repetition rate of 1 kHz or 10 Hz is generally employed to generate THz waves in ambient free space. The THz waves are generated through the optical excitation process induced by ultrashort fs lasers [10], which is easily described with the wave equation [7] as

$$\left[\nabla^2 - \frac{\epsilon^{(1)}(\omega)}{c^2} \frac{\partial^2}{\partial t^2} \right] \tilde{\mathbf{E}}_{\text{THz}}(z, t) = \frac{1}{c^2} \frac{\partial^2}{\partial t^2} \tilde{\mathbf{P}}^{\text{NL}}(z, t), \quad (2.2)$$

where the nonlinear polarization (density) term $\tilde{\mathbf{P}}^{\text{NL}}$ acts as a source of THz waves and $\epsilon^{(1)}$ is the relative dielectric constant. Nonlinear polarization arises from the optical excitation process (sources of THz waves are produced) which occur in the following cases. First, a semiconductor is illuminated by ultrashort pulses, where free carriers are generated. Second, ultrashort pulses either pass through a

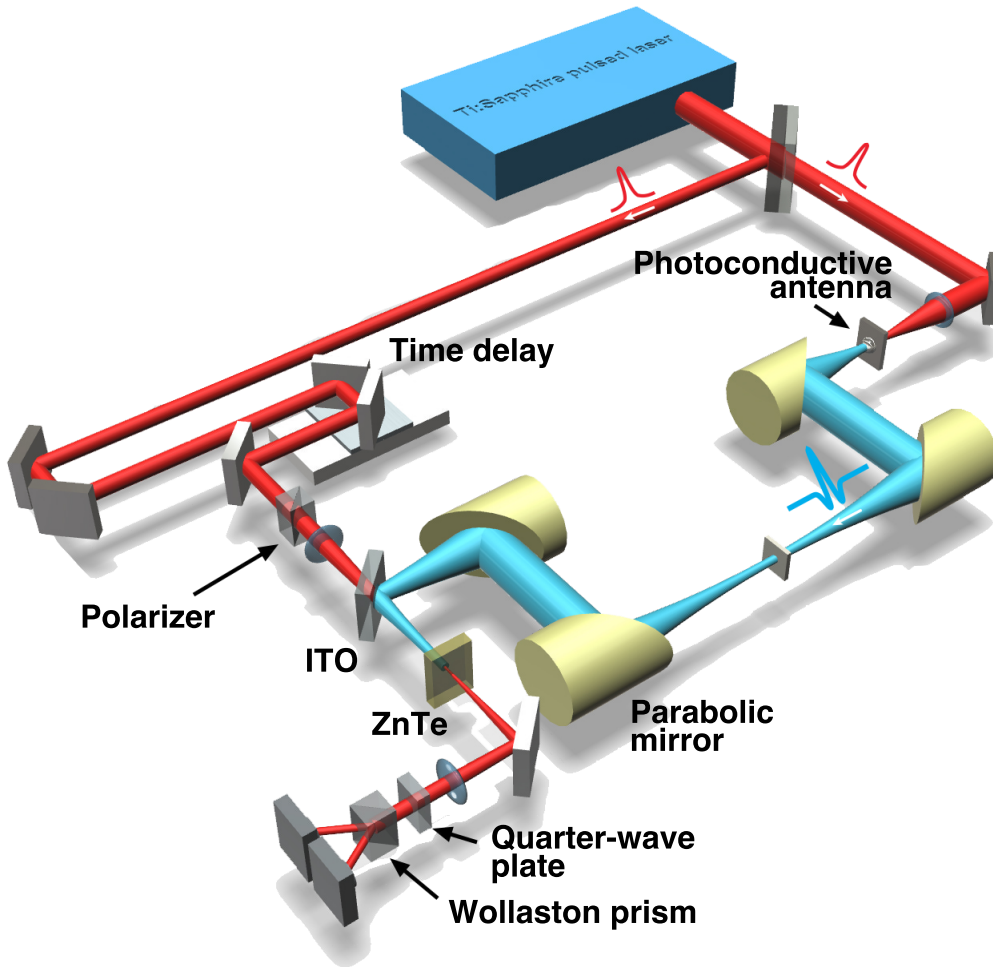


Figure 2.2: A schematic diagram of a conventional THz-TDS system. PCA : Photoconductive antenna, WP : Wollaston prism, QWP : quarter-wave plate.

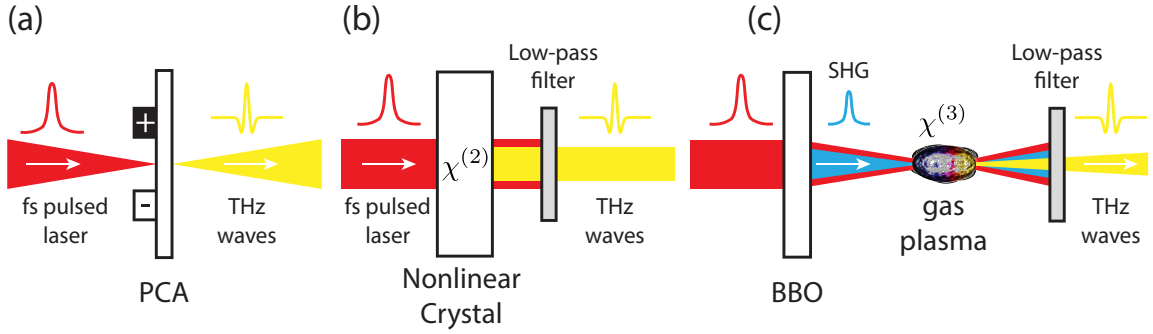


Figure 2.3: A variety of THz generation methods. (a) Photoconductive antenna. (b) Optical rectification in nonlinear medium. (c) Plasma induced from intense laser pulses. A silicon (Si) substrate or a Teflon substrate is widely used as a low-pass filter.

nonlinear medium or focus onto a nonlinear medium. Third, ultrashort pulses are focused in ambient air or in another gaseous condition. To generate THz waves, each aforementioned case is experimentally implemented using the photoconductive antenna (PCA), by optical rectification in nonlinear medium, and optical-ionized plasma, respectively (Fig. 2.3). Each generation method is detailed in section 2.3.

How could the generated THz waves be measured? Although there are a few THz detectors such as the bolometer, the pyroelectric detector or the Golaycell, these are all incoherent detectors. Electro-optic (EO) sampling or detection is widely used to measure THz waves by many research groups. The most powerful advantage of EO detection is directly measuring the THz electric field itself. It is to note that there is no further way to measure the phase of the THz waves during measurement. By using EO detection, the THz electric waveform itself can be obtained. Thus, the EO detection method is a coherent detection method in which the amplitude and phase information of THz waves can be obtained simultaneously [10]. For this reason, the waveform measurement in terahertz time domain spectroscopy (THz-TDS) allows one to obtain not only the spectral amplitude but also the spectral phase information by simply applying the Fourier transformation to the time domain signal without resorting to the Kramers-Kronig relationship. EO detection is well described in section 2.5.

Figure 2.4 shows a typical THz signal in the time domain, spectral amplitude and phase in frequency domain after applying the Fourier transformation to the time domain data. We find that the measured THz waveform has only a few cycles of oscillations and consequently has a broadband spectrum. The THz generation mechanism is explained in section 2.3.

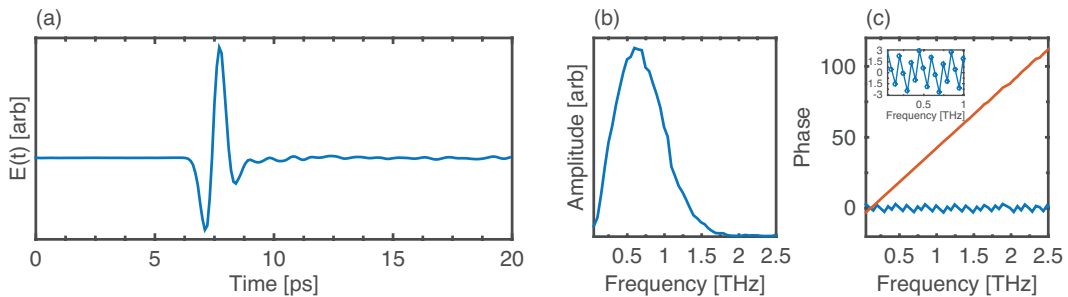


Figure 2.4: (a) Measured THz time domain signal through THz-TDS. (b) Frequency domain spectrum after applying the Fourier transformation to time domain data. (c) Phase information is also obtained simultaneously. Blue and red indicate phase and phase after applying unwrap function, respectively.

2.2 Advantage of THz-TDS

Terahertz time domain spectroscopy (THz TDS) has many advantages. Above all, THz TDS allows one to obtain not only the spectral amplitude but also the spectral phase information by simply applying the Fourier transformation to the time domain signal. It is difficult to directly obtain the optical constants (refractive index, absorption coefficient) of a sample as a function of frequency using conventional interferometers such as the Michelson interferometer or Fourier transform infrared spectroscopy (FT-IR). Since phase information as a function of frequency vanishes when there is no sample in the optical path of the aforementioned interferometers, phase information of the reference beam cannot be obtained. The Wiener–Khinchin theorem explains why the phase information cannot be obtained using conventional interferometer techniques [11].

The Wiener–Khinchin theorem can be derived by the autocorrelation between two electric waves denoted by $\tilde{E}(t)$ and $\tilde{E}(t + \tau)$, where τ represents the time-delay between the two waves. The intensity (irradiance) can be obtained from the superposition of the two waves given by

$$I = \int dt \left| \tilde{E}(t) + \tilde{E}(t + \tau) \right|^2. \quad (2.3)$$

Provided the interference term $a(\tau)$ of the two electric waves is expressed as

$$a(\tau) = \int dt \tilde{E}^*(t) \cdot \tilde{E}(t + \tau), \quad (2.4)$$

the intensity becomes¹

$$I = \int dt \left[|\tilde{E}(t)|^2 + |\tilde{E}(t + \tau)|^2 \right] + 2 \Re \{ a(\tau) \}. \quad (2.5)$$

Therefore the intensity is proportional to the last term of $a(\tau)$. The Fourier transformation is defined as [7, 12]

$$\tilde{E}(t) = \frac{1}{2\pi} \int_{-\infty}^{\infty} d\omega \tilde{F}(\omega) e^{-i\omega t} \equiv \mathcal{F}[\tilde{F}(\omega)], \quad \tilde{F}(\omega) = \int_{-\infty}^{\infty} dt \tilde{E}(t) e^{i\omega t} \equiv \mathcal{F}^{-1}[\tilde{E}(t)]. \quad (2.6)$$

By a change of variable, the second term $\tilde{E}(t + \tau)$ in Eq. (2.4) can be expressed as follows

$$\begin{aligned} \tilde{E}(t + \tau) &= \frac{1}{2\pi} \int d\omega \tilde{F}(\omega) e^{-i\omega(t+\tau)} \\ &= \frac{1}{2\pi} \int d\omega \left[\tilde{F}(\omega) e^{-i\omega\tau} \right] e^{-i\omega t} = \mathcal{F} \left[\tilde{F}(\omega) e^{-i\omega\tau} \right]. \end{aligned} \quad (2.7)$$

¹The two electric waves can be represented in terms of real and imaginary part as follows

$$\tilde{E}_i = E_i e^{-i\phi_i} \text{ for } i \in \{1, 2\}.$$

Then the intensity becomes

$$|\tilde{E}_1 + \tilde{E}_2|^2 = (\tilde{E}_1 + \tilde{E}_2)^* \cdot (\tilde{E}_1 + \tilde{E}_2) = |\tilde{E}_1|^2 + |\tilde{E}_2|^2 + 2 \Re(\tilde{E}_1^* \cdot \tilde{E}_2),$$

where

$$\Re(\tilde{E}_1^* \cdot \tilde{E}_2) = E_1 E_2 \cos(\phi_1 - \phi_2) = \Re(\tilde{E}_2^* \cdot \tilde{E}_1).$$

From this equation, we obtain

$$\mathcal{F}^{-1}[\tilde{E}(t+\tau)] = \int dt \tilde{E}(t+\tau) e^{i\omega t} = \tilde{F}(\omega) e^{-i\omega\tau}. \quad (2.8)$$

Therefore, the two terms of electric waves terms in Eq. (2.4) can be written as the Fourier component in the form

$$\begin{aligned} a(\tau) &= \int dt \tilde{E}^*(t) \cdot \tilde{E}(t+\tau) = \int dt \left[\frac{1}{2\pi} \int d\omega \tilde{F}(\omega) e^{-i\omega t} \right]^* \cdot \tilde{E}(t+\tau) \\ &= \frac{1}{2\pi} \int d\omega \tilde{F}^*(\omega) \cdot \underbrace{\left[\int dt \tilde{E}(t+\tau) e^{i\omega t} \right]}_{\tilde{F}(\omega) e^{-i\omega\tau}} = \frac{1}{2\pi} \int d\omega |\tilde{F}(\omega)|^2 e^{-i\omega\tau} = \mathcal{F}[|\tilde{F}(\omega)|^2]. \end{aligned} \quad (2.9)$$

Applying the Fourier transform to both sides of Eq. (2.9), we obtain the Wiener-Khinchin theorem given by

$$\mathcal{F}^{-1}[a(\tau)] = |\tilde{F}(\omega)|^2. \quad (2.10)$$

From this result, we find that the phase term in autocorrelation measured by conventional interferometer techniques such as FT-IR or Michelson interferometer vanishes when the Fourier transform is applied in the time-domain (or spectral-domain). THz-TDS is thus a powerful spectroscopic technique since it has the power to obtain the phase information either with and without a sample.

2.3 THz generation using the Photoconductive antenna

A photoconductive antenna (PCA) is an electrical switch that increases the electrical conductivity of a semiconductor by illuminated photons on the semiconductor with high enough energy exciting the electrons in the valence band of the semiconductor [2]. A fs Ti:Sapphire pulsed laser with a sufficiently high enough energy to excite electrons in the valence band of the semiconductor is generally used to yield photons. When the electrons in the valence band are excited to the conduction band by the pulsed

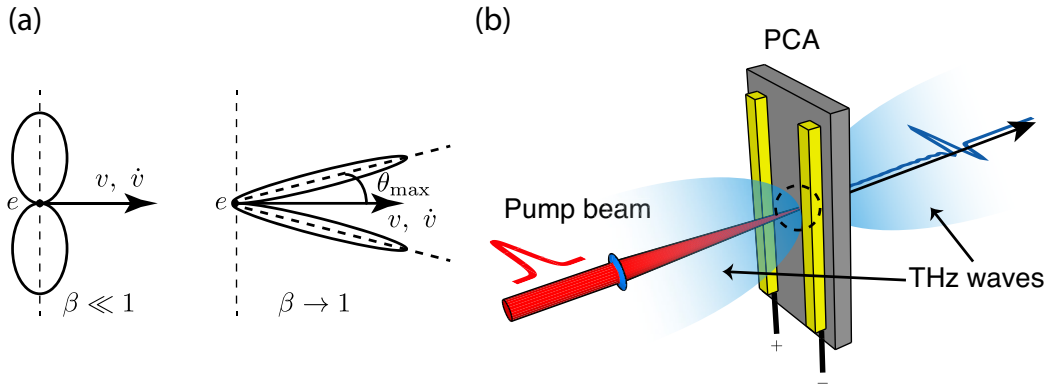


Figure 2.5: (a) The radiation power as a function of the solid angle for the velocity term $\beta \ll 1$ and $\beta \rightarrow 1$. (b) THz waves emitted from accelerated free carriers induced from PCA are radiated in the forward or backward direction of the PCA since the velocity of the accelerated free carriers is much smaller than the speed of light c , which is the same when $\beta \ll 1$.

beam, free carriers are produced in the conduction band.² The free carriers are then accelerated if a bias electric field is applied to the semiconductor. In our experiment setup, a bias electric field is generated by a step function signal using a 65 kHz function generator with a dc voltages of 30 V (TOELLNER TOE 7704). The two generation processes of the THz waves are described below.

2.3.1 Radiation by an accelerated electric point charge

An accelerated electron, which can be described as a moving electric point charge, generates radiation field into space [13,14]. An accelerated electric point charge can be expressed using the Liénard-Wiechert potential. The radiated electric field from the accelerated particle using the Liénard-Wiechert potential is given by [13,14]

$$\mathbf{E}_{\text{THz}}(\mathbf{x}, t) = \frac{e}{4\pi\epsilon_0 c} \left[\frac{\hat{\mathbf{n}} \times \left\{ (\hat{\mathbf{n}} - \boldsymbol{\beta}) \times \dot{\boldsymbol{\beta}} \right\}}{(1 - \hat{\mathbf{n}} \cdot \boldsymbol{\beta})^3 R} \right]_{\text{ret}}, \quad (2.11)$$

where e is the charge of an electron, c is the speed of light, $R(t')$ is the distance from the source point \mathbf{x}' to the field point \mathbf{x} at a retarded time t' as $R(t') = |\mathbf{x} - \mathbf{x}'|$, and the retarded time is defined by $t' = t - R/c$. $\boldsymbol{\beta}$ and $\hat{\mathbf{n}}$ are defined by

$$\boldsymbol{\beta} = \frac{1}{c} \frac{d}{dt'} \mathbf{x}'(t'), \quad \hat{\mathbf{n}} = \frac{\mathbf{R}}{R}. \quad (2.12)$$

The non-relativistic approximation has to be considered if β is much less than 1 ($\beta \ll 1$). Eq. (2.11) in the non-relativistic case is modified as [13,14]

$$\mathbf{E}_{\text{THz}}(\mathbf{x}, t) = \frac{e}{4\pi\epsilon_0 c} \left[\frac{\hat{\mathbf{n}} \times \left\{ \hat{\mathbf{n}} \times \dot{\boldsymbol{\beta}} \right\}}{R} \right]_{\text{ret}}, \quad (2.13)$$

Equation 2.13 is valid if β is much less than 1 ($\beta \ll 1$), which means that the velocity term β of the particle is much smaller than the speed of light c . In this nonrelativistic situation described in Fig. 2.5–(a), in the case of $\beta \ll 1$, there is no radiation in the forward or backward directions and the radiation has maximum power in the direction perpendicular to the propagation direction of the particle.

To understand the generation processes of THz waves produced from PCA, we start from Eq. (2.13) that can be slightly modified to

$$\begin{aligned} \mathbf{E}_{\text{THz}}(\mathbf{x}, t) &= \frac{e}{4\pi\epsilon_0 c} \left[\frac{\hat{\mathbf{n}} \times \left\{ \hat{\mathbf{n}} \times \dot{\boldsymbol{\beta}} \right\}}{R} \right]_{\text{ret}} \\ &= \frac{1}{4\pi\epsilon_0 c^2} \left[\frac{\hat{\mathbf{n}}}{R} \times \left\{ \hat{\mathbf{n}} \times \frac{d^2}{dt'^2} (e \mathbf{x}') \right\} \right]_{\text{ret}} = \frac{\mu_0}{4\pi} \frac{\hat{\mathbf{n}}}{R} \times \left(\hat{\mathbf{n}} \times \frac{d^2 \mathbf{p}}{dt'^2} \right)_{\text{ret}}, \end{aligned} \quad (2.14)$$

where \mathbf{p} is a dipole moment that has the same meaning of the polarization density [13]. From Eq. (2.14), we find that the polarization induced from a dipole moment can be a source of THz waves, which shows the same result induced from the wave equation Eq. (2.2). The continuity equation is given by [2,12]

$$\nabla' \cdot \mathbf{J}(\mathbf{x}', t') + \frac{\partial}{\partial t'} \rho(\mathbf{x}', t') = 0, \quad (2.15)$$

²A frequency of 1 THz is corresponding to a wavelength of 300 μm . Similarly, we find that a wavelength of 800 nm is corresponding to 375 THz. We thus find from an equation of $E = \hbar\omega$ (E means energy) that the photon energy at 800 nm is 1.53 eV, which is larger than the bandgap of GaAs (1.42 eV). Note that GaAs is the typical composition of the PCA.

where ρ and \mathbf{J} represent the charge carrier density and the photocurrent density, respectively. By integration by parts, the time derivative in Eq. (2.14) can be expressed as³

$$\begin{aligned}\frac{d\mathbf{p}}{dt'} &= \frac{d}{dt'} \int d^3x' \mathbf{x}' \rho(\mathbf{x}', t') = \int d^3x' \mathbf{x}' \frac{\partial \rho(\mathbf{x}', t')}{\partial t'} \\ &= - \int d^3x' \mathbf{x}' (\nabla' \cdot \mathbf{J}(\mathbf{x}', t')) = \int d^3x' \mathbf{J}(\mathbf{x}', t'),\end{aligned}\quad (2.18)$$

where the Leibniz rule is used. Provided I_{PC} is the photocurrent, Eq. (2.14) becomes

$$\begin{aligned}\mathbf{E}_{\text{THz}}(\mathbf{x}, t) &= \frac{\mu_0 \hat{\mathbf{n}}}{4\pi R} \times \left(\hat{\mathbf{n}} \times \frac{d}{dt'} \int d^3x' \mathbf{J}(\mathbf{x}', t') \right)_{\text{ret}} \\ &= \frac{\mu_0 \hat{\mathbf{n}}}{4\pi R} \times \left(\hat{\mathbf{n}} \times \frac{d}{dt'} I_{PC}(t') \right)_{\text{ret}} \propto \frac{d}{dt} I_{PC}(t),\end{aligned}\quad (2.19)$$

where $d/dt' = d/dt$ and $t' = t - R/c$. This is described in section A.68 in detail.

The emitted THz waves are therefore proportional to the time derivative of the photocurrent. If we let \mathbf{p} (I_{PC}) be parallel to the polar axis of $\hat{\theta}$, then the radiated electric field will be in the direction of θ since $\hat{\mathbf{n}}$ is the radial unit vector \hat{r} itself. This is also described in more detail in section C. Note that the polarization of THz waves generated from PCA is dependent on the direction of the bias electric field (Fig. 2.5(b)) [2].

The photo-induced current $I(t)$ is expressed in terms of the optical pulse and the impulse current response given by

$$I_{PC}(t) = \int dt' I_{\text{opt}}(t - t') en(t')v(t'), \quad (2.20)$$

where I_{opt} is the optical pulse with a Gaussian shape and e is the electron charge. n and v are the carrier density and the velocity difference between electron and hole, respectively [2, 15]. Figure 2.6 shows the calculated photocurrent $I(t)$ and the derivative of the current of the generated THz waves from the PCA. Due to the generation mechanism, the THz waves exhibit a sub-cycle pulsed shape.

2.3.2 Radiation induced by the nonlinear polarization

The nonlinear wave equation in Eq. (2.2) shows that the electric field can be generated by the nonlinear source term \mathbf{P}^{NL} . Before the polarization terms are divided into the linear and nonlinear terms, the wave equation for the field \mathbf{E} in free space with a given charge ρ and current density \mathbf{J} can

³By integration by parts, the integral of the photocurrent J in the one dimension with respect to the given 1 D range can be computed given by

$$\int_{\mathbf{V}} dx J(x) \left[\frac{d}{dx} x \right] = \left[\cancel{J(x)x} \right]_{\mathbf{V}} - \int_{\mathbf{V}} dx x \left[\frac{dJ(x)}{dx} \right] = - \int_{\mathbf{V}} dx x \left[\frac{dJ(x)}{dx} \right], \quad (2.16)$$

where the first term should be canceled out due to the physical reality. With the same analogy, the photocurrent J in 3 dimensions can be written by

$$\int_{\mathbf{V}} d^3x \mathbf{J}(\mathbf{x}) = \int_{\mathbf{V}} d^3x \mathbf{J}(\mathbf{x}) [\nabla \cdot \mathbf{x}] = - \int_{\mathbf{V}} d^3x \mathbf{x} [\nabla \cdot \mathbf{J}(\mathbf{x})]. \quad (2.17)$$

be expressed as [12]⁴

$$\nabla^2 \mathbf{E} - \frac{1}{c^2} \frac{\partial^2}{\partial t^2} \mathbf{E}(\mathbf{x}, t) = -\frac{1}{\epsilon_0} \left[-\nabla \rho(\mathbf{x}, t) - \frac{1}{c^2} \frac{\partial}{\partial t} \mathbf{J}(\mathbf{x}, t) \right]. \quad (2.22)$$

Analogous to Eqs. (A.52) and (A.62), the retarded solution for the field can be obtained as [12]

$$\mathbf{E}(\mathbf{x}, t) = -\frac{1}{4\pi\epsilon_0} \int d^3x' \frac{1}{R} \left[-\nabla' \rho(\mathbf{x}', t') - \frac{1}{c^2} \frac{\partial}{\partial t'} \mathbf{J}(\mathbf{x}', t') \right]_{\text{ret}}, \quad (2.23)$$

where $R = |\mathbf{R}| = |\mathbf{x} - \mathbf{x}'|$ and the retarded time is denoted by $t' = t - R/c$. For the electrically neutral media such as a semiconductor [1], ρ is zero. Thus, the field becomes

$$\mathbf{E}(\mathbf{x}, t) = \frac{1}{4\pi\epsilon_0 c^2} \int d^3x' \frac{1}{R} \left[\frac{\partial}{\partial t'} \mathbf{J}(\mathbf{x}', t') \right]_{\text{ret}}. \quad (2.24)$$

Note that we are interested only in the far-field solution of the radiated THz field. By Eqs. (A.68) and (A.82), the retarded field solution in the far-field is expressed (in analogy to Eq. (A.83)) as

$$\mathbf{E}(\mathbf{x}, t) = \frac{\mu_0}{4\pi r} \frac{\partial}{\partial t} \int d^3x' \mathbf{J} \left(\mathbf{x}', t' = t - \frac{R}{c} \right), \quad (2.25)$$

where $r = |\mathbf{x}|$ and $1/(\epsilon_0 c^2) = \mu_0$.

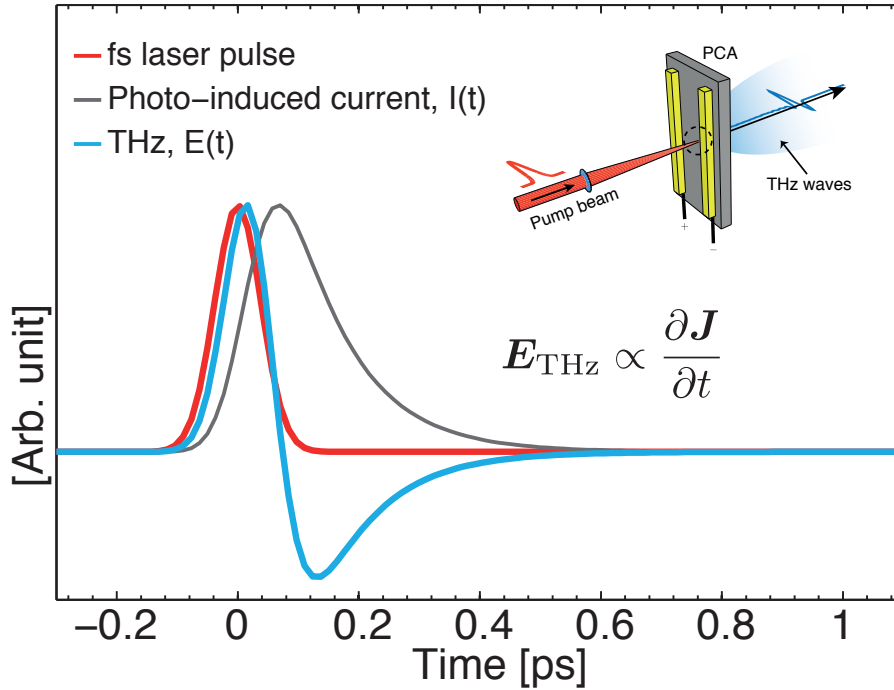


Figure 2.6: Calculated photocurrent (gray line) in the PCA and the electric field amplitude of the THz radiation (blue line) as a function of time. The red line indicates a temporal shape of the laser pulses. All the lines were normalized for the sake of clarity [2].

⁴See Jackson [12] p. 246. This equation can be obtained by

$$-\nabla [\text{Eq. (6.15)}] - \frac{\partial}{\partial t} [\text{Eq. (6.16)}] \quad (2.21)$$

with $-\partial \mathbf{A} / \partial t = \mathbf{E} + \nabla \Phi$. Eq. (6.15) and Eq. (6.16) are in Jackson [12].

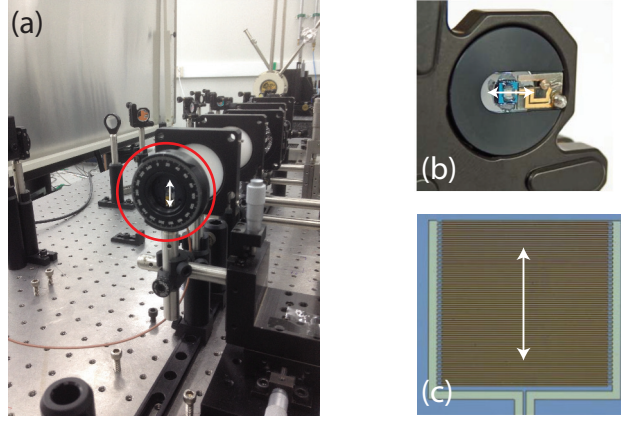


Figure 2.7: (a) The installed PCA. The generated THz waves from the PCA are vertically polarized. (b) Photo of an enlarged PCA. (c) The antenna structure of the PCA (BATOP optoelectronics).

In a similar fashion to Eq. (A.85), the radiated electric field in the far-field can be consequently obtained in the form [1, 15]

$$\mathbf{E}_{\text{THz}}(\mathbf{x}, t) \propto \frac{\partial}{\partial t} \mathbf{J}(t), \quad (2.26)$$

where the medium is assumed to be spatially homogeneous.⁵ The current density J is induced by the produced carriers excited by the optical pulsed beam, or

$$\mathbf{J} = \hat{z} J = \hat{z} en(t)v(t), \quad (2.27)$$

where \hat{z} is the direction of the current density, n is the carrier density, v is the average velocity of the carrier and e is the charge of a proton. From Eqs. (2.26) and (2.27), the radiated THz electric field becomes [1, 2, 15]

$$E_{\text{THz}}(t) \propto \frac{\partial}{\partial t} J(t) = ev \frac{\partial n}{\partial t} + en \frac{\partial v}{\partial t}. \quad (2.28)$$

The carrier density n and the carrier velocity v can be expressed as rate equations in the forms [1, 2, 15]

$$\frac{dn}{dt} = -\frac{n}{\tau_c} + G(t), \quad (2.29)$$

$$\frac{dv}{dt} = -\frac{v}{\tau_s} + \frac{e}{m} E, \quad (2.30)$$

where τ_c is the carrier trapping time, τ_s is the momentum relaxation time and m is the effective of the carriers. The generation rate G of the carrier by the optical beam can be written as

$$G(t) = n_0 \exp \left[-\frac{t^2}{\sigma^2} \right], \quad (2.31)$$

where n_0 represents the initial carrier density [15].

Since the carrier trapping time between electrons and holes is much shorter than their recombination time, the carrier lifetime is determined by the carrier trapping time τ_c . Thus, the carrier lifetime is considered to be τ_c [15]. According to the state of the arts of the semiconductor technology, the carrier trapping time τ_c can be reduced to the sub-picosecond range resulted from a high concentration of

⁵See the description above Eq. (A.85).

defects. By the Newton's second law⁶, the differential equation in Eq. (2.30) can be expressed as⁷

$$v(t) = \mu_e E \left[1 - \exp\left(-\frac{t}{\tau_s}\right) \right], \quad (2.42)$$

where the electron mobility μ_e is denoted as $\mu_e \equiv e\tau_s/m$. The momentum relaxation time τ_s is a characteristic parameter obtained from the electron mobility μ_e , which is about 30 fs for a low-temperature-grown GaAs (LT-GaAs) [2, 15].

The theoretical analysis shows that THz radiation from carrier density change is more dominant than THz radiation from carrier acceleration [15]. This can be understood by comparing the time parameters τ_c and τ_s . Since sub-femtosecond τ_s is sufficiently enough compared to sub-picosecond τ_c , the current density induced by change in carrier density change dn/dt becomes more prominent than the change in current density induced by the carrier acceleration dv/dt .

Figure 2.7 shows a PCA (iPCAp-21-05-1000-800-h) from BATOP optoelectronics installed in a THz-TDS setup. Although THz waves from a PCA are radiated in the forward or backward directions as in Fig. 2.5(b), only the forward THz waves can be detected since they are needed for the electro-optic (EO) sampling part to measure the THz waves.

⁶See D. J. Griffiths, *Introduction to electrodynamics* 2nd edition, p. 361.

⁷Let's solve a differential equation in Eq. (2.30) given by

$$\frac{dv}{dt} + \gamma v = \dot{v} + \gamma v = A, \quad (2.32)$$

where $\gamma = 1/\tau_s$ and $A = eE/m$. With the substitution $d/dt \rightarrow D$, a complementary solution for Eq. (2.32)

$$(D + \gamma)v(t) = 0, \quad (2.33)$$

which implies that

$$v(t) = c_1 e^{-\gamma t}, \quad (2.34)$$

where c_1 is an arbitrary constant. Since there is a constant factor A in right-hand side in Eq. (2.32), the particular solution v_p for Eq. (2.32) can be expressed as

$$v_p = c_2, \quad (2.35)$$

which follows that

$$1 \left| \begin{array}{l} \gamma \quad v_p = c_2 \\ \dot{v}_p(t) = 0 \\ Lv_p(t) = \gamma c_2. \end{array} \right. \quad (2.36)$$

It is noted that γc_2 in Eq. (5.164) have to be consistent with A in Eq. (2.32). Then v_p is represented in the form

$$v_p(t) = c_2 = \frac{A}{\gamma}. \quad (2.37)$$

Therefore we obtain the general solution $v(t)$ for Eq. (2.32) of the form

$$v(t) = c_1 e^{-\gamma t} + \frac{A}{\gamma}. \quad (2.38)$$

Because of the reality of the physical fields, there has to be a boundary condition as follows:

$$v(t=0) = c_1 + \frac{A}{\gamma} = 0, \quad (2.39)$$

which follows that

$$c_1 = -A/\gamma. \quad (2.40)$$

As a result, we obtain the general solution $v(t)$ given by

$$v(t) = \frac{A}{\gamma} \left[1 - e^{-\gamma t} \right]. \quad (2.41)$$

2.4 Other THz generation methods

2.4.1 Optical Rectification

The THz field can be generated using several different methods. Optical rectification is a commonly used method to generate the THz field which is shown in Fig. 2.8. Optical rectification is based on the second order nonlinear effect of nonlinear medium such as ZnTe and can be described by the Maxwell equations [7, 16] in Eq. (2.2), where \vec{P}^{NL} is a source of the THz waves reduced from the nonlinear polarization of the medium given by

$$\begin{aligned} P_i^{\text{NL}}(\Omega) &= \int_{-\infty}^{\infty} \sum_{j,k} \chi_{ijk}^{(2)}(\Omega; \omega_{\text{opt}}, -\omega_{\text{opt}} + \Omega) E_j(\omega_{\text{opt}}) E_k^*(\omega_{\text{opt}} - \Omega) d\omega_{\text{opt}} \\ &= \int_{-\infty}^{\infty} \sum_{j,k} \chi_{ijk}^{(2)}(\Omega; -\omega_{\text{opt}}, \Omega + \omega_{\text{opt}}) E_j^*(\omega_{\text{opt}}) E_k(\Omega + \omega_{\text{opt}}) d\omega_{\text{opt}}, \end{aligned} \quad (2.43)$$

where Ω and ω_{opt} represent THz frequency and optical frequency, respectively. This equation shows that the nonlinear response of the medium acts as a source term [7, 16]. For example, when the laser propagates through a ZnTe crystal, wave mixing between the two frequencies w_1 and w_2 occurs [17], or

$$P^{(2)} \propto \chi^{(2)} E_1 E_2 = \chi^{(2)} \frac{E_0^2}{2} \left[\underbrace{\cos(w_1 - w_2)t}_{\text{Optical rectification term}} + \cos(w_1 + w_2)t \right], \quad (2.44)$$

where

$$E_1 = E_0 \cos(w_1 t), \quad E_2 = E_0 \cos(w_2 t). \quad (2.45)$$

This electric field is generally called the ‘‘Terahertz field (THz)’’ since this field consists of THz frequency components when we use a pulsed laser whose central wavelength is λ and the full width at half maximum (FWHM) of $\Delta\lambda$ (*i.e.* $\Delta\omega$). The rectified term in Eq. (2.44) can thus be made. The THz field generated via optical rectification is further described in detailed in section A.6.1 in detail.

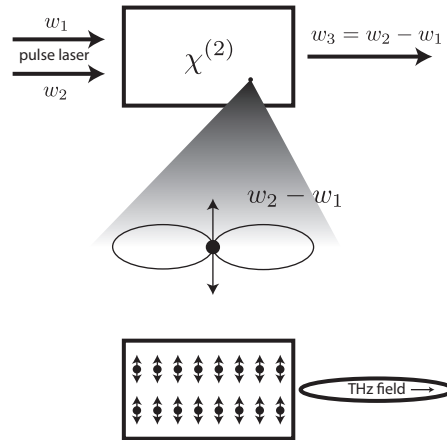


Figure 2.8: A simple physical picture of difference-frequency generation [7]

The interaction length expressed as the coherence length [2] between the pump pulse and generated THz waves has to be carefully considered due to efficient power and the spectrum of the generated THz waves. When we measure the THz waves by electro-optic detection using ZnTe, the thickness of ZnTe for probing THz waves plays an important role since the detectable frequency range is also determined by the coherence length of the used ZnTe. By considering the coherence length of ZnTe for a given THz frequency and optical frequency, the phase matching condition for the optical rectification process is given by [1, 18]

$$\Delta k = k(\Omega + \omega_{opt}) - k(\omega_{opt}) - k(\Omega) = 0, \quad (2.46)$$

where ω_{opt} and Ω are the optical and THz frequencies, respectively. This equation is identical to that in the case of electro-optic sampling [18]. The Taylor series for the wavenumber $k(\omega)$ about $\omega = \omega_{opt}$ is given by

$$k(\omega) = k(\omega_{opt}) + (\omega - \omega_{opt}) \left. \frac{dk}{d\omega} \right|_{\omega_{opt}} + \dots \quad (2.47)$$

We only consider the first two terms in the Taylor series. Then the Taylor series for the wavenumber $k(\Omega + \omega_{opt})$ about $\omega = \omega_{opt}$ is

$$k(\Omega + \omega_{opt}) \simeq k(\omega_{opt}) + (\Omega + \omega_{opt} - \omega_{opt}) \left. \frac{dk}{d\omega} \right|_{\omega_{opt}} = k(\omega_{opt}) + \Omega \left. \frac{dk}{d\omega} \right|_{\omega_{opt}}. \quad (2.48)$$

The group velocity is considered to calculate the term $dk/d\omega$ as follows

$$k = n(k) \frac{\omega}{c} \Leftrightarrow c \, dk = \omega \, dn + n \, d\omega, \quad (2.49)$$

where c is the speed of light. Then

$$c = \omega \frac{dn}{dk} + n \frac{d\omega}{dk} = \omega \frac{dn}{dk} + n \frac{d\omega}{dk} = \left(n + \omega \frac{dn}{d\omega} \right) \frac{d\omega}{dk}. \quad (2.50)$$

As a result, the group velocity is calculated as [19]

$$\frac{d\omega}{dk} = v_g = \frac{c}{n + \omega \frac{dn}{d\omega}}. \quad (2.51)$$

The term $dn/d\omega$ can be calculated by

$$\frac{dn}{d\omega} = \frac{d\lambda}{d\omega} \frac{dn}{d\lambda} = -\frac{2\pi c}{\omega^2} \frac{dn}{d\lambda} = -2\pi c \frac{\lambda^2}{(2\pi c)^2} \frac{dn}{d\lambda} = -\frac{\lambda^2}{2\pi c} \frac{dn}{d\lambda}, \quad (2.52)$$

where the relation of $\lambda = c \, t = 2\pi c/\omega$ in vacuum is used [19].

The group velocity as a function of wavelength and refractive index is

$$\frac{d\omega}{dk} = v_g = \frac{c}{n + \omega \frac{dn}{d\omega}} = \frac{c}{n - \frac{2\pi c}{\lambda} \frac{\lambda^2}{2\pi c} \frac{dn}{d\lambda}} = \frac{c}{n - \lambda \frac{dn}{d\lambda}}, \quad (2.53)$$

which implies that

$$\frac{dk}{d\omega} = \frac{1}{c} \left[n - \lambda \frac{dn}{d\lambda} \right]. \quad (2.54)$$

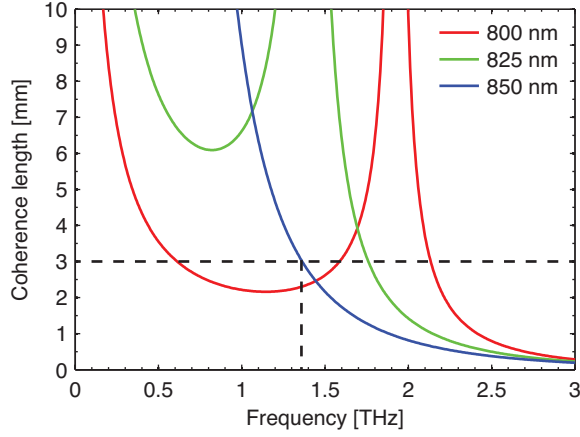


Figure 2.9: The coherence length of ZnTe as a function of THz frequency for given optical frequencies (wavelength).

From Eq. (2.54), Eq. (2.46) is reduced to

$$\begin{aligned}
 \Delta k(\omega) &= k(\Omega + \omega_{opt}) - k(\omega_{opt}) - k(\Omega) = k(\omega_{opt}) + \Omega \left. \frac{dk}{d\omega} \right|_{\omega_{opt}} - k(\omega_{opt}) - k(\Omega) \\
 &= \Omega \left. \frac{dk}{d\omega} \right|_{\omega_{opt}} - k(\Omega) = \frac{\Omega}{c} \left[n_{opt} - \lambda_{opt} \left. \frac{d}{d\lambda} n_{opt} \right|_{\lambda_{opt}} \right] - \frac{\Omega}{c} n_{THz} \\
 &= \frac{\Omega}{c} \left[n_{opt} - \lambda_{opt} \left. \frac{d}{d\lambda} n_{opt} \right|_{\lambda_{opt}} - n_{THz} \right].
 \end{aligned} \tag{2.55}$$

The coherence length [1, 18] is defined as $l_c = \pi/\Delta k$. Hence we obtain the coherence length given by

$$l_c(\Omega; \lambda_{opt}) = \frac{\pi c}{\Omega \left| n_{opt} - \lambda_{opt} \left. \frac{d}{d\lambda} n_{opt} \right|_{\lambda_{opt}} - n_{THz} \right|}, \tag{2.56}$$

where n_{opt} can be calculated from the Sellmeier's equation [18]. The optical refractive index of ZnTe from the Sellmeier equation [18] is given by

$$n_{opt}^2 = 4.27 + 3.01 \frac{\lambda_{opt}^2}{\lambda_{opt}^2 - 0.142}, \tag{2.57}$$

where λ_{opt} is the optical wavelength in μm . The THz refractive indices of ZnTe can be also calculated by [18]

$$n_{THz}^2 = \frac{289.27 - 6 f_{THz}^2}{29.16 - f_{THz}^2}, \tag{2.58}$$

where $f_{THz} = \Omega/2\pi$ is in THz. The effective optical refractive index $n_{opt} - \lambda_{opt} \left. \frac{d}{d\lambda} n_{opt} \right|_{\lambda_{opt}}$ at 800 nm is 3.2394. Since the unit in Eq. (2.58) is in THz, a factor of 10^{-12} has to be multiplied to Eq. (2.56).

Figure 2.9 shows the coherence length as a function of THz frequency at a given optical frequency. We find that the coherence length of 3 mm for a given the optical wavelength of 850 nm is about 1.37 THz. A ZnTe with a thickness of 1 mm or 2 mm is widely used in the THz detection processes.

2.4.2 Air plasma

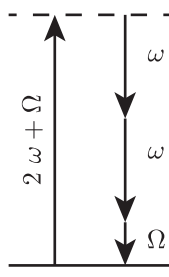


Figure 2.10: The energy-level diagram of the four-wave mixing [7, 10, 20].

THz wave generation in ambient air has been studied due to acceptable ultra broadband spectrum up to 100 THz as well as intense THz field strength [10]. As described in Eq. (2.2), THz waves can be generated from a source having the nonlinear polarization. In this case, the air plasma serves as a THz source which can be produced by a Ti:Sapphire laser amplifier whose central wavelength is 800 nm, repetition rate is 1 kHz and pulse energy is about 1 mJ.

THz waves are generated by focusing a fundamental pulse with a frequency of ω and a second harmonic pulse with a frequency of 2ω both produced by a type-I BBO crystal in air as shown in Fig. 2.3(c). Consider the third-order nonlinear polarization [7, 10, 20]

$$\tilde{P}^{(3)}(t) = \epsilon_0 \chi^{(3)} \tilde{E}^3(t) \quad (2.59)$$

induced by an applied field \tilde{E} having three components in the form [10, 20]

$$\tilde{E}(t) = \underbrace{\tilde{E}_{800}(t) e^{-i\omega t}}_{\tilde{E}_\omega(t)} + \underbrace{\tilde{E}_{800}(t) e^{-i\omega t}}_{\tilde{E}_\omega(t)} + \underbrace{\tilde{E}_{400}(t) e^{-i(2\omega t + \varphi)}}_{\tilde{E}_{2\omega}(t)} + c.c. \quad (2.60)$$

where the first and second terms are 800 nm pulses, the last term is a 400 nm pulse caused by the second harmonic generation and φ is the phase difference between the two pulses. Then Eq. (2.59) results in a 4ω term, a 2ω term, and a rectified term [20]. THz waves are thus generated through the four-wave mixing process as shown in Fig. 2.10 given by

$$E_{\text{THz}} \propto P^{(3)}(\Omega) \propto \chi^{(3)}(\Omega, 2\omega + \Omega, -\omega, -\omega) E_{2\omega} E_\omega^* E_\omega^* \cos(\varphi), \quad (2.61)$$

where Ω is the frequency of the emitted THz waves [10]. Note that it is possible to obtain the Ω frequency component owing to the *pulsed laser* whose center frequency (wavelength) is ω and full width at half maximum (FWHM) is $\Delta\omega$ which can produce a non-zero frequency component such as the Ω component as likely as the optical rectification described in section 2.4.1.

Since a widely used THz detection method such as electro-optic (EO) detection is not useful in obtaining ultra broadband spectrums due to the narrow bandwidths of EO materials caused by phonon modes, the THz detection method using gas photonics has been recently extensively investigated [10].

2.5 THz detection method: Electro optic detection

2.5.1 Introduction

Electro-optic (EO) medium such as ZnTe or GaP have a unique property that their refractive index of the medium is changed proportional to the applied external electric waves which is known as the linear EO effect or the Pockels effect. The Pockels effect is one of the nonlinear optical responses of EO medium. The THz detection method using the Pockels effect is generally called EO detection, which is a widely used technique to measure THz waves.

To measure the THz waves, the transmission axis of the quarter-wave plate must be defined to minimize the difference in the intensities of two photodiodes as there is no THz waves, which means that radiated THz waves are blocked. After defining the transmission axis of the quarter-wave plate, suppose that THz waves and a probe beam copropagate through a (110) ZnTe crystal as in Fig. 2.11. Then the THz waves serves as an applied external electric field to ZnTe. Here, the polarization of the probe beam is linearly changed due to birefringence in ZnTe. . The probe beam is elliptically polarized when it goes through a quarter-wave plate and then is separated to two orthogonal components by a prism such as the Wollaston prism or Rochon prism. The THz waves can be measured by differentiating the two intensities (detected by the photodiodes) of the two orthogonal components of the elliptical polarized probe beam. Finally, the whole THz time-domain signals can be obtained by varying the delay between the THz waves and the probe beam [21].

The Pockels effect is briefly explained in this section. As an external electric field is applied to an EO medium, the refractive index (n) of the EO medium can be defined as a function of electric field (E) [19, 22] . The Taylor expansion of n at $E = 0$ is given by

$$n(E) = n(E = 0) + \left. \frac{dn}{dE} \right|_{E=0} E + \frac{1}{2!} \left. \frac{d^2n}{dE^2} \right|_{E=0} E^2 + \dots . \quad (2.62)$$

The propagation of the electric field in the crystal (EO medium) can be described by the impermeability tensor η_{ij} defined as

$$\eta_{ij} = \epsilon_0 (\epsilon^{-1})_{ij}, \quad (2.63)$$

where ϵ_0 is the dielectric permittivity in free space and ϵ^{-1} is the inverse matrix of the dielectric tensor.

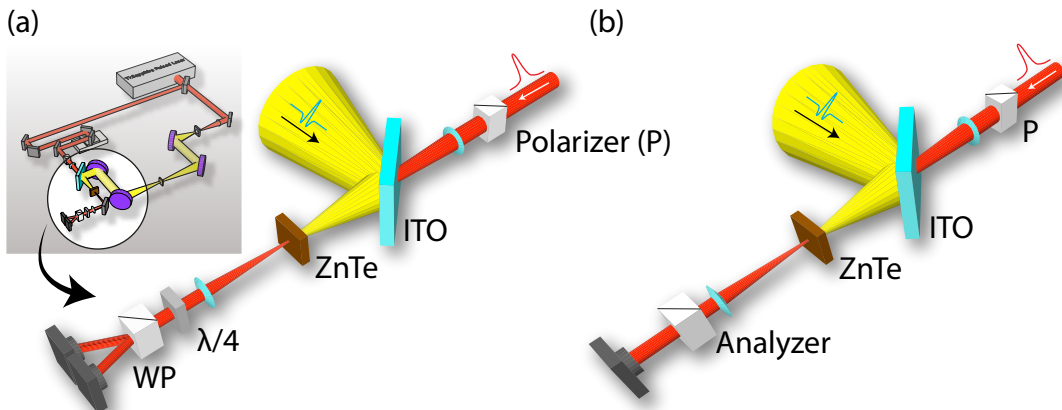


Figure 2.11: The schemes of electro-optic (EO) detection. A detailed description of EO detection can be found in section 2.5.

Hereafter, η is treated as a scalar for the sake of clarity. For simplicity, each coefficient in Eq. (2.62) is denoted as

$$n(E=0) = n(0), \quad (dn/dE)\Big|_{E=0} = a_1, \quad (d^2n/dE^2)\Big|_{E=0} = a_2. \quad (2.64)$$

Using Eq. (2.64), Eq. (2.63) is calculated as

$$\begin{aligned} \eta &= \frac{1}{n^2} = \frac{1}{\left[n(0) + a_1 E + \frac{a_2}{2} E^2\right]^2} = \frac{1}{\left[n(0) \left\{1 + \frac{a_1}{n(0)} E + \frac{a_2}{2 n(0)} E^2\right\}\right]^2} \\ &\simeq \frac{1}{n(0)^2} \left[1 - 2\left(\frac{a_1}{n(0)} E + \frac{a_2}{2n(0)} E^2\right)\right] = \frac{1}{n(0)^2} - \frac{2a_1}{n(0)^3} E - \frac{a_2}{n(0)^3} E^2. \end{aligned} \quad (2.65)$$

Therefore Eq. (2.65) is reduced to

$$\frac{1}{n^2} - \frac{1}{n(0)^2} = -\frac{2a_1}{n(0)^3} E - \frac{a_2}{n(0)^3} E^2, \quad (2.66)$$

which leads to the result

$$\eta(E) - \eta(E=0) = rE + sE^2, \quad (2.67)$$

where $r = -2a_1/n(0)^3$ is known as the linear EO coefficient or Pockels coefficient and $s = -a_2/n(0)^3$ is known as the quadratic EO coefficient or Kerr coefficient. Terms higher order terms than the quadratic term are ignored since these higher-order terms are too small compared to the linear and quadratic ones. As seen in Eq. (2.67), the Pockels effect indicates that the change in the refractive index of the EO medium is proportional to the applied electric field (E). On the other hand, the Kerr effect implies that the change in the refractive index of the EO medium is quadratic to the applied electric field [19, 22].

2.5.2 The Pockels effect and the Kerr effect

2.5.2.1 The electro-optic effects in terms of nonlinear polarization

For historical reasons, despite nonlinear effects such as the Pockels effect (the linear electro-optic effect) and the Kerr effect (the quadratic electro-optic effect) can be described by the nonlinear polarization in terms of higher-order electric susceptibility, these effects have been widely explained in terms of the index ellipsoid [7]. In this section, it is briefly explained that the Pockels effect and the Kerr effect are related to $\chi^{(2)}$ and $\chi^{(3)}$, respectively [7].

The Pockels effect, or, the precise terahertz Pockels effect at optical frequency, is defined by

$$P_i(\omega + \Omega_{\text{THz}}) = 2\epsilon_0 \sum_{j,k} \chi_{ijk}^{(2)}(\omega + \Omega_{\text{THz}}, \omega, \Omega_{\text{THz}}) E_j(\omega) E_k(\Omega_{\text{THz}}) = \epsilon_0 \sum_j \chi_{ij}^{(2)}(\omega + \Omega_{\text{THz}}) E_j(\omega), \quad (2.68)$$

where $\chi_{ij}^{(2)}(\omega + \Omega_{\text{THz}}) = 2 \sum_k \chi_{ijk}^{(2)}(\omega + \Omega_{\text{THz}}) E_k(\Omega_{\text{THz}})$ is the terahertz field induced susceptibility tensor and $P(2, 2) = 2!/(2-2)! = 2 (= 2!/(1!1!))$ represents also the number of distinct permutations for the frequency ω and Ω_{THz} [2, 7].

By the same analogy, the terahertz Kerr effect at optical frequency (Kerr effect) is defined by

$$P_i(\omega) = 6\epsilon_0 \sum_{j,k,l} \chi_{ijkl}^{(3)}(\omega, \omega, -\Omega_{\text{THz}}, \Omega_{\text{THz}}) E_j(\omega) E_k^*(\omega_{\text{THz}}) E_l(\omega_{\text{THz}}) = \epsilon_0 \sum_j \chi_{ij}^{(3)}(\omega) E_j(\omega), \quad (2.69)$$

where $\chi_{ij}^{(3)}(\omega) = 6 \sum_{k,l} \chi_{ijkl}^{(3)}(\omega) E_k^*(\omega_{\text{THz}}) E_l(\omega_{\text{THz}})$ is the terahertz field intensity induced susceptibility tensor and $P(3,3) = 3!/(3-3)! = 6$ represents also the number of distinct permutations for the frequency components ω , $-\omega$, and Ω_{THz} due to the fact that $E_k^*(\omega_{\text{THz}}) = E_k(-\omega_{\text{THz}})$ [7]. In addition to the Kerr effect, the THz-field-induced second harmonic (TFISH) is defined by

$$P_i(2\omega \pm \Omega_{\text{THz}}) = \epsilon_0 D \sum_{i,j,k,l} \chi_{ijkl}^{(3)}(2\omega \pm \Omega_{\text{THz}}, \omega, \omega, \pm \Omega_{\text{THz}}) E_j(\omega) E_k(\omega) E_l^{(*)}(\Omega_{\text{THz}}), \quad (2.70)$$

where $P_i = P_i(2\omega + \Omega_{\text{THz}})$ for $E_k(\Omega_{\text{THz}})$ and $P_i = P_i(2\omega - \Omega_{\text{THz}})$ for $E_k^*(\Omega_{\text{THz}})$ and $D (= 3 = 3!/(2!1!))$ [7].

The quadratic electro-optic effect is expected to be small compared to the linear electro-optic effect and is often neglected when the linear effect is present [7, 19]. However, the linear electro-optic effect must vanish in centro-symmetric crystals [7, 19], which is explained in section A.2 in detail. The two effects can be summarized in table 2.2. The reasons why $\chi^{(2)}$ and $\chi^{(3)}$ are related to the Pockels effect and the Kerr effect, respectively, are explained in the following section.

Crystal symmetry	Property	Existent effects
Non-centrosymmetry	$\chi^{(3)} \ll \chi^{(2)}$	Pockels, Kerr
Centrosymmetry	$\chi^{(3)} > \chi^{(2)} = 0$	Kerr

Table 2.2: The existent electro-optic effect for each crystal symmetry.

2.5.2.2 Induction of the Pockels effect in terms of refractive index from nonlinear susceptibility

Let us consider that a probe beam with frequency of ω propagates through a nonlinear medium with $\chi^{(2)}$ and $\chi^{(3)}$. In the presence of a strong pump beam with frequency of Ω , the probe beam is modulated by the nonlinear polarization of the medium. The nonlinear polarization induced by the Pockels effect in the nonlinear medium is defined by

$$P(\omega + \Omega) = 2\epsilon_0 \chi^{(2)}(\omega + \Omega) E(\omega) E(\Omega), \quad (2.71)$$

assuming that the incident pump and probe beams are linearly polarized for the sake of simplicity [7]. The displacement field D in the medium is expressed in terms of the dielectric constant and the intrinsic electric field of the probe beam as

$$D(\omega) = \epsilon(\omega) E(\omega). \quad (2.72)$$

The displacement field is defined in terms of the intrinsic electric field and polarization as [7, 12]

$$D(\omega) = \epsilon E = \epsilon_0(1 + \chi) E = \epsilon_0 E + \epsilon_0 \chi E = \epsilon_0 E(\omega) + P(\omega). \quad (2.73)$$

The Pockels effect can be produced when $P(\omega) \simeq P(\omega + \Omega)$ or $\omega + \Omega \simeq \omega$ [7].⁸ By substituting P by Eq. (2.71), the displacement field can be written as

$$\epsilon(\omega) E(\omega) = \epsilon_0 E(\omega) + 2\epsilon_0 \chi^{(2)}(\omega) E(\omega) E(\Omega), \quad (2.74)$$

⁸ $\omega + \Omega \simeq \omega$ means that frequency Ω is sufficiently small compared with ω . In other words, the electric field with frequency of Ω represents a static (DC) or low frequency electric field.

which is equivalent to ⁹

$$\epsilon(\omega) = \epsilon_0 + 2\epsilon_0\chi^{(2)}(\omega)E(\Omega). \quad (2.76)$$

Since the dimensionless dielectric constant ϵ/ϵ_0 is the square of the refractive index according to electromagnetic theory [7, 12], the refractive index can be obtained by Eq. (2.76) as

$$n(\omega) = \sqrt{\frac{\epsilon(\omega)}{\epsilon_0}} = \left[1 + 2\chi^{(2)}(\omega)E(\Omega)\right]^{1/2} \simeq 1 + \chi^{(2)}(\omega)E(\Omega). \quad (2.77)$$

Eq. (2.77) directly shows that $\chi^{(2)}$ has relation to the Pockels effect.

The dielectric constant should be composed of linear $\chi^{(1)}$ and nonlinear susceptibility $\chi^{(2)}$ as

$$\epsilon(\omega) = \epsilon_0 + \epsilon_0\chi^{(1)}(\omega) + 2\epsilon_0\chi^{(2)}(\omega)E(\Omega). \quad (2.78)$$

By the same analogy, the refractive index can be written in terms of n_0 and n_1 as

$$\begin{aligned} n(\omega) &= \sqrt{\frac{\epsilon(\omega)}{\epsilon_0}} = \left[\underbrace{1 + \chi^{(1)}(\omega)}_{n_0^2(\omega)} + 2\chi^{(2)}(\omega)E(\Omega)\right]^{1/2} \\ &= \left[n_0^2(\omega) + 2\chi^{(2)}(\omega)E(\Omega)\right]^{1/2} = n_0(\omega) \left[1 + \frac{2\chi^{(2)}(\omega)}{n_0^2(\omega)}E(\Omega)\right]^{1/2} \simeq n_0(\omega) \left[1 + \frac{\chi^{(2)}(\omega)}{n_0^2(\omega)}E(\Omega)\right] \\ &= n_0(\omega) + \underbrace{\frac{\chi^{(2)}(\omega)}{n_0(\omega)}}_{n_1} E(\Omega) = n_0(\omega) + n_1(\omega)E(\Omega) \equiv n_0(\omega) + \Delta n_1(\omega), \end{aligned} \quad (2.79)$$

where the linear refractive index n_0 is defined as $\sqrt{1 + \chi^{(1)}}$. We can see that the refractive index of the nonlinear medium is perturbed in the presence of an external electric field with low frequency. The magnitude of perturbed index Δn is proportional to the external electric field.

2.5.2.3 Induction of the Kerr effect in terms of refractive index from nonlinear susceptibility

Under the assumption that the incident pump beam $E(\Omega)$ and probe beam $E(\omega)$ are linearly polarized for the sake of simplicity [7], the nonlinear polarization induced by the Kerr effect in the nonlinear medium is defined as

$$P(\omega) = 6\epsilon_0\chi^{(3)}(\omega - \Omega + \Omega)E(\omega)E(-\Omega)E(\Omega) = 6\epsilon_0\chi^{(3)}(\omega)E(\omega)|E(\Omega)|^2, \quad (2.80)$$

where $E(-\Omega) = E^*(\Omega)$. Then the total polarization of the medium is described as

$$\begin{aligned} P(\omega) &= \epsilon_0\chi^{(1)}(\omega)E(\omega) + 6\epsilon_0\chi^{(3)}(\omega)|E(\Omega)|^2E(\omega) \\ &= \epsilon_0\left[\chi^{(1)}(\omega) + 6\chi^{(3)}(\omega)|E(\Omega)|^2\right]E(\omega) = \epsilon_0\chi_{\text{eff}}(\omega)E(\omega), \end{aligned} \quad (2.81)$$

⁹

$$\epsilon(\omega)E(\omega) = \epsilon_0E(\omega) + 2\epsilon_0\chi^{(2)}(\omega)E(\omega)E(\Omega) = \left[\epsilon_0 + 2\epsilon_0\chi^{(2)}(\omega)E(\Omega)\right]E(\omega). \quad (2.75)$$

where the effective susceptibility χ_{eff} is denoted by

$$\chi_{\text{eff}} = \chi^{(1)}(\omega) + 6\chi^{(3)}(\omega)|E(\Omega)|^2. \quad (2.82)$$

By the definition of the refractive index [7, 12], the refractive index n is obtained from the relative (dimensionless) dielectric constant given by

$$n^2(\omega) = \frac{\epsilon(\omega)}{\epsilon_0} = 1 + \chi_{\text{eff}}. \quad (2.83)$$

From Eq. (2.77), Eq. (2.83) becomes

$$\begin{aligned} n(\omega) &= \sqrt{\frac{\epsilon(\omega)}{\epsilon_0}} = \left[\underbrace{1 + \chi^{(1)}(\omega)}_{n_0^2(\omega)} + 6\chi^{(3)}(\omega)|E(\Omega)|^2 \right]^{1/2} = \left[n_0^2(\omega) + 6\chi^{(3)}(\omega)|E(\Omega)|^2 \right]^{1/2} \\ &= n_0(\omega) \left[1 + \frac{6\chi^{(3)}(\omega)}{n_0^2(\omega)}|E(\Omega)|^2 \right]^{1/2} \simeq n_0(\omega) \left[1 + \frac{3\chi^{(3)}(\omega)}{n_0^2(\omega)}|E(\Omega)|^2 \right] \\ &= n_0(\omega) + \underbrace{\frac{3\chi^{(3)}(\omega)}{n_0(\omega)}|E(\Omega)|^2}_{n_2} = n_0(\omega) + n_2(\omega)|E(\Omega)|^2 \equiv n_0(\omega) + \Delta n_2(\omega), \end{aligned} \quad (2.84)$$

From this equation, we can see that the refractive index of the nonlinear medium is perturbed in the presence of an external electric field and the magnitude of the perturbed index Δn_2 in relation to $\chi^{(3)}$ is proportional to the intensity of the external electric field.

In this section, we find that the Kerr effect has in a relationship with $\chi^{(3)}$. The induction processes of the Kerr effect can also be described by the same analogy from the former section 2.5.2.2¹⁰. The refractive index $n(\omega)$ of the nonlinear medium can be summarized in the form

$$n(\omega) = n_0(\omega) + n_1(\omega)E(\Omega) + n_2(\omega)|E(\Omega)|^2. \quad (2.89)$$

The represented n is slightly different but the same when compared with the Taylor expansion of n at $E = 0$ in Eq. (2.62).

2.5.3 The index ellipsoid in the electro-optic medium

First of all, the index ellipsoid of an anisotropic medium needs to be considered to understand the linear EO effect. Assume that a monochromatic plane wave propagates through an anisotropic medium.

¹⁰From Eq. (2.73), the displacement field can be written by

$$D(\omega) = \epsilon(\omega)E(\omega) = \epsilon_0 E(\omega) + 6\epsilon_0 \chi^{(3)}(\omega)E(\omega)|E(\Omega)|^2, \quad (2.85)$$

which implies

$$\epsilon(\omega) = \epsilon_0 + 6\epsilon_0 \chi^{(3)}(\omega)|E(\Omega)|^2. \quad (2.86)$$

From Eq. (2.86), the refractive index can be obtained given by

$$n(\omega) = \sqrt{\frac{\epsilon(\omega)}{\epsilon_0}} = \left[1 + 6\chi^{(3)}(\omega)|E(\Omega)|^2 \right]^{1/2} \simeq 1 + 3\chi^{(3)}(\omega)|E(\Omega)|^2. \quad (2.87)$$

Eq. (2.87) directly shows that $\chi^{(3)}$ is in a relationship with the Kerr effect.

By Eq. (2.78), the medium has the intrinsic susceptibility denoted by $\chi^{(1)}$ given by

$$\epsilon(\omega) = \epsilon_0 + \chi^{(1)}(\omega) + 6\epsilon_0 \chi^{(3)}(\omega)|E(\Omega)|^2. \quad (2.88)$$

The permittivity (ϵ_{ij}), the electric susceptibility (χ_{ij}), and the relative permittivity (ξ_{ij}) have a relation given by

$$\epsilon_{ij} = \epsilon_0 (1 + \chi_{ij}) = \epsilon_0 \xi_{ij}. \quad (2.90)$$

In an anisotropic medium such as an EO medium, the electric displacement \mathbf{D} is defined by

$$D_i = \sum_j \epsilon_{ij} E_j = \epsilon_0 \sum_j \xi_{ij} E_j, \quad (2.91)$$

which is precisely expressed by

$$\begin{pmatrix} D_x \\ D_y \\ D_z \end{pmatrix} = \epsilon_0 \begin{bmatrix} \xi_{xx} & \xi_{xy} & \xi_{xz} \\ \xi_{yx} & \xi_{yy} & \xi_{yz} \\ \xi_{zx} & \xi_{zy} & \xi_{zz} \end{bmatrix} \begin{pmatrix} E_x \\ E_y \\ E_z \end{pmatrix}. \quad (2.92)$$

If an anisotropic medium is optically inactive and lossless, then the relative permittivity tensor ξ_{ij} is a real symmetry tensor. Thus $\xi_{yx} = \xi_{xy}$, $\xi_{xz} = \xi_{zx}$, and $\xi_{yz} = \xi_{zy}$. Eq. (2.92) can be simplified by rotating the coordinates of (x, y, z) to the new coordinates of (X, Y, Z) as

$$\begin{pmatrix} D_X \\ D_Y \\ D_Z \end{pmatrix} = \epsilon_0 \begin{bmatrix} \xi_{XX} & 0 & 0 \\ 0 & \xi_{YY} & 0 \\ 0 & 0 & \xi_{ZZ} \end{bmatrix} \begin{pmatrix} E_X \\ E_Y \\ E_Z \end{pmatrix}, \quad (2.93)$$

which is expressed using a diagonal matrix of ξ_{ij} in Eq. (2.92). These new coordinates are known as the principal axes because the permittivity is represented as a diagonal matrix.

Consider the energy density of the stored electric field in an anisotropic medium defined by

$$U = \frac{1}{2} \mathbf{E} \cdot \mathbf{D} = \frac{1}{2} \sum_i \hat{e}_i E_i \cdot \epsilon_0 \sum_{jk} \hat{e}_j \xi_{jk} E_k = \frac{1}{2} \epsilon_0 \sum_{ijk} \delta_{ij} E_i \xi_{jk} E_k = \frac{1}{2} \epsilon_0 \sum_{jk} E_j \xi_{jk} E_k. \quad (2.94)$$

Using Eq. (2.93), Eq. (2.94) in the principal axes becomes

$$\begin{aligned} U &= \frac{1}{2} \epsilon_0 \left[\xi_{XX} E_X^2 + \xi_{YY} E_Y^2 + \xi_{ZZ} E_Z^2 \right] = \frac{1}{2} \epsilon_0 \left[\frac{\epsilon_0^2 \xi_{XX}^2 E_X^2}{\epsilon_0^2 \xi_{XX}} + \frac{\epsilon_0^2 \xi_{YY}^2 E_Y^2}{\epsilon_0^2 \xi_{YY}} + \frac{\epsilon_0^2 \xi_{ZZ}^2 E_Z^2}{\epsilon_0^2 \xi_{ZZ}} \right] \\ &= \frac{1}{2\epsilon_0} \left[\frac{D_X^2}{\xi_{XX}} + \frac{D_Y^2}{\xi_{YY}} + \frac{D_Z^2}{\xi_{ZZ}} \right]. \end{aligned} \quad (2.95)$$

The shapes of these ellipsoids can be described in terms of the principal coordinates (X, Y, Z) themselves [7]. If we replace $X, Y,$ and Z by

$$X = \frac{D_X}{\sqrt{2\epsilon_0 U}}, \quad Y = \frac{D_Y}{\sqrt{2\epsilon_0 U}}, \quad Z = \frac{D_Z}{\sqrt{2\epsilon_0 U}}, \quad (2.96)$$

then Eq. (2.95) becomes

$$\begin{aligned} 1 &= \left(\frac{D_X}{\sqrt{2\epsilon_0 U}} \right)^2 \frac{1}{\xi_{XX}} + \left(\frac{D_Y}{\sqrt{2\epsilon_0 U}} \right)^2 \frac{1}{\xi_{YY}} + \left(\frac{D_Z}{\sqrt{2\epsilon_0 U}} \right)^2 \frac{1}{\xi_{ZZ}} \\ \Leftrightarrow 1 &= \frac{X^2}{n_X^2} + \frac{Y^2}{n_Y^2} + \frac{Z^2}{n_Z^2}, \end{aligned} \quad (2.97)$$

where $\epsilon_j/\epsilon_0 = \xi_j = n_j^2$ ($j = X, Y, Z$) and n_j are the principal refractive indices.

Eq. (2.97) is known as the index ellipsoid or the optical indicatrix in the absence of an external electric field [7, 19]. Note that the index ellipsoid is formed when the incident wave propagates through a medium. If the coordinates do not correspond to the principal axes of (X, Y, Z) , then it is needed to go back to Eq. (2.91) and Eq. (2.92). In other words, it is considered that the index ellipsoid is changed in the presence of an external applied electric field that is another field and different with the incident wave.

The electric field \mathbf{E} is expressed in terms of the inverse of the electric displacement \mathbf{D} as

$$E_i = \sum_j (\epsilon^{-1})_{ij} D_j. \quad (2.98)$$

It is time to introduce the impermeability tensor, shortly introduced in the last section 2.5.1, which is used to derive the index ellipsoid of an anisotropic medium. The impermeability tensor η_{ij} is associated with the permittivity ϵ_{ij} as

$$\frac{\eta_{ij}}{\epsilon_0} = (\epsilon^{-1})_{ij}. \quad (2.99)$$

Therefore the electric field \mathbf{E} satisfies the following relation

$$E_i = \frac{1}{\epsilon_0} \sum_j \eta_{ij} D_j. \quad (2.100)$$

By using the preceding procedure, the energy density is computed as

$$U = \frac{1}{2} \mathbf{E} \cdot \mathbf{D} = \frac{1}{2} \sum_{ij} \hat{e}_i \frac{1}{\epsilon_0} \eta_{ij} D_j \cdot \sum_k \hat{e}_k D_k = \frac{1}{2\epsilon_0} \sum_{ijk} \delta_{ik} \eta_{ij} D_j D_k = \frac{1}{2\epsilon_0} \sum_{ij} \eta_{ij} D_j D_i, \quad (2.101)$$

where η_{ij} is defined by

$$\eta = \begin{bmatrix} \eta_{11} & \eta_{12} & \eta_{13} \\ \eta_{21} & \eta_{22} & \eta_{23} \\ \eta_{31} & \eta_{32} & \eta_{33} \end{bmatrix}. \quad (2.102)$$

Eq. (2.101) becomes

$$\begin{aligned} 2\epsilon_0 U &= \sum_{ij} \eta_{ij} D_j D_i = \eta_{11} D_1^2 + \eta_{22} D_2^2 + \eta_{33} D_3^2 \\ &+ (\eta_{12} + \eta_{21}) D_1 D_2 + (\eta_{23} + \eta_{32}) D_2 D_3 + (\eta_{13} + \eta_{31}) D_1 D_3. \end{aligned} \quad (2.103)$$

Since η is a real symmetric tensor, the last equation can be reduced as

$$2\epsilon_0 U = \eta_{11} D_1^2 + \eta_{22} D_2^2 + \eta_{33} D_3^2 + 2\eta_{12} D_1 D_2 + 2\eta_{23} D_2 D_3 + 2\eta_{13} D_1 D_3. \quad (2.104)$$

By using relations given by

$$x_j = \frac{D_j}{\sqrt{2\epsilon_0 U}} \text{ for } j \in \{1, 2, 3\}, \quad (2.105)$$

then Eq. (2.104) can be expressed as

$$\begin{aligned} & \eta_{11} \left(\frac{D_1}{\sqrt{2\epsilon_0 U}} \right)^2 + \eta_{22} \left(\frac{D_2}{\sqrt{2\epsilon_0 U}} \right)^2 + \eta_{33} \left(\frac{D_3}{\sqrt{2\epsilon_0 U}} \right)^2 \\ & + 2\eta_{12} \left(\frac{D_1}{\sqrt{2\epsilon_0 U}} \right) \left(\frac{D_2}{\sqrt{2\epsilon_0 U}} \right) + 2\eta_{13} \left(\frac{D_1}{\sqrt{2\epsilon_0 U}} \right) \left(\frac{D_3}{\sqrt{2\epsilon_0 U}} \right) + 2\eta_{23} \left(\frac{D_2}{\sqrt{2\epsilon_0 U}} \right) \left(\frac{D_3}{\sqrt{2\epsilon_0 U}} \right) = 1 \quad (2.106) \\ & \Leftrightarrow \eta_{11}x_1^2 + \eta_{22}x_2^2 + \eta_{33}x_3^2 + 2\eta_{12}x_1x_2 + 2\eta_{23}x_2x_3 + 2\eta_{13}x_1x_3 = 1, \end{aligned}$$

which is the general expression of the index ellipsoid.

From Eq. (C.29), considering the impermeability tensor of an anisotropic medium in the presence of an external electric field, the Taylor expansion of η_{ij} at $\mathbf{E} = 0$ is given by

$$\eta_{ij}(\mathbf{E}) = \epsilon_0 \left(\epsilon^{-1} \right)_{ij} = \eta_{ij}(\mathbf{E} = 0) + \sum_k \frac{\partial \eta_{ij}}{\partial E_k} E_k + \sum_{k,l} \frac{1}{2!} \frac{\partial^2 \eta_{ij}}{\partial E_k \partial E_l} E_k E_l \quad \text{for } i, j, k, l \in \{1, 2, 3\}, \quad (2.107)$$

where the higher order terms than the quadratic term are neglected since they are too small compared with the linear and quadratic coefficients [19, 22]. Therefore, the two EO coefficients are given as

$$\left. \frac{\partial \eta_{ij}}{\partial E_k} \right|_{\mathbf{E}=0} = r_{ijk}, \quad (2.108)$$

$$\left. \frac{1}{2} \frac{\partial^2 \eta_{ij}}{\partial E_k \partial E_l} \right|_{\mathbf{E}=0} = s_{ijkl}. \quad (2.109)$$

The Pockels coefficient (r) and the Kerr coefficient (s) are tensors with ranks 3 and 4, respectively. To be used effectively, the index of the tensor needs to be reduced. Hereafter, we will focus on the Pockels coefficient.

Suppose that an anisotropic medium is optically inactive and lossless. Then η_{ij} is the same as η_{ji} since ϵ_{ij} is the same as ϵ_{ji} [19]. Therefore, η is a symmetric tensor and the indices i , j , and k in Eq. (2.107) can be permuted as

$$\begin{aligned} (\eta_{ij} &= \eta_{ji}) \\ r_{ijk} &= r_{jik}. \end{aligned} \quad (2.110)$$

Using this permutation symmetry, the indices i and j of the tensor (r_{ijk}) for given k index can be abbreviated using the contracted indices defined as [19]

$$\begin{aligned} 1 &= (11) \\ 2 &= (22) \\ 3 &= (33) \\ 4 &= (23) = (32) \\ 5 &= (13) = (31) \\ 6 &= (12) = (21). \end{aligned} \quad (2.111)$$

Then the Pockels coefficient for $k \in \{1, 2, 3\}$ can be reduced by

$$\begin{aligned} r_{1k} &= r_{11k}, & r_{4k} &= r_{23k} = r_{32k}, \\ r_{2k} &= r_{22k}, & r_{5k} &= r_{13k} = r_{31k}, \\ r_{3k} &= r_{33k}, & r_{6k} &= r_{12k} = r_{21k}. \end{aligned} \quad (2.112)$$

Therefore, the third-rank tensor r_{ijk} having 27 components is simplified to a 6×3 tensor matrix. Using this notation, the impermeability tensor η in Eq. (2.107) becomes

$$\begin{aligned} \eta_{ij}(\mathbf{E}) &= \eta_{ij}(\mathbf{E} = 0) + \sum_k r_{ijk} E_k \quad \text{for } k \in \{1, 2, 3\} \\ &= \eta_I(\mathbf{E} = 0) + \sum_k r_{Ik} E_k \quad \text{for } I \in \{1, 2, 3, \dots, 6\}, k \in \{1, 2, 3\} \\ &= \eta_I(\mathbf{E}), \end{aligned} \quad (2.113)$$

where $\eta_I(0)$ for $I \in \{1, 2, 3, \dots, 6\}$ is given as

$$\eta(\mathbf{E} = 0) = \begin{pmatrix} \eta_1(\mathbf{E} = 0) \\ \eta_2(\mathbf{E} = 0) \\ \eta_3(\mathbf{E} = 0) \\ \eta_4(\mathbf{E} = 0) \\ \eta_5(\mathbf{E} = 0) \\ \eta_6(\mathbf{E} = 0) \end{pmatrix} = \begin{pmatrix} \frac{1}{n_1^2} \\ \frac{1}{n_2^2} \\ \frac{1}{n_3^2} \\ 0 \\ 0 \\ 0 \end{pmatrix}. \quad (2.114)$$

Note that $1/n_1^2$, $1/n_2^2$, and $1/n_3^2$ are the principal refractive indices of the anisotropic medium in the absence of an electric field. Here, 1, 2, 3 correspond to the principal axes x , y and z , respectively. Therefore Eq. (2.106) can be written as

$$\eta_1 x^2 + \eta_2 y^2 + \eta_3 z^2 + 2\eta_4 yz + 2\eta_5 zx + 2\eta_6 xy = 1, \quad (2.115)$$

where the indices in η is simplified by using the contracted indices shown in Eq. (2.113).

From Eq. (2.113), the impermeability tensor η in the presence of an electric field becomes

$$\eta(\mathbf{E}) = \begin{pmatrix} \frac{1}{n_x^2} \\ \frac{1}{n_y^2} \\ \frac{1}{n_z^2} \\ 0 \\ 0 \\ 0 \end{pmatrix} + \begin{bmatrix} r_{11} & r_{12} & r_{13} \\ r_{21} & r_{22} & r_{23} \\ r_{31} & r_{32} & r_{33} \\ r_{41} & r_{42} & r_{43} \\ r_{51} & r_{52} & r_{53} \\ r_{61} & r_{62} & r_{63} \end{bmatrix} \begin{pmatrix} E_x \\ E_y \\ E_z \end{pmatrix}, \quad (2.116)$$

where each element of the $\eta(\mathbf{E})$ is expressed as

$$\begin{aligned}
\eta_1(\mathbf{E}) &= \eta_1(\mathbf{E} = 0) + \sum_k r_{1k} E_k = \frac{1}{n_x^2} + \sum_k r_{1k} E_k, \\
\eta_2(\mathbf{E}) &= \eta_2(\mathbf{E} = 0) + \sum_k r_{2k} E_k = \frac{1}{n_y^2} + \sum_k r_{2k} E_k, \\
\eta_3(\mathbf{E}) &= \eta_3(\mathbf{E} = 0) + \sum_k r_{3k} E_k = \frac{1}{n_z^2} + \sum_k r_{3k} E_k, \\
\eta_4(\mathbf{E}) &= \eta_4(\mathbf{E} = 0) + \sum_k r_{4k} E_k = 0 + \sum_k r_{4k} E_k, \\
\eta_5(\mathbf{E}) &= \eta_5(\mathbf{E} = 0) + \sum_k r_{5k} E_k = 0 + \sum_k r_{5k} E_k, \\
\eta_6(\mathbf{E}) &= \eta_6(\mathbf{E} = 0) + \sum_k r_{6k} E_k = 0 + \sum_k r_{6k} E_k.
\end{aligned} \tag{2.117}$$

Therefore the index ellipsoid in EO medium in the presence of an external electric field can be written as

$$\begin{aligned}
&\left(\frac{1}{n_x^2} + \sum_k r_{1k} E_k\right) x^2 + \left(\frac{1}{n_y^2} + \sum_k r_{2k} E_k\right) y^2 + \left(\frac{1}{n_z^2} + \sum_k r_{3k} E_k\right) z^2 \\
&+ 2yz \sum_k r_{4k} E_k + 2zx \sum_k r_{5k} E_k + 2xy \sum_k r_{6k} E_k = 1 \text{ for } k \in \{x, y, z\}.
\end{aligned} \tag{2.118}$$

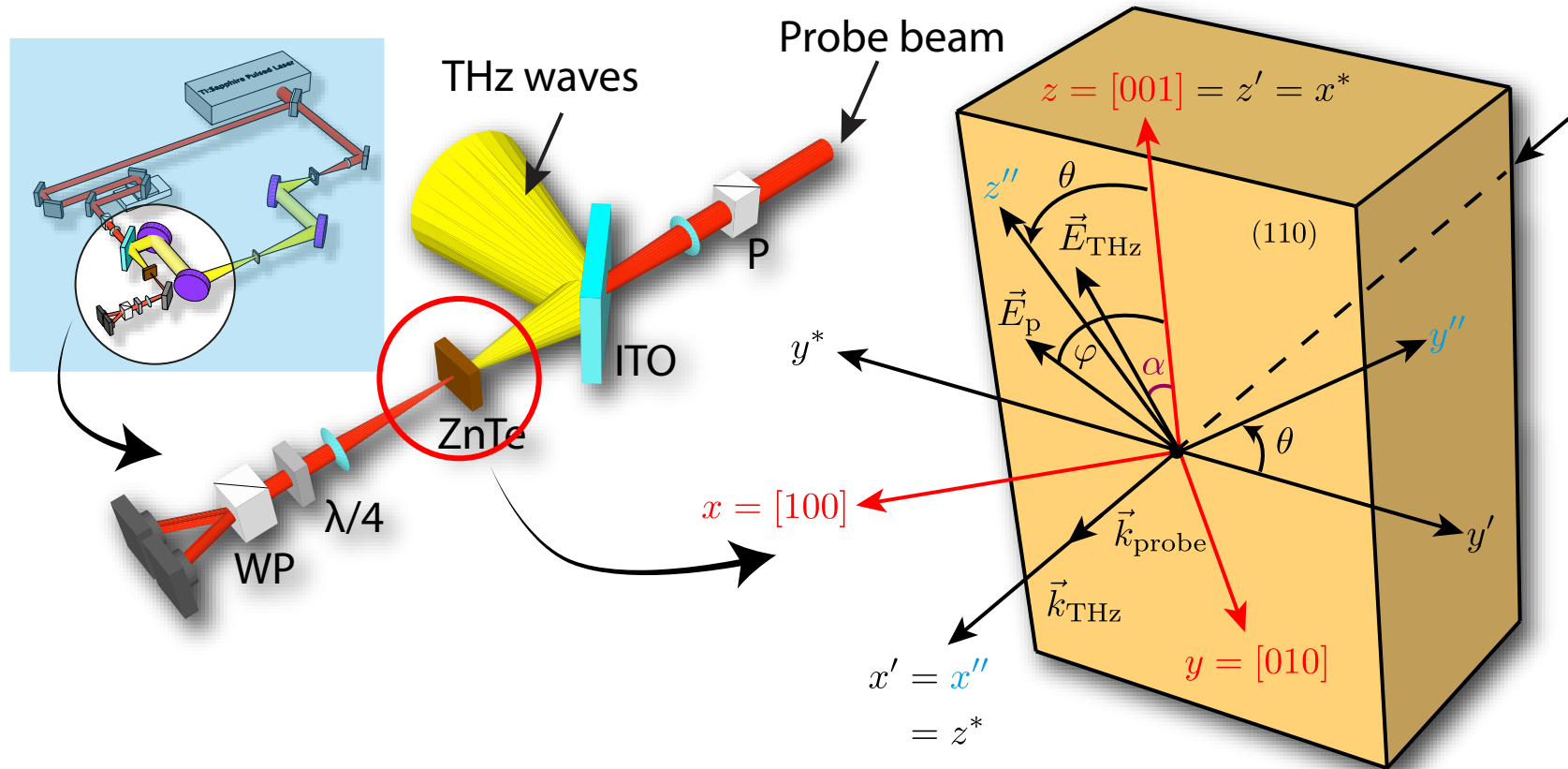


Figure 2.12: Geometry of the (110) ZnTe crystal represented as a THz sensor. A ZnTe has a (110) plane. The THz beam and probe beam counterpropagate through (110) ZnTe. α and φ are angles of the polarization of the THz beam and the polarization of the probe beam, respectively [21]. Here, the principal axes of the crystal and the lab frame are denoted as (x, y, z) and (x^*, y^*, z^*) , respectively.

2.5.4 THz detection process using the Jones matrix

Consider that a polarized probe beam is propagated through (110) ZnTe to measure the THz waves. We now define the transmission axis of a polarizer to be parallel to the x^* -axis of the lab frame shown in Fig. 2.12. Then the Jones matrix of a polarizer is given as

$$\begin{aligned} M_p &= \begin{bmatrix} \cos \varphi & -\sin \varphi \\ \sin \varphi & \cos \varphi \end{bmatrix} \begin{bmatrix} 1 & 0 \\ 0 & 0 \end{bmatrix} \begin{bmatrix} \cos \varphi & \sin \varphi \\ -\sin \varphi & \cos \varphi \end{bmatrix} \\ &= R(-\varphi) P_0 R(\varphi) = \begin{bmatrix} \cos^2 \varphi & \cos \varphi \sin \varphi \\ \cos \varphi \sin \varphi & \sin^2 \varphi \end{bmatrix}, \end{aligned} \quad (2.119)$$

where φ indicates the oriented angle between the lab frame and the slow axis of the polarizer. The rotation matrix R is defined as

$$R(\varphi) = \begin{bmatrix} \cos \varphi & \sin \varphi \\ -\sin \varphi & \cos \varphi \end{bmatrix}. \quad (2.120)$$

EO crystals such as ZnTe can be considered as a wave plate (or retardation plate) having a slow axis oriented at an angle θ and a phase shift Γ_{THz} induced by an external electric field, which are THz waves in this case [19], or

$$M_{\text{EO}} = R(-\theta) J(\Gamma_{\text{THz}}) R(\theta) = \begin{bmatrix} \cos \theta & -\sin \theta \\ \sin \theta & \cos \theta \end{bmatrix} \begin{bmatrix} 1 & 0 \\ 0 & e^{i \Gamma_{\text{THz}}} \end{bmatrix} \begin{bmatrix} \cos \theta & \sin \theta \\ -\sin \theta & \cos \theta \end{bmatrix} = M(\Gamma_{\text{THz}}). \quad (2.121)$$

If the incident wave having a linear polarization state parallel to the x^* axis of the lab frame is denoted as

$$\mathbf{E}_i = E_p \begin{pmatrix} 1 \\ 0 \end{pmatrix}, \quad (2.122)$$

then the transmitted electric field through a polarizer and ZnTe is¹¹

$$\begin{aligned} \mathbf{E} &= \underbrace{R(-\theta) J(\Gamma_{\text{THz}}) R(\theta)}_{\text{ZnTe}} \underbrace{R(-\varphi) P_0 R(\varphi)}_{\text{polarizer}} \mathbf{E}_i \\ &= \begin{bmatrix} \cos^2 \theta + \sin^2 \theta e^{i \Gamma_{\text{THz}}} & \cos \theta \sin \theta - \cos \theta \sin \theta e^{i \Gamma_{\text{THz}}} \\ \cos \theta \sin \theta - \cos \theta \sin \theta e^{i \Gamma_{\text{THz}}} & \sin^2 \theta + \cos^2 \theta e^{i \Gamma_{\text{THz}}} \end{bmatrix} \\ &\times \begin{bmatrix} \cos^2 \varphi & \cos \varphi \sin \varphi \\ \cos \varphi \sin \varphi & \sin^2 \varphi \end{bmatrix} \times E_p \begin{pmatrix} 1 \\ 0 \end{pmatrix} \\ &\simeq E_p \begin{bmatrix} \cos^2 \theta + \sin^2 \theta e^{i \Gamma_{\text{THz}}} & \cos \theta \sin \theta - \cos \theta \sin \theta e^{i \Gamma_{\text{THz}}} \\ \cos \theta \sin \theta - \cos \theta \sin \theta e^{i \Gamma_{\text{THz}}} & \sin^2 \theta + \cos^2 \theta e^{i \Gamma_{\text{THz}}} \end{bmatrix} \begin{pmatrix} \cos \varphi \\ \sin \varphi \end{pmatrix}. \end{aligned} \quad (2.124)$$

Now the phase retardation Γ_{THz} in ZnTe induced by THz waves is calculated. We used (110) ZnTe with thickness of 1 or 2 mm in all of the THz-TDS setups.

¹¹

$$\begin{bmatrix} \cos^2 \varphi & \cos \varphi \sin \varphi \\ \cos \varphi \sin \varphi & \sin^2 \varphi \end{bmatrix} \begin{pmatrix} 1 \\ 0 \end{pmatrix} = \begin{pmatrix} \cos^2 \varphi \\ \cos \varphi \sin \varphi \end{pmatrix} = \cos \varphi \begin{pmatrix} \cos \varphi \\ \sin \varphi \end{pmatrix} \simeq \begin{pmatrix} \cos \varphi \\ \sin \varphi \end{pmatrix}, \quad (2.123)$$

where the common factor $\cos \varphi$ can be neglected if interference effects are not important [19]. The optical probe beam with p-pol can be polarized by 45° by either a polarizer or a half-wave plate. The intensity of the optical probe beam with 45° polarization depends on which optical component is used. In the experiment, it is recommended to use a half-wave plate instead of a polarizer, which is fully described in section A.11.

2.5.5 Calculation of the phase retardation Γ_{THz}

A (110) oriented¹² ZnTe crystal [n-type, high-resistivity $\geq 10^6 \Omega/\text{cm}$ (un-doped)] with thickness of 2 mm is used for measuring the THz waveform by the EO detection method. ZnTe is a member of $\bar{4}3m$ in the point group, is a cubic crystal in the crystal system, and is isotropic in terms of optical symmetry [19]. Since a (100)-cut ZnTe crystal does not exhibit 2nd-order nonlinear response, there is no THz waves radiated from the (100)-cut ZnTe in the case of THz generation via the optical rectification. THz waves can not be measured by the (100)-cut ZnTe in the case of detection, which is explained in section A.6.2 in more detail.

ZnTe has no intrinsic birefringence since ZnTe is optically isotropic and only has birefringence when it is applied by an external electric field. Therefore, ZnTe has a refractive index of $n_x = n_y = n_z = n$ in the optical frequency provided that (x, y, z) is the principal axes of the crystal. Consider that the probe beam and THz waves counterpropagate through ZnTe, where the polarization of the probe beam and THz waves with respect to the z -axis of the ZnTe crystal are described in Fig. 2.12. Recall that the THz waves is an external electric field applied to the (110) ZnTe as the probe beam passes through the ZnTe crystal.

The Pockels coefficients of ZnTe in a point group of $\bar{4}3m$ is given by [19]

$$\mathbf{r} = \begin{bmatrix} 0 & 0 & 0 \\ 0 & 0 & 0 \\ 0 & 0 & 0 \\ r_{41} & 0 & 0 \\ 0 & r_{41} & 0 \\ 0 & 0 & r_{41} \end{bmatrix} \quad (2.125)$$

If x, y, z are the principal axes of the ZnTe crystal and z -axis is parallel to (001) of the crystal as shown in Fig. 2.12, then the index ellipsoid from Eq. (2.118) can be written as

$$\frac{x^2}{n^2} + \frac{y^2}{n^2} + \frac{z^2}{n^2} + 2r_{41}E_{THz}^x yz + 2r_{41}E_{THz}^y xz + 2r_{41}E_{THz}^z xy = 1, \quad (2.126)$$

where $E_{THz}^x, E_{THz}^y, E_{THz}^z$ are the components of the THz waves applied to ZnTe. There are cross-terms of xy, yz, xz in Eq. (2.126), which means that x, y, z are not the principal axes of the ZnTe anymore in the presence of an applied external electric field, which is THz waves.

The index ellipsoid as a function of the modified principal axes in the presence of the THz waves is calculated. As shown in Fig. 2.12, we can immediately see that the orthogonal components of THz waves have a relation as $E_{THz,x} = -E_{THz,y}$.¹³ Coordinates need to be transformed to find the new principal axes. Consider that the new coordinates (x', y', z') are formed when the current coordinates (x, y, z)

¹²The direction of a crystal plane and the plane of a crystal can be described by the Miller indices [23]. The set of all planes equivalent to (hkl) by symmetry is denoted by the notation $\{hkl\}$. And the all directions equivalent to $[hkl]$ by symmetry is denoted by $\langle hkl \rangle$ [23, 24].

¹³As shown in Fig. 2.12, the amplitude components of the THz waves are

$$\mathbf{E}_{THz} = \begin{pmatrix} E_{THz}^x \\ E_{THz}^y \\ E_{THz}^z \end{pmatrix} = E_{THz} \begin{pmatrix} \sin \alpha \cdot \cos(-45^\circ) \\ \sin \alpha \cdot \sin(-45^\circ) \\ \cos \alpha \end{pmatrix},$$

where $|\vec{E}| = E_{THz}$. Therefore $E_{THz}^x = -E_{THz}^y$.

are rotated by 45° with respect to the z -axis. Then the rotation matrix in this case is given by

$$\begin{aligned} \begin{pmatrix} x' \\ y' \\ z' \end{pmatrix} &= \begin{bmatrix} \cos 45^\circ & \sin 45^\circ & 0 \\ -\sin 45^\circ & \cos 45^\circ & 0 \\ 0 & 0 & 1 \end{bmatrix} \begin{pmatrix} x \\ y \\ z \end{pmatrix} \\ \Leftrightarrow \begin{pmatrix} x \\ y \\ z \end{pmatrix} &= \begin{bmatrix} \cos 45^\circ & -\sin 45^\circ & 0 \\ \sin 45^\circ & \cos 45^\circ & 0 \\ 0 & 0 & 1 \end{bmatrix} \begin{pmatrix} x' \\ y' \\ z' \end{pmatrix}. \end{aligned} \quad (2.127)$$

Using Eq. (2.127), Eq. (2.126) is transformed in the form

$$x'^2 \left(\frac{1}{n^2} + r_{41} E_{\text{THz}} \cos \alpha \right) + y'^2 \left(\frac{1}{n^2} - r_{41} E_{\text{THz}} \cos \alpha \right) + \frac{z'^2}{n^2} + 2r_{41} E_{\text{THz}} \sin \alpha y' z' = 1. \quad (2.128)$$

We can see the cross-term of $y' z'$ in Eq. (2.128). Another coordinates transform needs to be considered to remove the cross-term. Consider that the new coordinates (x'', y'', z'') are constructed by rotating the coordinates (x', y', z') by θ with respect to the x' -axis. The corresponding rotation matrix is given by

$$\begin{aligned} \begin{pmatrix} x'' \\ y'' \\ z'' \end{pmatrix} &= \begin{bmatrix} 1 & 0 & 0 \\ 0 & \cos \theta & \sin \theta \\ 0 & -\sin \theta & \cos \theta \end{bmatrix} \begin{pmatrix} x' \\ y' \\ z' \end{pmatrix} \\ \Leftrightarrow \begin{pmatrix} x' \\ y' \\ z' \end{pmatrix} &= \begin{bmatrix} 1 & 0 & 0 \\ 0 & \cos \theta & -\sin \theta \\ 0 & \sin \theta & \cos \theta \end{bmatrix} \begin{pmatrix} x'' \\ y'' \\ z'' \end{pmatrix}. \end{aligned} \quad (2.129)$$

Then Eq. (2.128) can be written as ¹⁴

$$\begin{aligned} &x''^2 \left[\frac{1}{n^2} + r_{41} E_{\text{THz}} \cos \alpha \right] \\ &+ y''^2 \left\{ \frac{1}{n^2} - r_{41} E_{\text{THz}} \left[\cos \alpha \cdot \sin^2 \theta + \cos(\alpha + 2\theta) \right] \right\} \\ &+ z''^2 \left\{ \frac{1}{n^2} - r_{41} E_{\text{THz}} \left[\cos \alpha \cdot \cos^2 \theta - \cos(\alpha + 2\theta) \right] \right\} \\ &+ y'' z'' r_{41} E_{\text{THz}} \left[\cos \alpha \cdot \sin 2\theta + 2 \sin \alpha \cdot \cos 2\theta \right] = 1, \end{aligned} \quad (2.131)$$

where we find that the (x'', y'', z'') coordinates can be the principle axes of the index ellipsoid if the

¹⁴ y'' term:

$$\begin{aligned} &\frac{\cos^2 \theta + \sin 2\theta}{n^2} - r_{41} E_{\text{THz}} \cos \alpha \cdot \cos^2 \theta + 2r_{41} E_{\text{THz}} \sin \alpha \cdot \cos \theta \cdot \sin \theta \\ &= \frac{1}{n^2} - r_{41} E_{\text{THz}} \left[\cos \alpha \cdot \cos^2 \theta + 0 - 2 \sin \alpha \cdot \cos \theta \cdot \sin \theta \right] \\ &= \frac{1}{n^2} - r_{41} E_{\text{THz}} \left[\cos \alpha \cdot \cos^2 \theta + (\cos \alpha \cdot \sin^2 \theta - \cos \alpha \cdot \sin^2 \theta) - 2 \sin \alpha \cdot \cos \theta \cdot \sin \theta \right] \\ &= \frac{1}{n^2} - r_{41} E_{\text{THz}} \left[\cos \alpha \cdot \sin^2 \theta + \cos \alpha (\cos^2 \theta - \sin^2 \theta) - 2 \sin \alpha \cdot \cos \theta \cdot \sin \theta \right] \\ &= \frac{1}{n^2} - r_{41} E_{\text{THz}} \left[\cos \alpha \cdot \sin^2 \theta + \cos \alpha \cdot \cos 2\theta - \sin \alpha \cdot \sin 2\theta \right] = \frac{1}{n^2} - r_{41} E_{\text{THz}} \left[\cos \alpha \cdot \sin^2 \theta + \cos(\alpha + 2\theta) \right] \end{aligned} \quad (2.130)$$

cross-term of $y''z''$ vanished. ¹⁵ ¹⁶

To eliminate the cross-term $y''z''$ in Eq. (2.131), a relation given by ¹⁷

$$2\theta = -\tan^{-1}(2 \tan \alpha) - n\pi \quad (2.139)$$

needs to be considered, where the condition of $\tan \alpha$ in Eq. (2.139) is

$$\tan \alpha = \tan(\alpha + n\pi) = \tan(\alpha - n\pi), \quad (2.140)$$

which implies that

$$-\frac{\pi}{2} \leq \alpha - n\pi < \frac{\pi}{2}, \quad (2.141)$$

so that

$$n\pi - \frac{\pi}{2} \leq \alpha < n\pi + \frac{\pi}{2}, \quad n = 0, 1, 2, \dots \quad (2.142)$$

From Eqs. (2.139) and Eq. (2.140), we finally obtain the index ellipsoid given by

$$\begin{aligned} & x''^2 \left(\frac{1}{n^2} + r_{41} E_{\text{THz}} \cos \alpha \right) \\ & + y''^2 \left\{ \frac{1}{n^2} - r_{41} E_{\text{THz}} \left[\cos \alpha \cdot \sin^2 \theta + \cos(\alpha + 2\theta) \right] \right\} \\ & + z''^2 \left\{ \frac{1}{n^2} - r_{41} E_{\text{THz}} \left[\cos \alpha \cdot \cos^2 \theta - \cos(\alpha + 2\theta) \right] \right\} = 1. \end{aligned} \quad (2.143)$$

For a small external electric field, the refractive indices for a probe beam propagating along the x''

¹⁵ z'' term:

$$\begin{aligned} & \frac{\cos^2 \theta + \sin 2\theta}{n^2} - r_{41} E_{\text{THz}} \cos \alpha \cdot \sin^2 \theta - 2r_{41} E_{\text{THz}} \sin \alpha \cdot \cos \theta \cdot \sin \theta \\ & = \frac{1}{n^2} - r_{41} E_{\text{THz}} \left[\cos \alpha \cdot \sin^2 \theta + 0 + 2 \sin \alpha \cdot \cos \theta \cdot \sin \theta \right] \\ & = \frac{1}{n^2} - r_{41} E_{\text{THz}} \left[\cos \alpha \cdot \sin^2 \theta + (\cos \alpha \cdot \cos^2 \theta - \cos \alpha \cdot \cos^2 \theta) + \sin \alpha \cdot \sin 2\theta \right] \\ & = \frac{1}{n^2} - r_{41} E_{\text{THz}} \left[\cos \alpha \cdot \cos^2 \theta - \cos \alpha (\cos^2 \theta - \sin^2 \theta) + \sin \alpha \cdot \sin 2\theta \right] \\ & = \frac{1}{n^2} - r_{41} E_{\text{THz}} \left[\cos \alpha \cdot \cos^2 \theta - \cos \alpha \cdot \cos 2\theta + \sin \alpha \cdot \sin 2\theta \right] = \frac{1}{n^2} - r_{41} E_{\text{THz}} \left[\cos \alpha \cdot \cos^2 \theta - \cos(\alpha + 2\theta) \right] \end{aligned} \quad (2.132)$$

¹⁶ $y''z''$ term:

$$r_{41} E_{\text{THz}} \left[\cos \alpha \cdot \sin 2\theta + 2 \sin \alpha \cdot \cos 2\theta \right]. \quad (2.133)$$

¹⁷When the coefficient of $y''z''$ term is zero, the coefficient given by

$$\cos \alpha \cdot \sin 2\theta + 2 \sin \alpha \cdot \cos 2\theta = 0 \quad (2.134)$$

becomes

$$\sin 2\theta + 2 \tan \alpha \cdot \cos 2\theta = 0. \quad (2.135)$$

Then we find that

$$2 \tan \alpha = -\frac{\sin 2\theta}{\cos 2\theta} = -\tan 2\theta = -\tan(n\pi + 2\theta) = \tan[-(n\pi + 2\theta)], \quad (2.136)$$

which implies that

$$n\pi + 2\theta = -\tan^{-1}[2 \tan \alpha], \quad (2.137)$$

where 2θ is given by

$$2\theta = -\tan^{-1}[2 \tan \alpha] - n\pi \quad n \in \mathbb{Z} \cup \{0\}. \quad (2.138)$$

direction (z^* direction) can be obtained as ¹⁸

$$\begin{aligned} n_{y''}(\alpha) &\simeq n + \frac{n^3}{2} E_{\text{THz}} r_{41} \left[\cos \alpha \cdot \sin^2 \theta + \cos(\alpha + 2\theta) \right] \\ n_{z''}(\alpha) &\simeq n + \frac{n^3}{2} E_{\text{THz}} r_{41} \left[\cos \alpha \cdot \cos^2 \theta - \cos(\alpha + 2\theta) \right]. \end{aligned} \quad (2.149)$$

We can see that $n_{y''}(\alpha)$ and $n_{z''}(\alpha)$ are different in Eq. (2.149). We find that the refractive index of ZnTe for a probe beam is changed due to an external THz waves. Therefore the polarization along y'' direction and z'' direction of the probe beam is changed and then the resulting polarization of probe beam is elliptical. Hence the phase retardation Γ_{THz} in ZnTe with thickness of L induced by THz waves is

$$\begin{aligned} \Gamma_{\text{THz}}(\omega) &= \frac{w}{c} \left\{ n_{y''}(\alpha) - n_{z''}(\alpha) \right\} L \\ &= \frac{wn^3 E_{\text{THz}} r_{41} L}{2c} \left[\cos \alpha (\sin^2 \theta - \cos^2 \theta) + 2 \cos(\alpha + 2\theta) \right], \end{aligned} \quad (2.150)$$

where c is the speed of light and ω is the optical angular frequency of the probe beam [21].

2.5.6 Electro-optic detection : Probing the index ellipsoid induced from elliptically polarized probe beams

There are two experimental schemes to measure THz waves as shown in Fig. 2.13. The key point to measure the generated THz waves is to measure the altered polarization of the probe beam due to THz waves applied to ZnTe. The first way is to use the balanced detection of the elliptically polarized probe beam through a quarter-wave plate. For this, a polarization beam splitter (PBS) such as a Wollaston prism or a Rochon prism as well as a quarter-wave plate are commonly used as shown in Fig. 2.13-(a). When the probe beam is transmitted through a quarter-wave plane (QWP), ZnTe, and a polarizer (P) propagates toward the Wollaston prism (WP), two orthogonal components of the transmitted field are

18

$$\begin{aligned} x''^2 \left(\frac{1}{n^2} + r_{41} E_{\text{THz}} \cos \alpha \right) + y''^2 \left\{ \frac{1}{n^2} - r_{41} E_{\text{THz}} \left[\cos \alpha \cdot \sin^2 \theta + \cos(\alpha + 2\theta) \right] \right\} \\ + z''^2 \left\{ \frac{1}{n^2} - r_{41} E_{\text{THz}} \left[\cos \alpha \cdot \cos^2 \theta - \cos(\alpha + 2\theta) \right] \right\} = 1 \end{aligned} \quad (2.144)$$

is equivalent to

$$\frac{x''^2}{n_{x''}^2} + \frac{y''^2}{n_{y''}^2} + \frac{z''^2}{n_{z''}^2} = 1. \quad (2.145)$$

By comparing coefficients of x'' , y'' , and z'' in Eqs. (2.144) and (2.145), we obtain

$$\frac{1}{n_{y''}^2} = \frac{1}{n^2} - r_{41} E_{\text{THz}} \left[\cos \alpha \cdot \sin^2 \theta + \cos(\alpha + 2\theta) \right], \quad (2.146)$$

which implies that

$$n_{y''}^2 = \frac{1}{\frac{1}{n^2} - r_{41} E_{\text{THz}} \left[\cos \alpha \cdot \sin^2 \theta + \cos(\alpha + 2\theta) \right]} = \frac{n^2}{1 - n^2 r_{41} E_{\text{THz}} \left[\cos \alpha \cdot \sin^2 \theta + \cos(\alpha + 2\theta) \right]}. \quad (2.147)$$

We thus find from this equation that

$$\begin{aligned} n_{y''} &= n \left\{ 1 - n^2 r_{41} E_{\text{THz}} \left[\cos \alpha \cdot \sin^2 \theta + \cos(\alpha + 2\theta) \right] \right\}^{-\frac{1}{2}} \\ &\simeq n \left\{ 1 + \frac{n^2}{2} r_{41} E_{\text{THz}} \left[\cos \alpha \cdot \sin^2 \theta + \cos(\alpha + 2\theta) \right] \right\}. \end{aligned} \quad (2.148)$$

Note that $n_{z''}$ can be obtained using the same method.

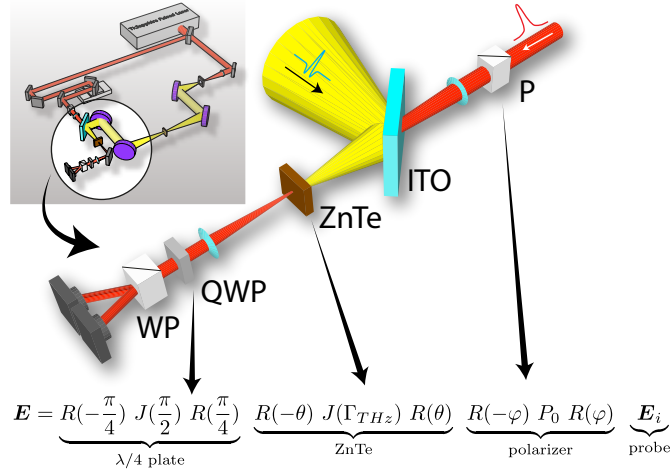


Figure 2.13: The electro-optic detection using a quarter-wave plate and a Wollaston prism.

then separated. Using Eq. (2.124), this procedure can be written as

$$\mathbf{E} = \underbrace{R\left(-\frac{\pi}{4}\right) J\left(\frac{\pi}{2}\right) R\left(\frac{\pi}{4}\right)}_{\lambda/4 \text{ plate}} \underbrace{R(-\theta) J(\Gamma_{\text{THz}}) R(\theta)}_{\text{ZnTe}} \underbrace{R(-\varphi) P_0 R(\varphi)}_{\text{Polarizer}} \underbrace{\mathbf{E}_i}_{\text{Probe beam}}, \quad (2.151)$$

where $J(\pi/2)$ represents a Jones matrix of a quarter-wave plate given by [19]

$$J\left(\frac{\pi}{2}\right) = \begin{bmatrix} 1 & 0 \\ 0 & e^{i\frac{\pi}{2}} \end{bmatrix}. \quad (2.152)$$

The probe beam was defined as the lab frame of (x^*, y^*) . The $\pi/4$ in Jones matrix of a quarter-wave plate indicates the oriented angle between the x^* direction and the slow axis of a quarter-wave plate. Equation (2.151) can be fully calculated as

$$\mathbf{E} = \begin{pmatrix} A(\theta, \Gamma_{\text{THz}}) \cos \varphi + B(\theta, \Gamma_{\text{THz}}) \sin \varphi \\ C(\theta, \Gamma_{\text{THz}}) \cos \varphi + D(\theta, \Gamma_{\text{THz}}) \sin \varphi \end{pmatrix} = \begin{pmatrix} E_{x^*} \\ E_{y^*} \end{pmatrix}, \quad (2.153)$$

where each coefficient is denoted as A, B, C, and D, yielding

$$\begin{aligned} A(\theta, \Gamma_{\text{THz}}) &= (1/2 - i/2) \cos \theta \sin \theta + (1/2 + i/2) \cos^2 \theta \\ &\quad + (1/2 + i/2) e^{i\Gamma_{\text{THz}}} \sin^2 \theta - (1/2 - i/2) e^{i\Gamma_{\text{THz}}} \cos \theta \sin \theta, \\ B(\theta, \Gamma_{\text{THz}}) &= (1/2 + i/2) \cos \theta \sin \theta + (1/2 - i/2) \sin^2 \theta \\ &\quad + (1/2 - i/2) e^{i\Gamma_{\text{THz}}} \cos^2 \theta - (1/2 + i/2) e^{i\Gamma_{\text{THz}}} \cos \theta \sin \theta, \end{aligned} \quad (2.154)$$

$$\begin{aligned} C(\theta, \Gamma_{\text{THz}}) &= (1/2 + i/2) \cos \theta \sin \theta + (1/2 - i/2) \cos^2 \theta \\ &\quad + (1/2 - i/2) e^{i\Gamma_{\text{THz}}} \sin^2 \theta - (1/2 + i/2) e^{i\Gamma_{\text{THz}}} \cos \theta \sin \theta, \\ D(\theta, \Gamma_{\text{THz}}) &= (1/2 - i/2) \cos \theta \sin \theta + (1/2 + i/2) \sin^2 \theta \\ &\quad + (1/2 + i/2) e^{i\Gamma_{\text{THz}}} \cos^2 \theta - (1/2 - i/2) e^{i\Gamma_{\text{THz}}} \cos \theta \sin \theta. \end{aligned} \quad (2.155)$$

The elliptically polarized beam through a quarter-wave plate is separated into two orthogonal components by a polarization beam splitter (PBS) such as a Wollaston prism or a Rochon prism. The intensity difference ΔI of the polarization components ¹⁹ of the transmitted probe beam through a PBS can therefore be written as [21]

$$\Delta I = |E_{x^*}|^2 - |E_{y^*}|^2 = I_p \sin \Gamma_{\text{THz}} \sin [2(\varphi - \theta)], \quad (2.157)$$

where I_p is the intensity of the probe beam and equals $|E_p|^2$. The calculation processes for Eq. (2.153) obtained by Eq. (2.151) and Eq. (2.157) obtained by Eq. (2.153) with Eqs. (2.154) and (2.155) are fully described by a Matlab code in the last part of this section A.11.

When the phase retardation Γ_{THz} in Eq. (2.150) induced by THz waves is small, then Eq. (2.157) is approximately reduced as

$$\begin{aligned} \Delta I &= I_p \sin \{2(\varphi - \theta)\} \sin \Gamma_{\text{THz}} \simeq I_p \sin \{2(\varphi - \theta)\} \Gamma_{\text{THz}} \\ &= I_p \frac{wn^3 E_{\text{THz}} r_{41} L}{2c} \sin \{2(\varphi - \theta)\} \left[\cos \alpha (\sin^2 \theta - \cos^2 \theta) + 2 \cos(\alpha + 2\theta) \right], \end{aligned} \quad (2.158)$$

where the last two terms can be simplified using a relation (2.138) following as

$$\begin{aligned} &\sin \{2(\varphi - \theta)\} \left[\cos \alpha (\sin^2 \theta - \cos^2 \theta) + 2 \cos(\alpha + 2\theta) \right] \\ &= \sin \{2(\varphi - \theta)\} \left[-\cos \alpha \cos 2\theta + 2 \cos(\alpha + 2\theta) \right] \\ &= \sin \{2(\varphi - \theta)\} \left(\cos \alpha \cos 2\theta - 2 \sin \alpha \sin 2\theta \right) \\ &= \left(\sin 2\varphi \cos 2\theta - \cos 2\varphi \sin 2\theta \right) \left(\cos \alpha \cos 2\theta - 2 \sin \alpha \sin 2\theta \right) \end{aligned}$$

19

$$\begin{aligned} \Delta I &= |E_{x^*}|^2 - |E_{y^*}|^2 \\ &= I_p \left[2 \cos \varphi \cos^4 \theta \sin \Gamma_{\text{THz}} \sin \varphi - 2 \cos \varphi \sin \Gamma_{\text{THz}} \sin \varphi \sin^4 \theta \right. \\ &\quad \left. - 2 \cos^2 \varphi \cos \theta \sin \Gamma_{\text{THz}} \sin^3 \theta - 2 \cos^2 \varphi \cos^3 \theta \sin \Gamma_{\text{THz}} \sin \theta \right. \\ &\quad \left. + 2 \cos \theta \sin \Gamma_{\text{THz}} \sin^2 \varphi \sin^3 \theta + 2 \cos^3 \theta \sin \Gamma_{\text{THz}} \sin^2 \varphi \sin \theta \right] \\ &= I_p \sin \Gamma_{\text{THz}} \left[2 \cos \varphi \cos^4 \theta \sin \varphi - 2 \cos \varphi \sin \varphi \sin^4 \theta \right. \\ &\quad \left. - 2 \cos^2 \varphi \cos \theta \sin^3 \theta - 2 \cos^2 \varphi \cos^3 \theta \sin \theta + 2 \cos \theta \sin^2 \varphi \sin^3 \theta + 2 \cos^3 \theta \sin^2 \varphi \sin \theta \right] \\ &= I_p \sin \Gamma_{\text{THz}} \left[2 \cos \varphi \sin \varphi \left\{ \cos^2 \theta (1 - \sin^2 \theta) - \sin^2 \theta (1 - \cos^2 \theta) \right\} \right. \\ &\quad \left. - 2 \cos^2 \varphi \cos \theta \sin \theta \left\{ \sin^2 \theta + \cos^2 \theta \right\} + 2 \cos \theta \sin \varphi \sin \theta \left\{ \sin \varphi \sin^2 \theta + \cos^2 \theta \sin \varphi \right\} \right] \\ &= I_p \sin \Gamma_{\text{THz}} \left[2 \cos \varphi \sin \varphi \left\{ \cos^2 \theta - \cos^2 \theta \sin^2 \theta - \sin^2 \theta + \sin^2 \theta \cos^2 \theta \right\} \right. \\ &\quad \left. - 2 \cos^2 \varphi \cos \theta \sin \theta + 2 \cos \theta \sin \varphi \sin \theta \left\{ \sin \varphi (1 - \cos^2 \theta) + \cos^2 \theta \sin \varphi \right\} \right] \\ &= I_p \sin \Gamma_{\text{THz}} \left[2 \cos \varphi \sin \varphi \left\{ \cos^2 \theta - \sin^2 \theta \right\} - 2 \cos^2 \varphi \cos \theta \sin \theta \right. \\ &\quad \left. + 2 \cos \theta \sin \varphi \sin \theta \left\{ \sin \varphi - \sin \varphi \cos^2 \theta + \cos^2 \theta \sin \varphi \right\} \right] \\ &= I_p \sin \Gamma_{\text{THz}} \left[2 \cos \varphi \sin \varphi \cos 2\theta - 2 \cos^2 \varphi \cos \theta \sin \theta + 2 \cos \theta \sin^2 \varphi \sin \theta \right] \\ &= I_p \sin \Gamma_{\text{THz}} \left[\sin 2\varphi \cos 2\theta - 2 \cos \theta \sin \theta (\cos^2 \varphi - \sin^2 \varphi) \right] \\ &= I_p \sin \Gamma_{\text{THz}} \left[\sin 2\varphi \cos 2\theta - \cos 2\varphi \sin 2\theta \right] = I_p \sin \Gamma_{\text{THz}} \sin(2\varphi - 2\theta). \end{aligned} \quad (2.156)$$

$$\begin{aligned}
&= \cos \alpha \cos^2 2\theta \sin 2\varphi - \underbrace{\cos \alpha \sin 2\theta}_{-2 \sin \alpha \cos 2\theta} \cos 2\theta \cos 2\varphi \\
&+ \underbrace{(-2) \sin \alpha \cos 2\theta}_{\cos \alpha \sin 2\theta} \sin 2\theta \sin 2\varphi + 2 \sin \alpha \sin^2 2\theta \cos 2\varphi \\
&= \cos \alpha \cos^2 2\theta \sin 2\varphi + 2 \sin \alpha \cos 2\varphi \cos^2 2\theta + \cos \alpha \sin 2\varphi \sin^2 2\theta + 2 \sin \alpha \sin^2 2\theta \cos 2\varphi \\
&= \left(\cos \alpha \sin 2\varphi + 2 \sin \alpha \cos 2\varphi \right) \cos^2 2\theta + \left(\cos \alpha \sin 2\varphi + 2 \sin \alpha \cos 2\varphi \right) \sin^2 2\theta \\
&= \left(\cos \alpha \sin 2\varphi + 2 \sin \alpha \cos 2\varphi \right) \left(\cos^2 2\theta + \sin^2 2\theta \right) = \cos \alpha \sin 2\varphi + 2 \sin \alpha \cos 2\varphi. \tag{2.159}
\end{aligned}$$

Therefore we obtain the intensity difference ΔI as a function of two polarization angles of α for THz waves and φ for probe beams with respect to (001) given as [21]

$$\Delta I(\alpha, \varphi) = I_p \frac{wn^3 E_{\text{THz}} r_{41} L}{2c} \left(\cos \alpha \sin 2\varphi + 2 \sin \alpha \cos 2\varphi \right), \tag{2.160}$$

where we find that the THz waves is proportional to the intensity difference ΔI .

It is concluded that the polarization of the probe beam is changed by THz waves and the whole THz waveform in time-domain is measured by a balanced detection of the transmitted probe beam through PBS, a quarter-wave plate, and ZnTe by varying the time delay between probe beam and THz waves shown in Fig. 2.2.

Figure.2.14 describes the whole THz detection processes. In section A.6.2, the brief process of EO sampling with (110) ZnTe as well as (100) ZnTe is shown. The balanced detection was carried out using a Lock-in amplifier, which is explained in Appendix B.1.

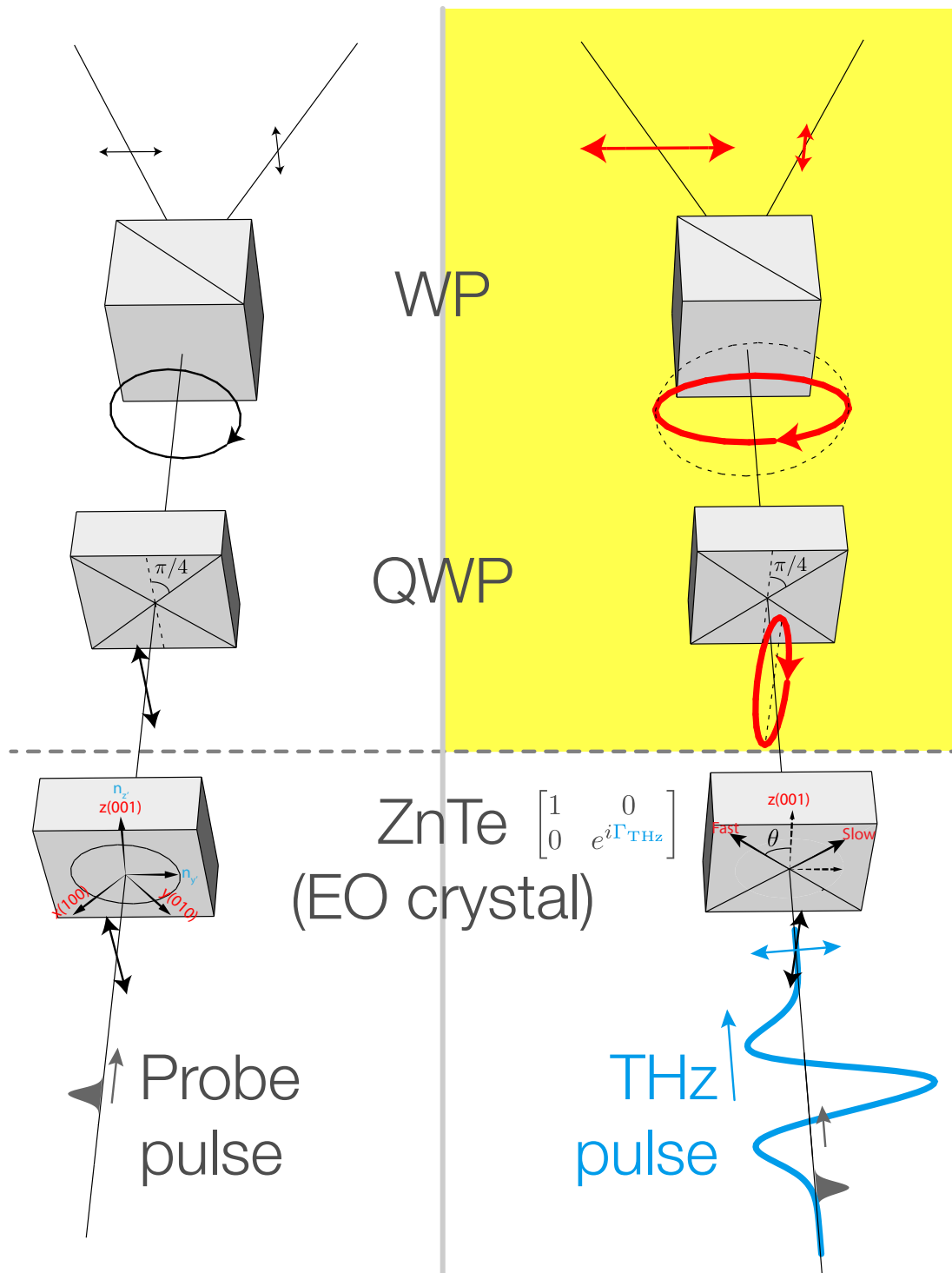


Figure 2.14: Schematic diagram of a typical setup for free-space EO detection. The polarization of the probe beam does not change without THz waves. The polarization of the probe, however, is changed by birefringence in ZnTe induced by THz waves. By sweeping in time-domain using time-delay, the whole THz waveform can be measured. QWP and WP indicate a quarter-wave plate and a Wollaston prism, respectively.

2.5.7 Electro-optic detection : Probing the index ellipsoid induced from linear polarized probe beam

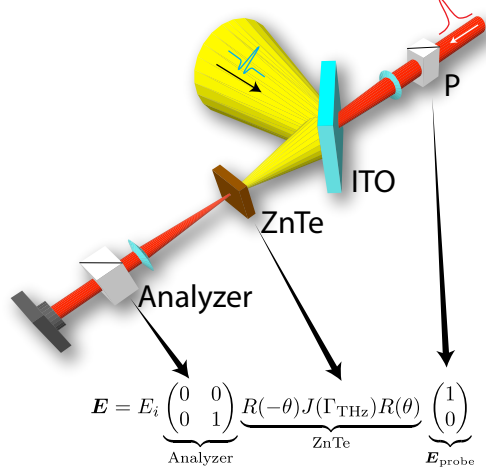


Figure 2.15: The electro-optic detection using crossed polarizers.

Recall that ZnTe is a member of $\bar{4}3m$ in the point group, is a cubic crystal in crystal system, and isotropic in terms of optical symmetry [19]. ZnTe has no intrinsic birefringence since ZnTe is optically isotropic and it must be remembered that the birefringence in ZnTe is induced by the external electric field.

The transmitted probe beam through a ZnTe and crossed polarizers can be written by the Jones matrix given as

$$\begin{aligned} \mathbf{E} &= E_p \underbrace{\begin{bmatrix} 0 & 0 \\ 0 & 1 \end{bmatrix}}_{\text{Analyzer}} \underbrace{R(-\theta)J(\Gamma_{\text{THz}})R(\theta)}_{\text{ZnTe}} \underbrace{\begin{pmatrix} 1 \\ 0 \end{pmatrix}}_{\mathbf{E}_{\text{Probe}}} \\ &= E_p \begin{pmatrix} 0 \\ \cos \theta \sin \theta - e^{i\Gamma_{\text{THz}}} \cos \theta \sin \theta \end{pmatrix}, \end{aligned} \quad (2.161)$$

where the polarization of the incident wave has a linear polarization in the direction of x^* axis of the lab frame for sake of simplicity. The corresponding Jones matrix of an analyzer is shown in Eq. (2.161). Then the intensity from a photodiode becomes²⁰

$$\begin{aligned} I &= |\mathbf{E}|^2 = 2 I_p \cos^2 \theta \sin^2 \theta (1 - \cos \Gamma_{\text{THz}}) \\ &= I_p \cos^2 \theta \sin^2 \theta \sin^2 \left(\frac{\Gamma_{\text{THz}}}{2} \right), \end{aligned} \quad (2.163)$$

where I_p is the intensity of the probe beam which equals $|E_p|^2$. Using Eq. (2.138), the above equation is slightly changed into

$$I = I_p \left[\tan^{-1}(2 \tan \alpha) \right] \sin^2 \left(\frac{\Gamma_{\text{THz}}}{2} \right), \quad (2.164)$$

²⁰

$$|1 - e^{i\Gamma_{\text{THz}}}|^2 = (1 - e^{-i\Gamma_{\text{THz}}})(1 - e^{i\Gamma_{\text{THz}}}) = 2 - 2 \frac{e^{i\Gamma_{\text{THz}}} + e^{-i\Gamma_{\text{THz}}}}{2} = 2(1 - \cos \Gamma_{\text{THz}}). \quad (2.162)$$

which is then a function of the polarization of the THz waves with respect to the x^* -axis of the lab frame.

Provided $\Gamma_{\text{THz}} \ll 1$, Eq. (2.164) shows that the intensity is proportional to Γ_{THz}^2 , and not to Γ_{THz} . Recall that Γ_{THz} is proportional to E_{THz} . Thus, Eq. (2.164) implies that the intensity is proportional to the square of the THz electric field (E_{THz}^2). However, it has been confirmed experimentally and theoretically that it is possible to measure the THz time-domain waveform in the crossed polarizer geometry [25].

The key point in measuring THz waveforms in this geometry is that the crossed polarizers cannot eliminate the background light perfectly. The major contributor of the background light is the probe beam since the polarization of the linear polarized probe beam is a bit rotated due to the residue birefringence in ZnTe by the probe beam itself such that the polarization of the probe beam through ZnTe has become slightly elliptically polarized (*i.e.* imperfectly linear polarized). Here, the residue birefringence, or called as the optical bias, means birefringence by the higher order terms of optical susceptibilities χ than $\chi^{(1)}$ of ZnTe induced by the probe beam [26]. Thus, the higher order term $\chi^{(j)}$ means $\chi^{(2)}$ or $\chi^{(3)}$ of ZnTe induced by the probe beam [26].

For this reason, the analyzer cannot completely get rid of the polarization component of the transmitted probe beam. Suppose that η is the contribution by the scattering light in ZnTe and Γ_{ob} is the optical bias in ZnTe induced by the imperfectly linear polarized probe beam (shortly called as “background light”). Then the total phase retardation in ZnTe by the probe beam and THz waves can be represented as the Jones matrix given by

$$\begin{bmatrix} 1 & 0 \\ 0 & e^{i\Gamma_{\text{THz}}} \end{bmatrix} \rightarrow \begin{bmatrix} 1 & 0 \\ 0 & e^{i(\Gamma_{ob} + \Gamma_{\text{THz}})} \end{bmatrix}. \quad (2.165)$$

From Eq. (2.161) and the substitution $\Gamma_{\text{THz}} \rightarrow \Gamma_{ob} + \Gamma_{\text{THz}}$, all the detection processes in this geometry can be written as [25]

$$I = I_p \left[\eta + \sin^2 \left(\Gamma_{ob} + \Gamma_{\text{THz}} \right) \right], \quad (2.166)$$

where the phase term of η is neglected since the scattering has a random phase and two phase retardations are twice for sake of simplicity.

The optical bias induced by the probe beam is sufficiently larger than the phase retardation induced by THz waves, however, the optical bias is much smaller than 1 since ZnTe has no intrinsic birefringence except the optical bias. Therefore, Eq. (2.166) for $\Gamma_{\text{THz}} \ll \Gamma_{ob}$ is calculated as²¹

$$I = I_p \left[\eta + \Gamma_{ob}^2 + 2 \Gamma_{ob} \Gamma_{\text{THz}} \right]. \quad (2.168)$$

According to Eq. (2.168) and $\Gamma_{\text{THz}} \propto E_{\text{THz}}$, the intensity measured by a photodiode attached to a lock-in amplifier is proportional to THz waves since the optical bias induced by the probe beam is nearly constant. Thus, THz waves can consequently be measured to have nearly the same THz signal waveform measured by the method described in section 2.5.6.

²¹For $\Gamma_{\text{THz}} \ll \Gamma_{ob}$, let's $a = \Gamma_{ob}$ and $b = \Gamma_{\text{THz}}$. Then

$$\begin{aligned} \sin^2 \left(\Gamma_{ob} + \Gamma_{\text{THz}} \right) &= \sin^2 X = \left(X - \frac{X^3}{3!} + \dots \right) \left(X - \frac{X^3}{3!} + \dots \right) \\ &= X^2 - \frac{X^4}{3!} - \frac{X^4}{3!} + \dots \simeq X^2 \\ &= \left[a \left(1 + \frac{b}{a} \right) \right]^2 \simeq a^2 \left(1 + \frac{2b}{a} \right) = a^2 + 2ab = \Gamma_{ob}^2 + 2 \Gamma_{ob} \Gamma_{\text{THz}}. \end{aligned} \quad (2.167)$$

We considered the scattering contribution η and the optical bias Γ_{ob} to explain EO detection in the crossed polarizers geometry. It is again needed to take into account the EO detection method in section 2.5.6 by considering the two terms, η and Γ_{ob} . This part is discussed in section A.7.

2.6 Spectral components from time-domain THz waveform

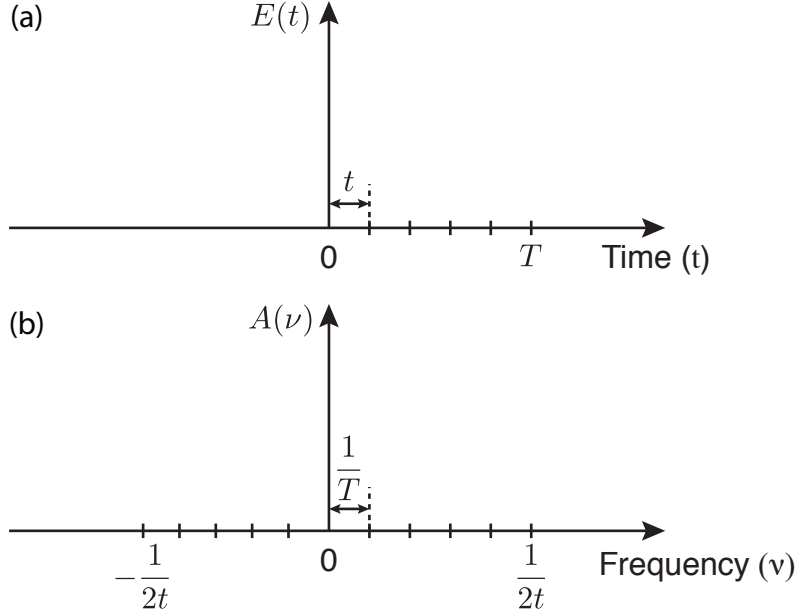


Figure 2.16: Simple schematic representation by Fourier transformation.

Let's consider that sub-cycle THz waveform $\tilde{E}(t)$ measured by the EO sampling is recorded within a T time window with a time step t . Corresponding to Eq. (2.6), the spectral amplitude and phase information from the THz signal can be obtained by applying the Fourier transform to the time-domain THz signal given by

$$\tilde{E}(\omega) = \int_{-\infty}^{\infty} dt \tilde{E}(t) e^{i\omega t} = A(\omega) e^{i\phi(\omega)}, \quad (2.169)$$

where the spectral amplitude and phase are denoted as A and ϕ , respectively.

At the same time, we should take into account the frequency-domain axis corresponding to the measured time window as in Fig. 2.16(a). By the definition of the Fourier transform, the corresponding frequency range is from $-\frac{1}{2t}$ to $\frac{1}{2t}$ with a frequency resolution of $1/T$ as shown in Fig. 2.16(b). In Matlab, we can easily define the frequency domain as follows.

```
% Let the matrix of time-domain be time. Then
f=fft(signal); % Apply the Fourier transform to data.
freq=transpose( (1/ (time(2)-time(1)) ) * ( 0:length(f)-1 ) / length(f) ); % Frequency axis!
% freq number of matrix = (n/2-1-0)+1=n/2

% If length(time) is even number, then frequency axis is defined by
% freq=(1/(time(2)-time(1)))*(-length(f)/2:length(f)/2-1)/length(f);

% If length(time) is odd number, then frequency axis is defined by
% freq=(1/(time(2)-time(1)))*(-length(f)-1)/2 : (length(f)-1)/2 /length(f);
```

2.7 Summary

The generation and detection methods of THz waves were discussed in the previous sections. Figure 2.17 shows a THz-TDS setup in a linear configuration composed of 4 Teflon THz lenses whose focal lengths are 100 mm. The THz waves are generated by PCA as shown in Fig. 2.17 and are then measured by probe beams. The PCA is biased using a step function signal generated from a 65 kHz function generator with dc voltages of 30 V (TOELLNER TOE 7704). In the detection processes, a THz pulse and a probe laser pulse should be co-propagated and merged at (110) ZnTe having a thickness of 2 mm [n-type, high-resistivity $\geq 10^6 \Omega/\text{cm}$ (un-doped)]. We used an indium tin oxide (ITO) coated glass with thickness of 1 mm to co-propagate the two pulses. It is to note that an ITO glass reflects THz waves and transmits the probe beam. A silicon (Si) wafer or a Pellicle beam splitter (PBS) can also be an alternative to the ITO glass. Si and PBS, however, reflects the probe beam and transmits THz waves.

THz waves detected by the EO detection method are measured with a Lock-in amplifier, which is further explained in section B.1. The Lock-in amplifier was used to record the photo currents from the two photodiodes (or one photodiode). The reference signal of the Lock-in amplifier was locked to a step function signal provided by a 65 kHz function generator.

Figure 2.18 shows the two constructed two THz-TDS setups. One is a THz-TDS in a linear configuration composed of 4 Teflon lenses whose focal lengths are 100 mm. The other is a conventional THz-TDS comprised of 4 off-axis parabolic mirrors. A pair of the parabolic mirrors with focal lengths 150 mm were used to focus THz waves at the focal plane. The whole THz-TDS setup is purged with dry air to reduce the absorption by water vapor in the THz frequency range. The pressure of the dry air

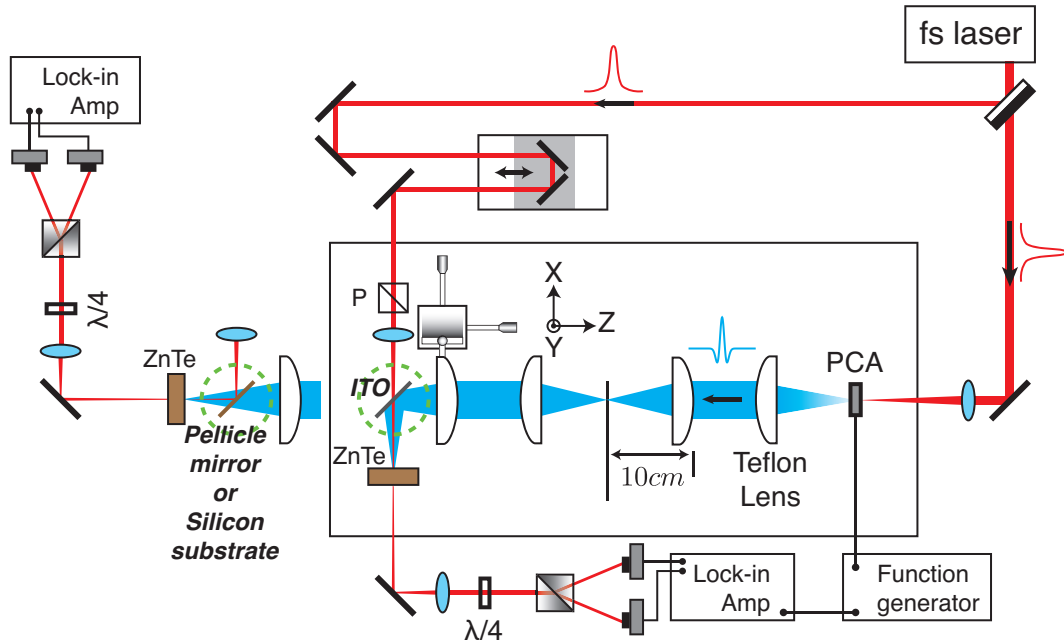


Figure 2.17: The THz-TDS setup of in a linear configuration. There are two ways to co-propagate the THz waves and probe beam to ZnTe. One is to use an ITO wafer to reflect THz waves. The other is to use a Pellicle beam splitter or silicon substrate to reflect the probe beam. The PCA is biased by using a step function signal generated from a 65 kHz function generator with 30 V dc voltages (TOELLNER TOE 7704). The Lock-in amplifier was used to record the photo currents from the two photodiodes (or one photodiode). The reference signal of the Lock-in amplifier was locked to a step function signal provided by the 65 kHz function generator.



Figure 2.18: The constructed THz-TDS using (a) 4 Teflon lenses and (b) 4 parabolic mirrors, respectively. (c) The whole THz-TDS setup is purged with dry air to reduce the absorption by water vapor in the THz frequency range. (d) Enlarged sample section of THz-TDS in a linear configuration. (e) THz-TDS setup purged with acrylic box.

was in a range between 3 MPa to 4 MPa.

Chapter 3. Data analysis

3.1 Extraction of the complex refractive index

Let's consider that a plane wave $E_i(\omega)$ with angular frequency of ω propagates through the sample in the z direction at normal incidence as shown in Fig. 3.1. A primary ray is partially transmitted and partially reflected between the front side and the other side of the sample [27]. By multiple reflection, the successive internally reflected and transmitted rays can be represented respectively as

$$E_i \tilde{t}_{12}, E_i \tilde{t}_{12} \tilde{r}_{21}, E_i \tilde{t}_{12} \tilde{r}_{21}^2, E_i \tilde{t}_{12} \tilde{r}_{21}^3, \dots \quad (3.1)$$

and

$$E_i \tilde{t}_{12} \tilde{t}_{21}, E_i \tilde{t}_{12} \tilde{r}_{21}^2 \tilde{t}_{21}, E_i \tilde{t}_{12} \tilde{r}_{21}^4 \tilde{t}_{21}, \dots, \quad (3.2)$$

where \tilde{t}_{ij} and \tilde{r}_{ij} are the Fresnel coefficients from medium i to medium j given by

$$\tilde{t}_{ij} = \frac{2\tilde{n}_i}{(\tilde{n}_i + \tilde{n}_j)}, \quad \tilde{r}_{ij} = \frac{\tilde{n}_j - \tilde{n}_i}{\tilde{n}_j + \tilde{n}_i}, \quad (3.3)$$

where \tilde{n}_j is the complex refractive index of the j -th medium defined by

$$\tilde{n}_j(\omega) = n_j(\omega) + i\kappa_j(\omega). \quad (3.4)$$

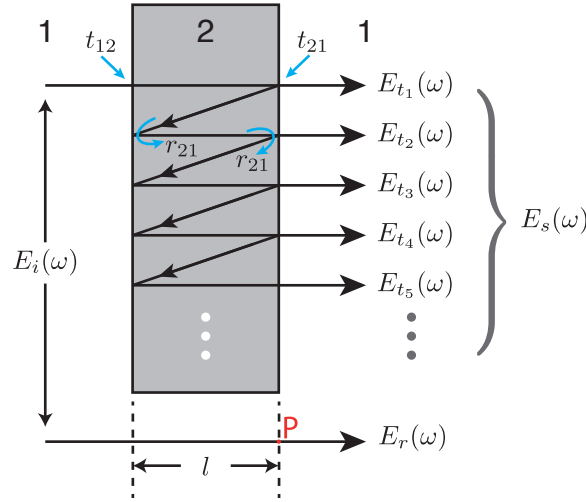


Figure 3.1: The reflected rays are represented with the tilted angles for sake of clarity. E_i , E_{t_i} , and E_r are the initial wave, the successive transmitted waves, and the reference wave, respectively. By designating medium 1 as air and medium 2 as the sample, the transmission and reflection Fresnel coefficients are represented as t_{12} and r_{12} , respectively. The transmission of transmitted waves through the sample is determined at point P .

In general, the refractive index is the real part of \tilde{n}_j and the extinction coefficient denoted by α can be obtained from the imaginary part of \tilde{n}_j ($\kappa = \kappa_2 = \kappa_s$) given by ¹

$$\alpha(\omega) = \frac{2}{c} \omega \kappa(\omega). \quad (3.7)$$

The consequent phenomenon caused by the multiple reflection within the slab is called as the Fabry-Pérot effect.

Designating subscripts for reference (air) and sample as $1 = a$ and $2 = s$, respectively, the successive transmitted rays \tilde{E}_{t_i} are explicitly expressed in terms of the Fresnel coefficients and the phase term as

$$\begin{aligned} \tilde{E}_{t_1} &= \tilde{t}_{12} \tilde{t}_{21} E_i e^{ik\tilde{n}_s l} \\ \tilde{E}_{t_2} &= \tilde{t}_{12} \tilde{r}_{21}^2 \tilde{t}_{21} E_i e^{ik\tilde{n}_s 3l} \\ \tilde{E}_{t_3} &= \tilde{t}_{12} \tilde{r}_{21}^4 \tilde{t}_{21} E_i e^{ik\tilde{n}_s 5l}, \\ &\vdots \end{aligned} \quad (3.8)$$

where the sequence $l, 3l, 5l, \dots$ in the optical path length term of $\tilde{n}_s l$ represents subsequent back and forth reflection and $k = c/\omega$. Then the total transmitted waves \tilde{E}_s through a sample can be written by the sum of the whole successive transmitted terms in the form

$$\begin{aligned} \tilde{E}_s &= \tilde{t}_{12} \tilde{t}_{21} E_i e^{ik\tilde{n}_s l} + \tilde{t}_{12} \tilde{r}_{21}^2 \tilde{t}_{21} E_i e^{ik\tilde{n}_s 3l} + \tilde{t}_{12} \tilde{r}_{21}^4 \tilde{t}_{21} E_i e^{ik\tilde{n}_s 5l} + \dots \\ &= \tilde{t}_{12} \tilde{t}_{21} E_i e^{ik\tilde{n}_s l} \left[1 + \tilde{r}_{21}^2 e^{ik\tilde{n}_s 2l} + \tilde{r}_{21}^4 e^{ik\tilde{n}_s 4l} + \dots \right] \\ &= \tilde{t}_{12} \tilde{t}_{21} E_i e^{ik\tilde{n}_s l} \left\{ 1 + \sum_{j=1}^{\delta} \left[\tilde{r}_{21} e^{ik\tilde{n}_s l} \right]^{2j} \right\}, \end{aligned} \quad (3.9)$$

where δ is the number of Etalon waves. On the other hand, the reference wave passing through the optical path of $n_a l$ is given by

$$\tilde{E}_r = E_i e^{ikn_a l}. \quad (3.10)$$

Therefore the transmission, *i.e.* the theoretical transfer function \tilde{H} in the presence of a single sample, is obtained as

$$\begin{aligned} \tilde{H}(\omega) &= \frac{\tilde{E}_s}{\tilde{E}_r} = \tilde{t}_{12} \tilde{t}_{21} e^{ik(\tilde{n}_s - n_a)l} \left\{ 1 + \sum_{j=1}^{\delta} \left[\tilde{r}_{21} e^{ik\tilde{n}_s l} \right]^{2j} \right\} \\ &= \frac{4\tilde{n}_s(\omega)n_a}{(\tilde{n}_s(\omega) + n_a)^2} e^{i\frac{\omega}{c}[\tilde{n}_s(\omega) - n_a]l} \left\{ 1 + \sum_{j=1}^{\delta} \left[\frac{\tilde{n}_s(\omega) - n_a}{\tilde{n}_s(\omega) + n_a} e^{i\frac{\omega}{c}\tilde{n}_s(\omega)l} \right]^{2j} \right\}. \end{aligned} \quad (3.11)$$

¹Consider that the plane wave propagates along the x direction through a medium with a complex refractive index \tilde{n} and thickness of d . If $\tilde{E}_0(\omega)$ is the incident wave, the transmitted wave can be written as

$$\tilde{E}(\omega) = \tilde{E}_0(\omega) e^{i(kd)} = \tilde{E}_0(\omega) e^{i\left[\frac{\omega}{c}\tilde{n}(\omega)d\right]} = \tilde{E}_0(\omega) e^{-\frac{\omega}{c}\kappa d} e^{i\left[\frac{\omega}{c}nd\right]}. \quad (3.5)$$

Then the transmission (T) is calculated in the form

$$T = \left| \frac{\tilde{E}(\omega)}{\tilde{E}_0(\omega)} \right|^2 = e^{-\frac{2\omega}{c}\kappa d} \equiv e^{-\alpha(\omega)d}, \quad (3.6)$$

where α represents the extinction coefficient defined by Eq. (3.7).

The transmission of the measured THz waves carried out by THz-TDS can be written in the form

$$\tilde{H}_{\text{exp}}(\omega) = \frac{\tilde{E}_s^{\text{exp}}(\omega)}{\tilde{E}_r^{\text{exp}}(\omega)} = \frac{A_s(\omega) e^{i\phi_s(\omega)}}{A_r(\omega) e^{i\phi_r(\omega)}} \equiv \rho(\omega) e^{i\Delta\phi(\omega)}, \quad (3.12)$$

where $\rho = A_s/A_r$ is the transmission amplitude and $\Delta\phi = \phi_s - \phi_r$ is the spectral phase difference. By comparing Eq. (3.11) and Eq. (3.12), we can extract the optical constants (the refractive index (n) and the extinction coefficient (α)) without using the Kramers-Kronig relationship. There are many ways to calculate the optical constant from the theoretical transfer function.

3.1.1 Optical constants for an optically thick sample with low absorption

Provided that the investigated material which is optically thick has a low absorption in the THz frequency range, κ_s is sufficiently small compared to n_s ($\kappa_s \ll n_s$) and the Fabry-Pérot interference terms can be neglected due to the optically thick thickness. Then the transfer function Eq. (3.11) is simplified in the form²

$$\tilde{H}(\omega) = \frac{4n_s(\omega)n_a}{(n_s(\omega) + n_a)^2} e^{-\frac{\omega}{c}\kappa_s l} e^{i\frac{\omega}{c}(n_s(\omega)-n_a)l}. \quad (3.13)$$

By comparing the measured transmission Eq. (3.12) and the theoretical transfer function Eq. (3.13), the refractive index and the extinction coefficient of the sample can be extracted. The measured transmission Eq. (3.12) for a thick sample (*i.e.* no Etalon signals) is physically equivalent to the theoretical transfer function Eq. (3.13) given by

$$\tilde{H}(\omega) = \frac{4n_s(\omega)n_a}{(n_s(\omega) + n_a)^2} e^{-\frac{\omega}{c}\kappa_s(\omega)l} e^{i\frac{\omega}{c}(n_s(\omega)-n_a)l} \equiv \rho(\omega) e^{i\Delta\phi(\omega)}, \quad (3.14)$$

where it should be noted that $\rho = A_s/A_r$ and $\Delta\phi$ are the experimentally measured transmission amplitude and the spectral phase difference, respectively. Then the optical constants can be obtained by comparing the imaginary part as well as the real part of the both sides in Eq. (3.14) as follows:

$$\text{Im } \tilde{H}(\omega) = e^{i\frac{\omega}{c}(n_s(\omega)-n_a)l} = e^{i\Delta\phi(\omega)}, \quad (3.15)$$

which leads to

$$\frac{\omega}{c}(n_s(\omega) - n_a)l = \Delta\phi(\omega), \quad (3.16)$$

so that we obtain the refractive index as

$$n_s(\omega) = n_a + \frac{c}{\omega l} \Delta\phi(\omega). \quad (3.17)$$

Next,

$$\text{Re } \tilde{H}(\omega) = \frac{4n_s(\omega)n_a}{(n_s(\omega) + n_a)^2} e^{-\frac{\omega}{c}\kappa_s(\omega)l} = \rho(\omega), \quad (3.18)$$

2

$$\begin{aligned} \tilde{H}(\omega) &= \frac{4\tilde{n}_s(\omega)n_a}{(\tilde{n}_s(\omega) + n_a)^2} e^{i\frac{\omega}{c}(\tilde{n}_s(\omega)-n_a)l} \simeq \frac{4n_s(\omega)n_a}{(n_s(\omega) + n_a)^2} e^{i\frac{\omega}{c}(\tilde{n}_s(\omega)-n_a)l} \\ &= \frac{4n_s(\omega)n_a}{(n_s(\omega) + n_a)^2} e^{-\frac{\omega}{c}\kappa_s l} e^{i\frac{\omega}{c}(n_s(\omega)-n_a)l}. \end{aligned}$$

which implies that

$$\kappa_s(\omega) = -\frac{c}{\omega l} \ln \left[\rho(\omega) \frac{(n_s(\omega) + n_a)^2}{4n_s(\omega)n_a} \right]. \quad (3.19)$$

Furthermore, the extinction coefficient is expressed as³

$$\alpha(\omega) = \frac{2\omega}{c} \kappa_s(\omega) = -\frac{2}{l} \ln \left[\rho(\omega) \frac{(n_s(\omega) + n_a)^2}{4n_s(\omega)n_a} \right]. \quad (3.21)$$

As a result, the refractive index and the extinction coefficient of the sample are obtained as Eqs. (3.17) and (3.21), respectively.

3.1.2 Optical constants of two identical samples with different thicknesses

The Fresnel coefficient term $4n_s n_a / (n_s + n_a)^2$ in Eq. (3.11) can be eliminated provided that there are two identical samples with different thicknesses (d_1, d_2). When d_2 is large compared to d_1 , the successive transmitted electric fields at point P shown in Fig. 3.2 can be expressed as

$$\tilde{E}_{t_1}(\omega) = \tilde{t}_{12} \tilde{t}_{21} E_i e^{ik[\tilde{n}_s d_1 + n_a(d_2 - d_1)]}, \quad (3.22)$$

$$\tilde{E}_{t_2}(\omega) = \tilde{t}_{12} \tilde{t}_{21} E_i e^{ik\tilde{n}_s d_2}, \quad (3.23)$$

where the interference terms caused by the Fabry-Pérot effect can be neglected in case of the optically thick thickness. The phase term $n_a(d_2 - d_1)$ is included in \tilde{E}_{t_1} in Eq. (3.22) since the transmitted wave through a sample with thickness of d_1 is in phase at point P with respect to \tilde{E}_{t_2} . From the transmitted waves, the relative transfer function can be written as

$$\begin{aligned} \tilde{H}^{\text{theory}}(\omega) &= \frac{\tilde{E}_{t_2}(\omega)}{\tilde{E}_{t_1}(\omega)} = \frac{e^{ik\tilde{n}_s d_2}}{e^{ik[\tilde{n}_s d_1 + n_a(d_2 - d_1)]}} = e^{i\frac{\omega}{c}(\tilde{n}_s - n_a)(d_2 - d_1)} \\ &= e^{-\frac{\omega}{c}\kappa_s(d_2 - d_1)} e^{i\frac{\omega}{c}(n_s - n_a)(d_2 - d_1)} \end{aligned} \quad (3.24)$$

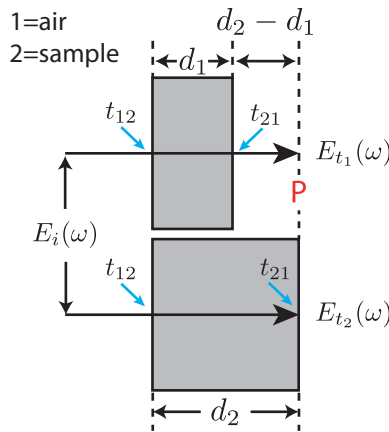


Figure 3.2: The diagram of transmitted waves through two identical samples with different thickness. The relative transmission of transmitted waves through two samples is determined at point P .

3

$$\alpha(\omega) = \frac{2\omega}{c} \kappa_s(\omega) = -\frac{2\omega}{c} \times \frac{c}{\omega l} \ln \left[\rho(\omega) \frac{(n_s(\omega) + n_a)^2}{4n_s(\omega)n_a} \right] = -\frac{2}{l} \ln \left[\rho(\omega) \frac{(n_s(\omega) + n_a)^2}{4n_s(\omega)n_a} \right]. \quad (3.20)$$

which implies that

$$\tilde{H}^{\text{theory}}(\omega) \equiv \frac{\tilde{E}_{t_2}^{\text{exp}}(\omega)}{\tilde{E}_{t_1}^{\text{exp}}(\omega)} = \frac{A_{t_2}(\omega)e^{i\phi_{t_2}(\omega)}}{A_{t_1}(\omega)e^{i\phi_{t_1}(\omega)}}, \quad (3.25)$$

where A_{t_j} and $e^{i\phi_{t_j}}$ are the spectral amplitude and phase corresponding to the experimentally measured THz waveform $\tilde{E}_{t_j}^{\text{exp}}$, respectively. We find by comparing the imaginary part as well as the real part of the both sides in Eq (3.25) that

$$\text{Im } \tilde{H}^{\text{theory}}(\omega) = e^{i\frac{\omega}{c}(n_s - n_a)(d_2 - d_1)} = e^{i(\phi_{t_2} - \phi_{t_1})}, \quad (3.26)$$

$$\text{Re } \tilde{H}^{\text{theory}}(\omega) = e^{-\frac{\omega}{c}\kappa_s(d_2 - d_1)} = \frac{A_{t_2}}{A_{t_1}}, \quad (3.27)$$

so that we obtain

$$n_s(\omega) = n_a + \frac{c}{\omega(d_2 - d_1)} \Delta\phi, \quad (3.28)$$

$$\kappa_s(\omega) = -\frac{c}{\omega(d_2 - d_1)} \ln\left(\frac{A_{t_2}}{A_{t_1}}\right), \quad (3.29)$$

where $\Delta\phi = \phi_{t_2} - \phi_{t_1}$ is the spectral phase difference between the two sample THz signals. A reference paper [28] would be a help to understand.

3.1.3 Numerical calculation: The fixed-point iteration method

The fixed-point iteration method is one of numerical methods to obtain the complex refractive index in the THz frequency range [29, 30]. In this section, we only consider the situation for a sample with an optically thick thickness for sake of simplicity.

We now recall from Eq. (3.11) the expression for the transfer function with $\delta = 0$, yielding

$$\tilde{H}(\omega) = \frac{4\tilde{n}_s(\omega)n_a}{(\tilde{n}_s(\omega) + n_a)^2} e^{i\frac{\omega}{c}[\tilde{n}_s(\omega) - n_a]l}. \quad (3.30)$$

By taking the Fresnel coefficient to have the form

$$\varphi \equiv \frac{4\tilde{n}_s(\omega)n_a}{(\tilde{n}_s(\omega) + n_a)^2} = re^{i\theta}, \quad (3.31)$$

the transfer function becomes

$$\tilde{H}(\omega) = re^{i\theta} e^{-\frac{\omega}{c}\kappa_s l} e^{i\frac{\omega}{c}(n_s(\omega) - n_a)l}, \quad (3.32)$$

which implies that

$$\tilde{H}(\omega) = \rho(\omega)e^{i\Delta\phi(\omega)}, \quad (3.33)$$

where $\rho = A_s/A_r$ is the transmission amplitude and $\Delta\phi = \phi_s - \phi_r$ is the spectral phase difference obtained by the measurement. We then find by comparing the real and imaginary parts of Eq. (3.33) that

$$\Delta\phi(\omega) = \frac{\omega}{c}(n_s(\omega) - n_a)l + \theta, \quad \rho(\omega) = re^{-\frac{\omega}{c}\kappa_s l}. \quad (3.34)$$

The Fresnel coefficient can be rigorously expressed by taking $\tilde{n}_s = n_s + i\kappa_s = r_1 e^{i\phi_1}$ and $\tilde{n}_s + n_a =$

$n_s + n_a + i\kappa_s = r_2 e^{i\phi_2}$ as

$$\varphi = \frac{4n_a r_1 e^{i\phi_1}}{r_2^2 e^{i2\phi_2}} = 4n_a \frac{r_1}{r_2^2} e^{i(\phi_1 - 2\phi_2)}. \quad (3.35)$$

By comparing the real and imaginary parts of this equation, we obtain

$$\arg \varphi = \phi_1 - 2\phi_2 = \theta, \quad (3.36)$$

$$|\varphi| = 4n_a \frac{r_1}{r_2^2} = r, \quad (3.37)$$

which lead to

$$\theta = \tan^{-1} \left(\frac{\kappa_s}{n_s} \right) - 2 \tan^{-1} \left(\frac{\kappa_s}{n_s + n_a} \right), \quad (3.38)$$

$$r = \frac{4n_a \sqrt{n_s^2 + \kappa_s^2}}{(n_s + n_a)^2 + \kappa_s^2}. \quad (3.39)$$

Therefore, we find by substituting Eqs. (3.38) and (3.39) into Eqs. (3.34) that the the complex refractive index can be expressed as [31]

$$n_s(\omega) = n_a + \frac{c}{\omega l} \left[\Delta\phi(\omega) - \tan^{-1} \left(\frac{\kappa_s(\omega)}{n_s(\omega)} \right) + 2 \tan^{-1} \left(\frac{\kappa_s(\omega)}{n_s(\omega) + n_a} \right) \right], \quad (3.40)$$

$$\kappa_s(\omega) = -\frac{c}{\omega l} \left[\ln \rho(\omega) - \ln \left(\frac{4n_a \sqrt{n_s^2 + \kappa_s^2}}{(n_s + n_a)^2 + \kappa_s^2} \right) \right]. \quad (3.41)$$

From these equations, we can see that n_s and κ_s are strongly coupled to each other. Since n_s and κ_s generally cannot be expressed separately, the numerical method should be considered when we obtain the complex refractive index.

When the Fresnel coefficient \tilde{t}_{ij} is considered as 1, we find from Eqs. (3.40) and (3.41) that the complex refractive index becomes

$$n_s(\omega) \equiv n_0(\omega) = n_a + \frac{c}{\omega l} \Delta\phi(\omega), \quad \kappa_s(\omega) \equiv \kappa_0(\omega) = -\frac{c}{\omega l} \ln \rho(\omega), \quad (3.42)$$

where these parameters are considered as the initial values of this method. Note that Eqs. (3.40) and (3.41) can be expressed in terms of generating functions as

$$n_s(\omega) = g_1(n_s, \kappa_s), \quad \kappa_s(\omega) = g_2(n_s, \kappa_s). \quad (3.43)$$

Using the initial values in Eq. (3.42), the complex refractive index denoted by n_1 and κ_1 can be obtained for a fixed κ_0 and n_0 , respectively, as follows: By succeeding iterations given by

$$\begin{aligned} g_1(n_0, \kappa_0) &= n_1, & g_2(n_0, \kappa_0) &= \kappa_1, \\ g_1(n_1, \kappa_0) &= n_2, & g_2(n_0, \kappa_1) &= \kappa_2, \\ g_1(n_2, \kappa_0) &= n_3, & g_2(n_0, \kappa_2) &= \kappa_3, \\ &\vdots & &\vdots \\ g_1(n_j, \kappa_0) &= n_s(\kappa_0) \equiv n'_1, & g_2(n_0, \kappa_j) &= \kappa_s(n_0) \equiv \kappa'_1, \end{aligned} \quad (3.44)$$

we obtain n'_1 for a fixed κ_0 and κ'_1 for a fixed n_0 . Next, n'_2 for a fixed κ'_1 and κ'_2 for a fixed n'_1 can be

obtained by the same iteration method. We thus obtain the final complex refractive index by repeating the iteration. The fixed-point iteration method is described in more detail in Ref. [29,30].

3.1.4 Examples: optical constants of dolomite stone and Teflon

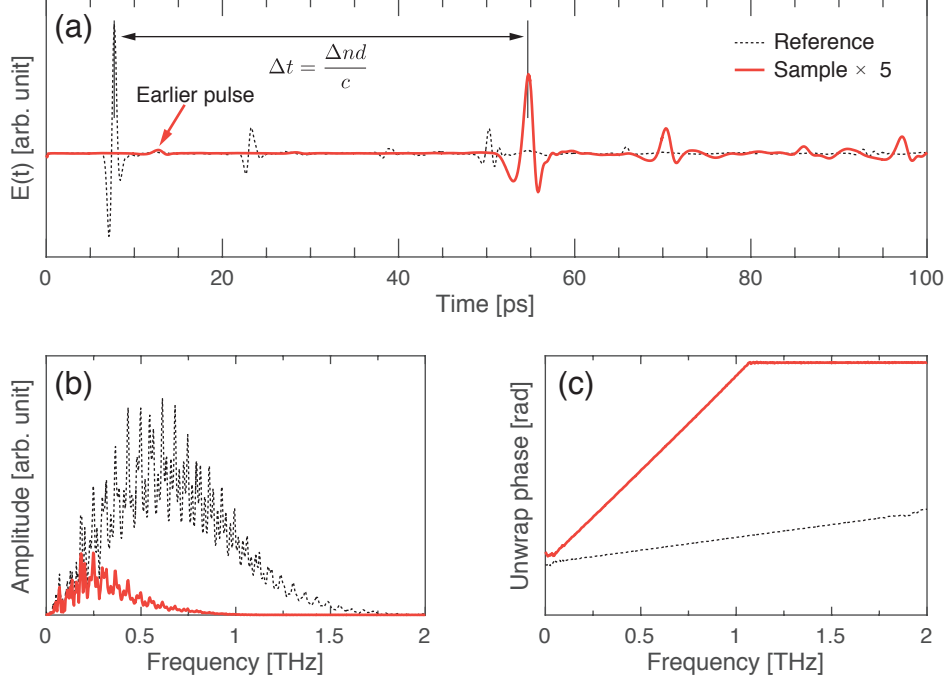


Figure 3.3: (a) Measured time-domain THz waveforms with and without a sample. The THz waves through a sample are time-delayed from the reference peak as much as Δt . Note that there is an earlier pulse than the main THz signal near 55 ps, which comes from the reflected optical probe beam. (b) Amplitude spectrums and (c) phase information of reference and sample THz signals after Fourier transformation. Here the sample is dolomite stone with a thickness of 8.31 mm.

Figure 3.3(a) shows the measured time-domain THz waveforms with and without a sample. When the sample is placed in the optical path, the total optical path becomes longer so that the THz waves through the sample are time-delayed from the reference peak as much as⁴

$$\Delta t = \frac{\Delta n d}{c}, \quad (3.47)$$

where c is the speed of light, d is the thickness of the sample, and $\Delta n = n_s - n_a$. Note that there is an earlier pulse than the main THz signal through the sample (red solid line) near 55 ps, which comes from the reflected optical probe beam. This is described in section A.9 in detail.

By applying Fourier transformation to the reference and sample THz waveforms, the spectral amplitude and phase information are simultaneously obtained as shown in Fig. 3.3(b) and (c). Here, the

⁴When t_1 is time at point P of a reference wave and t_2 is time at point P of a transmitted wave through a sample as shown in Fig. 3.1, the refractive index n_s can be roughly obtained, giving

$$- \begin{cases} n_s d = c t_2 \\ n_a d = c t_1 \\ (n_s - n_a) d = c(t_2 - t_1), \end{cases} \quad (3.45)$$

which implies that

$$n_s = n_a + \frac{c}{d}(t_2 - t_1), \quad (3.46)$$

which leads to Eq. (3.47).

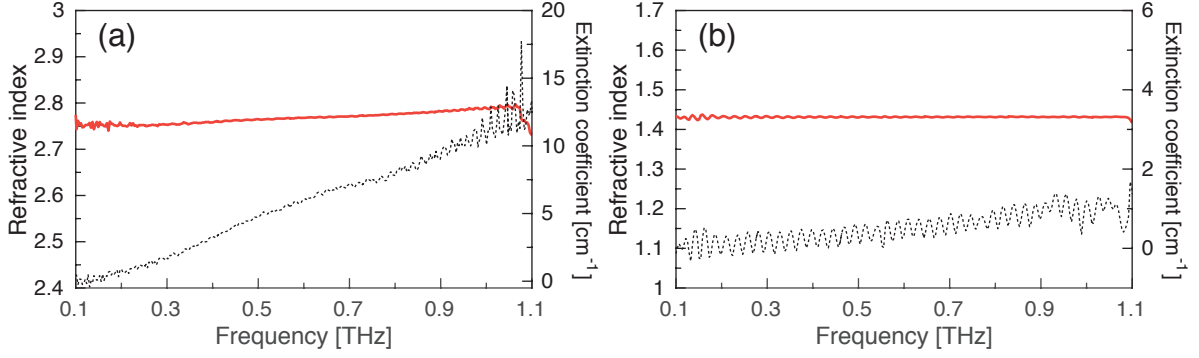


Figure 3.4: The extracted refractive index (red solid line) and the extinction coefficient (black dotted line) of (a) dolomite and (b) Teflon.

phase term at zero frequency measured by THz-TDS must be zero [32]. Using matlab, the unwrapped phase can be corrected by the translational symmetry.

Figure 3.4 shows the refractive index and the extinction coefficient of dolomite and Teflon measured by THz-TDS in a transmission configuration.

3.2 Dynamic range in TDS transmission spectroscopy

In principle, $\alpha_{\max}(\omega)$ at each frequency component can be obtained when the spectral amplitude in the presence of a sample $A_s(\omega)$ is attenuated to the noise level [33]. From Eq. (3.19), the expected maximum extinction coefficient $\alpha_{\max}(\omega)$ measured by THz-TDS in a transmission configuration becomes [33]

$$\alpha_{\max}(\omega) = \frac{2}{l} \ln \left\{ DR(\omega) \frac{4 n_s(\omega) n_a}{[n_s(\omega) + n_a]^2} \right\}, \quad (3.48)$$

where the dynamic range $DR(\omega)$ *i.e.* the measurable range is given as [33]

$$DR(\omega) = \frac{A_r(\omega)}{\text{Noise}}. \quad (3.49)$$

Figure 3.5 shows the dynamic range of dolomite and Teflon measured by the transmission THz-

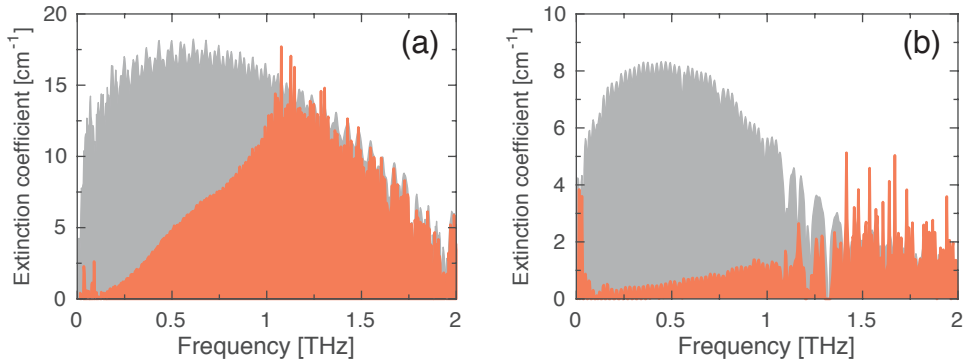


Figure 3.5: The dynamic range of (a) dolomite and (b) Teflon measured by the transmission THz-TDS. The gray and red shaded areas represent the $\alpha_{\max}(\omega)$ and $\alpha(\omega)$ of each sample, respectively. The measurement ranges for (a) and (b) are valid for frequencies below 1 THz and 1.5 THz by comparing the two curves, respectively.

TDS. The gray and red shaded areas represent the $\alpha_{\max}(\omega)$ and $\alpha(\omega)$ of each sample, respectively. Comparing the two curves, we can see from Fig. 3.5(b) that the measurement range by THz-TDS is valid for frequencies below 1.5 THz.

3.3 Dielectric constant and complex refractive index

From the electromagnetic theory [7, 12], the speed of light is defined as⁵

$$c = v n = \frac{1}{\sqrt{\epsilon_0 \mu_0}}, \quad (3.50)$$

where v is the phase velocity and n is the index of refraction. Then the refractive index can be explicitly written by a complex variable in terms of the electric permittivity (ϵ) and the magnetic permeability (μ) given by

$$\tilde{n}^2 = \frac{c^2}{v^2} = \frac{\tilde{\epsilon} \mu}{\epsilon_0 \mu_0} = \frac{\tilde{\epsilon}}{\epsilon_0}, \quad (3.51)$$

where $\mu = \mu_0$ for a non-magnetic material. The term $\tilde{\epsilon}/\epsilon_0 = 1 + \chi$, where χ is the electric susceptibility, is called the dimensionless dielectric constant or the relative dielectric constant or the dielectric constant for simplicity [7, 12]. The complex refractive index is generally represented by

$$\tilde{n} = n + i\kappa, \quad (3.52)$$

where n and κ are the real and imaginary parts of \tilde{n} . According to Eq. (3.51) and Eq. (3.52), the dielectric constant can be obtained by

$$\tilde{n}^2 = (n + i\kappa)^2 = (n^2 - \kappa^2) + i 2n\kappa = \epsilon_r + i \epsilon_i = \frac{\tilde{\epsilon}}{\epsilon_0}, \quad (3.53)$$

where

$$\epsilon_r = \text{Re} \left[\frac{\tilde{\epsilon}}{\epsilon_0} \right], \quad \epsilon_i = \text{Im} \left[\frac{\tilde{\epsilon}}{\epsilon_0} \right]. \quad (3.54)$$

⁵The relation in Eq. (3.50) is detailed explained in Griffiths [13] pp. 375–376, and 382–383, Yariv [19] pp. 10–11.

Chapter 4. THz spectroscopy of natural mineral compounds

4.1 THz spectroscopy of natural stones and its application

Terahertz (THz) time-domain spectroscopy probes the optical properties of the naturally occurring solid aggregates of minerals, or stones, in THz frequency range. Refractive index and extinction coefficient measurement reveals that most natural stones including mudstone, sandstone, granite, tuff, gneiss, diorite, slate, marble, and dolomite are fairly transparent in the THz frequency domain. Dolomite in particular has nearly a uniform refractive index of 2.7 over the broad frequency range from 0.1 to 1 THz. The high index of refraction allows flexibility in lens design with a shorter accessible focal length or a thinner lens with a given focal length. Good agreement between the experiment and calculation in the THz beam profile confirms that dolomite has high homogeneity as a lens material, suggesting the possibility of using natural stones for THz optical elements.

4.1.1 Introduction

Science and technology on THz frequency waves has become one of the most active areas of research during the past two decades [3]. The THz frequency waves are located in the frequency ranges from 0.1–10 THz (30–3000 μm in wavelength) between microwave and far-infrared (FIR) electromagnetic waves. Various research in the THz frequency range have become possible through the development of the generation and detection methods as well as spectroscopic methods with these waves. In contrast to the measurements with other light sources such as X-ray or FIR waves, one of the important aspects of THz waves used for material characterization application is the direct field amplitude measurement using THz time-domain spectroscopy (THz-TDS). Both the spectral amplitude and phase information of a sample can be obtained simultaneously through the THz-TDS, without resorting to a complex analysis [34]. Previous studies demonstrated the powerful spectroscopic capability of THz-TDS in characterizing many materials including polymers [35], explosive materials [36], solid-state materials [37, 38], chemical compounds in liquid [39], ions [40], biomaterials [41], and even the material phase transitions [42].

Recently, there have been enormous efforts devoted to fabricate THz optical components [43–50]. Among the THz components, lenses and off-axis parabolic mirrors play a crucial role in THz-TDS systems since they are the basic optical elements in focusing and collimating THz waves. For example, planoconvex lenses are commonly used in a THz-TDS system of a linear configuration [43]. The lenses operating in the THz frequency range are fabricated of various materials: high resistive silicon [44, 45], polytetrafluoroethylene (PTFE, Teflon) [35, 44–46], high-density polyethylene (HDPE) [35, 43, 46], TPX [45], TOPAS [45, 46], Zeonex [47], Picarin [48], micropowders [49], and polymeric compounds [50]. Special lenses such as the off-axis metallic diffractive lens [51], the diffractive paper lens [52], the variable-focus lens using the medical white oil [53] and the THz Brewster lens [54] have been recently reported.

Here we demonstrate a THz lens made out of natural dolomite stone. For this, we first investigate various natural stones using THz-TDS to determine their optical constants such as the refractive index and the absorption coefficient. Despite the optical constants of a limited set of stones were previously studied in the THz frequency range [55–57], most stones from nature yet needed to be studied. In this study, we investigate mudstone, sandstone, tuff, diorite, marble, granite, gneiss, slate, and dolomite.

While these stones are opaque in the optical frequency range, this study reveals that most of them are mostly transparent in the frequency ranges from 0.2 to 1 THz. Some natural stones, in particular the dolomite, exhibit a rather flat and high index of refraction throughout the measured THz frequency range. Materials with a higher refractive index allow the lens fabrication with more flexibility in lens fabrication suggesting that the dolomite can be considered as a material for THz lens fabrication.

The contents in this paper are listed as follows. After the THz transmission measurement of natural stones in a conventional THz-TDS setup is described, the extraction process of the complex refractive index from the investigated stones is explained. The fabrication procedure of a THz lens using dolomite is then explained. Lastly, focused intensity profile measurements of the fabricated dolomite lens with respect to selected frequencies are presented.

4.1.2 Measurement of optical constants of natural stones

4.1.2.1 Experimental procedure

To measure the refractive index and the extinction coefficient of various natural stones, a conventional THz-TDS setup was used [38]. THz waves were generated from a large-area photoconductive antenna (PCA) [58] illuminated by ultrafast optical pulses that were temporally 100 fs short, wavelength-centered at 840 nm, and produced from a mode-locked Ti:sapphire laser oscillator operating at 80 MHz repetition rate. When a THz pulse guided by four off-axis parabolic mirrors propagated through a sample located at the focus, another ultrafast optical pulse splitted off before the PCA and time-delayed by a linear translation stage probed the electric field profile of the THz wave as a function of the time delay via optical gating [45]. The temporal THz signals with and without the sample were separately measured via electro-optic (EO) sampling [21, 59], where the polarization rotation of the probe pulse through a (110)-oriented ZnTe EO crystal with thickness of 2 mm was mapped after a quarter-wave plate and a Wollaston prism by a pair of balanced photodiodes. By varying the time-delay of the probe beam with respect to the THz pulse, the temporal electric field waveform of the THz pulse was recorded. To obtain accurate spectral information, we took a long-time window measurement of up to 200 ps which corresponded to a spectral resolution of 5 GHz, with a temporal step size of 100 fs. The whole THz-TDS setup was purged with dry air to reduce the absorption by water vapor in the THz frequency range [60, 61].

4.1.2.2 Retrieval of the refractive index and extinction coefficient

Waveform measurement in THz-TDS allows one to obtain not only the spectral amplitude but also the spectral phase information by simply applying the Fourier transformation to the time domain signal. THz-TDS directly measures the electric field while conventional IR spectroscopy such as FT-IR (Fourier transform IR spectroscopy) measures intensity [27]. The spectral phase information is thus obtained without resorting to the Kramers-Kronig relationship. The transmitted THz electric field out from the sample is given as a sum of successive transmitted and reflected electric fields at both sides of the sample, which is often referred to as the Fabry-Pérot etalon signal. If air and the sample are denoted by subscripts 1 and 2, respectively, the transmission $\hat{T}(\omega)$ of the sample with a thickness of l , which is

separately measured in the experiment, is given by

$$\begin{aligned}\widehat{T}(\omega) &= t_{21}t_{12} e^{i\frac{\omega}{c}(\tilde{n}_s(\omega)-n_a)l} \left\{ 1 + \sum_{j=1}^{\delta} \left[r_{21}e^{i\frac{\omega}{c}\tilde{n}_s(\omega)l} \right]^{2j} \right\} \\ &= \rho(\omega) e^{i\Delta\phi(\omega)} \left\{ FP(\omega) \right\},\end{aligned}\quad (4.1)$$

where $\tilde{n}_s = n_s + i\kappa_s$ and n_a are the complex indices of refraction of the sample and the air, respectively. Here, δ is the number of echoes of a THz signal, ρ is the transmission amplitude and $\Delta\phi$ is the spectral phase difference between THz signals with and without the sample. t_{ij} and r_{ij} are the Fresnel coefficients given by $t_{ij} = 2\tilde{n}_i/(\tilde{n}_i + \tilde{n}_j)$, $r_{ij} = (\tilde{n}_j - \tilde{n}_i)/(\tilde{n}_j + \tilde{n}_i)$ and $FP(\omega)$ is the Fabry-Pérot term. By comparing the real and imaginary parts of the right-hand side of Eq. (4.1), the full expression of the complex index

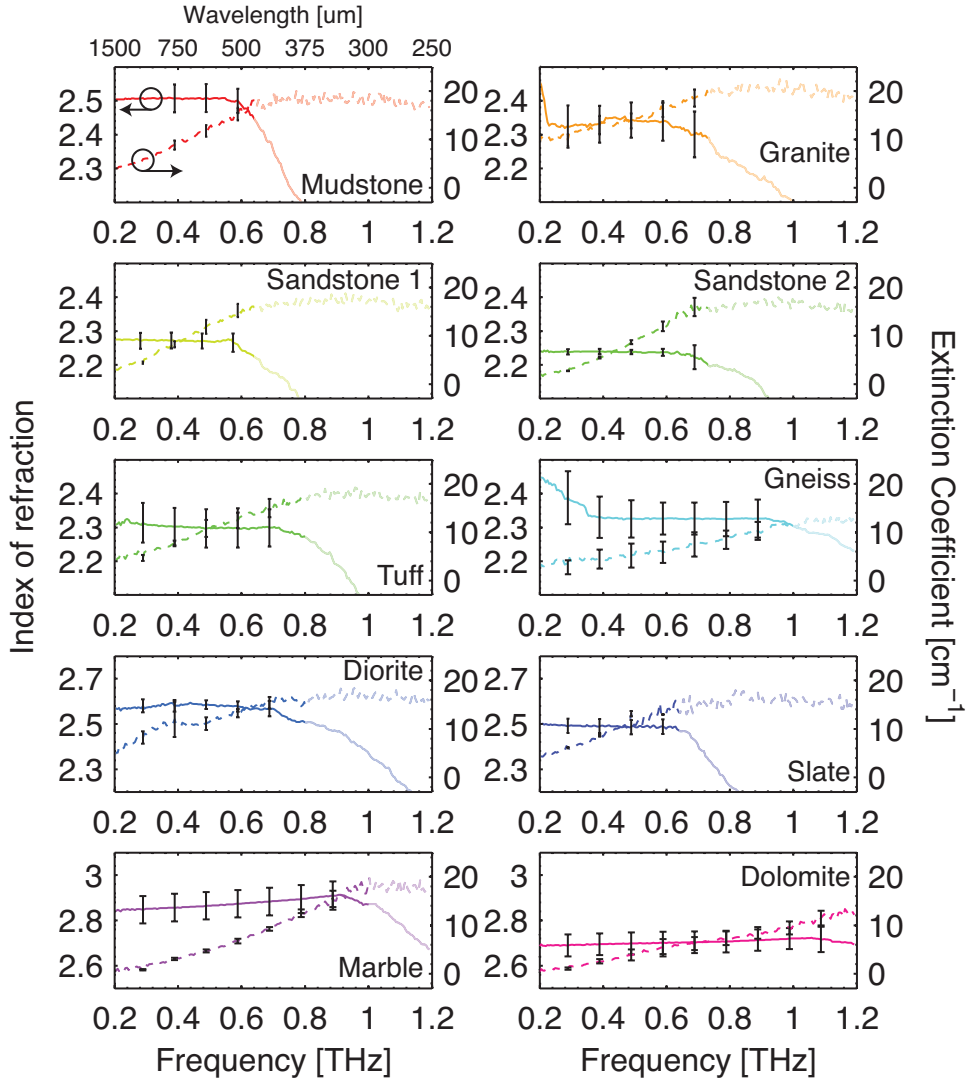


Figure 4.1: Measured refractive indices and extinction coefficients of stones in the frequency range from 0.2 to 1.2 THz corresponds to wavelengths between 1500 μm to 250 μm . Solid lines and dashed lines represent the extracted refractive indices and extinction coefficients of investigated stones, respectively.

of refraction of the sample becomes

$$\begin{aligned} n_s &= n_a + \frac{c}{\omega l} \left(\Delta\phi - \tan^{-1} \frac{\kappa_s}{n_s} + 2 \tan^{-1} \frac{\kappa_s}{n_s + n_a} \right) \\ \kappa_s &= \frac{c}{\omega l} \left(\log \frac{4n_a \sqrt{n_s^2 + \kappa_s^2}}{(n_s + n_a)^2 + \kappa_s^2} - \log \rho \right). \end{aligned} \quad (4.2)$$

For the retrieval of refractive index and extinction coefficient, we used the fixed-point iteration method [29, 30], in which the initial values of the complex index of refraction was chosen in the fixed-point iteration as $t_{ij} = 1$, given by $n_s = n_a + \frac{c}{\omega l} \Delta\phi$, $\kappa_s = -\frac{c}{\omega l} \log \rho$. From the imaginary part of the complex refractive index, we can obtain the extinction coefficient as

$$\alpha(\omega) = \frac{2\omega}{c} \kappa_s(\omega). \quad (4.3)$$

The detailed derivation of the transfer function Eq. 4.1 and extraction of the complex refractive index is explained in 3.1.

4.1.2.3 Optical constants of stones

The optical constants of nine different types of natural stones were measured: slate, gneiss, and marble in metamorphic rocks, mudstone, sandstone, and dolomite in sedimentary rocks, and granite, tuff and diorite in igneous rocks [62]. The samples were provided by the Korea Institute of Geoscience and Mineral Resources (<http://www.kigam.re.kr>). Figure 4.1 shows the retrieved refractive indices and the extinction coefficients of the investigated stones, respectively, extracted by the aforementioned method in Sec. 4.1.2.2. Table 4.1 lists the typical values of the refractive indices n and the extinction coefficients α , both measured at the frequency of 0.5 THz. The sample thickness that varied from 6.8 to 9.4 mm is also listed. The flat lateral sizes of the stone samples were about 2×2 cm². All the stones show rather flat refractive indices and low extinction coefficients of below 20 cm⁻¹ over the measured frequency range of 0.2–1.2 THz.

Materials	n	α	Thickness
Metamorphic rock			
Slate	2.48(3)	10.8(2)	8.65
Gneiss	2.32(5)	6.(4)	9.40
Marble	2.87(6)	5.0(3)	6.81
Sedimentary rock			
Mudstone	2.50(4)	13.(2)	8.62
Sandstone 1	2.27(2)	12.8(8)	8.95
Sandstone 2	2.24(1)	9.1(4)	9.22
Dolomite	2.70(5)	4.(1)	8.31
Igneous rock			
Granite	2.34(5)	14.(2)	7.48
Tuff	2.30(6)	11.(2)	8.41
Diorite	2.58(2)	12.(2)	8.01

Table 4.1: Refractive indices n , extinction coefficients α (cm⁻¹) and thicknesses (mm) of the investigated natural stones at 0.5 THz.

4.1.2.4 Verification of stones using its components

We conducted X-ray diffraction measurements to investigate the relationship between the THz optical constants and constituent minerals of the rocks whose results are listed in Table 4.2. The investigated stones show correlation between the refractive index and constituents. The relation between refractive index and quartz component ratio is clearly shown in Fig. 4.2-(a). The refractive index converges to 2.2 as the ratio of quartz component increases. Extinction coefficients with respect to refractive indices are shown in Fig. 4.2-(b), where it can be seen that the height (the extinction coefficient) of dolomite is much shorter than other rocks throughout the measured frequency range. Dolomite also exhibits a rather flat and high index of refraction.

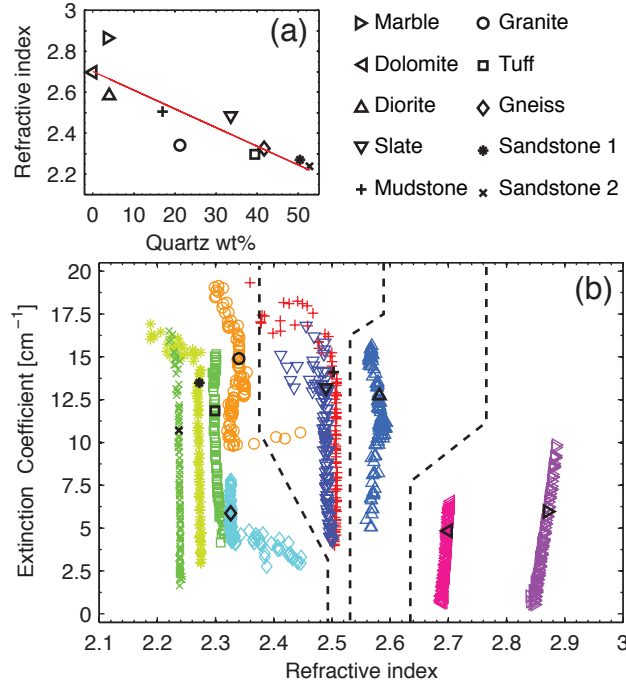


Figure 4.2: a) Quartz weight % with respect to refractive index at 0.5 THz. (b) The extinction coefficient with respect to the refractive index. Each dotted lines represents a guide to the particle sizes of the rocks [62].

4.1.3 Lens fabrication using dolomite

Dolomite shows low absorption and nearly a uniform refractive index of 2.7 over the measured THz frequency range. Compared with Teflon which is widely used for THz lenses, dolomite has a higher index of refraction (see Table 4.3). Note that a material with a high refractive index allows more flexibility in designing lenses with shorter accessible focal lengths, or a thinner lens for a given focal length. The index of refraction of dolomite is equivalent to that of commercial silicon that is used for semi-hemispherical THz lenses.

A planoconvex lens with dolomite was designed using the lens maker's formula [27]. When a collimated incident wave is assumed, the radius of curvature is given by

$$R = (n - 1) f, \quad (4.4)$$

Table 4.2: Mineral concentration of the investigated stones.

Mineral	Mudstone	Granite	Sandstone	SandStone A	SandStone B	Gneiss	Diorite	Dolomite	Slate	Marble	Tuff
Quartz	17.0	21.2		50.4	52.7	41.7	4.0	0	33.6	3.6	39.4
Plagioclase	43.8	44.6		23.5	22.5	33.9	17.1	0	5.9	0	36.5
K-feldspar	0	16.6		0	0	17.6	0	0	0	0	0
Biotite	1.3	4.1		5.9	1.8	6.8	8.8	0	0	0	1.9
Muscovite	5.3	0		15.2	6.9	0	0	0	51.2	0	13.5
Chlorite	16.6	4.4		3.5	7.1	0	4.2	0	7.7	0	8.7
Calcite	12.5	0		1.5	8.9	0	0	8.2	0	74.5	0
Pyrite	3.5	0		0	0	0	0	0	0	0	0
Hematite	0	2.6		0	0	0	0	0	0	0	0
Hornblende	0	6.3		0	0	0	65.9	10.8	0	0	0
Dolomite	0	0		0	0	0	0	75.5	0	9.2	0
Talc	0	0		0	0	0	0	5.5	0	0	0
Pyrrhotite	0	0		0	0	0	0	0	1.5	0	0
Phlogopite	0	0		0	0	0	0	0	0	12.6	0

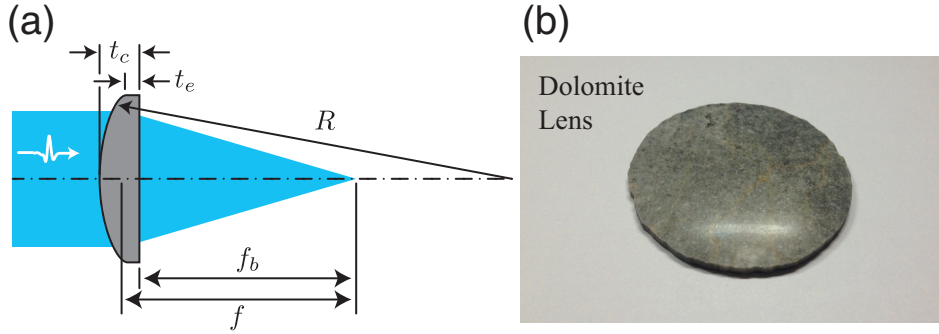


Figure 4.3: (a) Specification of the fabricated dolomite lens. f = effective focal length, f_b = back focal length, t_c = center thickness, t_e = edge thickness, R = radius curvature. (b) Photo of the fabricated dolomite lens.

where R , n , and f indicate the radius of curvature, the refractive index of the lens material, and the expected focal length of the lens, respectively. It is advantageous to use a material satisfying $(n - 1) > 1$ in Eq. (4.4) since the focal length of the lens is shorter than the radius of curvature, as shown in Fig. 4.3–(a). A commercial polishing plate with a radius of curvature of $R = 16.19$ cm was used for the convex surface, which gave an expected focal length of $f = 95.2$ mm for dolomite since the refractive index of dolomite at 0.5 THz was $n = 2.70$.

Dolomite lens were fabricated using conventional lens making procedures which is described for example in Ref. [63]. A brief description is given here. First, the bulk dolomite stone is cut into a hexahedron with a size of $50.2 \times 50.2 \times 5$ mm³ using a diamond wheel cutter. The dolomite block is shaped into a cylindrical blank by cutting the sides with a grinding machine. Both faces are then grounded into typical lens shapes, where one face is grounded to have a spherical curvature and the other to have a flat surface. The dolomite blank is rubbed on a rotating polishing plate (a concave polishing plate having a radius of curvature of 16.19 cm and a flat plate for each faces) covered with silicon carbide (SiC) micro-powders (300 mesh number) compounded with water until the painted surface vanished. SiC powders of 600 and 1200 mesh numbers were then sequentially used to smoothly grind the surfaces. After the grinding process, a polishing film (3M 261X Imperial Lapping film, 3 μ m grade) doped with aluminium oxide (Al_2O_3) was employed to roughly polish the smoothed surface. Then, fine polishing was done with a cerium oxide (CeO_2) abrasive composed of 1 μ m-size powder.

The expected surface quality of the dolomite lens in the THz frequency range was over $\lambda/1000$. The radius of curvature of the dolomite lens was 16.19 cm which is the same as that of the polishing plate. The thickness of the lens at the center, t_c , and at the edge, t_e , were measured to be 4.1 mm, and 2.1 mm, respectively. The difference between t_c and t_e is the calculated value (1.958 mm) concerning the radius of the lens. The expected focal length, f , is estimated to be 95.2 mm, as previously mentioned, and the back focal length, f_b , is 93.1 mm. All the parameters of the lens are graphically shown in Fig. 4.3–(a)

Materials	n	α	Reference
Teflon (PTFE)	1.42	0.178	[35, 44–46]
HDPE	1.534	2.172	[35, 46]
Dolomite	2.70(5)	4.(1)	This work
Silicon	3.41	0.46	[44, 45]

Table 4.3: Refractive indices n and extinction coefficients α (cm⁻¹) of dolomite and typical lens materials at 0.5 THz.

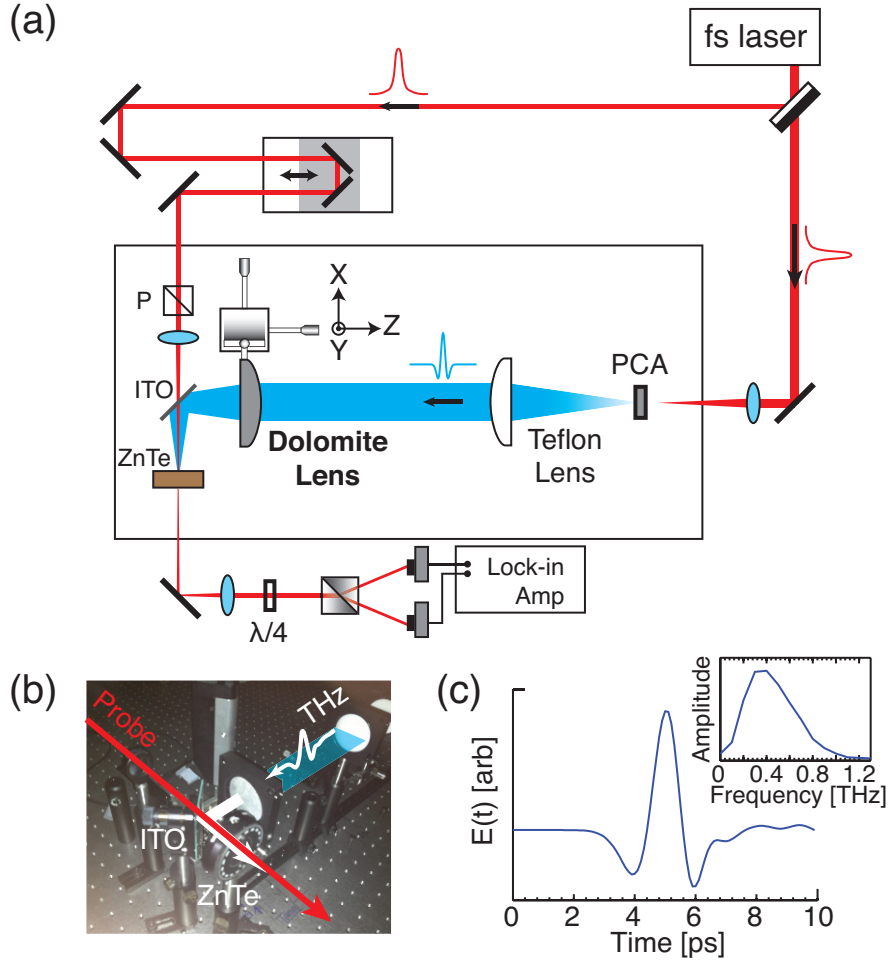


Figure 4.4: (a) Schematic of our linear configuration THz-TDS setup using two THz lenses; a Teflon lens and the fabricated dolomite lens. Overall intensity profiles were measured by moving the lens with an XYZ translation stage. (b) Image of the THz-TDS setup corresponding to the boxed area of (a). The THz field was focused on to ZnTe by the fabricated dolomite lens. ITO playing a role as a dichroic polarization beam splitter reflects the THz field and transmits the probe beam. (c) A temporal THz amplitude signal measured at the focal point and the corresponding amplitude spectrum after Fourier transformation.

and the actual photo image of the fabricated lens in Fig. 4.3-(b).

4.1.4 Results and Discussion

The shape of the focused THz field was examined by field profile measurement with a THz-TDS setup in a linear configuration as depicted in Fig. 4.4-(a). The image of the setup is shown in Fig. 4.4-(b). In this configuration, the diverging THz wave generated from the PCA was collimated by a Teflon lens with a focal length of 10 cm, and was focused by the dolomite lens. Then, the THz pulse and the probe laser pulse were merged by an ITO wafer, and THz signal was detected by the ZnTe crystal. The focal point of the dolomite lens was determined so that the measured THz signal is maximum by scanning the spatial amplitude with an XYZ translation stage. The field profile of the dolomite lens was obtained by scanning a two-dimensional (2D) area of $9 \times 9 \text{ cm}^2$ with an interval of $300 \mu\text{m}$. At each point of the measured 2D area, the temporal profile measurement over a 10 ps time window was carried out. The maximum THz signal in the center pixel of the 2D area and the corresponding spectral amplitude

obtained by the Fourier transform are shown in Figs. 4.4–(c).

The experimentally measured geometry of the beam profile shown in Fig. 4.5–(a) is theoretically equivalent to a Fraunhofer diffraction pattern arising from a circular aperture. The dolomite lens and Teflon lens had same diameters of 2 inches. The second lens, here the dolomite lens, has the size of the aperture in the Fraunhofer diffraction. This lens crops the THz waves reaching the lens and only the circular segment propagates through the lens and forms the diffraction pattern in the focal plane [11]. The THz pulse in our experimental condition has a broadband spectrum and therefore the performance of the dolomite lens can be determined by analyzing the beam profiles at various frequencies. The amplitude profile $E(r)$ is fitted the Bessel pattern [11] given by

$$E(r) = E(0) \left| \frac{2 J_1(kW_0r/2f)}{kW_0r/2f} \right|, \quad (4.5)$$

where r is the radial distance on the focal plane and J_1 is the first kind Bessel function of order one. Here, k is the wavenumber, f (95.2 mm) is the focal length of the lens and W_0 is the diameter of the

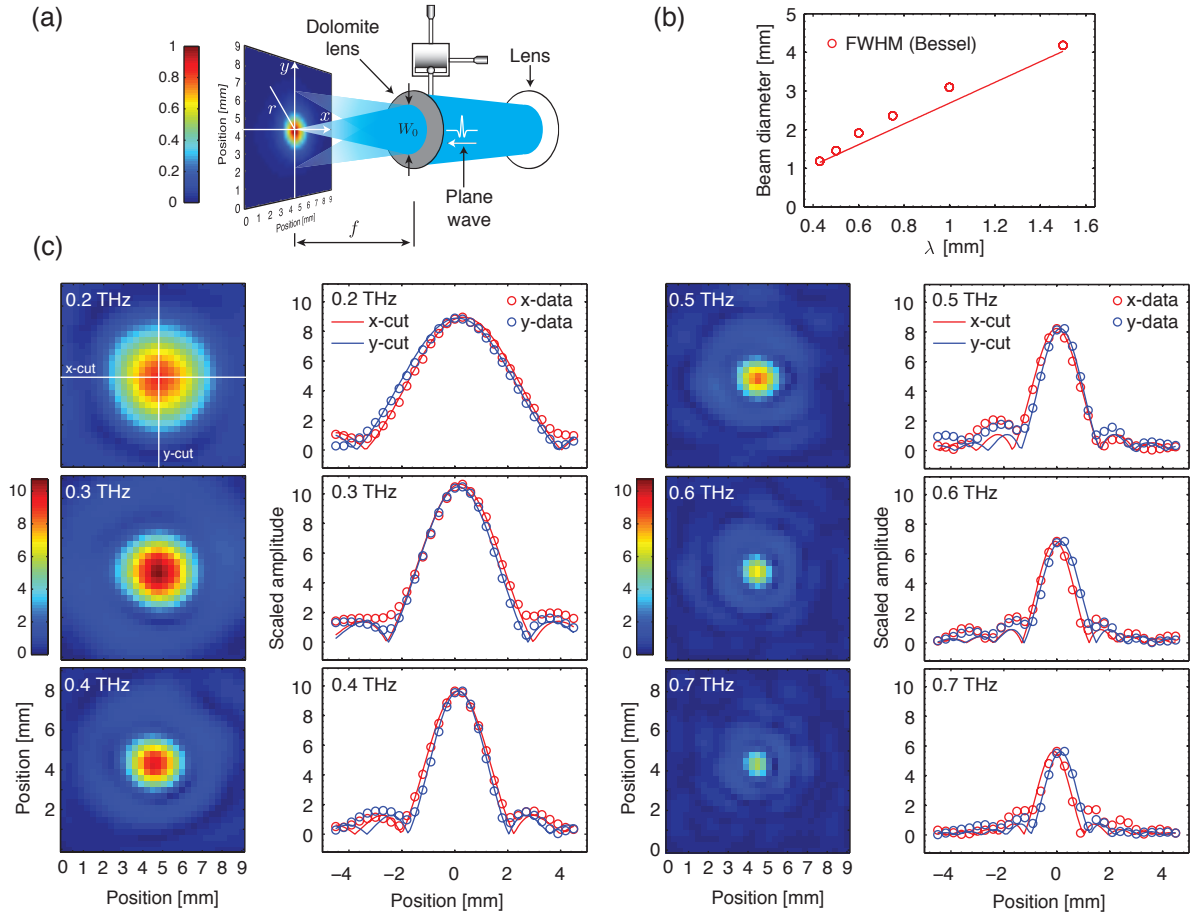


Figure 4.5: (a) Beam profile measurement geometry, where W_0 in Eq. (5) is the diameter of the collimated beam. (b) Extracted diameters (FWHM) of the focused THz field at various wavelengths obtained by numerical fitting of the amplitude profile to the Bessel function. (c) Transmission amplitudes with respect to frequency. All the amplitudes were divided by the amplitude of the THz signal measured without the fabricated dolomite lens. The colorbar indicates the magnitude of the signal with respect to the THz signal measured without the dolomite lens. The lines (solid line) fitted by the Bessel function plotted in the horizontal and vertical directions across the THz amplitude profile (open circle) are indicated in the figures (Normalized amplitude vs. position with respect to frequency).

lens. The derivation of Eq. (4.5) is detailed in the section A.10.2 in detail.

Figure 4.5-(b) summarizes the extracted diameters (FWHM) of the focused THz field as a function of wavelength obtained from the numerical fit of the amplitude profiles to the Bessel pattern in Eq. (4.5). The measured THz beam amplitude profiles at various frequencies and the corresponding x -, and y -cross sections of the profiles are shown in Fig. 4.5-(c). The amplitude profiles were scaled by the THz signal amplitude without the dolomite lens. The corresponding ratio, N_{ij} , is given by

$$N_{ij}(\omega_k) = \left| \frac{E_{ij}(\omega_k)}{E_{\text{no lens}}(\omega_k)} \right|, \quad (4.6)$$

where $|E_{ij}(\omega_k)|$ and $|E_{\text{no lens}}(\omega_k)|$ are the amplitudes of THz signals with and without the fabricated dolomite lens, respectively. The amplitude attenuation increases as a function of the frequency as shown in Fig. 4.5-(c). Nevertheless, the experimental result agrees well with the calculation of the THz beam profile. This result verifies that dolomite has high homogeneity as a lens material although dolomite has more absorption than other lens materials.

As expected, the beam diameters show decreasing behavior as the frequency increases. They are compared with a theoretical line calculated at a focal length of $f = 95.2$ mm and the lens diameter of $W_0 = 50$ mm (maximal f -number = 1.9). The theoretical line is calculated FWHM, $W(\lambda)$, from the Bessel pattern in Eq. (4.5) as

$$W(\lambda) = \frac{4.43f}{\pi W_0} \lambda. \quad (4.7)$$

Good agreement between the experiment and calculation confirms again that the fabricated lens made out of dolomite shows good performance in the THz frequency range.

4.1.5 Conclusion

The use of natural stones as an optical elemental material in the THz frequency range is described. We measured optical constants of various natural stones using THz-TDS. Among the investigated stones, dolomite in particular exhibited the flat refractive index and low absorption over the measured THz frequency range. We fabricated a dolomite planoconvex lens using the manufacturing process of conventional lenses. The measured focused beam profiles was well explained by far-field diffraction theory in the THz frequency range. With the proof-of-principle demonstration of THz lens made out of dolomite, we suggest the possibility of using natural stones as THz optical elements for scientific and economic reasons.

4.1.6 Appendix

In the lens fabrication processes, chromatic aberration and the spherical aberration should be considered [27]. First, the chromatic aberration for a plano-convex lens having a focal length f can be derived from the lens-maker's formula as [11, 27]

$$f = \frac{R}{(n - 1)}, \quad (4.8)$$

where n is the refractive index of the lens and R is the radius of curvature. The refractive index of dolomite in the THz frequency range is shown in Fig. 4.1. From the measured data, the refractive index

of dolomite is in the range of 2.689 (at 0.15 THz) to 2.723 (at 1 THz) so that the variation δn is 0.034. The induced variation of the focal length can be obtained given by

$$\delta f = R \left| \frac{1}{2.689 - 1} - \frac{1}{2.723 - 1} \right| \propto \left| \frac{1}{2.689 - 1} - \frac{1}{2.723 - 1} \right| \simeq 0.012 \simeq 1\%. \quad (4.9)$$

Therefore, chromatic aberration can be ignored since the refractive index of dolomite is nearly constant.

The spherical aberration, however, can not be ignored. From the paraxial-ray approximation, the gaussian formula for a single spherical surface is [11, 27]

$$\frac{n_1}{s_o} + \frac{n_2}{s_{ih}} = \frac{n_2 - n_1}{R}. \quad (4.10)$$

Provided the object point is located at infinity, Eq. (4.10) becomes

$$\frac{n_2}{f} = \frac{n_2 - n_1}{R}, \quad (4.11)$$

where f is the focal length of the paraxial rays denoted by $s_{ih} = f$. According to ray optics [11, 27, 64], the spherical aberration of a single surface can be described by the third-order expression of the first-order theory as¹

$$\frac{n_1}{s_o} + \frac{n_2}{s_{ih}} = \frac{n_2 - n_1}{R} + \frac{1}{2}Kh^2 \quad (4.12)$$

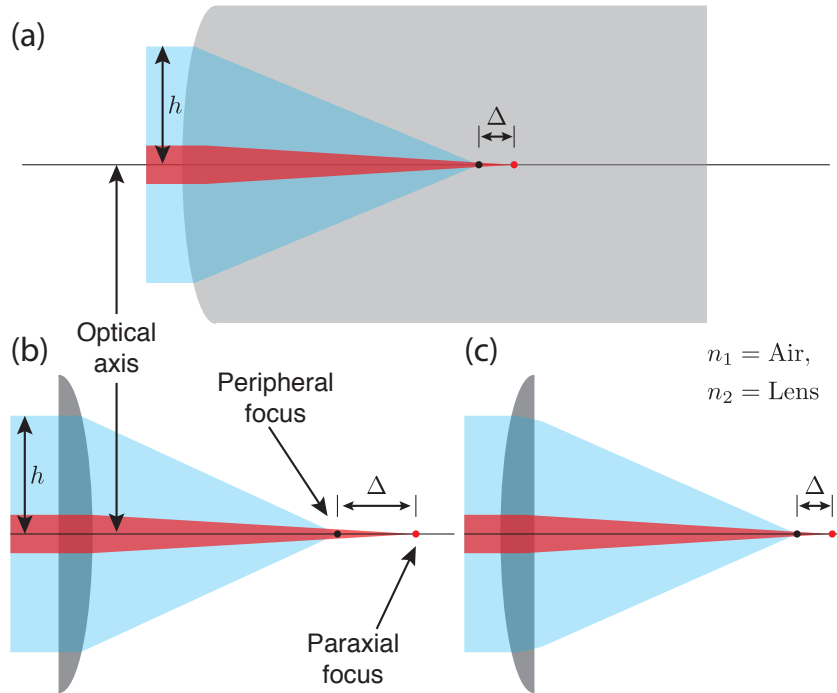


Figure 4.6: (a) The spherical aberration formed by a single spherical surface [11, 64]. (b) The spherical aberration formed by a plano-convex lens. (c) Reduction of aberration by turning the lens [11].

¹See Hecht, *Optics 4th edition* [11], p. 154, 254. See also Jenkins, *Fundamentals of optics* [64], p. 152.

with

$$K = \frac{n_1}{s_o} \left(\frac{1}{R} + \frac{1}{s_o} \right)^2 + \frac{n_2}{s_{ih}} \left(\frac{1}{R} - \frac{1}{s_{ih}} \right)^2 \quad (4.13)$$

$$\simeq \frac{n_1^2 R}{n_2 f} \left(\frac{1}{R} + \frac{1}{s_o} \right)^2 \left(\frac{1}{R} + \frac{n_1 + n_2}{n_1 s_o} \right), \quad (4.14)$$

where n_2 is the refractive index of the lens and n_1 is the refractive index of the surrounding medium. The object distance, the image distance, the radius of curvature, and the distance from the optical axis are denoted as s_o , s_i , R , and h , respectively².

From Eq. (4.12) through the substitution of $s_o \rightarrow \infty$, the third-order expression is slightly modified to

$$\frac{n_2}{s_{ih}} = \frac{n_2 - n_1}{R} + \frac{h^2 n_1^2}{2n_2 f R^2} \simeq \frac{n_2}{f} + \frac{h^2 n_1^2}{2n_2 f R^2}, \quad (4.19)$$

and is further reduced as

$$s_{ih} \equiv f' = f \left[1 + \frac{h^2}{2n_{\text{lens}}^2 R^2} \right]^{-1}, \quad (4.20)$$

where $n_{\text{lens}} = n_2$, $n_1 = 1$ in air, and f is the focus for the paraxial rays.

²By the paraxial approximation and the substitution $s_o \rightarrow \infty$, Eq. (4.12) can be written as

$$\frac{n_1}{s_o} + \frac{n_2}{s_{ih}} \simeq \frac{n_2}{s_{ih}} \simeq \underbrace{\frac{n_2}{f}}_{\text{Paraxial}} = \frac{n_2 - n_1}{R}. \quad (4.15)$$

From this relation, we obtain

$$\frac{n_2}{s_{ih}} = \frac{n_2 - n_1}{f} - \frac{n_1}{s_o} \Leftrightarrow \frac{1}{s_{ih}} = \frac{1}{f} - \frac{n_1}{n_2 s_o}, \quad (4.16)$$

$$\frac{1}{f} = \frac{n_2 - n_1}{n_2} \frac{1}{R}. \quad (4.17)$$

Then Eq. (4.13) becomes

$$\begin{aligned} K &= \frac{n_1}{s_o} \left(\frac{1}{R} + \frac{1}{s_o} \right)^2 + \underbrace{\frac{n_2}{s_{ih}}}_{\text{Eq. (4.16)}} \left(\frac{1}{R} - \underbrace{\frac{1}{s_{ih}}}_{\text{Eq. (4.16)}} \right)^2 \\ &\simeq \frac{n_1}{s_o} \left(\frac{1}{R} + \frac{1}{s_o} \right)^2 + \left(\frac{n_2}{f} - \frac{n_1}{s_o} \right) \left(\frac{1}{R} - \underbrace{\frac{1}{f}}_{\text{Eq. (4.17)}} + \frac{n_1}{n_2 s_o} \right)^2 \\ &= \frac{n_1}{s_o} \left(\frac{1}{R} + \frac{1}{s_o} \right)^2 + \left(\frac{n_2}{f} - \frac{n_1}{s_o} \right) \left(\frac{1}{R} - \frac{n_2 - n_1}{n_2} \frac{1}{R} + \frac{n_1}{n_2 s_o} \right)^2 \\ &= \frac{n_1}{s_o} \left(\frac{1}{R} + \frac{1}{s_o} \right)^2 + \left(\frac{n_2}{f} - \frac{n_1}{s_o} \right) \frac{n_1^2}{n_2^2} \left(\frac{1}{R} + \frac{1}{s_o} \right)^2 = \left(\frac{1}{R} + \frac{1}{s_o} \right)^2 \left[\frac{n_1}{s_o} + \frac{n_1^2}{n_2^2} \left(\frac{n_2}{f} - \frac{n_1}{s_o} \right) \right] \\ &= \left(\frac{1}{R} + \frac{1}{s_o} \right)^2 \left[\frac{n_1}{s_o} + \frac{n_1^2}{n_2} \frac{1}{f} - \frac{n_1^3}{n_2^2} \frac{1}{s_o} \right] = \left(\frac{1}{R} + \frac{1}{s_o} \right)^2 \frac{n_1^2}{n_2} \frac{1}{f} \left[\frac{n_2 f}{n_1 s_o} + 1 - \frac{n_1 f}{n_2 s_o} \right] \\ &= \left(\frac{1}{R} + \frac{1}{s_o} \right)^2 \frac{n_1^2}{n_2} \frac{1}{f} \left[1 + \frac{n_2 f}{n_1 n_2 s_o} - \frac{n_1^2 f}{n_1 n_2 s_o} \right] = \left(\frac{1}{R} + \frac{1}{s_o} \right)^2 \frac{n_1^2}{n_2} \frac{1}{f} \left[1 + \frac{n_2^2 - n_1^2}{n_1 s_o} \underbrace{\frac{f}{n_2}}_{\text{Eq. (4.17)}} \right] \\ &= \left(\frac{1}{R} + \frac{1}{s_o} \right)^2 \frac{n_1^2}{n_2} \frac{1}{f} \left[1 + \frac{(n_2 + n_1)(n_2 - n_1)}{n_1 s_o} \frac{R}{n_2 - n_1} \right] = \left(\frac{1}{R} + \frac{1}{s_o} \right)^2 \frac{n_1^2}{n_2} \frac{1}{f} \left[1 + \frac{R}{n_1 s_o} (n_2 + n_1) \right] \\ &= \frac{n_1^2 R}{n_2 f} \left(\frac{1}{R} + \frac{1}{s_o} \right)^2 \left[\frac{1}{R} + \frac{n_2 + n_1}{n_1 s_o} \right]. \end{aligned} \quad (4.18)$$

The longitudinal spherical aberration Δ formed by a single spherical surface shown in Fig. 4.6(a) can therefore be obtained by the difference between the paraxial focus f and the focal length f' for rays with a distance h from the optical axis given by

$$\Delta = |f' - f|. \quad (4.21)$$

The plano-convex lens is approximately the same optical system as a single spherical surface since one of the two radii of curvatures is infinity. For the fabricated THz dolomite lens, the parameters are $n_{\text{lens}}=2.7$, $h=25$ mm (half of the 2 inch lens) and $R=161.9$ cm. By Eq. (4.20), the focal length for rays with a distance h from the optical axis is

$$f' = 95.2 \text{ mm} \left[1 + \frac{25^2 \text{ mm}^2}{2 \times 2.7^2 \times 161.9^2 \text{ mm}^2} \right]^{-1} \simeq 95.045 \text{ mm}. \quad (4.22)$$

Hence, we obtain the aberration $\Delta \simeq 0.155$ mm.

4.2 Lattice vibrations of natural seraphinite gemstone

Here we report the first observations in terahertz frequency lattice vibrations in naturally occurring seraphinite gemstones. Seraphinite is a particular form of clinoclone minerals in the chlorite group, where the THz frequency response of any chlorite minerals has been unknown. Based on our THz time-domain spectroscopic measurements, we show that there are three absorption modes at 0.8, 0.96 and 1.2 THz. The 0.96 THz mode is, in particular, strong and narrow ($Q=8$) which is comparable to the previously reported 0.53 THz mode in α -lactose monohydrate. A polarization-dependent study reveals the $A_u(z')$ -symmetry in the 0.8 and 1.2 THz modes and the $B_u(x', y')$ -symmetry in the 0.96 THz mode. The anisotropy in the phonon-polariton dispersions shows an excellent agreement with the theoretical analysis based on Kurosawa's formula.

4.2.1 Introduction

Science and technology related to terahertz (THz) frequency electromagnetic waves [3] have tremendously progressed during the past decades, providing an intellectual and technological bridge between traditional studies in optics and microwave electronics [2]. In particular, THz time-domain spectroscopy (THz-TDS) [65] has played a crucial role in investigating new properties and phenomena of materials. Many materials have spectral fingerprints in the THz frequency range, where the spectroscopic capability of utilizing ultra-broadband THz frequency waves has opened a rich variety of potential applications. These include polymorph material classification [66], hazardous material detection, functional study of bio-medical materials [67], high-speed in-door communications, high-altitude telecommunications, quality control, process monitoring and etc [3].

THz-TDS directly measures electric-field responses of materials. Spectral phase information can thus be obtained without resorting to the Kramers-Kronig relationship [21]. When a THz pulse passes through a sample having a thickness of d , the transmission amplitude spectrum $\rho(\omega)$ and the transmission phase spectrum $\phi(\omega)$ can be obtained by

$$\tilde{T}(\omega) = \frac{\tilde{E}_s(\omega)}{\tilde{E}_r(\omega)} = \rho(\omega) e^{i\phi(\omega)} \tilde{F}(\omega), \quad (4.23)$$

where $\tilde{E}_s(\omega)$ and $\tilde{E}_r(\omega)$ are the transmitted electric-fields with and without the sample, respectively, and $\tilde{F}(\omega)$ is the Fabry-Pérot effect caused by internal reflections in the sample. The complex refractive index of the sample defined by $\tilde{n} = n + i\kappa$ can be obtained by the fixed point iteration method [30] as following:

$$n(\omega) = n_a + \frac{c}{\omega d} \phi(\omega), \quad \kappa(\omega) = -\frac{c}{\omega d} \log \rho(\omega), \quad (4.24)$$

where n_a is the refractive index of air and c is the speed of light. The extinction coefficient is also obtained by

$$\alpha(\omega) = \frac{2\omega}{c} \kappa(\omega). \quad (4.25)$$

Dielectric properties of various materials have been studied including crystal dielectrics, semiconductors [65], plastics [35], explosives [68], liquids [39], biomaterials [41], metamaterials [69], silicate glasses [70] and natural mineral compounds [31, 71] and etc. Furthermore, advanced optical properties such as birefringence [37], anisotropic single crystal measurement [72–74], optical activity [75], magneto/electro-optical effects [76] and electromagnons [77] in the THz frequency range are also under active investigation.

In this paper, the first observations of strong absorption modes in naturally occurring seraphinite in the THz frequency range are reported. Seraphinite is the special name for a particular form of a clinochlore mineral having gem-grade quality, which exhibits a green feather-like uneven color distribution of chatoyant fibers. Its name is based on its appearance, where the Greek word “seraphim” means the wings of a celestial being is used. Clinochlore, often referred to as chlorite jade (although it is not a real jade [78]), is a member of the chlorite group [79]. Seraphinite contains Mg and has a chemical formula [80] of $(\text{Mg}, \text{Fe}^{2+})_5\text{Al}(\text{Si}_3\text{Al})\text{O}_{10}(\text{OH})_8$. Figure 4.7 shows the atomic structure of seraphinite [81]. It has a monoclinic layered structure in the space group $C2/m$ at room temperature [82]. As shown in Fig. 4.7, seraphinite has a substructure consisting of two different layers: a talc-like layer and a brucite-like layer [83]. Both layers are mainly octahedra in which magnesium (or aluminum) atoms are centered around oxygen atoms. The talc-like layer has additional SiO_4 tetrahedras at the top and the bottom of each octahedra. Since the layers are electrically charged (the talc-like layer is negative and the brucite-like layer is positive), pseudo random piling in clinochlore could induce polariton behaviors upon light illumination. We show that the absorptions at 0.8, 1.2 and 0.96 THz frequencies (each corresponding to 26.64, 39.96 and 31.97 cm^{-1} in wave numbers, respectively) are the phonon-polariton coupled modes [84] for infrared (IR)-active optic phonons having $A_u(z')$ and $B_u(x', y')$ -symmetries [85–87].

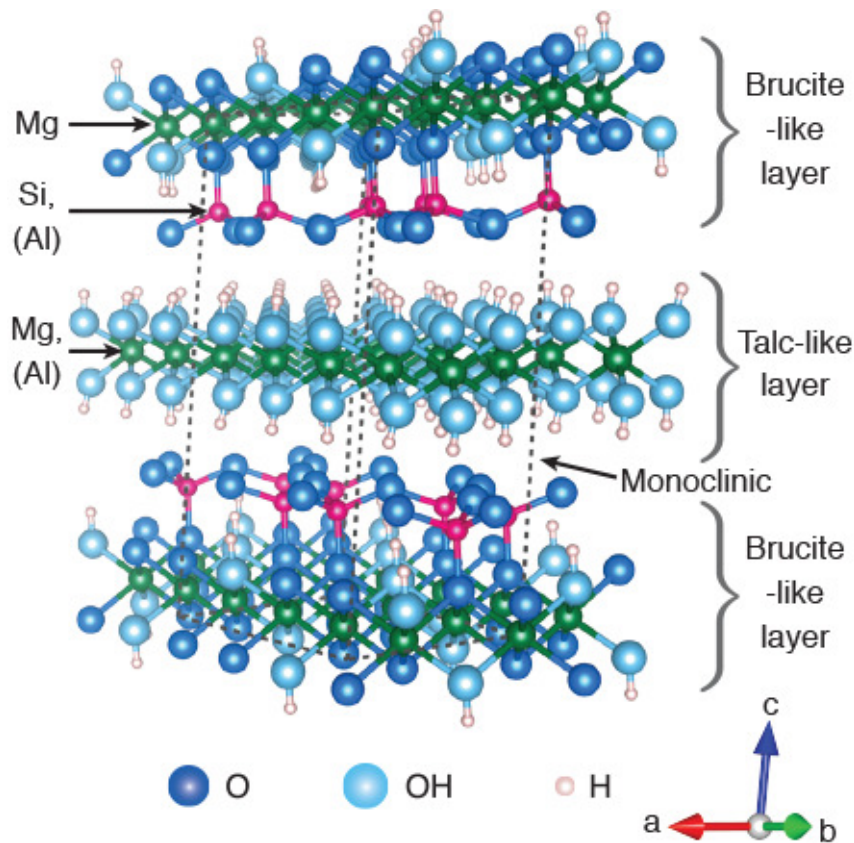


Figure 4.7: Atomic structure of seraphinite. The atomic position parameters are from Ref. [81]. The unit cell parameters are $a = 5.350(3)$, $b = 9.267(5)$, $c = 14.27(1)$, and $\gamma (\angle(a, c)) = 96.35(5)^\circ$.

4.2.2 Experimental procedure

All experiments were performed using a conventional THz-TDS setup [31]. Ultrafast laser pulses whose wavelengths are centered at 840 nm were produced by a Ti:sapphire mode-locked laser oscillator operating at a repetition rate of 80 MHz. They were used to generate THz pulses from a photo-conductive antenna (PCA). Upon illumination of each laser pulse having a 120-fs-short pulse duration, a THz pulse having less than a picosecond pulse duration was produced. The electric-field of the THz pulse was measured by electro-optic sampling by using another optical pulse (the probe pulse) split off from the first laser pulse.

When directed through a (110)-oriented ZnTe crystal with a thickness of 1 mm, the polarization of the optical probe pulse was rotated with an angle linearly proportional to the electric-field amplitude of the co-propagating THz pulse via the Pockels effect. The whole setup was covered by an acrylic box purged with dry air to eliminate water vapor absorptions.

Samples were prepared with two different cuts with respect to the feather-like pattern: parallel (\parallel)-cut and perpendicular (\perp)-cut as shown in Fig. 4.8. The sample thickness was $d = 0.96$ mm for the \perp -cut and 0.8 mm for the \parallel -cut, where the sample area was over 5×5 mm². Sample rotation was done by using a motorized rotation mount. The sample was attached on an aluminum metal holder with a hole diameter of 5 mm, which is sufficiently large compared to the Rayleigh diffraction limit corresponding to the measured THz frequency range.

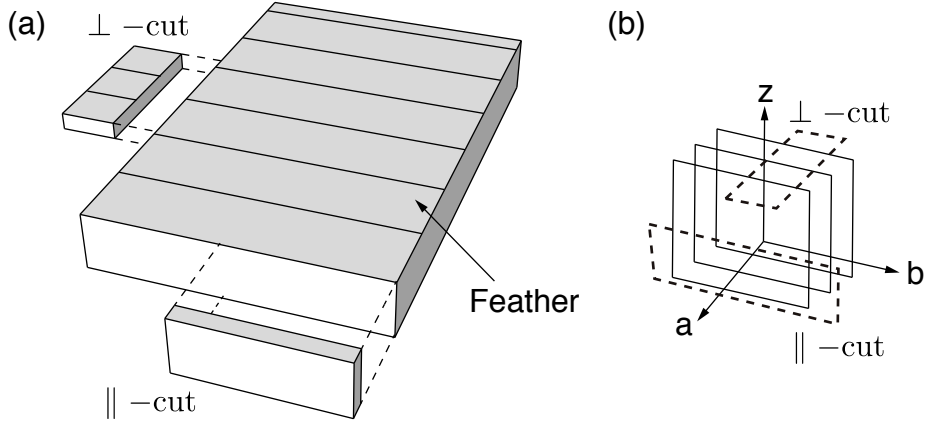


Figure 4.8: (a) Schematic representation of bulk seraphinite. The \perp -cut and \parallel -cut seraphinite samples are prepared as illustrated in (a). We assumed that the sample plane of each seraphinite is approximately corresponding to crystal axes as shown in (b)

4.2.3 Results

When the THz-TDS recorded the time-domain electric-field amplitude of THz pulses transmitted through the sample, the typical measurements are as shown in Fig. 4.9(a). The transmitted THz pulses through the \perp -cut and \parallel -cut samples (blue solid and red dash-dot lines, respectively) are time-delayed from the reference peak (black dotted line). The time delay is given by $\Delta t = (n_g - n_a)d/c$, where n_g is the group index of the sample. By varying the azimuthal angle of the samples, the THz waveforms were measured as shown in Fig. 4.9(b). The periodical delay of the peak position is due to the birefringence of the seraphinite.

When the time-domain data is converted to the frequency-domain data through Fourier transfor-

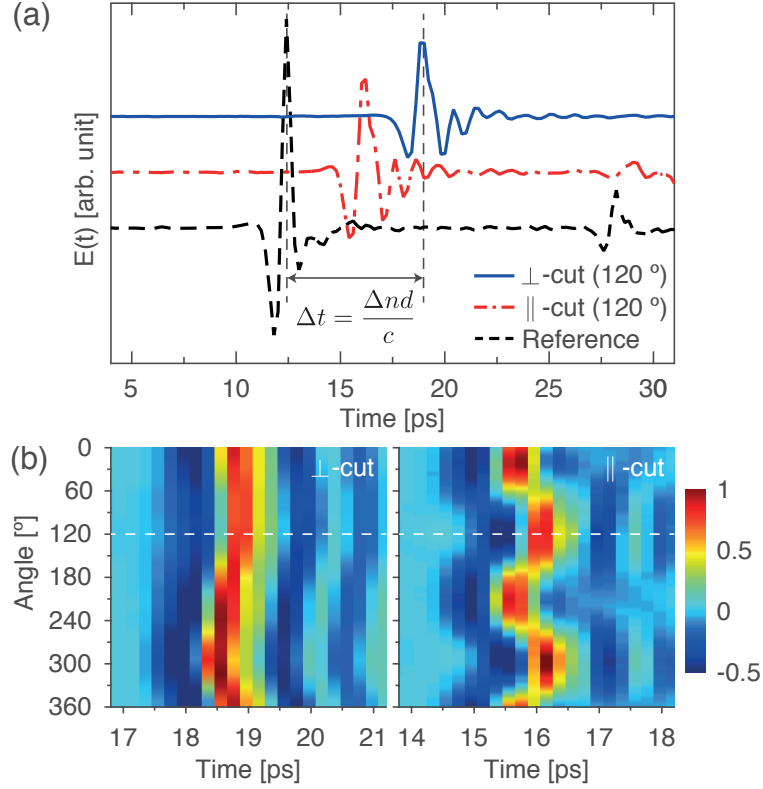


Figure 4.9: (a) Measured electric-field amplitudes of a THz pulse at the azimuthal angle of 120° transmitted through the \perp -cut (blue solid line) and \parallel -cut (red dash-dot line) seraphinite sample, respectively, compared with the reference signal (black dotted line). The time delay Δt between the main peaks of the two signals corresponds to the differential index Δn between the sample ($n_g = 3.0$) and air ($n_a = 1$) times the thickness ($d = 0.96$ mm) divided by c . (b) Polarization-dependent THz waveforms measured by varying the azimuthal angle of the \perp -cut and \parallel -cut seraphinites with respect to linearly-polarized incident THz waves. The THz waveforms are normalized for the sake of comparison.

mation, the index of refraction $n(\omega)$ and the extinction coefficient $\alpha(\omega)$ are obtained respectively by comparing the spectral responses with and without the sample. Both the real and imaginary parts of the electric susceptibility (or the index of refraction and absorption of the sample) are obtained from Eqs. (4.24) and (4.25) through the fixed point iteration method [30]. Figure 4.10 shows the experimental result. The index of refraction $n(\omega, \theta)$ and the extinction coefficient $\alpha(\omega, \theta)$ of the \perp -cut and \parallel -cut seraphinites are shown as a function of the azimuthal angle (θ) with respect to the THz polarization direction in Fig. 4.10(a)-(d).

4.2.3.1 The strong absorption mode at 0.96 THz

When the extinction coefficient of the \perp -cut seraphinite at $\theta = 120^\circ$ in Fig. 4.10(b) is fitted with two Lorentzian line-shapes [7], the 0.96 THz (ν) strong absorption exhibits a full width at half maximum (FWHM) of $\Delta\nu = 0.12$ THz as shown in Fig. 4.10(e). The corresponding Q factor ($\nu/\Delta\nu$) of 8.14 is extremely high comparable to the well-known THz absorption peak at 0.53 THz of the α -lactose monohydrate [88]. Since the Q factor characterizes the resonance narrowness, materials with a large Q , in particular of a solid-state material, can be useful for making devices such as band-pass filters, frequency standards and etc. For the 0.96 THz mode at $\theta = 120^\circ$ of \perp -cut seraphinite, the oscillator strength [89] defined by $f = 8\pi^2\sigma_{\max}\Delta\omega/\omega^2$, where $\sigma = \omega \text{Im}[\tilde{\epsilon}(\omega)]/4\pi$ is the conductivity, equals $f = 0.072$. The

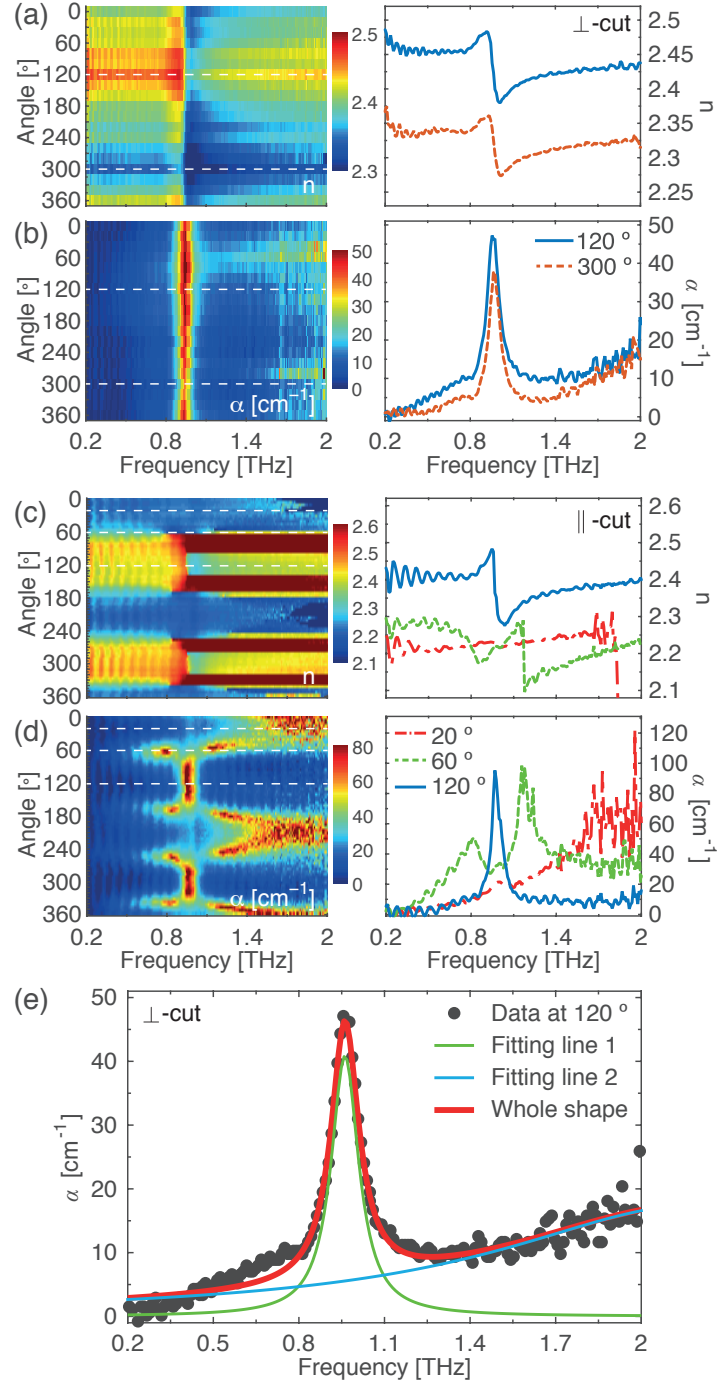


Figure 4.10: (a, c) The index of refraction $n(\omega, \theta)$ for $\theta \in \{0, \dots, 360\}$ and (b, d) the extinction coefficient $\alpha(\omega, \theta)$ for $\theta \in \{0, \dots, 360\}$ of \perp -cut and \parallel -cut seraphinites measured as a function of the azimuthal angle (θ) with respect to the THz polarization direction, respectively; (a) $n_{\perp}(\omega, 120^{\circ})$ and $n_{\perp}(\omega, 300^{\circ})$, (b) $\alpha_{\perp}(\omega, 120^{\circ})$ and $\alpha_{\perp}(\omega, 300^{\circ})$. The strong absorption mode is measured at 0.96 THz. (c, d) $n_{\parallel}(\omega, \theta)$ and $\alpha_{\parallel}(\omega, \theta)$ at $\theta = 20^{\circ}$, 60° , and 120° . (e) The strong absorption mode of \perp -cut seraphinite. When the extinction coefficient at azimuthal angle of $\theta = 120^{\circ}$ of \perp -cut seraphinite was fitted to two Lorentzian functions, the 0.96 THz absorption peak has a linewidth of 0.12 THz (FWHM).

Table 4.4: The characteristics of the strong absorption line of \perp -cut seraphinite at 0.96 THz.

Materials	Fitting function	ν [THz]	$\Delta\nu$ [THz]	Q -factor ($\nu/\Delta\nu$)	Oscillator strength f	Technique	References
Seraphinite	Lorentzian	0.960	0.120	8.14	0.072	THz-TDS	This work
α -Lactose	Lorentzian	0.525	0.069	7.60	0.016	THz-TDS	Ref. [88]

retrieved parameters for the 0.96 THz absorption peak are summarized in Table 4.4.

4.2.3.2 The dielectric tensor for a monoclinic structure

The crystalline structure of seraphinite belongs to the space group of C2/m. The factor group analysis [90] predicts that the dipole momenta of A_u and B_u modes are inclined along the z' -axis and placed on the ab -plane, respectively, where a , b and c denote monoclinic crystal axes and x' , y' , and z' denote the principal coordinates. The principle coordinates of this crystal is related to the crystallographic coordinates (a , b , c) as follows: $x' \parallel a$, $y' \parallel b$, and $\angle(a, c) = 96.35(5)^\circ$ [81].

To understand the polarization dependence of the extinction coefficients in Figs. 4.10(c) and (d), we consider the (relative) dielectric tensor $\tilde{\epsilon}(\omega)$ represented with the principal coordinates (x' , y' , z')

$$\tilde{\epsilon}(\omega) = \begin{bmatrix} \tilde{\epsilon}_{x'x'}(\omega) & \tilde{\epsilon}_{x'y'}(\omega) & 0 \\ \tilde{\epsilon}_{x'y'}(\omega) & \tilde{\epsilon}_{y'y'}(\omega) & 0 \\ 0 & 0 & \tilde{\epsilon}_{z'z'}(\omega) \end{bmatrix}. \quad (4.26)$$

The non-zero components of the dielectric tensor in Eq. (4.26) are described by the generalized Drude-Lorentz model [91, 92] as follows

$$\tilde{\epsilon}_{ij}(\omega) = \epsilon_{ij}^\infty + \sum_{n \in \{A_u, B_u\}} \tilde{S}_n(\omega) \Gamma_i^n \Gamma_j^n \quad (4.27)$$

for $i, j \in \{x', y', z'\}$, where ϵ_{ij}^∞ denotes the high frequency contribution and the angle dependence factors are given by

$$\Gamma_{x'}^n = \sin \theta_n \cos \phi_n, \quad \Gamma_{y'}^n = \sin \theta_n \sin \phi_n, \quad \Gamma_{z'}^n = \cos \theta_n. \quad (4.28)$$

The complex oscillator term \tilde{S}_n is defined by

$$\tilde{S}_n = \frac{\omega_{p,n}}{\omega_{0,n}^2 - \omega^2 - i\gamma_n\omega}, \quad (4.29)$$

where $\omega_{p,n}$, $\omega_{0,n}$, γ_n are the plasma frequency, the transverse frequency, and the damping coefficient of the n -th mode that belong to the A_u modes and B_u modes, respectively. θ_n and ϕ_n denote the polar angle and the azimuthal angle between the n -th dipole moment and the z' -axis as shown in Fig. 4.11(a).

4.2.3.3 The relation between the polarizability and the susceptibility

From electromagnetic theory [12], the polarizability P and the complex refractive index n of a material are given in terms of the effective susceptibility χ_{eff} [7] by

$$\tilde{P}(\omega, \theta) = \epsilon_0 \tilde{\chi}_{\text{eff}}(\omega, \theta) \tilde{E}, \quad (4.30)$$

$$\tilde{n}(\omega, \theta) = \sqrt{1 + \tilde{\chi}_{\text{eff}}(\omega, \theta)}, \quad (4.31)$$

where θ is the polarization angle. According to the complex refractive index defined by $\tilde{n} = n + i\kappa$, the effective susceptibility in Eq. (4.31) can be obtained throughout the measured THz frequency range as

$$\tilde{\chi}_{\text{eff}}(\omega, \theta) = \left[n(\omega, \theta) + i\kappa(\omega, \theta) \right]^2 - 1. \quad (4.32)$$

Therefore, the angle dependence of the polarizability \tilde{P} is the same as that of the susceptibility $\tilde{\chi}_{\text{eff}}$ obtained from the complex refractive index \tilde{n} [12].

4.2.3.4 The isotropic excitation behavior in the \perp -cut seraphinite

In a monoclinic crystal, the dipole moments of $A_u(z')$ modes are aligned with the z' -axis and $B_u(x', y')$ modes are placed on the ab -plane. Therefore, when the incident wave propagating along the z' direction transmits through the \perp -cut crystal (the crystal surface is the $x'y'$ -plane) as shown in Fig. 4.11(b), A_u modes are not excited and only B_u modes are excited. In this case, the dielectric

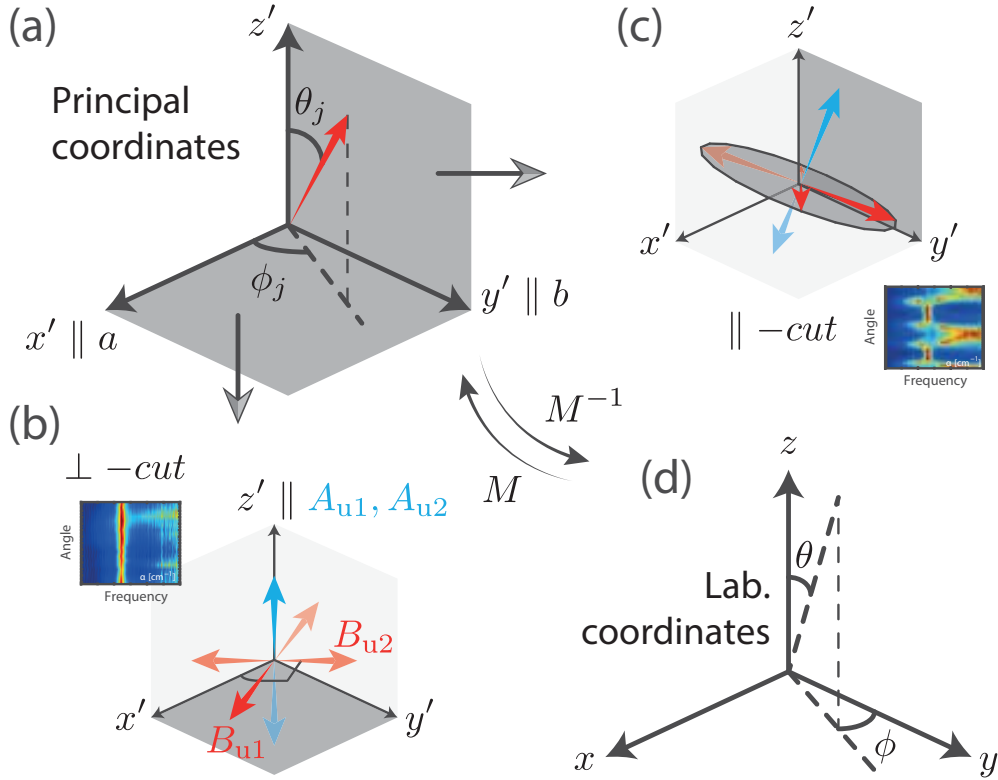


Figure 4.11: (Color online) (a) The principle coordinates. (b) The sample coordinates of the \perp -cut sample. (c) The sample coordinates of the the \parallel -cut sample. (d) The lab-frame coordinates are transformed from the principle or sample coordinates via M , where θ_j and ϕ_j represent the polar angle and the azimuthal angle between the j -th dipole moment (red arrow) and the z' -axis. The crystal surface is represented by dark gray color in each figure.

function is given by ³

$$\tilde{\varepsilon}_{ij} = \varepsilon_{ij}^{\infty} + \sum_{n \in \{B_u\}} \tilde{S}_n \Gamma_i(\phi_n) \Gamma_j(\phi_n) \quad (4.37)$$

for $i, j \in \{x', y'\}$, where $\Gamma_{x'}(\phi_n) = \cos \phi_n$, $\Gamma_{y'}(\phi_n) = \sin \phi_n$, and $\theta_n = \pi/2$ for $B_u(x', y')$ modes. However, when the two dipole moments $B_{u,1}$ and $B_{u,2}$ are orthogonal with each other (*i.e.*, $\phi_2 = \phi_1 + \pi/2$), the dielectric tensor elements in Eqs. (4.37) becomes ϕ_n -independent since $\tilde{\varepsilon}_{x'x'} = \varepsilon_{x'x'}^{\infty} + \tilde{S}_{B_u}$, $\tilde{\varepsilon}_{x'y'} = \varepsilon_{x'y'}^{\infty}$, $\tilde{\varepsilon}_{y'y'} = \varepsilon_{y'y'}^{\infty} + \tilde{S}_{B_u}$ when $\tilde{S}_{B_{u,1}} = \tilde{S}_{B_{u,2}}$ is assumed.⁴ Therefore, the isotropic behavior (no angle dependence) of the 0.96 THz mode excitation in the \perp -cut seraphinite in Fig. 4.10(b) can be understood by the fact that there exist two B_u modes being orthogonal with each other and of the same resonant frequency at 0.96 THz.

4.2.3.5 The anisotropic excitation behavior in the \parallel -cut seraphinite

To understand the \parallel -cut measurement in Fig. 4.10(d), we assume that the sample was cut slightly tilted from the principal $y'z'$ plane so that the dipole moments of the A_u modes are slightly tilted from the sample z' -axis. So, the (x', y', z') coordinates now represent the sample coordinate system, as depicted in Fig. 4.11(b). Then, the incident electric-field $\mathbf{E}'_{x'y'z'}$ in the sample coordinates is represented through a coordinate transformation from the lab-frame measurements \mathbf{E}_{xyz} in Fig. 4.11(d), or

$$\mathbf{E}'_{x'y'z'} = \left[R_z^{\text{vec}}(\phi) R_x^{\text{vec}}(\theta) \right] \mathbf{E}_{xyz} \equiv M(\theta, \phi) \mathbf{E}_{xyz}, \quad (4.41)$$

where each rotation operation $R_j^{\text{vec}}(\theta)$ represents the coordinate rotation by a counter-clockwise angle θ about the j -axis.⁵

The induced polarizability $\tilde{\mathbf{P}}'_{x'y'z'}$ in the sample coordinates is given, in terms of the linear electric

³For \perp -cut, the dipole moments of A_u modes are aligned with z' -axis and B_u modes are aligned with ab -plane shown in Fig. 4.11(a), which can be reduced by using Eq (4.27) in the forms

$$\tilde{\varepsilon}_{x'x'} = \varepsilon_{x'x'}^{\infty} + \sum_{j \in \{B_u\}} \tilde{S}_j \cos^2 \phi_j \quad (4.33)$$

$$\tilde{\varepsilon}_{x'y'} = \varepsilon_{x'y'}^{\infty} + \sum_{j \in \{B_u\}} \tilde{S}_j \cos \phi_j \sin \phi_j \quad (4.34)$$

$$\tilde{\varepsilon}_{y'y'} = \varepsilon_{y'y'}^{\infty} + \sum_{j \in \{B_u\}} \tilde{S}_j \sin^2 \phi_j \quad (4.35)$$

$$\tilde{\varepsilon}_{z'z'} = \varepsilon_{z'z'}^{\infty} + \sum_{j \in \{A_u\}} \tilde{S}_j. \quad (4.36)$$

⁴Provided the related two identical dipole moments $B_{u,1}$ and $B_{u,2}$ are orthogonal, the dielectric tensor elements from Eq. (4.33) to Eq. (4.36) are reduced given by

$$\begin{aligned} \tilde{\varepsilon}_{x'x'} &= \varepsilon_{x'x'}^{\infty} + \tilde{S}_{B_u} [\cos^2 \phi_b + \cos^2(\phi_b + \pi/2)] \\ &= \varepsilon_{x'x'}^{\infty} + \tilde{S}_{B_u}, \end{aligned} \quad (4.38)$$

$$\begin{aligned} \tilde{\varepsilon}_{x'y'} &= \varepsilon_{x'y'}^{\infty} + \tilde{S}_{B_u} [\cos \phi_b \sin \phi_b \\ &\quad + \cos(\phi_b + \pi/2) \sin(\phi_b + \pi/2)] = \varepsilon_{x'y'}^{\infty}, \end{aligned} \quad (4.39)$$

$$\begin{aligned} \tilde{\varepsilon}_{y'y'} &= \varepsilon_{y'y'}^{\infty} + \tilde{S}_{B_u} [\sin^2 \phi_b + \sin^2(\phi_b + \pi/2)] \\ &= \varepsilon_{y'y'}^{\infty} + \tilde{S}_{B_u}, \end{aligned} \quad (4.40)$$

where \tilde{S}_{B_u} and ϕ_b are the oscillator term and the azimuthal angle of $B_{u,1}$, respectively. $\phi_b + \pi/2$ is the azimuthal angle of $B_{u,2}$ mode. This implies that $\varepsilon_{x'y'}^{\infty}$ should be small and $\varepsilon_{x'x'}^{\infty}$ has to be the same as $\varepsilon_{y'y'}^{\infty}$. It is concluded that the related two identical dipole moments for B_u modes are orthogonal, which makes it possible to observe isotropic behavior from \perp -cut in Fig. 4.10(b). Therefore, dielectric tensor elements for \perp -cut are defined by Eqs. (4.36), (4.38), (4.39) and (4.40) from which it can be explained that the B_u mode at 0.96 THz is constantly measured in sample rotation.

⁵ M represents the extrinsic rotation matrix. Then M can be written as

$$M = R_z^{\text{vec}}(\phi) R_y^{\text{vec}}(-\theta') R_x^{\text{vec}}(\theta). \quad (4.42)$$

susceptibility tensor $\tilde{\chi}^{(1)}(\omega) = \tilde{\epsilon}(\omega) - \mathbf{I}$ and the electric-field $\mathbf{E}'_{x'y'z'}$, by

$$\tilde{\mathbf{P}}'_{x'y'z'} = \epsilon_0 \begin{bmatrix} \tilde{\chi}_{x'x'}^{(1)} & \tilde{\chi}_{x'y'}^{(1)} & 0 \\ \tilde{\chi}_{x'y'}^{(1)} & \tilde{\chi}_{y'y'}^{(1)} & 0 \\ 0 & 0 & \tilde{\chi}_{z'z'}^{(1)} \end{bmatrix} \mathbf{E}'_{x'y'z'}. \quad (4.43)$$

The polarizability $\tilde{\mathbf{P}}_{xyz}$ in the lab-frame coordinates is then given by

$$\tilde{\mathbf{P}}_{xyz} = M(\theta, \phi)^{-1} \tilde{\mathbf{P}}'_{x'y'z'}. \quad (4.44)$$

When the incident electric wave is linearly-polarized along the z -axis, the angular dependence of the polarizability can be obtained from the z -component of $\tilde{\mathbf{P}}_{xyz}$ as a function of θ as

$$\tilde{P}_z(\theta) = \epsilon_0 \tilde{\chi}_{x'x'}^{(1)} \sin^2 \theta + \epsilon_0 \tilde{\chi}_{z'z'}^{(1)} \cos^2 \theta, \quad (4.45)$$

where $\phi = 0$ is chosen in M for simplicity.⁶ Then, the π periodicity of the polarization angle for the B_u mode at 0.96 THz in Fig. 4.10(d) can be simply explained by the θ dependence in Eq. (4.45).

However, the A_u modes at 0.8 THz and 1.2 THz have a period of $\pi/2$, which needs to be accounted for higher-order polarizabilities. The monoclinic crystal in the space group of C2/m is centro-symmetric, so the next non-vanishing contribution is from the third-order susceptibility $\tilde{\chi}^{(3)}$ given in the sample coordinates (x', y', z') by

$$\tilde{\chi}_{ijkl}^{(3)}(\omega) = \sum_{n \in \{A_u, B_u\}} \tilde{S}_n(\omega) \Gamma_i^n \Gamma_j^n \Gamma_k^n \Gamma_l^n. \quad (4.49)$$

The z -component of $\tilde{\mathbf{P}}_{xyz}^{(3)}$ is given by

$$\begin{aligned} \tilde{P}_z^{(3)} &= 3\epsilon_0 \sum_{ijkl} M_{zi}^{-1} \tilde{\chi}_{ijkl}^{(3)}(\omega) E_j(\omega) E_k(-\omega) E_l(\omega) \\ &= 3\epsilon_0 \sum_{n \in \{A_u, B_u\}} \tilde{S}_n \left[\sin^4 \theta_n \sin^4 \phi_n \sin^4 \theta + \cos^4 \theta_n \cos^4 \theta + 6 \cos^2 \theta_n \sin^2 \theta_n \sin^2 \phi_n \cos^2 \theta \sin^2 \theta \right]. \end{aligned} \quad (4.50)$$

Figure 4.12 shows the measured $\text{Im}[\tilde{\chi}_{\text{eff}}]$ numerically fitted to Eq. (4.45) for 0.96 THz and to Eq. (4.71) for 0.80 THz and 1.20 THz, respectively. The tilting angles of the A_u modes, with respect to the z' -axis,

In our case, $R_y^{\text{vec}}(-\theta')$ is neglected and R_j^{vec} means the rotation matrix that rotates a given vector about the global j -axis (extrinsic rotation case). Further explanation about the rotation matrix is described in section C.

⁶Since the absorption behavior comes from the imaginary part of polarization, the imaginary part of Eq. (4.45) has to be obtained by

$$P_z(\theta)/\epsilon_0 = \chi_{x'x'}^{(1)} \sin^2 \theta + \chi_{z'z'}^{(1)} \cos^2 \theta, \quad (4.46)$$

where the imaginary terms are denoted as $\text{Im}[\tilde{P}_j] = P_j$ and $\text{Im}[\tilde{\chi}_{ij}^{(1)}] = \chi_{ij}^{(1)}$ for $i, j \in \{x', y', z'\}$. It is noted that the electric susceptibility $\chi^{(1)}$ is the same as $\epsilon \equiv \text{Im}[\tilde{\epsilon}]$. From this relation, we obtain the imaginary terms from Eq. (4.27) given by

$$\chi_{ij}^{(1)}(\omega) = \sum_{k \in \{A_u, B_u\}} L_k(\omega) \Gamma_i^k \Gamma_j^k, \quad (4.47)$$

where the Lorentzian L_k is the imaginary part of the complex oscillator term \tilde{S}_n defined by

$$L_k = \frac{\omega_{p,k} \gamma_k \omega}{(\omega_{0,k}^2 - \omega^2)^2 + \gamma_k^2 \omega^2}. \quad (4.48)$$

The B_u mode at 0.96 THz for the \parallel -cut in Fig. 4.10(d) has a period of π in the frequency-domain, which can be explained by Eq. (4.46) by substituting Eqs. (4.47) into $\chi_{ij}^{(1)}$. However, the fact that the A_u modes at 0.8 THz and 1.2 THz have a period of $\pi/2$ in the frequency-domain cannot be described by Eq. (4.46).

are obtained as $\theta_1 = 228^\circ$, $\phi_1 = -120^\circ$ for 0.8 THz and $\theta_2 = -139^\circ$, $\phi_2 = -117^\circ$ for 1.20 THz. The last equation is fully explained in the appendix 4.2.6.1.

4.2.4 Discussion

We now turn our attention to the origin of the observed THz absorptions. First, the possibility of water vapor absorption [93], which occurs at 26 and 58 cm^{-1} , is excluded by the subsequent temperature dependence of the mode frequency at elevated temperatures. To our knowledge, scientific literatures regarding seraphinite, or even including most hydrous/anhydrous layered silicates, are very limited and theoretical prediction is not available for phonon modes. Therefore, we can only compare it with indirect information from chlorite, which has similar local bonding networks of Si-O and Mg-O in their block-layered structures. In a chlorite mineral, far infrared absorptions are observed [94] at 120, 140, and 220 cm^{-1} . In addition, inelastic neutron scattering (INS) of chlorite reveals that there is only acoustic phonon branch below 1.5 THz [95], which can be Raman-active at $\sim 50 \text{ cm}^{-1}$. The phonon modes of chlorite can be inferred from the theoretical and experimental results on a magnesium-olivine, forsterite (Mg_2SiO_4). Forsterite is composed of isolated silicate tetrahedra but shares the same local bonding of Si-O and Mg-O with chlorite. The zone boundary acoustic mode is calculated at 100 cm^{-1} [96] and the optic modes are calculated at 130, 180 and 250 cm^{-1} [97]. Therefore, we explain the absorption peak at 0.96 THz of seraphinite phenomenologically in the context of the phonon-polariton coupled mode. It

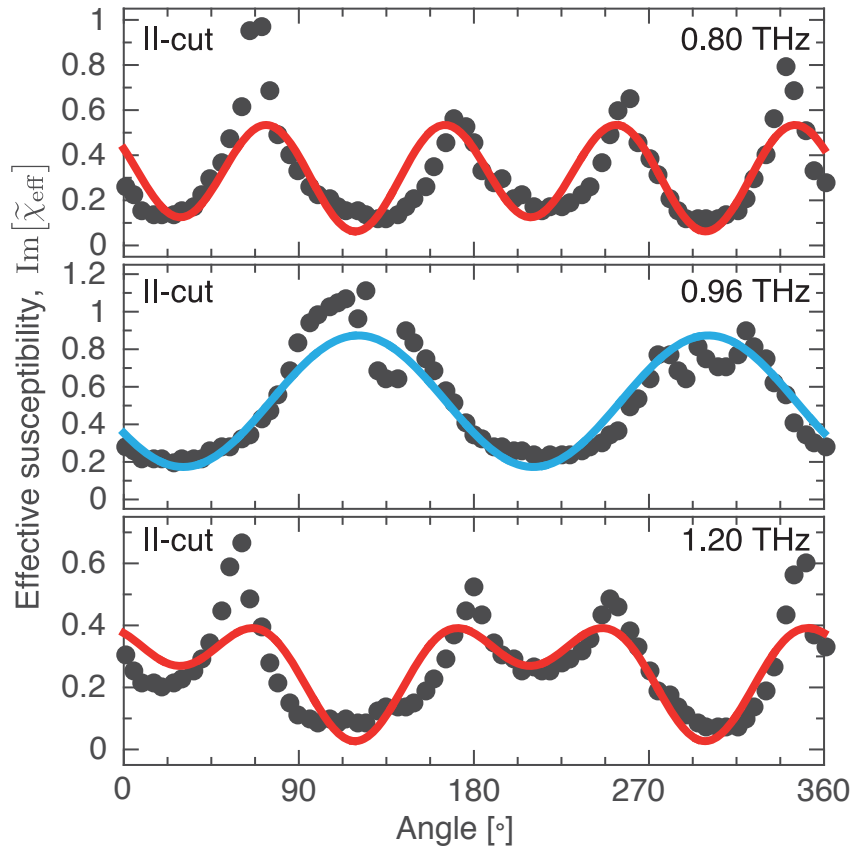


Figure 4.12: (Color online) The effective susceptibility χ_{eff} of the ||-cut seraphinite is extracted by Eq. (4.32). $\chi_{\text{eff}}(0.96 \text{ THz})$ for B_u mode (blue) is fitted to Eq. (4.45). $\chi_{\text{eff}}(0.8 \text{ THz})$ and $\chi_{\text{eff}}(1.20 \text{ THz})$ corresponding to A_u modes (red) are fitted to Eq. (4.71) represented by the red solid line.

can be understood that the infrared (IR)-active phonon modes originates from its monoclinic crystalline structure with the space group of C2/m [85–87].

The dispersion relation can be obtained by considering the relative dielectric function $\tilde{\epsilon}$ which is defined for an applied electric-field \tilde{E} and the induced polarizability \tilde{P} as [98]

$$\tilde{\epsilon}(\omega) = \frac{\epsilon(\omega)}{\epsilon_0} = 1 + \frac{1}{\epsilon_0} \frac{\tilde{P}(\omega)}{\tilde{E}(\omega)}. \quad (4.51)$$

When the dielectric function $\tilde{\epsilon}$ of Eq. (4.51) is written in terms of the longitudinal and transverse modes (LO and TO), Eq. (4.51) is reduced to a factorized form of its poles and zeros given by [99]

$$\tilde{\epsilon}(\omega) = \epsilon^\infty \prod_{j=1}^N \frac{\Omega_{\text{LO}_j}^2 - \omega^2 - i\omega\Gamma_{\text{LO}_j}}{\Omega_{\text{TO}_j}^2 - \omega^2 - i\omega\Gamma_{\text{TO}_j}}, \quad (4.52)$$

where ϵ^∞ is the high frequency dielectric constant, Ω_{TO_j} (Ω_{LO_j}) and Γ_{TO_j} (Γ_{LO_j}) are the resonant frequency and the damping constant of the j -th TO (LO) mode, respectively. By substituting zero for the angular frequency ω of Eq. (4.52) [100], the zero frequency dielectric constant is obtained as

$$\tilde{\epsilon}(0) = \epsilon^\infty \prod_{j=1}^N \frac{\Omega_{\text{LO}_j}^2}{\Omega_{\text{TO}_j}^2}, \quad (4.53)$$

which is the Lyddane-Sachs-Teller (LST) relation [101]. When we assume zero damping in Eq. (4.52), the Kurosawa formula [102] is obtained as

$$\tilde{\epsilon}(\omega) = \epsilon^\infty \prod_{j=1}^N \frac{\Omega_{\text{LO}_j}^2 - \omega^2}{\Omega_{\text{TO}_j}^2 - \omega^2}. \quad (4.54)$$

So, the phonon-polariton dispersion is obtained using either Eq. (4.52) or Eq. (4.54) given by

$$\frac{c^2 \tilde{k}^2(\omega)}{\omega^2} = \tilde{n}^2(\omega) = \tilde{\epsilon}(\omega), \quad (4.55)$$

where \tilde{n} is the complex index of refraction defined in Eq. (4.24) and $\tilde{k}(\omega)$ is the complex wave vector.

However, since the measured range of frequency is limited to 2 THz, Eq. (4.55) needs correction [84]. When we apply the parameter ϵ_{exp} defined by

$$\epsilon_{\text{exp}} = \epsilon^\infty \prod_{j=2}^N \frac{\Omega_{\text{LO}_j}^2}{\Omega_{\text{TO}_j}^2} \quad (4.56)$$

to the measured data, the modified phonon-polariton dispersion for a single mode is given by

$$\tilde{k}(\omega) = \frac{\omega}{c} \left[\epsilon_{\text{exp}} \frac{\Omega_{\text{LO}_1}^2 - \omega^2 - i\omega\Gamma_{\text{LO}_1}}{\Omega_{\text{TO}_1}^2 - \omega^2 - i\omega\Gamma_{\text{TO}_1}} \right]^{1/2}. \quad (4.57)$$

The fitting parameter ϵ_{exp} is a dielectric constant measured at the highest frequency throughout a frequency range from 0.2 to 2 THz.

Figure 4.13 shows the phonon-polariton dispersion curve [ω vs. $k(\omega)$] (closed circles) retrieved from

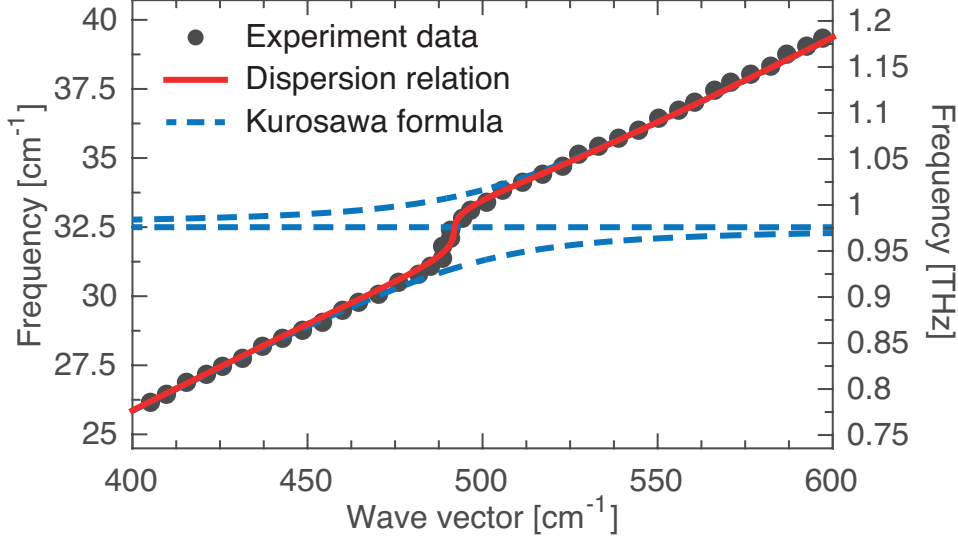


Figure 4.13: (Color online) The Phonon-polariton dispersion of the experimental results of \perp -cut seraphinite measured at an azimuthal angle of 120° . The dispersion relation and the experimental data are indicated with a red solid line and closed circles, respectively. The dispersion relation and the measured data are plotted with respect to the real parts of Eq. (4.57) and Eq. (4.59), respectively. The Kurosawa formula is represented with a blue dotted line, which is also computed using the real part of Eq. (4.57) in the case of no damping.

the measurement of the \perp -cut sample at $\theta = 120^\circ$. The real part of $\tilde{k}(\omega)$ is⁷

$$\text{Re}[\tilde{k}(\omega)] = \frac{\omega}{c} \sqrt{n^2(\omega) + \kappa^2(\omega)}, \quad (4.59)$$

which is shown in comparison with the theoretical guide (red solid line) calculated from the real part of Eq. (4.57). The Kurosawa formula (blue dotted line) is also computed using the real part of Eq. (4.57) in the case of no damping. It is noted that $(\varepsilon_{\text{exp}})^{1/2}$ can be extracted by $\sqrt{n^2(\omega) + \kappa^2(\omega)}|_{\omega \rightarrow \omega^\infty}$ in Eq. (4.59), where ω^∞ represents the highest frequency component. In the unit of cm^{-1} , the fitting parameters are estimated from the measurement as $\Omega_{\text{TO}_1} = 32.5 \text{ cm}^{-1}$, $\Omega_{\text{LO}_1} = 32.6 \text{ cm}^{-1}$, $\Gamma_{\text{TO}_1} = 2.74 \text{ cm}^{-1}$, $\Gamma_{\text{LO}_1} = 2.67 \text{ cm}^{-1}$, and $(\varepsilon_{\text{exp}})^{1/2} = 2.44$ for the \perp -cut seraphinite. The splitting ($0.1 \text{ cm}^{-1} = 3 \text{ GHz}$) is about three times smaller than the spectral resolution ($10 \text{ GHz} = 1/T$ and $T = 100 \text{ ps}$) in our THz-TDS. Thus, the Ω_{TO_1} and Ω_{LO_1} extracted through numerical fitting for the resonance at 0.96 THz should be understood as $\Omega_{\text{TO}_1} = 32.5 \pm 0.17 \text{ cm}^{-1}$, $\Omega_{\text{LO}_1} = 32.6 \pm 0.17 \text{ cm}^{-1}$. It is noted that Ω_{LO_1} is bigger than Ω_{TO_1} ($\Omega_{\text{LO}_j} > \Omega_{\text{TO}_j}$) since ε^∞ is in general smaller than $\varepsilon(0)$ by the LST relation for all the optical phonon modes [23, 101, 102]. Provided that $1/\omega$ is substituted by ξ , the factorized dielectric

7

$$\text{Re}[\tilde{k}(\omega)] \equiv k(\omega) = \frac{\omega}{c} \text{Re}[\sqrt{\tilde{\varepsilon}(\omega)}] = \frac{\omega}{c} \sqrt{n^2(\omega) + \kappa^2(\omega)}. \quad (4.58)$$

function of Eq. (4.52) can be expanded for $\xi \rightarrow 0$ in the form [99]⁸

$$\begin{aligned} \tilde{\varepsilon}(\omega) \simeq \varepsilon^\infty \prod_{j=1}^N \left[1 + i\Gamma_{\text{LO}_j} \xi + O(\xi^2) \right] \\ \times \left[1 - i\Gamma_{\text{TO}_j} \xi + O(\xi^2) \right] \Big|_{\xi \rightarrow 0}. \end{aligned} \quad (4.62)$$

By further calculation, Eq. (4.62) is equivalent to⁹

$$\tilde{\varepsilon}(\omega) \simeq \varepsilon^\infty \left[1 + i \sum_{j=1}^N (\Gamma_{\text{LO}_j} - \Gamma_{\text{TO}_j}) \xi \right]_{\xi \rightarrow 0}, \quad (4.64)$$

which is the generalized form of Lowndes condition for all IR-active branches induced by Schubert [99, 103]. Equation (4.64) for $\text{Im}[\tilde{\varepsilon}(\omega)] > 0$ shows that there are the optical phonons with conditions for $\Gamma_{\text{LO}} < \Gamma_{\text{TO}}$ as well as $\Gamma_{\text{LO}} > \Gamma_{\text{TO}}$ satisfying $\sum_{j=1}^N (\Gamma_{\text{LO}_j} - \Gamma_{\text{TO}_j}) \xi > 0$ [99]. The resonance mode at 0.96 THz of \perp -cut is expected as one of the optical modes when $\Gamma_{\text{LO}} < \Gamma_{\text{TO}}$. Therefore, the above theoretical interpretation based on Kurosawa's formula with and without the damping terms shows an excellent agreement with the observed dispersion anisotropy in the THz frequency range.

4.2.5 Conclusion

In summary, we have reported a spectral fingerprint of crystalline seraphinite, a type of gemstone, in the THz frequency range. In our measurements conducted with THz-TDS, the strong IR-active modes at 0.80, 0.96 and 1.20 THz in seraphinite have been founded in seraphinite. In particular, the 0.96 THz mode has exhibited a strong and narrow ($Q=8$) absorption, comparable to that of the previously reported 0.53 THz mode in the α -lactose monohydrate. The polarization-dependent THz-TDS measurements have furthermore revealed the birefringence of the investigated crystal which originated from its crystalline

⁸By replacing $1/\omega$ with ξ , the factorized dielectric function of Eq. (4.52) becomes

$$\begin{aligned} \tilde{\varepsilon}(\omega) &= \varepsilon^\infty \prod_{j=1}^N \frac{\Omega_{\text{LO}_j}^2 - \omega^2 - i\omega\Gamma_{\text{LO}_j}}{\Omega_{\text{TO}_j}^2 - \omega^2 - i\omega\Gamma_{\text{TO}_j}} = \varepsilon^\infty \prod_{j=1}^N \frac{\frac{\Omega_{\text{LO}_j}^2}{\omega^2} - 1 - i\frac{\Gamma_{\text{LO}_j}}{\omega}}{\frac{\Omega_{\text{TO}_j}^2}{\omega^2} - 1 - i\frac{\Gamma_{\text{TO}_j}}{\omega}} \\ &= \varepsilon^\infty \prod_{j=1}^N \frac{\Omega_{\text{LO}_j}^2 \xi^2 - 1 - i\Gamma_{\text{LO}_j} \xi}{\Omega_{\text{TO}_j}^2 \xi^2 - 1 - i\Gamma_{\text{TO}_j} \xi} = \varepsilon^\infty \prod_{j=1}^N \frac{1 - \Omega_{\text{LO}_j}^2 \xi^2 + i\Gamma_{\text{LO}_j} \xi}{1 - \Omega_{\text{TO}_j}^2 \xi^2 + i\Gamma_{\text{TO}_j} \xi}. \end{aligned} \quad (4.60)$$

When $\omega \rightarrow \infty$, *i.e.*, $\xi \rightarrow 0$, this equation can be evaluated as

$$\begin{aligned} \tilde{\varepsilon}(\omega) &= \varepsilon^\infty \prod_{j=1}^N \left[1 - \Omega_{\text{LO}_j}^2 \xi^2 + i\Gamma_{\text{LO}_j} \xi \right] \left[1 - \Omega_{\text{TO}_j}^2 \xi^2 + i\Gamma_{\text{TO}_j} \xi \right]^{-1} \\ &\simeq \varepsilon^\infty \prod_{j=1}^N \left[1 + i\Gamma_{\text{LO}_j} \xi - \Omega_{\text{LO}_j}^2 \xi^2 \right] \left[1 - i\Gamma_{\text{TO}_j} \xi + \Omega_{\text{TO}_j}^2 \xi^2 \right], \end{aligned} \quad (4.61)$$

which leads to Eq. (4.62).

⁹The higher order terms than ξ^2 can be neglected since the higher terms than ξ^2 are too small. The dielectric function of Eq. (4.62) can then be reduced as

$$\begin{aligned} \tilde{\varepsilon}(\omega) &= \varepsilon^\infty \left[1 + i(\Gamma_{\text{LO}_1} - \Gamma_{\text{TO}_1}) \xi \right] \left[1 + i(\Gamma_{\text{LO}_2} - \Gamma_{\text{TO}_2}) \xi \right] \times \cdots \\ &= \varepsilon^\infty \left[1 + i(\Gamma_{\text{LO}_1} - \Gamma_{\text{TO}_1}) \xi + i(\Gamma_{\text{LO}_2} - \Gamma_{\text{TO}_2}) \xi + i^2 O(\xi^2) \right] \times \cdots \\ &= \varepsilon^\infty \left[1 + i(\Gamma_{\text{LO}_1} - \Gamma_{\text{TO}_1}) \xi + i(\Gamma_{\text{LO}_2} - \Gamma_{\text{TO}_2}) \xi + i(\Gamma_{\text{LO}_3} - \Gamma_{\text{TO}_3}) \xi + \cdots \right], \end{aligned} \quad (4.63)$$

which leads to Eq. (4.64).

monoclinic structure with the space group C2/m, $A_u(z')$ -symmetry of the 0.80 and 1.20 THz modes and the $B_u(x', y')$ -symmetry of the 0.96 THz mode. Theoretical interpretation based on Kurosawa's formula has shown an excellent agreement with the observed phonon-polariton dispersion anisotropy.

THz absorption lines in solid-state materials are rare. There have been no known spectral lines for gemstones in the THz frequency range. Gems are often optically superior materials and thus optical gemology that utilizes visible, near-infrared, UV, and even X-rays light sources, has been established to study and characterize gems. However, to the best of our knowledge, THz waves have never been used so far for that purpose. It is hoped that THz spectroscopy may become useful for identification and characterization of various gemstones.

4.2.6 Appendix

4.2.6.1 The 3rd-order polarization

Since the monoclinic crystal in the space group of C2/m is a centrosymmetric material, the higher term that follows the linear susceptibility is $\chi^{(3)}$. The third-order polarization for broadband waves is represented by [7]

$$\tilde{P}_i^{(3)}(\omega) = \epsilon_0 \int_{-\infty}^{\infty} d\omega_q \int_{-\infty}^{\infty} d\omega_n \sum_{jkl} \sum_{nq} \tilde{\chi}_{ijkl}^{(3)}(\omega) E_j(\omega_q) E_k(\omega_n) E_l(\omega - \omega_q - \omega_n), \quad (4.65)$$

where $\tilde{\chi}_{ijkl}^{(3)}(\omega) = \tilde{\chi}_{ijkl}^{(3)}(\omega; \omega_q, \omega_n, \omega_m)$ is the third-order susceptibility. Provided that the incident wave is a monochromatic wave with a single frequency ω for sake of simplicity, the i -th component of a possible nonlinear polarization can be expressed in the form [7]

$$\tilde{P}_i(\omega) = 3\epsilon_0 \sum_{jkl} \tilde{\chi}_{ijkl}^{(3)}(\omega) E_j(\omega) E_k(-\omega) E_l(\omega), \quad (4.66)$$

where $\tilde{\chi}_{ijkl}^{(3)}(\omega) = \tilde{\chi}_{ijkl}^{(3)}(\omega; \omega, -\omega, \omega)$ is one of four-wave-mixing processes. The third-order susceptibility $\tilde{\chi}_{ijkl}^{(3)}$ for space group of C2/m can be expressed as a reduced form with $\tilde{\chi}_{im}^{(3)}$ defined by [104]

$$\tilde{\chi}^{(3)} = \begin{bmatrix} \tilde{\chi}_{11} & 0 & \tilde{\chi}_{13} & 0 & \tilde{\chi}_{15} & \tilde{\chi}_{16} & \tilde{\chi}_{17} & \tilde{\chi}_{18} & 0 & 0 \\ 0 & \tilde{\chi}_{22} & 0 & \tilde{\chi}_{24} & 0 & 0 & 0 & 0 & \tilde{\chi}_{29} & \tilde{\chi}_{20} \\ \tilde{\chi}_{31} & 0 & \tilde{\chi}_{33} & 0 & \tilde{\chi}_{35} & \tilde{\chi}_{36} & \tilde{\chi}_{37} & \tilde{\chi}_{38} & 0 & 0 \end{bmatrix}. \quad (4.67)$$

The subscripts m corresponds to the three Cartesian components listed in Table 4.5 [104]. If the third-order susceptibility is given by $\chi_{im}^{(3)}$, the applied electric field components in Eq. (4.66) are written as [104]

jkl	xxx	yyy	zzz	yzz	yyz	xzz	xxz	xyy	xyx	xyz
m	1	2	3	4	5	6	7	8	9	0

Table 4.5: Cartesian components corresponding to subscript m [104].

$$\left(\begin{array}{c} F_{xxx} \\ F_{yyy} \\ F_{zzz} \\ F_{yzz} + F_{zyz} + F_{zzy} \\ F_{yyz} + F_{yzy} + F_{zyy} \\ F_{xzz} + F_{zxx} + F_{zzx} \\ F_{xxz} + F_{xzx} + F_{zxx} \\ F_{xyy} + F_{yxy} + F_{yyx} \\ F_{xxy} + F_{xyx} + F_{yxx} \\ F_{xyz} + F_{xzy} + F_{yxz} + F_{yzx} + F_{zxy} + F_{zyx} \end{array} \right), \quad (4.68)$$

where F_{jkl} represents $F_m = E_j(\omega)E_k(-\omega)E_l(\omega)$.

By using Eqs. (4.67) and (4.68), the third-order polarization of Eq. (4.66) becomes

$$\tilde{P}_i(\omega) = 3\epsilon_0 \sum_m \tilde{\chi}_{im}^{(3)}(\omega) F_m. \quad (4.69)$$

By the same analogy described in section 4.2.3.5, the i -th polarization component in the principal coordinates can be obtained by simply substituting m in Eq. (4.69) for $j, k, l \in \{x', y', z'\}$, where the electric field components in F_m are given by Eq. (4.41). The imaginary part of $\chi_{ijkl}^{(3)}$ in the principal coordinates is a function of θ_j and ϕ_j due to inclination to the z' -axis given by

$$\chi_{ijkl}^{(3)} = \sum_{n \in \{A_u, B_u\}} L_n \Gamma_i^k \Gamma_j^k \Gamma_k^k \Gamma_l^k. \quad (4.70)$$

According to Eq. (4.44), we obtain the z -component of $\mathbf{P}_{xyz}^{(3)}$ denoted as $P_z^{(3)}$ given by

$$P_z^{(3)}/3\epsilon_0 = \sum_{j \in \{A_u, B_u\}} L_j \left[\sin^4 \theta_j \sin^4 \phi_j \sin^4 \theta + \cos^4 \theta_j \cos^4 \theta + 6 \cos^2 \theta_j \sin^2 \theta_j \sin^2 \phi_j \cos^2 \theta \sin^2 \theta \right], \quad (4.71)$$

where ϕ is zero for the sake of simplicity.

Chapter 5. THz spectroscopy of the polarization dependence of the resonant material confined in a sub-wavelength slit

We have used terahertz time-domain spectroscopy to probe the polarization dependence of α -lactose in the near-field vicinity of a sub-wavelength-scale metal slit. The experimental result shows that the 0.53-THz absorption of this material has an abnormal polarization dependence strongly coupled to the slit orientation. In particular, the waves polarized with a parallelly-oriented slit do not electrically interact with the material within a slit extremely narrow compared to the wavelength, which results in complete vanishing of the otherwise resonant absorption. This phenomenon can be understood in the context of Bethe's sub-wavelength diffraction: the far-field wave diffracted from a sub-wavelength-scale aperture originates from the magnetic near field and not from the electric near field; thus the measured E-field in the far-field has no origin from the near-field E-field component.

5.1 Introduction

Recent advances in science and technology involved with terahertz (THz = 10^{12} Hz) frequency waves have made a broad impact to a variety of research fields including physics, chemistry, material science, and electric engineering [2, 3]. Many applications with THz waves have been also developed in areas including material characterization, stand-off detection, noninvasive diagnostics, and biomedical sensing. Biomedical sensing applications are particularly promising because of the unique spectral nature of THz waves in bio-organic materials [1]. However, acquiring spectral information of biological materials requires micrometer-size spatial resolution which is not simple to achieve due the large wavelength of THz waves ($\lambda = 300 \mu\text{m}$ for 1 THz). To overcome the spatial resolution limited by Abbe's diffraction of the freely propagating large-wavelength waves, several methods have been considered: for example, near-field emission and/or detection [105–107], or sub-wavelength-size material platforms [108–111]. Many of these methods often use some form of metallic structures in sub-wavelength dimension to confine, focus, guide or bend the THz wave in the vicinity of the material which could strongly alter the wave properties of the interacting THz-wave in terms of polarization, spectral phase, and amplitude. So, a priori understanding of THz-wave interaction with these structures is required for applying THz spectroscopy to sub-wavelength-scale materials.

As it is well known, the wave diffraction through a sub-wavelength-size metal hole, for example, is completely different from a case of with a large hole mainly because of the interplay between the cavity field and edge currents of the aperture [112–115]. At the limit of extreme sub-wavelength-sized aperture transmission, the diffracted electric field results from effective magnetic dipole radiation [116, 117]. Other examples of sub-wavelength optical phenomena manifesting the vectorial nature of electromagnetic wave around metal structures include extraordinary light transmission [118, 119], strong electric field enhancement [120, 121], diffraction phase shift [122] and anomalous Young's double slit experiment [123], all of which are found in the diffraction from a slit or a slit system with sub-wavelength dimensions.

In this paper, we report THz polarization spectroscopy of an organic material kept in a sub-wavelength-size metal slit. Using α -lactose monohydrate which has strong absorption line at 0.53 THz [88, 124], we investigated the temporal and spectral amplitude changes of the transmitted THz wave within a slit with respect to the slit width. Experimental results reveal that the spectral response

of the material is strongly coupled with the polarization state of the THz wave and that the material does not interact with the THz wave when an extreme sub-wavelength-sized slit is used.

5.2 Experimental description

The experiment was performed using conventional THz time-domain spectroscopy (THz-TDS) [31] as shown in Fig. 5.1(a). THz pulses were produced from a commercial photo-conductive antenna (BATOP optoelectronics) pumped by femtosecond near-infrared pulses from a Ti:sapphire mode-locked laser oscillator. Measurements were made by laser-gated electro-optical sampling with a 2-mm-thick (110) ZnTe crystal [21]. The temporal amplitude profile of the THz pulse was recorded to compute the THz spectrum [31, 122, 123]. The fabricated slit was placed at the focus of the propagating THz waves in a one-dimensional $4-f$ geometry THz beam delivery system comprised of two teflon lenses whose focal lengths were $f = 100$ mm.

The sub-wavelength slit with a wedge shape shown in Fig. 5.1(b) was manufactured at the National Nanofab Center (Korea) to conduct systematic experiments by mechanical actuators with travel length of 25 mm without a change of a sample. Figure 5.1(b) shows a schematic structure of the fabricated wedge-shaped slits. A 500 nm copper film was deposited on a 525 μm thick silicon wafer of high resistivity (20,000 $\Omega\cdot\text{cm}$). Each slit is comprised of 20 mm length with a wedge top of 6 μm length and a wedge bottom of 60 μm length. To put α -lactose (Sigma Aldrich) into the slit, a compound of α -lactose dissolved in the ionized water was prepared. Candle wax, a kind of hydrophobic material, was used to confine the compound into an area of 24 mm \times 21 mm. Ionized water was evaporated for 12 hours to completely eliminate the water content. By this method, we could obtain a reference slit and a sample

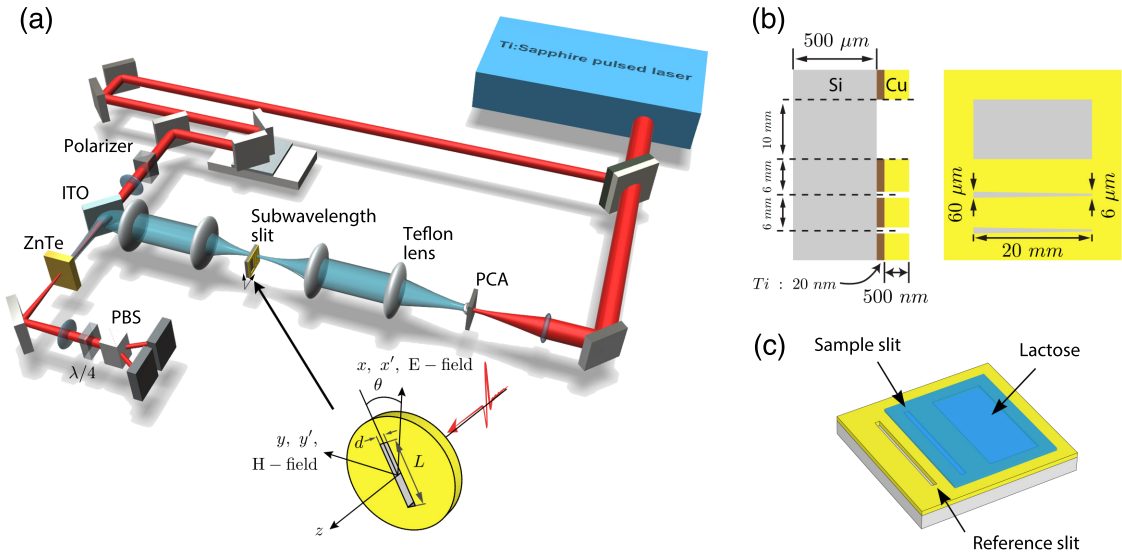


Figure 5.1: (a) Schematic experimental setup. The sub-wavelength-scale slits were located at the focus of the THz wave. Inset shows the polarization angle defined with respect to the slit direction. The wedge-shaped slits are consists of identical single slits with a width of d and a length of L . The polarization of the electric field and magnetic field are parallel to the slit direction for $\theta = 0$ and $\theta = \pi/2$, respectively, where the slit direction is along the slit length of L . (b) The geometry of the fabricated wedge-shaped pair of slits in the side and front views. The slits are fabricated in copper film deposited on a silicon substrate. (c) A reference slit and a sample slit obtained by using a compound of α -lactose and water. A rectangular hole with 10 mm \times 20 mm was used to estimate the thickness of spread lactose.

slit as depicted in Fig. 5.1(c). A rectangular hole with 10 mm \times 20 mm in Fig. 5.1(c) was used to estimate the thickness (d_s) of lactose on the slit. The estimated thickness d_s is about 200 μm which was obtained by $d_s = c\Delta t/(n_s - n_{\text{air}})$, where c is the speed of light, Δt is the delayed time between the maximums of the reference and sample signals in the time-domain, n_s is the refractive index of lactose and n_{air} is the refractive index of air [125].

From recent research [120–123], it is found that the source of the diffracted electric field through a sub-wavelength sized slit is related to the slit direction defined by the orientation (\mathbf{L}) of the slit's length L as shown in Fig. 5.1(a), which is described in detail section 5.3. With the same analogy, we carried out experiments with slits in both orthogonal ($\theta = \pi/2$, $\mathbf{E} \perp \mathbf{L}$) and parallel ($\theta = 0$, $\mathbf{E} \parallel \mathbf{L}$) directions of the slits with respect to the THz polarization (\mathbf{E}). All the experiments was purged with dry air to remove water vapor in the THz frequency range [126].

5.3 Theoretical background

5.3.1 Boundary conditions by Bethe

Let us assume that a linearly polarized electromagnetic wave with a wavelength of λ for $z < 0$ propagates along the z -direction toward a metallic slit with a width of d and a length of L located at $z = 0$. Then the diffracted field through the slit can be explained by Kirchhoff's diffraction theory providing that the width d of the slit is large enough compared with the wavelength λ ($d \gg \lambda$) [12, 27].

We consider a metallic sub-wavelength slit with a width of d and a length of L assuming that d is sufficiently small compared to L and λ ($d \ll L, \lambda$). Although the Kirchhoff's theory fails in the sub-wavelength region, we can extrapolate the behavior of the diffracted electric field (E field) corresponding to the slit direction according to the waveguide theory [12, 116, 122, 123]. The waveguide theory predicts that the E field perpendicular to the slit direction for $\theta = \pi/2$ can propagate into the slit because the cutoff frequency is proportional to $1/L$. However, the electric field parallel to the slit direction for $\theta = 0$ is difficult to propagate by the same analogy [12].¹ In contrast to the E field, the magnetic field (H field) perpendicular or parallel to the slit direction is always considered as constant over the slit due to the boundary condition [116, 122, 123], which is described in detail below.

Corresponding to the electromagnetic wave theory [12, 13], the boundary conditions between two

¹Let us assume that a linearly polarized electromagnetic wave with a wavelength of λ for $z < 0$ propagates along the z -direction through a metallic slit with a width of d and a length of L ($d \ll L$) located at $z = 0$. According to the electromagnetic theory [12] (in p. 361), TE modes in a rectangular waveguide with inner dimensions L and d are then induced by the z component of the H field given by

$$H_z(x, y) = H_0 \cos\left(\frac{m\pi x}{L}\right) \cos\left(\frac{n\pi y}{d}\right), \quad (5.1)$$

which leads to E fields in the direction of x and y given by [12, 13] (Jackson pp. 360-362, Griffiths pp. 366-367)

$$E_x = \frac{i\omega\mu}{\gamma^2} \frac{\partial}{\partial y} H_z, \quad E_y = -\frac{i\omega\mu}{\gamma^2} \frac{\partial}{\partial x} H_z \quad (5.2)$$

with

$$\gamma^2 = \mu\epsilon\omega^2 - k^2. \quad (5.3)$$

By the boundary condition, the cutoff frequency ω_{mn} is then obtained, giving [12, 13] (same pages)

$$\omega_{mn} = \frac{\gamma_{mn}}{\sqrt{\mu\epsilon}} = \frac{\pi}{\sqrt{\mu\epsilon}} \sqrt{\frac{m^2}{L^2} + \frac{n^2}{d^2}}. \quad (5.4)$$

The lowest cutoff frequency that occurs at $(m, n) = (1, 0)$ becomes

$$\omega_{10} = \frac{\pi}{\sqrt{\mu\epsilon}} \frac{1}{L}, \quad (d \ll L), \quad (5.5)$$

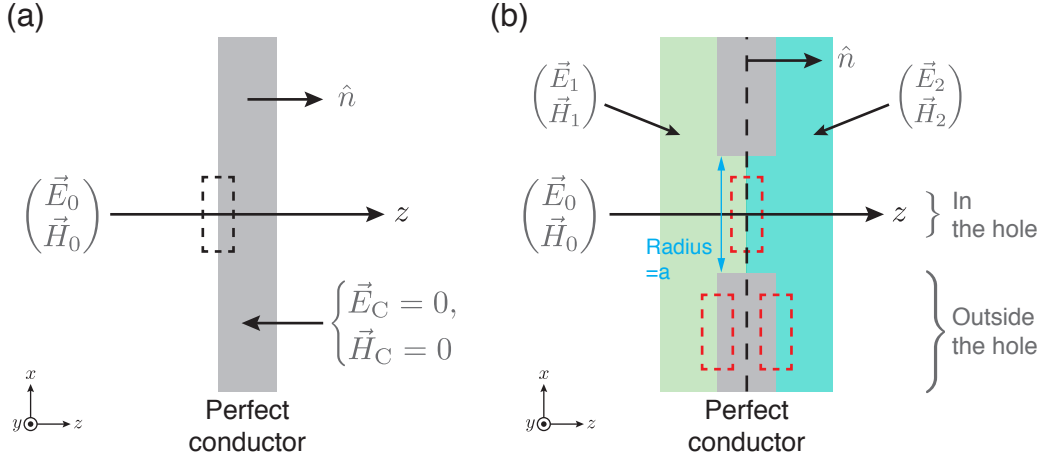


Figure 5.2: (a), (b) Red dotted rectangular boxes represent the boundary section for the boundary condition. Tangential and normal components are in the direction of x and z , respectively.

different media are obtained in terms of their normal and tangential components given by

$$\text{Tangential components (t):} \quad \hat{n} \times (\mathbf{E}_2 - \mathbf{E}_1) = 0, \quad \hat{n} \times (\mathbf{H}_2 - \mathbf{H}_1) = \mathbf{K}, \quad (5.7)$$

$$\text{Normal components (n):} \quad \hat{n} \cdot (\mathbf{D}_2 - \mathbf{D}_1) = \sigma, \quad \hat{n} \cdot (\mathbf{B}_2 - \mathbf{B}_1) = 0, \quad (5.8)$$

where σ , \mathbf{K} , \hat{n} are the surface charge density, the surface current and a normal unit vector pointing from medium 1 to medium 2, respectively.

Let \mathbf{H}_0 and \mathbf{E}_0 be the initial H field and E field for $z < 0$ on the left-hand side of the perfect conductor screen at $z = 0$ if there is no hole as shown in Fig. 5.2(a). Provided \mathbf{E}_C and \mathbf{H}_C denote the E field and H field in the conductor, there are no E field and H field in the perfect conductor, which leads to the boundary conditions between the conductor and free space as

$$\hat{n} \times (\mathbf{E}_C - \mathbf{E}_0) = 0, \quad (5.9a)$$

$$(\mathbf{H}_C - \mathbf{H}_0) \cdot \hat{n} = 0, \quad (5.9b)$$

so that

$$\mathbf{E}_{0t} = 0, \quad H_{0n} = 0. \quad (5.10)$$

We therefore obtain the initial electromagnetic field \mathbf{H}_0 and \mathbf{E}_0 fields which can be reduced as only having tangential and normal components, respectively, with respect to the plane of incidence given by

$$\mathbf{E}_0 = \mathbf{E}_{0n}, \quad \mathbf{H}_0 = \mathbf{H}_{0t}. \quad (5.11)$$

which leads to the conclusion that there is only an E field polarized in the y direction (E_y in Eq. (5.2)) since $H_z = H_0 \cos(\pi x/L)$ gives rise to $\partial H_z / \partial y = 0$. In other words, the incident E field perpendicular to the slit orientation can well propagate through the slit due to the lowest cutoff frequency. Note that the lowest cutoff frequency in free space for $d \ll L$ is expressed as

$$\omega_{10} = \frac{\pi}{\sqrt{\mu_0 \epsilon_0}} \frac{1}{L} = \pi \frac{c}{L} \propto \frac{c}{L}. \quad (5.6)$$

However, since $H_z = H_0 \cos(\pi y/d)$ for $(m, n) = (0, 1)$ leads $\partial H_z / \partial x = 0$, there is only E field polarized in the x direction (E_x in Eq. (5.2)), which implies that the E field parallel to the slit orientation is difficult to propagate through the slit due to the cutoff frequency $\omega_{01} = \pi/(d\sqrt{\mu\epsilon})$ that is much higher than ω_{10} .

5.3.1.1 Bethe's zero-order approximation

As described in the earlier section, the E and H fields for $z > 0$ become zero if there is no hole in the screen², where the field for $z > 0$ in this case is called as “the zero-order field,” or “the zero approximation” or “the zero-order approximation” by other researchers [116,117]. We therefore see that the zero-order approximation satisfies the boundary conditions everywhere on the screen ($z = 0$) [116].

Let us now assume that there is a small hole with radius of a on the screen as described in Fig. 5.2(b). Note that the radius of a that is sufficiently small compared to λ of the incident field and the thickness of the screen is sufficiently thick compared to the skin-depth of the incident field.³ Since the hole is very small compared to λ of the incident field, the zero-order approximation can be considered as trial solutions of the E and H fields for $z > 0$. By Eqs. (5.7) and (5.8), we find that boundary conditions in the hole are given by

$$H_t \Big|_{\text{left-side of the screen}} = H_t \Big|_{\text{right-side of the screen}}, \quad (5.12)$$

$$E_n \Big|_{\text{left-side of the screen}} = E_n \Big|_{\text{right-side of the screen}}. \quad (5.13)$$

It should be noted that the field components on the right-side of the screen have to vanish according to the zero-order approximation, in which leads to inconsistent results such that the field components on the left-side of the screen in Eqs. (5.12) and (5.13) become zero. In other words, there are non-zero fields at $z < 0$ and zero fields at $z > 0$; this gives us discontinuous boundary conditions at $z = 0$ [116].

5.3.1.2 Bethe's first-order approximation

In order to eliminate the discontinuity in the hole that occurs from the zero-order approximation, Bethe added the scattered field ($\mathbf{E}_1, \mathbf{H}_1$) on the left-hand side of the screen and the diffracted field ($\mathbf{E}_2, \mathbf{H}_2$) on the right-hand side of the screen [116,117]. If we treat ($\mathbf{E}_1, \mathbf{H}_1$) as the scattered field propagating in the $-z$ direction and ($\mathbf{E}_2, \mathbf{H}_2$) as the diffracted field propagating in the $+z$ direction both of which are originating from the origin $z = 0$ for the sake of understanding [117], we can imagine that $\mathbf{H}_1, \mathbf{E}_1$ and $\mathbf{H}_2, \mathbf{E}_2$ are induced from the left-hand side and the right-hand side of the screen, respectively, as described in Fig. 5.3. This assumption by Bethe's intuition is called as “Bethe's first-order approximation” [117]. So, the actual field can be then expressed as

$$\mathbf{H} = \begin{cases} \mathbf{H}_0 + \mathbf{H}_1 & \text{for } z < 0, \\ \mathbf{H}_2 & \text{for } z > 0, \end{cases} \quad \mathbf{E} = \begin{cases} \mathbf{E}_0 + \mathbf{E}_1 & \text{for } z < 0, \\ \mathbf{E}_2 & \text{for } z > 0. \end{cases} \quad (5.14)$$

From Eq. (5.7), the boundary condition in the hole becomes

$$\hat{n} \times [\mathbf{E}_2 - (\mathbf{E}_0 + \mathbf{E}_1)] = 0, \quad (5.15)$$

which leads to

$$E_{2t} = \cancel{E_{0t}}^0 + E_{1t}, \quad (5.16)$$

so that

$$E_{2t} = E_{1t} \text{ (in the hole, at } z = 0\text{)}. \quad (5.17)$$

²The electromagnetic field through the screen becomes zero because of the skin depth.

³See Griffiths pp. 347-348 [13].

At $z = 0$ outside the hole, we also find from Eq. (5.7) that

$$\begin{aligned} \hat{n} \times [\mathbf{E}_C^0 - (\mathbf{E}_0 + \mathbf{E}_1)] &= 0 \\ &= \hat{n} \times (\mathbf{E}_2 - \mathbf{E}_C^0), \end{aligned} \quad (5.18)$$

which implies that

$$E_{2t} = E_{0t}^0 + E_{1t}, \quad E_{2n} = 0, \quad (5.19)$$

so that

$$E_{2t} = E_{1t} = 0 \quad (\text{outside the hole, at } z = 0). \quad (5.20)$$

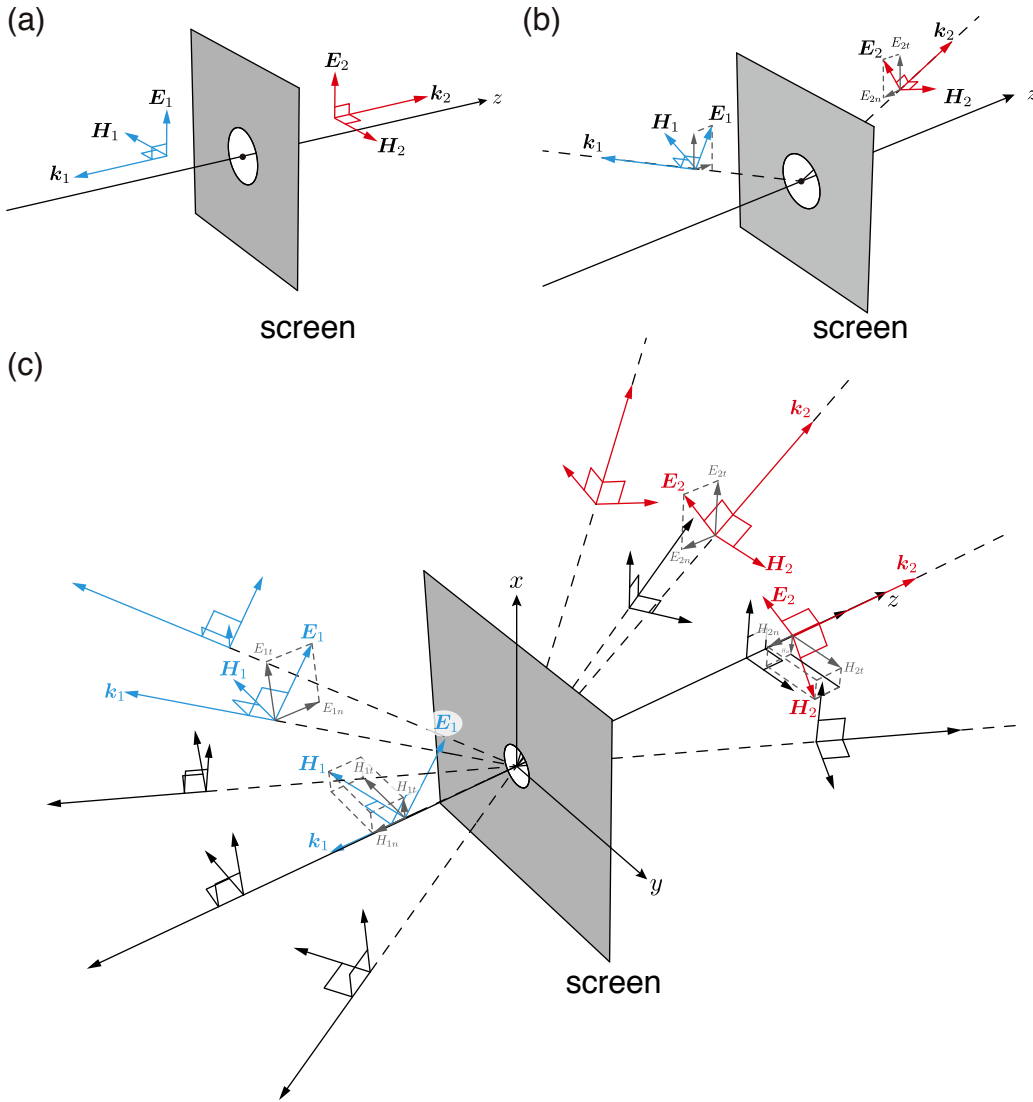


Figure 5.3: Schematic representations for the scattered field (\mathbf{E}_1 , \mathbf{H}_1) and the diffracted field (\mathbf{E}_2 , \mathbf{H}_2) propagating in (a) the normal direction, (b) the inclined direction and (c) the overall direction (upper half-plane) from the origin $z = 0$.

We then find from Eqs. (5.17) and (5.20) that the tangential components of E fields for the trial solution for $\forall z > 0, \forall x$ and y can be written as [116]

$$E_{1x}(x, y, -z) = E_{2x}(x, y, z) \quad (5.21)$$

noting that this equation is even in z and satisfied correspondingly for the y component.

In a similar fashion, the boundary conditions for the normal components in the hole as well as at $z = 0$ outside the hole are obtained as follows: In the hole, we see by Eq. (5.8) that

$$\hat{n} \cdot [\mathbf{B}_2 - (\mathbf{B}_0 + \mathbf{B}_1)] = 0, \quad (5.22)$$

which implies that

$$H_{2n} = \cancel{H_{0n}}^0 + H_{1n} = H_{1n} \text{ (in the hole, at } z = 0), \quad (5.23)$$

where $B_j = \mu_j H_j$ and the relation $\mu_1 = \mu_2 = \mu_0$ in the hole is used.⁴ Furthermore, at $z = 0$ outside the hole, we find by Eq. (5.8) that

$$\begin{aligned} \hat{n} \cdot [\cancel{\mathbf{B}_C}^0 - (\mathbf{B}_0 + \mathbf{B}_1)] &= 0, \\ &= \hat{n} \cdot (\mathbf{B}_2 - \cancel{\mathbf{B}_C}^0) \end{aligned} \quad (5.24)$$

which becomes

$$B_{2n} = \cancel{B_{0n}}^0 + B_{1n}, \quad B_{2n} = 0, \quad (5.25)$$

so that

$$H_{2n} = H_{1n} = 0 \text{ (outside the hole, at } z = 0), \quad (5.26)$$

where $B_j = \mu_j H_j$ with $\mu_1 = \mu_2 = \mu_0$. By analogy with Eq. (5.21), we find by Eqs. (5.23) and (5.26) that the normal components of the H fields for the trial solution for $\forall z > 0$, and $\forall x$ and y can be written in the form [116]

$$H_{1z}(x, y, -z) = H_{2z}(x, y, z). \quad (5.27)$$

Since we treat $(\mathbf{E}_1, \mathbf{H}_1)$ as the scattered field propagating in the $-z$ direction and $(\mathbf{E}_2, \mathbf{H}_2)$ as the diffracted field propagating in the $+z$ direction with respect to the origin $z = 0$, the trial solution Eq. (5.21) will make⁵ [116]

$$H_{1x}(x, y, -z) = -H_{2x}(x, y, z) \text{ for } \forall z > 0, \text{ and } \forall x, y \quad (5.28)$$

and Eq. (5.27) will further make [116]

$$E_{1z}(x, y, -z) = -E_{2z}(x, y, z) \text{ for } \forall z > 0, \text{ and } \forall x, y, \quad (5.29)$$

where these results is easily seen if \mathbf{E}_1 and \mathbf{E}_2 are symmetrical and \mathbf{H}_1 and \mathbf{H}_2 are anti-symmetrical with respect to the xy plane perpendicular to the z axis [117].

⁴ $\mu = \mu_0$ means that the material is a non-magnetic material.

⁵If we treat $(\mathbf{E}_1, \mathbf{H}_1)$ as the scattered field propagating toward the $-z$ direction and $(\mathbf{E}_2, \mathbf{H}_2)$ as the diffracted field propagating toward the $+z$ direction from the origin ($z = 0$) for the sake of understanding, we can see by the boundary condition of in Griffiths [13] pp. 343-344 (or Griffiths 3rd edition p. 389) that the scattered and the diffracted E fields are in phase as described in Fig. 5.3.

According to Bethe's first-order approximation [116], all the boundary conditions for \mathbf{E}_1 and \mathbf{H}_1 are satisfied if \mathbf{E}_2 satisfies the boundary condition Eq. (5.20) and if we put the trial solutions with relations in Eqs. (5.21), (5.27), (5.28), and (5.29) for $z > 0$. Note that $(\mathbf{E}_1, \mathbf{H}_1)$ and $(\mathbf{E}_2, \mathbf{H}_2)$ are utilized to eliminate the discontinuity in the boundary conditions occurring at the edge of the hole [116, 117]. Since the boundary conditions should be continuous in the hole (*i.e.* at $z = 0$), we need to consider the boundary conditions for the tangential components of the H fields and the normal components of the E fields in the hole. By comparing the tangential components of H fields in the hole, we get

$$\hat{n} \times [\mathbf{H}_2 - (\mathbf{H}_0 + \mathbf{H}_1)] = \mathbf{K}, \quad (5.30)$$

which leads to

$$H_{2t} = H_{0t} + H_{1t} \text{ (in the hole, at } z = 0\text{)}. \quad (5.31)$$

By comparing the normal components of E fields in the hole, we also find that

$$\hat{n} \cdot [\mathbf{D}_2 - (\mathbf{D}_0 + \mathbf{D}_1)] = \sigma, \quad (5.32)$$

which becomes

$$E_{2n} = E_{0n} + E_{1n} \text{ (in the hole, at } z = 0\text{)}, \quad (5.33)$$

where $D_j = \epsilon_j E_j$ and the relation $\epsilon_1 = \epsilon_2 = \epsilon_0$ is used.

We therefore find by substituting Eq. (5.28) into Eq. (5.31) that⁶ [116]

$$H_{2t} = H_{0t} + H_{1t} = H_{0t} - H_{2t}, \quad (5.34)$$

which implies that

$$H_{2t} = \frac{1}{2} H_{0t}. \quad (5.35)$$

We also find by substituting Eq. (5.29) into Eq. (5.33) that [116]

$$E_{2n} = E_{0n} + E_{1n} = E_{0n} - E_{2n}, \quad (5.36)$$

so that

$$E_{2n} = \frac{1}{2} E_{0n}. \quad (5.37)$$

Since Eqs. (5.35) and (5.37) are regardless of the shape and size of the hole, so we can apply this condition to the case of a single slit as well as a hole. For this reason, the constant H field is regardless of the slit direction when the incident field is a transverse field [116, 122, 123]. It is noted that H_0 and E_0 are considered as constants over the hole since the radius of the hole is small enough compared to λ [116].

5.3.2 Bethe's diffraction theory by a small hole

5.3.2.1 Maxwell's equations by Stratton

When the incident H field \mathbf{H}_0 is perpendicular to the slit direction, the diffracted E field can be understood by the radiation occurring from the magnetic dipole moment at the far field zone [12, 116]. In

⁶Note that Eqs. (5.21), (5.27), (5.28), and (5.29) are defined for $z > 0$. However, since the boundary conditions $z = 0$ should be continuous in the hole, the relations for $z > 0$ and $z = 0$ obtained by the boundary conditions should coincide at $z = 0$.

order to explain the the magnetic dipole radiation, Bethe used concepts of the magnetic charge density as well as the magnetic current density from J. A. Stratton's paper [116,127]. According to Stratton [127], Maxwell's equations can be written in the forms [116,127]

$$\nabla \cdot \mathbf{E} = \frac{\rho}{\epsilon}, \quad \nabla \times \mathbf{E} = - \left[\mathbf{J}_m + \frac{\partial \mathbf{B}}{\partial t} \right], \quad (5.38)$$

$$\nabla \cdot \mathbf{H} = \frac{\rho_m}{\mu}, \quad \nabla \times \mathbf{H} = \mathbf{J} + \frac{\partial \mathbf{D}}{\partial t}, \quad (5.39)$$

where ρ and \mathbf{J} are the electric volume charge density and the electric volume current density. Note that ρ_m and \mathbf{J}_m represent the magnetic volume charge density and the magnetic volume current density.

If there are no electric current and no electric charge, Maxwell's equations become

$$\nabla \cdot \mathbf{E} = 0, \quad \nabla \times \mathbf{E} = - \left[\mathbf{J}_m + \frac{\partial \mathbf{B}}{\partial t} \right], \quad (5.40)$$

$$\nabla \cdot \mathbf{H} = \frac{\rho_m}{\mu}, \quad \nabla \times \mathbf{H} = \frac{\partial \mathbf{D}}{\partial t}. \quad (5.41)$$

According to electromagnetic theory [12,13], the B field and E field can be expressed in terms of the electric vector potential (\mathbf{A}) and the scalar potential (Φ) as

$$\mathbf{B} = \nabla \times \mathbf{A}, \quad \mathbf{E} = -\nabla\Phi - \frac{\partial}{\partial t}\mathbf{A}. \quad (5.42)$$

In a similar fashion, the D field can be written by introducing the magnetic vector potential (\mathbf{F}_m) as [116]

$$\mathbf{D} = \nabla \times \mathbf{F}_m, \quad (5.43)$$

which automatically satisfies

$$\nabla \cdot \mathbf{D} = \nabla \cdot (\nabla \times \mathbf{F}_m) = 0, \quad (5.44)$$

so that $\nabla \cdot \mathbf{E} = 0$ in Eq. (5.40). By substituting Eq. (5.43) into the H field in Eq. (5.41), we obtain

$$\nabla \times \mathbf{H} = \frac{\partial}{\partial t}(\nabla \times \mathbf{F}_m), \quad (5.45)$$

which implies that

$$\nabla \times \left[\mathbf{H} - \frac{\partial}{\partial t}\mathbf{F}_m \right] = 0. \quad (5.46)$$

By introducing the magnetic scalar potential (Φ_m) in analogy to the electric potential, we then obtain⁷ [116]

$$\mathbf{H} - \frac{\partial}{\partial t}\mathbf{F}_m = -\nabla\Phi_m. \quad \left(\mathbf{H} = -\nabla\Phi_m + \frac{\partial}{\partial t}\mathbf{F}_m \right) \quad (5.47)$$

Noting that the magnetic scalar potential or the magnetic vector potential satisfies the wave equation in analogy with the electric case [12,127], we find by substituting \mathbf{E} into \mathbf{D}/ϵ , \mathbf{B} into $\mu\mathbf{H}$, and multiplying

⁷See Jackson [12] p. 239.

the resulting equation by ϵ in the curl- \mathbf{E} in Eq. (5.40) that⁸

$$\nabla \times \mathbf{D} = -\epsilon \mathbf{J}_m - \mu \epsilon \frac{\partial}{\partial t} \mathbf{H}. \quad (5.48)$$

By substituting Eqs. (5.43) and (5.47) into Eq. (5.48), we obtain

$$\nabla \times (\nabla \times \mathbf{F}_m) = -\epsilon \mathbf{J}_m - \mu \epsilon \frac{\partial}{\partial t} \left[-\nabla \Phi_m + \frac{\partial}{\partial t} \mathbf{F}_m \right], \quad (5.49)$$

which implies that

$$\nabla (\nabla \cdot \mathbf{F}_m) - \nabla^2 \mathbf{F}_m = \nabla \left[\mu \epsilon \frac{\partial}{\partial t} \Phi_m \right] - \mu \epsilon \frac{\partial^2}{\partial t^2} \mathbf{F}_m - \epsilon \mathbf{J}_m, \quad (5.50)$$

so that

$$\nabla^2 \mathbf{F}_m - \mu \epsilon \frac{\partial^2}{\partial t^2} \mathbf{F}_m = \epsilon \mathbf{J}_m + \nabla \left[\nabla \cdot \mathbf{F}_m - \mu \epsilon \frac{\partial}{\partial t} \Phi_m \right]. \quad (5.51)$$

We therefore find by considering the Lorentz condition that⁹ [12]

$$\nabla^2 \mathbf{F}_m(\mathbf{x}, t) - \mu \epsilon \frac{\partial^2}{\partial t^2} \mathbf{F}_m(\mathbf{x}, t) = \epsilon \mathbf{J}_m(\mathbf{x}, t), \quad (5.52)$$

where

$$\nabla \cdot \mathbf{F}_m - \mu \epsilon \frac{\partial}{\partial t} \Phi_m = 0. \quad (5.53)$$

We also find by substituting Eqs. (5.47) and (5.53) into the divergence- \mathbf{H} in Eq. (5.41) that

$$\begin{aligned} \frac{\rho_m}{\mu} &= \nabla \cdot \left[-\nabla \Phi_m + \frac{\partial}{\partial t} \mathbf{F}_m \right] \\ &= -\nabla^2 \Phi_m + \frac{\partial}{\partial t} (\nabla \cdot \mathbf{F}_m) = -\nabla^2 \Phi_m + \mu \epsilon \frac{\partial^2}{\partial t^2} \Phi_m, \end{aligned} \quad (5.54)$$

which leads to the result

$$\nabla^2 \Phi_m(\mathbf{x}, t) - \mu \epsilon \frac{\partial^2}{\partial t^2} \Phi_m(\mathbf{x}, t) = -\frac{\rho_m(\mathbf{x}, t)}{\mu}. \quad (5.55)$$

Provided the charge density and the current density given by $\rho_m(\mathbf{x}', t') = \rho_m(\mathbf{x}')e^{-i\omega t'}$ and $\mathbf{J}_m(\mathbf{x}', t') = \mathbf{J}_m(\mathbf{x}')e^{-i\omega t'}$ [12] (Jackson p. 407) varies sinusoidally with time, the retarded solutions for Eqs. (5.52) and (5.55) can be written through the use of the Green function as (detailed in section A.5)

$$\Phi_m(\mathbf{x}, t) = \frac{1}{4\pi} \int d^3x' \frac{[\rho_m(\mathbf{x}', t')/\mu]_{\text{ret}}}{R}, \quad (5.56)$$

$$\mathbf{F}_m(\mathbf{x}, t) = \frac{1}{4\pi} \int d^3x' \frac{[-\epsilon \mathbf{J}_m(\mathbf{x}', t')]_{\text{ret}}}{R}, \quad (5.57)$$

8

$$\begin{aligned} \nabla \times \mathbf{E} &= - \left[\mathbf{J}_m + \frac{\partial \mathbf{B}}{\partial t} \right], \\ \Leftrightarrow \nabla \times \frac{\mathbf{D}}{\epsilon} &= - \left[\mathbf{J}_m + \mu \frac{\partial \mathbf{H}}{\partial t} \right], \end{aligned}$$

which implies that Eq. (5.48).

⁹See Jackson [12] p. 240.

which further makes

$$\begin{aligned}\Phi_{\text{m}}(\mathbf{x}, t) &= \frac{1}{4\pi\mu} \int d^3x' \frac{[\rho_{\text{m}}(\mathbf{x}', t')]_{\text{ret}}}{R} \\ &= \frac{1}{4\pi\mu} \int d^3x' \frac{\rho_{\text{m}}(\mathbf{x}') e^{-i\omega t'}}{R} \delta \left[t' - \left(t - \frac{R}{v} \right) \right],\end{aligned}\quad (5.58)$$

and

$$\begin{aligned}\mathbf{F}_{\text{m}}(\mathbf{x}, t) &= -\frac{\epsilon}{4\pi} \int d^3x' \frac{[\mathbf{J}_{\text{m}}(\mathbf{x}', t')]_{\text{ret}}}{R} \\ &= -\frac{\epsilon}{4\pi} \int d^3x' \frac{[\mathbf{J}_{\text{m}}(\mathbf{x}') e^{-i\omega t'}]}{R} \delta \left[t' - \left(t - \frac{R}{v} \right) \right],\end{aligned}\quad (5.59)$$

so that

$$\Phi_{\text{m}}(\mathbf{x}, t) = \frac{1}{[4\pi\mu]} \int d^3x' \rho_{\text{m}}(\mathbf{x}') \frac{e^{i\omega \frac{R}{v}}}{R} e^{-i\omega t}, \quad (5.60)$$

$$\mathbf{F}_{\text{m}}(\mathbf{x}, t) = - \left[\frac{\epsilon}{4\pi} \right] \int d^3x' \mathbf{J}_{\text{m}}(\mathbf{x}') \frac{e^{i\omega \frac{R}{v}}}{R} e^{-i\omega t}, \quad (5.61)$$

where $R = |\mathbf{R}| = |\mathbf{x} - \mathbf{x}'|$, \mathbf{x} is the field point, \mathbf{x}' is the source point and $\mu\epsilon = 1/v^2$. Note that [] is presented only in SI units. If the magnetic current and charge density exist only on the surface, we find by replacing \mathbf{J}_{m} with the magnetic surface current density \mathbf{K}_{m} and ρ_{m} by the magnetic surface charge density η_{m} that [\[116\]](#)

$$\Phi_{\text{m}}(\mathbf{x}, t) = \frac{1}{[4\pi\mu]} \int d^2x' \eta_{\text{m}}(\mathbf{x}') \frac{e^{ikR}}{R} e^{-i\omega t}, \quad (5.62)$$

$$\mathbf{F}_{\text{m}}(\mathbf{x}, t) = - \left[\frac{\epsilon}{4\pi} \right] \int d^2x' \mathbf{K}_{\text{m}}(\mathbf{x}') \frac{e^{ikR}}{R} e^{-i\omega t}, \quad (5.63)$$

which lead to the results

$$\Phi_{\text{m}}(\mathbf{x}) = \frac{1}{[4\pi\mu]} \int d^2x' \eta_{\text{m}}(\mathbf{x}') \phi(\mathbf{x}, \mathbf{x}'), \quad (5.64)$$

$$\mathbf{F}_{\text{m}}(\mathbf{x}) = - \left[\frac{\epsilon}{4\pi} \right] \int d^2x' \mathbf{K}_{\text{m}}(\mathbf{x}') \phi(\mathbf{x}, \mathbf{x}') \quad (5.65)$$

with

$$\phi(\mathbf{x}, \mathbf{x}') = \frac{e^{ikR}}{R}, \quad (5.66)$$

where $k = \omega/v$.

By using these results, the explicit expressions for the magnetic and electric fields can be obtained. We then find from Eq. [\(5.47\)](#) that

$$\begin{aligned}\mathbf{H}(\mathbf{x}, t) &= -\nabla\Phi_{\text{m}} + \frac{\partial}{\partial t}\mathbf{F}_{\text{m}} \\ &= -\frac{e^{-i\omega t}}{4\pi\mu} \nabla \int d^2x' \eta_{\text{m}}(\mathbf{x}') \frac{e^{ikR}}{R} - \frac{\epsilon}{4\pi} \int d^2x' \mathbf{K}_{\text{m}}(\mathbf{x}') \frac{e^{ikR}}{R} \cdot \left[\frac{\partial}{\partial t} e^{-i\omega t} \right] \\ &= -\frac{e^{-i\omega t}}{4\pi\mu} \nabla \int d^2x' \eta_{\text{m}}(\mathbf{x}') \frac{e^{ikR}}{R} + i\omega \frac{\epsilon}{4\pi} \int d^2x' \mathbf{K}_{\text{m}}(\mathbf{x}') \frac{e^{ikR}}{R} \cdot e^{-i\omega t} \\ &= \frac{1}{4\pi} \int d^2x' \left\{ -\frac{1}{\mu} \nabla \left[\eta_{\text{m}}(\mathbf{x}') \phi(\mathbf{x}, \mathbf{x}') \right] + i\omega \epsilon \mathbf{K}_{\text{m}} \phi(\mathbf{x}, \mathbf{x}') \right\} e^{-i\omega t}.\end{aligned}\quad (5.67)$$

Noting that the gradients ∇ are taken with respect to the field point \mathbf{x} , we find that the integrand in this equation becomes [116]

$$\nabla \left[\eta_m(\mathbf{x}') \phi(\mathbf{x}, \mathbf{x}') \right] = \eta_m(\mathbf{x}') \nabla \phi(\mathbf{x}, \mathbf{x}'), \quad (5.68)$$

which leads to the H field, yielding

$$\mathbf{H}(\mathbf{x}, t) = \frac{1}{4\pi} \int d^2x' \left\{ -\frac{1}{\mu} \eta_m(\mathbf{x}') \nabla \phi(\mathbf{x}, \mathbf{x}') + i\omega \epsilon \mathbf{K}_m \phi(\mathbf{x}, \mathbf{x}') \right\} e^{-i\omega t}, \quad (5.69)$$

so that we obtain the explicit expression for the H field, giving [116]

$$\mathbf{H}(\mathbf{x}) = \frac{1}{[4\pi]} \int d^2x' \left\{ i\omega[\epsilon] \mathbf{K}_m \phi(\mathbf{x}, \mathbf{x}') - \frac{1}{[\mu]} \eta_m(\mathbf{x}') \nabla \phi(\mathbf{x}, \mathbf{x}') \right\}, \quad (5.70)$$

where the integral is to be performed over the area of the hole.

In addition to the H field, we also find from Eq. (5.43) that

$$\begin{aligned} \mathbf{D}(\mathbf{x}, t) &= \nabla \times \mathbf{F}_m \\ &= -\frac{\epsilon}{4\pi} \nabla \times \int d^2x' \mathbf{K}_m(\mathbf{x}') \frac{e^{ikR}}{R} e^{-i\omega t}, \\ &= -\frac{\epsilon}{4\pi} \int d^2x' \nabla \times [\mathbf{K}_m(\mathbf{x}') \phi(\mathbf{x}, \mathbf{x}')] e^{-i\omega t}. \end{aligned} \quad (5.71)$$

Noting that the gradients ∇ are taken with respect to the field point \mathbf{x} , we find that the integrand in this equation becomes [116]

$$\begin{aligned} \nabla \times [\mathbf{K}_m(\mathbf{x}') \phi(\mathbf{x}, \mathbf{x}')] &= \nabla \phi(\mathbf{x}, \mathbf{x}') \times \mathbf{K}_m(\mathbf{x}') + \phi(\mathbf{x}, \mathbf{x}') \nabla \times \mathbf{K}_m(\mathbf{x}') \\ &= -\mathbf{K}_m(\mathbf{x}') \times \nabla \phi(\mathbf{x}, \mathbf{x}'), \end{aligned} \quad (5.72)$$

which leads to the D field, giving

$$\mathbf{D}(\mathbf{x}, t) = \frac{\epsilon}{4\pi} \int d^2x' \mathbf{K}_m(\mathbf{x}') \times \nabla \phi(\mathbf{x}, \mathbf{x}') e^{-i\omega t} \quad (5.73)$$

which implies that

$$\mathbf{D}(\mathbf{x}) = \frac{\epsilon}{4\pi} \int d^2x' \mathbf{K}_m(\mathbf{x}') \times \nabla \phi(\mathbf{x}, \mathbf{x}'). \quad (5.74)$$

Furthermore, we find by substituting $\epsilon \mathbf{E}$ into \mathbf{D} that the explicit expression for the E field is given by [116]

$$\mathbf{E}(\mathbf{x}) = \frac{1}{[4\pi]} \int d^2x' \mathbf{K}_m(\mathbf{x}') \times \nabla \phi(\mathbf{x}, \mathbf{x}'), \quad (5.75)$$

where the integral is to be performed over the area of the hole.

Hereafter, \mathbf{x} and \mathbf{r} represent an any position vector on (x, y, z) and (x, y) , respectively, or

$$\begin{aligned} \mathbf{x} &= (x, y, z), \\ \mathbf{r} &= (x, y) = (x, y, z = 0). \end{aligned}$$

5.3.2.2 Continuity equation

The continuity equation can be obtained by taking the divergence of $\nabla \times \mathbf{E}$ in Eq. (5.38), giving

$$\begin{aligned}\nabla \cdot (\nabla \times \mathbf{E}) &= -\nabla \cdot \left[\mathbf{J}_m + \frac{\partial \mathbf{B}}{\partial t} \right] \\ &= -\nabla \cdot \mathbf{J}_m - \frac{\partial}{\partial t} (\nabla \cdot \mathbf{B}) \quad \rho_m \\ &= -\nabla \cdot \mathbf{J}_m - \frac{\partial}{\partial t} \rho_m.\end{aligned}\tag{5.76}$$

Noting that $\nabla \cdot (\nabla \times \mathbf{E}) = 0$ is the identical equation, we find from Eq. (5.76) that the continuity equation is given by [116]

$$\nabla \cdot \mathbf{J}_m(\mathbf{x}, t) + \frac{\partial}{\partial t} \rho_m(\mathbf{x}, t) = 0,\tag{5.77}$$

which implies that¹⁰

$$\nabla \cdot \mathbf{J}_m(\mathbf{x}) = i\omega \rho_m(\mathbf{x}),\tag{5.79}$$

where $\mathbf{J}_m(\mathbf{x}, t) = \mathbf{J}_m(\mathbf{x})e^{-i\omega t}$ and $\rho_m(\mathbf{x}, t) = \rho_m(\mathbf{x})e^{-i\omega t}$. Analogous to Eq. (5.79), the continuity equation for the case when the magnetic current and charge density are located on a surface can be written as

$$\nabla \cdot \mathbf{K}_m(\mathbf{x}) = i\omega \eta_m(\mathbf{x}).\tag{5.80}$$

5.3.2.3 Magnetic surface charge density η_m

We now recall from Eq. (5.70) the expression for H field, giving

$$\mathbf{H}(\mathbf{x}) = \frac{1}{4\pi} \int d^2x' \left\{ i\omega \epsilon \mathbf{K}_m \phi(\mathbf{x}, \mathbf{x}') - \frac{1}{\mu} \eta_m(\mathbf{x}') \nabla \phi(\mathbf{x}, \mathbf{x}') \right\},\tag{5.81}$$

which can be rewritten in free space as

$$\begin{aligned}\mathbf{H}(\mathbf{x}) &= \frac{c^2}{4\pi} \int d^2x' \left\{ i\frac{\omega}{c} \epsilon_0 \frac{\mathbf{K}_m}{c} \phi(\mathbf{x}, \mathbf{x}') - \frac{1}{c^2 \mu_0} \eta_m(\mathbf{x}') \nabla \phi(\mathbf{x}, \mathbf{x}') \right\} \\ &= \frac{c^2 \epsilon_0}{4\pi} \int d^2x' \left\{ ik_0 \frac{\mathbf{K}_m}{c} \phi(\mathbf{x}, \mathbf{x}') - \eta_m(\mathbf{x}') \nabla \phi(\mathbf{x}, \mathbf{x}') \right\},\end{aligned}\tag{5.82}$$

where $\epsilon = \epsilon_0$ in free space, $k_0 = \omega/c$ and $\mu = \mu_0$ for the non-magnetic materials. Here, since the radius a of the hole is sufficiently small compared to the wavelength λ of the incident wave, the phase difference between \mathbf{x} on the screen at $z \gg 0$ and \mathbf{x}' in the hole induced by the phase retardation e^{ikR} in ϕ may be very small, so the retardation (e^{ikR}) can be neglected.¹¹ We find from Eq. (5.80) that K is of the order $\omega \eta a$, since it is easily seen that if $\mathbf{K}_m = \hat{x}K$, then $\nabla \cdot \mathbf{K}_m(\mathbf{x}) = \nabla \cdot \hat{x}K$ leads to $\frac{\partial}{\partial x} K = i\omega \eta_m$, such that $K = i\omega \int \eta_m dx$, where the integral is integrated over the boundary of the hole. Furthermore, we find

¹⁰

$$\begin{aligned}\nabla \cdot \mathbf{J}_m(\mathbf{x}, t) + \frac{\partial}{\partial t} \rho_m(\mathbf{x}, t) &= \nabla \cdot \mathbf{J}_m(\mathbf{x})e^{-i\omega t} + \rho_m(\mathbf{x}) \frac{\partial}{\partial t} e^{-i\omega t} \\ &= e^{-i\omega t} [\nabla \cdot \mathbf{J}_m(\mathbf{x}) - i\omega \rho_m(\mathbf{x})] = 0,\end{aligned}\tag{5.78}$$

which implies that Eq. (5.79).

¹¹Let us assume that δ_1 is the phase difference between \mathbf{x}_1 on the screen at $z \gg 0$ and \mathbf{x}'_1 in the hole. Similarly, let δ_2 be the phase difference between \mathbf{x}_1 on the screen at $z \gg 0$ and \mathbf{x}'_2 in the hole. Since the radius a of the hole is sufficiently small compared to the wavelength λ of the incident wave, \mathbf{x}'_1 is nearly the same as \mathbf{x}'_2 , which leads to the same phase retardation. In other words, the phase retardation can be neglected.

from Eq. (5.82) that

$$\left[k_0 \frac{K_m}{c} \phi \right]_{\text{order}} = k_0 \frac{\omega \eta a}{c} \phi = k_0^2 \eta a \phi, \quad \left[\eta_m \nabla \phi \right]_{\text{order}} = \eta \frac{\phi}{a}, \quad (5.83)$$

which implies that the first term of Eq. (5.82) is of the order of $(k_0 a)^2$ times the second term of Eq. (5.82) [116]. The first term of Eq. (5.82) can thus be also neglected. We therefore find that Eqs. (5.64) and (5.81) then reduce to¹² [116]

$$\Phi_m(\mathbf{x}) = \frac{1}{4\pi\mu} \int d^2x' \eta_m(\mathbf{x}') \frac{1}{|\mathbf{x} - \mathbf{x}'|}, \quad (5.84)$$

$$\mathbf{H}(\mathbf{x}) = -\frac{1}{4\pi\mu} \int d^2x' \eta_m(\mathbf{x}') \nabla \left(\frac{1}{|\mathbf{x} - \mathbf{x}'|} \right) = -\nabla \Phi_m(\mathbf{x}). \quad (5.85)$$

Since the tangential component of \mathbf{H} should be constant over the hole according to the boundary condition in Eq. (5.35), Eq. (5.85) can be written in the form

$$(\mathbf{H}_{2t} =) \mathbf{H}_t(\mathbf{x}) = \frac{1}{2} \mathbf{H}_0, \quad (5.86)$$

where \mathbf{H}_0 is a constant vector tangential to the hole.¹³ If $\Phi_m(\mathbf{x})$ is given by [116]

$$\begin{aligned} \Phi_m(\mathbf{x}) &= -\frac{1}{2} \mathbf{H}_0 \cdot \mathbf{x} \\ &= -\frac{1}{2} (\hat{x} H_{0x} + \hat{y} H_{0y}) \cdot (\hat{x} x + \hat{y} y + \hat{z} z) \\ &= -\frac{1}{2} (H_{0x} x + H_{0y} y), \end{aligned} \quad (5.87)$$

where H_{0x} and H_{0y} are constants with a relation $\sqrt{H_{0x}^2 + H_{0y}^2} = H_0$, we then see from Eq. (5.85) that

$$\begin{aligned} \nabla \Phi_m(\mathbf{x}) &= -\frac{1}{2} \left[\hat{x} \frac{\partial}{\partial x} + \hat{y} \frac{\partial}{\partial y} + \hat{z} \frac{\partial}{\partial z} \right] (H_{0x} x + H_{0y} y) \\ &= -\frac{1}{2} (\hat{x} H_{0x} + \hat{y} H_{0y}) = -\frac{1}{2} \mathbf{H}_0, \end{aligned} \quad (5.88)$$

which leads to Eq. (5.86)¹⁴

$$\mathbf{H}_t(\mathbf{x}) = -\nabla \Phi_m(\mathbf{x}) = \frac{1}{2} \mathbf{H}_0. \quad (5.89)$$

Using this result, we therefore find from Eq. (5.84) that

$$\Phi_m(\mathbf{x}) = \frac{1}{4\pi\mu} \int d^2x' \eta_m(\mathbf{x}') \varphi(\mathbf{x}, \mathbf{x}') = -\frac{1}{2} \mathbf{H}_0 \cdot \mathbf{x}, \quad (5.90)$$

which tells us that Φ_m as well as \mathbf{H} can be obtained when we know the magnetic charge density η_m . Since Φ_m , $\nabla \Phi_m$ and \mathbf{H}_t are tangential to the hole, the results given by Eqs. (5.87), (5.88), (5.89), and

¹²H field may be considered as the magneto-static field by the charge density η_m [116].

¹³See below Eq. (5.37).

¹⁴From Eq. (5.85), the tangential component of the H field is the tangential component of the gradient of Φ_m . Since \mathbf{H}_0 is only composed of tangential components, the gradient of Φ_m becomes a vector with tangential components only.

(5.90) can be rewritten as

$$(\mathbf{H}_{2t} =) \mathbf{H}_t(\mathbf{r}) = \frac{1}{2} \mathbf{H}_0, \quad (5.91)$$

$$\Phi_m(\mathbf{r}) = -\frac{1}{2} \mathbf{H}_0 \cdot \mathbf{r} = -\frac{1}{2} (H_{0x}x + H_{0y}y), \quad (5.92)$$

$$\nabla \Phi_m(\mathbf{r}) = -\frac{1}{2} (\hat{x}H_{0x} + \hat{y}H_{0y}) = -\frac{1}{2} \mathbf{H}_0, \quad (5.93)$$

$$\mathbf{H}_t(\mathbf{r}) = -\nabla \Phi_m(\mathbf{r}) = \frac{1}{2} \mathbf{H}_0, \quad (5.94)$$

$$\Phi_m(\mathbf{r}) = \frac{1}{4\pi\mu} \int d^2x' \eta_m(\mathbf{r}') \varphi(\mathbf{r}, \mathbf{r}') = -\frac{1}{2} \mathbf{H}_0 \cdot \mathbf{r}, \quad (5.95)$$

where $\mathbf{x}' = \mathbf{r}'$ is the source point over the hole and $\mathbf{x} \rightarrow \mathbf{r}$ represents the field point on the xy plane.¹⁵

A constant \mathbf{H} field in the hole can be produced by an ellipsoidal magnetic dipole distribution having the same direction of the magnetic field [116]. The magnetic charge distribution on an ellipsoid having a height of h along the z -axis as in Fig. 5.4(a) will be identical to the surface charge distribution provided that h is sufficiently small [116]. The cross section of the ellipsoid in the xy plane will be a hole with a radius of a . We then find that the equation for the ellipsoid with $h \ll a$ is given by

$$\frac{x'^2}{a^2} + \frac{y'^2}{a^2} + \frac{z'^2}{h^2} = 1, \quad (5.96)$$

which implies that the ordinate of the ellipsoid in Fig. 5.4(a) can be expressed as

$$z' = h \sqrt{1 - \frac{x'^2}{a^2} - \frac{y'^2}{a^2}} = \frac{h}{a} \sqrt{a^2 - (x'^2 + y'^2)}, \quad (5.97)$$

where (x', y', z') represents a source point. By taking the divergence of both sides of Eq. (5.97), we obtain

$$\begin{aligned} \nabla' z' &= \frac{h}{a} \nabla' [a^2 - (x'^2 + y'^2)]^{1/2} \\ &= \frac{h}{a} \left[\hat{r}' \frac{\partial}{\partial r'} + \hat{\theta}' \frac{1}{r'} \frac{\partial}{\partial \theta'} + z' \frac{\partial}{\partial z'} \right] [a^2 - r'^2]^{1/2} \\ &= \frac{h}{a} \hat{r}' \frac{1}{2} [a^2 - r'^2]^{1/2} (-2) r' = -\hat{r}' \frac{h}{a} \frac{r'}{\sqrt{a^2 - r'^2}}, \end{aligned} \quad (5.98)$$

where $r'^2 = x'^2 + y'^2$ and the cylindrical coordinates are used. We thereby find from Eq. (5.98) that the gradient of z' make a vector in the direction of \hat{r}' , *i.e.* the normal direction to the surface of the ellipsoid. Since the electric surface charge density $\sigma = \mathbf{P} \cdot \hat{n}$ is proportional to $\mathbf{E} \cdot \hat{n}$,¹⁶ we thus deduce that η_m is proportional to the equation given by [116]

$$\eta_m(\mathbf{x}') \propto \mathbf{H}_0 \cdot \nabla' \sqrt{a^2 - r'^2} = -\frac{\mathbf{H}_0 \cdot \mathbf{r}'}{\sqrt{a^2 - r'^2}}, \quad (5.99)$$

where $\mathbf{r}' = \hat{r}' r'$. The magnetic charge density can then be obtained by determining a proportional constant C , to yield

$$\eta_m(\mathbf{r}') = -C \frac{\mathbf{H}_0 \cdot \mathbf{r}'}{\sqrt{a^2 - r'^2}}. \quad (5.100)$$

¹⁵These results come from Eq. (5.92) because Eq. (5.92) is satisfied through the substitution $\mathbf{x} \rightarrow \mathbf{r}$ due to the tangential H_0 field comprised of two dimensional components.

¹⁶See Jackson [12] p. 153 and Griffiths [13] p. 153 (Griffiths 3rd edition pp. 167-168).

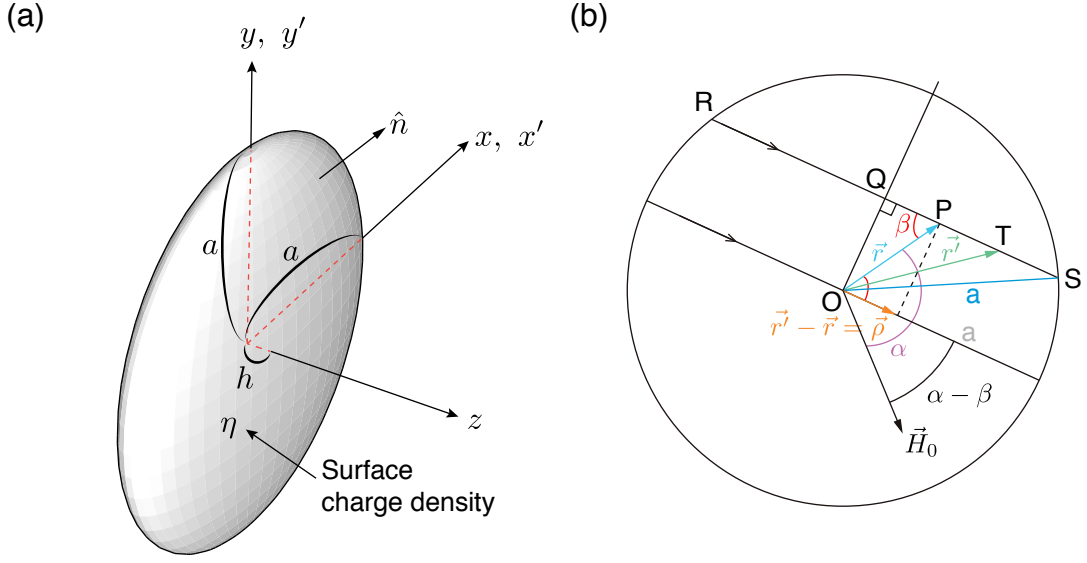


Figure 5.4: (a) The magnetic surface charge density η_m over the hole. (b) Representation for the integral in Eq. (5.101).

By substituting Eq. (5.100) into Eq. (5.95), we find that

$$\text{Int} = C \frac{1}{4\pi\mu} \int d^2x' \left[\frac{\mathbf{H}_0 \cdot \mathbf{r}'}{\sqrt{a^2 - r'^2}} \right] \frac{1}{|\mathbf{r} - \mathbf{r}'|} = \frac{1}{2} \mathbf{H}_0 \cdot \mathbf{r}, \quad (5.101)$$

where $\mathbf{x}' = \mathbf{r}'$ is the source point over the hole. By introducing $\rho = |\mathbf{r} - \mathbf{r}'| = |\mathbf{r}' - \mathbf{r}|$ and the angle β between two vectors $\mathbf{r}' - \mathbf{r}$ and \mathbf{r} , we obtain [116]

$$\mathbf{H}_0 \cdot \boldsymbol{\rho} = \mathbf{H}_0 \cdot (\mathbf{r}' - \mathbf{r}) = H_0 \rho \cos(\alpha - \beta), \quad (5.102)$$

where α is the angle between \mathbf{x} and \mathbf{H}_0 . All the parameters are illustrated in Fig. 5.4(b). Through the use of a change of variables, the area element in Eq. (5.101) can be expressed in terms of ρ and β as follows: $d^2x' \rightarrow d\beta d\rho \rho$. We then find by a change of variables and substituting Eq. (5.102) into the left-hand side of Eq. (5.101) that [116]

$$\begin{aligned} \text{Int} &= C \frac{1}{4\pi\mu} \int d^2x' \frac{\mathbf{H}_0 \cdot \mathbf{r}'}{\sqrt{a^2 - r'^2}} \frac{1}{\rho} \\ &= C \frac{1}{4\pi\mu} \int_0^{2\pi} d\beta \int_0^{\rho(\beta)} d\rho \rho \frac{\mathbf{H}_0 \cdot \mathbf{r} + H_0 \rho \cos(\alpha - \beta)}{\sqrt{a^2 - r'^2}} \frac{1}{\rho} \\ &= C \frac{1}{4\pi\mu} \int_0^{2\pi} d\beta \int_0^{\rho(\beta)} d\rho \left[\frac{\mathbf{H}_0 \cdot \mathbf{r}}{\sqrt{a^2 - r'^2}} + \frac{H_0 \rho \cos(\alpha - \beta)}{\sqrt{a^2 - r'^2}} \right]. \end{aligned} \quad (5.103)$$

Let us now consider in detail the situation in Fig. 5.4(b). The two integrals in Eq. (5.103) can be solved by integration along a whole chord such as \overline{RS} [116]. We find from Fig. 5.4(b) that [116]

$$\begin{aligned} a^2 - r'^2 &= a^2 - (\overline{OQ}^2 + \overline{QT}^2) = (a^2 - \overline{OQ}^2) - \overline{QT}^2 \\ &= \overline{QS}^2 - \overline{QT}^2 \equiv s^2 - \xi^2, \end{aligned} \quad (5.104)$$

$$\overline{QT} \equiv \xi = \overline{QP} + \overline{PT} = r \cos \beta + |\mathbf{r}' - \mathbf{r}| = r \cos \beta + \rho, \quad (5.105)$$

where $s \equiv \overline{QS}$ is the half the length of the chord and $\xi \equiv \overline{QT}$ goes from $-s$ to s . By using a change of variables in Eqs. (5.104) and (5.105), we obtain

$$\begin{aligned} \text{Int} &= C \frac{1}{4\pi\mu} \int_0^\pi d\beta \int_{-s}^s d\xi \left[\frac{\mathbf{H}_0 \cdot \mathbf{r}}{\sqrt{s^2 - \xi^2}} + \frac{H_0 \rho \cos(\alpha - \beta)}{\sqrt{s^2 - \xi^2}} \right] \\ &= C \frac{1}{4\pi\mu} \left[\int_0^\pi d\beta \mathbf{H}_0 \cdot \mathbf{r} \int_{-s}^s d\xi \frac{1}{\sqrt{s^2 - \xi^2}} + H_0 \int_0^\pi d\beta \cos(\alpha - \beta) \int_{-s}^s d\xi \frac{\rho}{\sqrt{s^2 - \xi^2}} \right], \end{aligned} \quad (5.106)$$

where $\int_0^{2\pi} d\beta \int_0^\rho d\rho \rightarrow \int_0^\pi d\beta \int_{-s}^s d\xi$. Here the first integral with respect to ξ can be solved by taking $\xi = s \sin t$ such that $d\xi = s \cos t dt$, which gives $t = -\pi/2$ for $\xi = -s$ and $t = \pi/2$ for $\xi = s$. This leads to the result

$$\begin{aligned} \int_{-s}^s d\xi \frac{1}{\sqrt{s^2 - \xi^2}} &= \int_{-\pi/2}^{\pi/2} s \cos t dt \frac{1}{\sqrt{s^2 - s^2 \sin^2 t}} \\ &= \int_{-\pi/2}^{\pi/2} \cos t dt \frac{1}{\sqrt{1 - \sin^2 t}} = \int_{-\pi/2}^{\pi/2} \cancel{\cos t} dt \frac{1}{\cancel{\cos t}} \\ &= \frac{\pi}{2} - \frac{(-\pi)}{2} = \pi. \end{aligned} \quad (5.107)$$

In a similar fashion, the second integral with respect to ξ can be solved by taking $t = s^2 - \xi^2$ such that $-2\xi d\xi = dt \rightarrow \xi d\xi = -(1/2)dt$, which gives $t = 0$ for $\xi = -s$ and $t = 0$ for $\xi = s$. We thus find from Eq. (5.105) that

$$\begin{aligned} \int_{-s}^s d\xi \frac{\rho}{\sqrt{s^2 - \xi^2}} &= \int_{-s}^s d\xi \frac{\xi - r \cos \beta}{\sqrt{s^2 - \xi^2}} \\ &= \int_{-s}^s d\xi \frac{\xi}{\sqrt{s^2 - \xi^2}} - r \cos \beta \int_{-s}^s d\xi \frac{1}{\sqrt{s^2 - \xi^2}} \\ &= -\int_0^0 \frac{1}{2} dt \frac{1}{\sqrt{t}} - r \cos \beta \int_{-s}^s d\xi \frac{1}{\sqrt{s^2 - \xi^2}} = -\pi r \cos \beta. \end{aligned} \quad (5.108)$$

The integral in Eq. (5.106) can therefore be solved to obtain

$$\begin{aligned} \text{Int} &= \frac{C}{4\pi\mu} \left[\int_0^\pi d\beta \mathbf{H}_0 \cdot \mathbf{r} \left\{ \int_{-s}^s d\xi \frac{1}{\sqrt{s^2 - \xi^2}} \right\} + H_0 \int_0^\pi d\beta \cos(\alpha - \beta) \left\{ \int_{-s}^s d\xi \frac{\rho}{\sqrt{s^2 - \xi^2}} \right\} \right] \\ &= \frac{C}{4\pi\mu} \left[\pi \int_0^\pi d\beta \mathbf{H}_0 \cdot \mathbf{r} - \pi H_0 r \int_0^\pi d\beta \cos(\alpha - \beta) \cos \beta \right] \\ &= \frac{C\pi}{4\pi\mu} \left[\mathbf{H}_0 \cdot \mathbf{r} \int_0^\pi d\beta - H_0 r \int_0^\pi d\beta \cos(\alpha - \beta) \cos \beta \right], \end{aligned} \quad (5.109)$$

where the last integral is evaluated as¹⁷

$$\begin{aligned} \int_0^\pi d\beta \cos(\alpha - \beta) \cos \beta &= \int_0^\pi d\beta \left[(\cos \alpha \cos \beta + \sin \alpha \sin \beta) \cos \beta \right] \\ &= \int_0^\pi d\beta \left[\cos \alpha \cos^2 \beta + \sin \alpha \sin \beta \cos \beta \right] \\ &= \cos \alpha \int_0^\pi d\beta \cos^2 \beta + \sin \alpha \int_0^\pi d\beta \sin \beta \cos \beta = \frac{\pi}{2} \cos \alpha, \end{aligned} \quad (5.110)$$

¹⁷See Eqs. (C.70d) and (C.70f) in section C.

yielding

$$\begin{aligned} \text{Int} &= \frac{C\pi}{4\pi\mu} \left[\mathbf{H}_0 \cdot \mathbf{r} \int_0^\pi d\beta - \frac{\pi}{2} H_0 r \cos \alpha \right] = \frac{C\pi}{4\pi\mu} \left[\pi \mathbf{H}_0 \cdot \mathbf{r} - \frac{\pi}{2} H_0 r \cos \alpha \right] \\ &= \frac{C\pi}{4\pi\mu} \left[\pi H_0 r \cos \alpha - \frac{\pi}{2} H_0 r \cos \alpha \right] = \frac{C}{[4\pi\mu]} \frac{\pi^2}{2} H_0 r \cos \alpha. \end{aligned} \quad (5.111)$$

We hence find from Eq. (5.101) through Eq. (5.111) that

$$\text{Int} = \frac{C}{[4\pi\mu]} \frac{\pi^2}{2} H_0 r \cos \alpha = \frac{1}{2} H_0 r \cos \alpha, \quad (5.112)$$

yielding

$$C = \frac{[4\pi\mu]}{\pi^2}, \quad (5.113)$$

so that we find from Eq. (5.100) that the magnetic surface charge density η_m is given by

$$\eta_m(\mathbf{r}') = -\frac{[4\pi\mu]}{\pi^2} \frac{\mathbf{H}_0 \cdot \mathbf{r}'}{\sqrt{a^2 - r'^2}}. \quad (5.114)$$

5.3.2.4 Magnetic surface current density K_m

Let us recall from Eq. (5.80) that the expression for the continuity equation induced by the magnetic current and charge density can be written as

$$\nabla \cdot \mathbf{K}_m(\mathbf{x}) = i\omega\eta_m(\mathbf{x}). \quad (5.115)$$

Since the magnetic current and charge densities are confined in the region of the hole, Eq. (5.115) can be explicitly expressed through the substitution $\mathbf{x} \rightarrow \mathbf{r}'$ as $\nabla \cdot \mathbf{K}_m(\mathbf{r}') = i\omega\eta_m(\mathbf{r}')$. We then find that the both sides of Eq. (5.115) become

$$\begin{aligned} \nabla \cdot \mathbf{K}_m(\mathbf{r}') &= \left[\hat{x}' \frac{\partial}{\partial x} + \hat{y}' \frac{\partial}{\partial y'} \right] \cdot (\hat{x}' K_{x'} + \hat{y}' K_{y'}) \\ &= \frac{\partial}{\partial x'} K_{x'} + \frac{\partial}{\partial y'} K_{y'}, \end{aligned} \quad (5.116)$$

$$\begin{aligned} i\omega\eta_m(\mathbf{r}') &= -i\omega \frac{[4\pi\mu]}{\pi^2} \frac{(H_{0x'} + H_{0y'}) \cdot (\hat{x}' x' + \hat{y}' y')}{\sqrt{a^2 - r'^2}} \\ &= -i\omega \frac{[4\pi\mu]}{\pi^2} \left[\frac{H_{0x'} x'}{\sqrt{a^2 - r'^2}} + \frac{H_{0y'} y'}{\sqrt{a^2 - r'^2}} \right], \end{aligned} \quad (5.117)$$

which implies that¹⁸

$$\frac{\partial}{\partial x'} K_{x'} = -i\omega \frac{[4\pi\mu]}{\pi^2} \frac{H_{0x'} x'}{\sqrt{a^2 - r'^2}}, \quad (5.118)$$

$$\frac{\partial}{\partial y'} K_{y'} = -i\omega \frac{[4\pi\mu]}{\pi^2} \frac{H_{0y'} y'}{\sqrt{a^2 - r'^2}}. \quad (5.119)$$

¹⁸The reason for obtaining Eqs. (5.118) and (5.119) from Eqs. (5.116) and (5.117) is as follows: If $f(x', y')$ is defined as

$$f(x', y') = \sqrt{a^2 - x'^2 - y'^2},$$

we then find that

$$\frac{\partial}{\partial x'} f(x', y') = \frac{-x'}{\sqrt{a^2 - x'^2 - y'^2}}, \quad \frac{\partial}{\partial y'} f(x', y') = \frac{-y'}{\sqrt{a^2 - x'^2 - y'^2}}.$$

Integrating both sides of Eq. (5.118), we get

$$K_{x'}(x', y') = -i\omega \frac{[4\pi\mu]}{\pi^2} H_{0x'} \int dx' \frac{x'}{\sqrt{a^2 - x'^2 - y'^2}}, \quad (5.120)$$

where $H_{0x'}$ and $H_{0y'}$ are constants. By taking $a^2 - x'^2 - y'^2 = t$ such that $-2x'dx' = dt$, the integral is evaluated as¹⁹

$$K_{x'}(x', y') = i\omega \frac{[4\pi\mu]}{\pi^2} H_{0x'} \sqrt{a^2 - x'^2 - y'^2}, \quad (5.121)$$

and correspondingly for the y' component in Eq. (5.119). We thus find that the magnetic surface current density is given by [116]

$$\begin{aligned} \mathbf{K}_m(\mathbf{r}') &= \hat{x}' K_{x'} + \hat{y}' K_{y'} \\ &= i\omega \frac{[4\pi\mu]}{\pi^2} \sqrt{a^2 - x'^2 - y'^2} (\hat{x}' H_{0x'} + \hat{y}' H_{0y'}) \\ &= i\omega \frac{[4\pi\mu]}{\pi^2} \sqrt{a^2 - r'^2} \mathbf{H}_0. \end{aligned} \quad (5.122)$$

5.3.2.5 Additional magnetic surface current density \mathbf{K}_e

We recall the expression for the electric field in Eq. (5.75), giving

$$\mathbf{E}(\mathbf{x}) = \frac{1}{4\pi} \int d^2x' \mathbf{K}_m(\mathbf{r}') \times \nabla\phi(\mathbf{x}, \mathbf{r}'), \quad (5.123)$$

where $\mathbf{x}' = \mathbf{r}'$ is the source point over the hole. Since \mathbf{K}_m in Eq. (5.122) is of the order $\omega a H_0$, $\nabla\phi$ is of the order $1/a^2$ ($\phi \simeq 1/r$ so that $\frac{\partial}{\partial x}\phi \simeq -1/r^2$), and the integral Eq. (5.123) goes over an area of order a^2 , one may find that the resultant order obtained by substituting \mathbf{K}_m in Eq. (5.122) into Eq. (5.123) is $[\omega a H_0] \times [1/a^2] \times [a^2] = \omega a H_0$, which is inconsistent with the order of the E field since the E field is of the same order as H_0 [116]. For this reason, Bethe added an additional magnetic surface current density \mathbf{K}_e that satisfies the boundary condition in Eq. (5.37) and does not contribute to the magnetic charge density η_m . This can be mathematically expressed as [116]

$$\nabla \cdot \mathbf{K}_e(\mathbf{x}) = 0, \quad (5.124)$$

where this equation can be further expressed as $\nabla \cdot \mathbf{K}_e(\mathbf{r}') = 0$ through the substitution $\mathbf{x} \rightarrow \mathbf{r}'$ since \mathbf{K}_e should be tangential with respect to the hole [116].

Since the normal component of E should be constant over the hole by the boundary condition in Eq. (5.37), Eq. (5.123) can then be written as

$$(\mathbf{E}_{2n} =) \mathbf{E}_n(\mathbf{x}) = \frac{1}{2} \mathbf{E}_0 = \frac{1}{2} (\hat{z} E_0), \quad (5.125)$$

where \mathbf{E}_0 is considered as a constant, yielding the constant E_0 . Since the position vector is defined as

19

$$\begin{aligned} K_{x'}(x', y') &= -i\omega \frac{[4\pi\mu]}{\pi^2} H_{0x'} \int dt \frac{(-1)}{2} \frac{1}{\sqrt{t}} \\ &= i\omega \frac{[4\pi\mu]}{\pi^2} \frac{H_{0x'}}{2} \left(\frac{1}{2}\right) t^{-\frac{1}{2}+1} = i\omega \frac{[4\pi\mu]}{\pi^2} H_{0x'} \sqrt{a^2 - x'^2 - y'^2} \end{aligned}$$

$\mathbf{x} = (x, y, z)$, we obtain²⁰

$$\nabla \times \left[\frac{1}{4} \mathbf{E}_0 \times \mathbf{x} \right] = \frac{1}{2} \mathbf{E}_0 = \mathbf{E}_m(\mathbf{x}). \quad (5.126)$$

We then find from Eq. (5.43) that the the vector potential is in the form²¹

$$\mathbf{F}_m(\mathbf{x}) = \frac{\epsilon}{4} \mathbf{E}_0 \times \mathbf{x}. \quad (5.128)$$

Here, the right-hand side of Eq. (5.128) can be evaluated as

$$\mathbf{E}_0 \times \mathbf{x} = \begin{vmatrix} \hat{x} & \hat{y} & \hat{z} \\ 0 & 0 & E_0 \\ x & y & z \end{vmatrix} = (-1)^{1+1} \hat{x}(-E_0 y) + (-1)^{1+2} \hat{y}(-E_0 x) + (-1)^{1+3} \cdot 0 = -\hat{x} E_0 y + \hat{y} E_0 x, \quad (5.129)$$

which implies that the vector potential \mathbf{F}_m lies within the xy plane perpendicular to the z axis; in other words, the vector potential \mathbf{F}_m is tangential to the hole. Note that the following equation is evaluated as

$$\mathbf{E}_0 \times \mathbf{r} = \begin{vmatrix} \hat{x} & \hat{y} & \hat{z} \\ 0 & 0 & E_0 \\ x & y & 0 \end{vmatrix} = (-1)^{1+1} \hat{x}(-E_0 y) + (-1)^{1+2} \hat{y}(-E_0 x) + (-1)^{1+3} \cdot 0 = -\hat{x} E_0 y + \hat{y} E_0 x, \quad (5.130)$$

which gives the same result as in Eq. (5.129). For this reason, Eq. (5.128) is expressed through the substitution $\mathbf{x} \rightarrow \mathbf{r}$ as

$$\mathbf{F}_m(\mathbf{r}) = \frac{[\epsilon]}{4} \mathbf{E}_0 \times \mathbf{r}. \quad (5.131)$$

From Eq. (5.65), the vector potential \mathbf{F}_m induced by the magnetic current density \mathbf{K}_e can be written as

$$\mathbf{F}_m(\mathbf{r}) = - \left[\frac{\epsilon}{4\pi} \right] \int d^2 x' \mathbf{K}_e(\mathbf{r}') \frac{1}{|\mathbf{r} - \mathbf{r}'|}, \quad (5.132)$$

where the retardation term e^{ikR} is neglected due to the same reason described in section 5.3.2.3. We then find by substituting Eq. (5.131) into Eq. (5.132) that

$$\text{Int} = - \frac{1}{[4\pi]} \int d^2 x' \mathbf{K}_e(\mathbf{r}') \frac{1}{|\mathbf{r} - \mathbf{r}'|} = \frac{1}{4} \mathbf{E}_0 \times \mathbf{r}, \quad (5.133)$$

where \mathbf{K}_e can be decomposed into its x and y components as $\mathbf{K}_e = \hat{x} K_e^x + \hat{y} K_e^y$ by noting that \mathbf{K}_e is tangential to the hole. Using Eq. (5.129) and comparing both sides of Eq. (5.133), the integral in

²⁰If $\mathbf{E}_0 = \hat{z} E_0$ is a constant vector in the z direction and $\mathbf{x} = (x, y, z)$, we obtain

$$\begin{aligned} \nabla \times (\mathbf{E}_0 \times \mathbf{x}) &= \mathbf{E}_0 (\nabla \cdot \mathbf{x}) - \cancel{\mathbf{x} (\nabla \cdot \mathbf{E}_0)} + \cancel{(\mathbf{x} \cdot \nabla) \mathbf{E}_0} - (\mathbf{E}_0 \cdot \nabla) \mathbf{x} \\ &= \mathbf{E}_0 \left[\left(\hat{x} \frac{\partial}{\partial x} + \hat{y} \frac{\partial}{\partial y} + \hat{z} \frac{\partial}{\partial z} \right) \cdot (\hat{x} x + \hat{y} y + \hat{z} z) \right] - \left[\hat{z} E_0 \cdot \left(\hat{x} \frac{\partial}{\partial x} + \hat{y} \frac{\partial}{\partial y} + \hat{z} \frac{\partial}{\partial z} \right) \right] \mathbf{x} \\ &= \mathbf{E}_0 (1 + 1 + 1) - E_0 \frac{\partial}{\partial z} (\hat{x} x + \hat{y} y + \hat{z} z) = 3\mathbf{E}_0 - E_0 \hat{z} = \hat{z} 2E_0 \end{aligned}$$

which implies that

$$\nabla \times \left[\frac{1}{4} \mathbf{E}_0 \times \mathbf{x} \right] = \frac{1}{2} \mathbf{E}_0.$$

²¹We find from Eq. (5.43) that

$$\mathbf{E} = \nabla \times \frac{\mathbf{F}_m}{\epsilon}. \quad (5.127)$$

By comparing this equation with Eq. (5.126), we obtain Eq. (5.128).

Eq. (5.133) is decomposed into its vector components as

$$\frac{1}{[4\pi]} \int d^2x' K_e^{x'} \frac{1}{|\mathbf{r} - \mathbf{r}'|} = \frac{1}{4} E_0 y, \quad (5.134)$$

$$-\frac{1}{[4\pi]} \int d^2x' K_e^{y'} \frac{1}{|\mathbf{r} - \mathbf{r}'|} = \frac{1}{4} E_0 x, \quad (5.135)$$

The following equations can then be obtained by multiplying both sides of above equations by a factor of 2, yielding

$$\frac{1}{\pi^2} \int d^2x' \left[\frac{2\pi^2}{[4\pi]} K_e^{x'} \right] \frac{1}{|\mathbf{r} - \mathbf{r}'|} = \frac{1}{2} E_0 y, \quad (5.136)$$

$$-\frac{1}{\pi^2} \int d^2x' \left[\frac{2\pi^2}{[4\pi]} K_e^{y'} \right] \frac{1}{|\mathbf{r} - \mathbf{r}'|} = \frac{1}{2} E_0 x, \quad (5.137)$$

where each equation is familiar to Eq. (5.101). Recall that the magnetic scalar potential induced by η_m has been represented as

$$\Phi_m(\mathbf{r}) = \frac{1}{\pi^2} \int d^2x' \left[\frac{\mathbf{H}_0 \cdot \mathbf{r}'}{\sqrt{a^2 - r'^2}} \right] \frac{1}{|\mathbf{r} - \mathbf{r}'|} = \frac{1}{2} \mathbf{H}_0 \cdot \mathbf{r}. \quad (5.138)$$

Assuming \mathbf{H} is tangential to the x axis in Fig. 5.4(a), Eq. (5.138) becomes

$$\frac{1}{\pi^2} \int d^2x' \left[\frac{H_0 x'}{\sqrt{a^2 - r'^2}} \right] \frac{1}{|\mathbf{r} - \mathbf{r}'|} = \frac{1}{2} H_0 x. \quad (5.139)$$

By analogy with Eq. (5.139), the vector components of \mathbf{K}_e in Eqs. (5.136) and (5.137) can be written as [116]

$$\frac{2\pi^2}{[4\pi]} K_e^{x'} = \frac{E_0 y'}{\sqrt{a^2 - r'^2}}, \quad (5.140)$$

$$-\frac{2\pi^2}{[4\pi]} K_e^{y'} = \frac{E_0 x'}{\sqrt{a^2 - r'^2}}, \quad (5.141)$$

which implies that

$$K_e^{x'} = \frac{[4\pi]}{2\pi^2} \frac{E_0 y'}{\sqrt{a^2 - r'^2}}, \quad (5.142)$$

$$K_e^{y'} = -\frac{[4\pi]}{2\pi^2} \frac{E_0 x'}{\sqrt{a^2 - r'^2}}. \quad (5.143)$$

We therefore find by combining Eqs. (5.142) and (5.143) that the additional magnetic surface current density \mathbf{K}_e is given by

$$\begin{aligned} \mathbf{K}_e(\mathbf{r}') &= \hat{x}' K_e^{x'} + \hat{y}' K_e^{y'} \\ &= \frac{[4\pi]}{2\pi^2} \frac{1}{\sqrt{a^2 - r'^2}} (\hat{x}' E_0 y' - \hat{y}' E_0 x'). \end{aligned} \quad (5.144)$$

We thus find by introducing Eq. (5.130) into Eq. (5.144) that²²

$$\mathbf{K}_e(\mathbf{r}') = \frac{[4\pi]}{2\pi^2} \frac{1}{\sqrt{a^2 - r'^2}} \mathbf{r}' \times \mathbf{E}_0. \quad (5.145)$$

5.3.2.6 Total magnetic surface current density \mathbf{K}_e

The total magnetic surface current density can be obtained by combining Eqs. (5.122) and Eq. (5.145) yielding

$$\begin{aligned} \mathbf{K}_m^{\text{total}} &= \mathbf{K}_m + \mathbf{K}_e \\ &= i\omega \frac{[4\pi\mu]}{\pi^2} \sqrt{a^2 - r'^2} \mathbf{H}_0 + \frac{[4\pi]}{2\pi^2} \frac{1}{\sqrt{a^2 - r'^2}} \mathbf{r}' \times \mathbf{E}_0. \end{aligned} \quad (5.146)$$

5.3.2.7 Diffracted E field by a small hole

We recall from Eq. (5.75) that the E field induced by the magnetic surface current density can be obtained by replacing \mathbf{K}_m with $\mathbf{K}_m^{\text{total}}$, giving

$$\mathbf{E}(\mathbf{x}) = \frac{1}{4\pi} \int d^2x' \mathbf{K}_m^{\text{total}}(\mathbf{r}') \times \nabla\phi(\mathbf{x}, \mathbf{r}'), \quad (5.147)$$

where

$$\phi(\mathbf{x}, \mathbf{r}') = \frac{e^{ikR}}{R}, \quad (5.148)$$

\mathbf{r}' is the source point over the hole, $R = |\mathbf{x} - \mathbf{r}'|$ and $k = \omega/v$. In the far-field zone (*i.e.* $|\mathbf{r}'| \ll |\mathbf{x}|$), we find from Eq. (A.82) that R in the integrands of Eq. (5.123) can be expanded as²³

$$R = |\mathbf{x} - \mathbf{r}'| \simeq r - \frac{\mathbf{x} \cdot \mathbf{r}'}{r}, \quad \frac{1}{R} \simeq \frac{1}{r} + \frac{\mathbf{x} \cdot \mathbf{r}'}{r^3}, \quad (5.149)$$

where $|\mathbf{x}| = r$ and $|\mathbf{r}'| = r'$. The Green function ϕ is then evaluated as

$$\begin{aligned} \phi(\mathbf{x}, \mathbf{r}') &= \frac{e^{ikR}}{R} \simeq \frac{1}{r} \exp \left[ik \left(r - \frac{\mathbf{x} \cdot \mathbf{r}'}{r} \right) \right] = \frac{1}{r} e^{ikr} \exp \left[-ik \frac{\mathbf{x} \cdot \mathbf{r}'}{r} \right] \\ &\simeq \frac{1}{r} e^{ikr} \left[1 + \left(-ik \frac{\mathbf{x} \cdot \mathbf{r}'}{r} \right) + \dots \right] = \phi_0(r) \left[1 - ik \hat{\mathbf{r}} \cdot \mathbf{r}' \right] \end{aligned} \quad (5.150)$$

with

$$\phi_0(r) = \frac{1}{r} e^{ikr}, \quad (5.151)$$

where $\hat{\mathbf{r}} = \mathbf{x}/r$ is the unit vector in the direction of \mathbf{x} . If $\hat{\mathbf{R}}$ is the unit vector in the direction of the vector $(\mathbf{x} - \mathbf{r}')$ defined by $\hat{\mathbf{R}} = (\mathbf{x} - \mathbf{r}')/|\mathbf{x} - \mathbf{r}'|$, $\nabla\phi$ in Eq. (5.147) becomes

$$\begin{aligned} \nabla \frac{e^{ikR}}{R} &= e^{ikR} \nabla \left(\frac{1}{R} \right) + \frac{1}{R} \nabla (e^{ikR}) = e^{ikR} \hat{\mathbf{R}} \frac{\partial}{\partial R} \left(\frac{1}{R} \right) + \frac{1}{R} \hat{\mathbf{R}} \frac{\partial}{\partial R} (e^{ikR}) \\ &= \hat{\mathbf{R}} e^{ikR} \left[\frac{-1}{R^2} + \frac{ik}{R} \right] \simeq \hat{\mathbf{R}} e^{ikR} \frac{ik}{R} = \hat{\mathbf{R}} ik \phi(\mathbf{x}, \mathbf{r}'), \end{aligned} \quad (5.152)$$

²² $\mathbf{E}_0 \times \mathbf{r} = -\hat{x}E_0y + \hat{y}E_0x$, which implies that $\mathbf{r} \times \mathbf{E}_0 = \hat{x}E_0y - \hat{y}E_0x$.

²³Eq. (A.82) is described in section A.5.

where the unit vector \hat{R} can be reduced by Eq. (5.149). Noting that $\mathbf{r}' \ll \mathbf{x}$ leads to $\mathbf{x} - \mathbf{r}' \simeq \mathbf{x}$ yields

$$\hat{R} = \frac{\mathbf{x} - \mathbf{r}'}{|\mathbf{x} - \mathbf{r}'|} \simeq \frac{\mathbf{x}}{r} = \hat{r}, \quad (5.153)$$

so that

$$\nabla \phi(\mathbf{x}, \mathbf{r}') = \hat{r} ik \phi(\mathbf{x}, \mathbf{r}') = \hat{r} ik \phi_0(r) [1 - ik \hat{r} \cdot \mathbf{r}']. \quad (5.154)$$

We then find from Eqs. (5.150) through (5.154) that Eq. (5.147) reduces to [116]

$$\begin{aligned} \mathbf{E}(\mathbf{x}) &= \frac{1}{[4\pi]} \int d^2x' \mathbf{K}_m^{\text{total}}(\mathbf{r}') \times \hat{r} ik \phi(\mathbf{x}, \mathbf{r}') = -\frac{ik}{[4\pi]} \int d^2x' \hat{r} \times \mathbf{K}_m^{\text{total}}(\mathbf{r}') \phi(\mathbf{x}, \mathbf{r}') \\ &= -\hat{r} \frac{ik}{[4\pi]} \times \int d^2x' \mathbf{K}_m^{\text{total}}(\mathbf{r}') \phi(\mathbf{x}, \mathbf{r}') \\ &= -\hat{r} \frac{ik}{[4\pi]} \times \int d^2x' \mathbf{K}_m^{\text{total}}(\mathbf{r}') \phi_0(r) [1 - ik \hat{r} \cdot \mathbf{r}']. \end{aligned} \quad (5.155)$$

By substituting Eq. (5.146) into this equation, we obtain

$$\begin{aligned} \mathbf{E}(\mathbf{x}) &= -\hat{r} \frac{ik}{[4\pi]} \times \int d^2x' \phi_0(r) \left(i\omega \frac{[4\pi\mu]}{\pi^2} \sqrt{a^2 - r'^2} \mathbf{H}_0 + \frac{[4\pi]}{2\pi^2} \frac{1}{\sqrt{a^2 - r'^2}} \mathbf{r}' \times \mathbf{E}_0 \right) (1 - ik \hat{r} \cdot \mathbf{r}') \\ &= \hat{r} \frac{k}{[4\pi]} \times \int d^2x' \left[\omega \frac{[4\pi\mu]}{\pi^2} \sqrt{a^2 - r'^2} \mathbf{H}_0 \phi_0(r) - k \frac{[4\pi]}{2\pi^2} \frac{1}{\sqrt{a^2 - r'^2}} \mathbf{r}' \times (\hat{r} \cdot \mathbf{r}') \phi_0(r) \mathbf{E}_0 \right. \\ &\quad \left. - i \left\{ \frac{[4\pi]}{2\pi^2} \frac{1}{\sqrt{a^2 - r'^2}} \mathbf{r}' \times \mathbf{E}_0 \phi_0(r) + k\omega \frac{[4\pi\mu]}{\pi^2} \sqrt{a^2 - r'^2} (\hat{r} \cdot \mathbf{r}') \phi_0(r) \mathbf{H}_0 \right\} \right], \end{aligned} \quad (5.156)$$

where we only treat the real part of this equation to calculate the E field since the real part of the E field is the only physically meaningful quantity. For this reason, we obtain

$$\text{Re } \mathbf{E}(\mathbf{x}) = \hat{r} k\omega \frac{[\mu]}{\pi^2} \phi_0(r) \times \mathbf{H}_0 \int d^2x' \sqrt{a^2 - r'^2} - \hat{r} \frac{k^2}{2\pi^2} \phi_0(r) \times \left[\int d^2x' \frac{(\hat{r} \cdot \mathbf{r}')}{\sqrt{a^2 - r'^2}} \mathbf{r}' \times \mathbf{E}_0 \right], \quad (5.157)$$

where \mathbf{H}_0 and \mathbf{E}_0 are constant vectors and ϕ_0 is a function of $r = |\mathbf{x}|$.

By taking $a^2 - r'^2 = t$ such that $-2r' dr' = dt$, the first integral in this equation can be evaluated in terms of the polar coordinates as

$$\begin{aligned} \text{Int 1} &= \int d^2x' \sqrt{a^2 - r'^2} = \int_0^{2\pi} d\theta' \int_0^a dr' r' \sqrt{a^2 - r'^2} \\ &= 2\pi \int_{a^2}^0 \frac{(-1)}{2} dt \sqrt{t} = \pi \int_0^{a^2} dt t^{1/2} = \pi \frac{1}{\frac{1}{2} + 1} t^{\frac{1}{2} + 1} \Big|_0^{a^2} = \frac{2\pi}{3} a^3. \end{aligned} \quad (5.158)$$

By using a change of variables, the second integral in Eq. (5.157) is evaluated as

$$\begin{aligned} \text{Int 2} &= \int d^2x' \frac{(\hat{r} \cdot \mathbf{r}')}{\sqrt{a^2 - r'^2}} \mathbf{r}' \times \mathbf{E}_0 = \int_0^{2\pi} d\theta' \int_0^a dr' r' \frac{(\hat{r} \cdot \mathbf{r}')}{\sqrt{a^2 - r'^2}} \mathbf{r}' \times \mathbf{E}_0 \\ &= \int_0^a dr' \frac{r'}{\sqrt{a^2 - r'^2}} \int_0^{2\pi} d\theta' (\hat{r} \cdot \mathbf{r}') \mathbf{r}' \times \mathbf{E}_0 = \int_0^a dr' \frac{r'^3}{\sqrt{a^2 - r'^2}} \int_0^{2\pi} d\theta' (\hat{r} \cdot \hat{r}') \hat{r}' \times \mathbf{E}_0, \end{aligned} \quad (5.159)$$

where $\mathbf{r}' = \hat{r}' r'$. Figure 5.5 shows the representation of the integral with respect to θ' in Eq. (5.159).

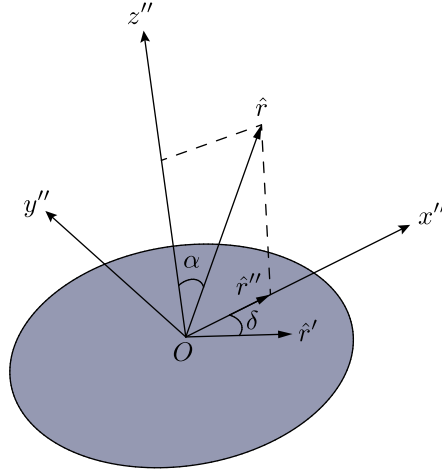


Figure 5.5: Representation of integration in Eq. (5.159). α is an angle defined as $\angle(\hat{r}, \hat{z}'')$ and δ is an angle defined as $\angle(\hat{r}', \hat{r}'')$.

We find from Fig. 5.5 that vectors \hat{r} and \hat{r}' can be described in terms of the Cartesian coordinates (x'', y'', z'') as

$$\hat{r}' = \hat{x}'' \cos \delta + \hat{y}'' (-\sin \delta), \quad (5.160a)$$

$$\hat{r} = \hat{x}'' \sin \alpha + \hat{z}'' \cos \alpha, \quad (5.160b)$$

yielding

$$\hat{r} \cdot \hat{r}' = \cos \delta \sin \alpha. \quad (5.161)$$

From Eqs. (5.160a) through (5.161), the integral with respect to θ' in Eq. (5.159) becomes²⁴

$$\begin{aligned} \text{Int 3} &= \int_0^{2\pi} d\theta' (\hat{r} \cdot \hat{r}') \hat{r}' \times \mathbf{E}_0 = -\mathbf{E}_0 \times \int_0^{2\pi} d\theta' (\hat{r} \cdot \hat{r}') \hat{r}' \\ &= -\mathbf{E}_0 \times \int_0^{2\pi} d\delta \cos \delta \sin \alpha (\hat{x}'' \cos \delta - \hat{y}'' \sin \delta) \\ &= -\mathbf{E}_0 \times \sin \alpha \left[\hat{x}'' \int_0^{2\pi} d\delta \cos^2 \delta - \hat{y}'' \int_0^{2\pi} d\theta' \cos \delta \sin \delta \right] \\ &= -\mathbf{E}_0 \times \hat{x}'' \pi \sin \alpha, \end{aligned} \quad (5.162a)$$

which can be expressed in terms of \hat{r} by noting that $\mathbf{E}_0 = \hat{z} E_0 = \hat{z}'' E_0$ is in the z'' direction, giving

$$\text{Int 3} = -\pi \hat{z}'' E_0 \times (\hat{x}'' \sin \alpha + \hat{z}'' \cos \alpha) = -\pi \mathbf{E}_0 \times \hat{r}, \quad (5.162b)$$

where $\hat{z}'' \times \hat{z}'' = 0$. We thereby find from Eq. (5.162b) that Eq. (5.159) is evaluated as

$$\text{Int 2} = -\pi \int_0^a dr' \frac{r'^3}{\sqrt{a^2 - r'^2}} \mathbf{E}_0 \times \hat{r} = -\pi \mathbf{E}_0 \times \hat{r} \int_0^a dr' \frac{r'^3}{\sqrt{a^2 - r'^2}}, \quad (5.163)$$

²⁴The Cartesian coordinates (x'', y'', z'') can be obtained by rotating the original coordinates (x', y', z') such that δ in (x'', y'', z'') has the same meaning as θ' in (x', y', z') , which can be described by the Jacobian.

where the integral in this equation can be obtained by taking $r' = a \sin t$ such that $dr' = a \cos t dt$, to obtain²⁵

$$\begin{aligned}
\text{Int 4} &= \int_0^a dr' \frac{r'^3}{\sqrt{a^2 - r'^2}} = a \int_0^{\frac{\pi}{2}} dt \cos t \frac{a^3 \sin^3 t}{\sqrt{a^2 - a^2 \sin^2 t}} \\
&= \int_0^{\frac{\pi}{2}} dt \frac{a^3 \sin^3 t}{a \cos t} = a^3 \int_0^{\frac{\pi}{2}} dt \sin^3 t = a^3 \int_0^{\frac{\pi}{2}} dt \sin t \left(\frac{1 - \cos 2t}{2} \right) \\
&= \frac{a^3}{2} \left[\int_0^{\frac{\pi}{2}} dt \sin t - \int_0^{\frac{\pi}{2}} \sin t \cos 2t \right] = \frac{a^3}{2} \left[\int_0^{\frac{\pi}{2}} dt \sin t - \frac{1}{2} \int_0^{\frac{\pi}{2}} (\sin 3t - \sin t) \right] \\
&= \frac{a^3}{2} \left[\frac{3}{2} \int_0^{\frac{\pi}{2}} dt \sin t - \frac{1}{2} \int_0^{\frac{\pi}{2}} dt \sin 3t \right] = \frac{a^3}{2} \left(-\frac{3}{2} \cos t \Big|_0^{\frac{\pi}{2}} + \frac{1}{2} \frac{1}{3} \cos 3t \Big|_0^{\frac{\pi}{2}} \right) \\
&= \frac{a^3}{2} \left(-\frac{3}{2}(-1) + \frac{1}{6}(-1) \right) = \frac{a^3}{2} \frac{4}{3} = \frac{2}{3} a^3.
\end{aligned} \tag{5.164}$$

Hence, we find by substituting (5.164) into Eq. (5.163) that the second integral in Eq. (5.157) can be solved to obtain

$$\text{Int 2} = -\frac{2\pi}{3} a^3 \mathbf{E}_0 \times \hat{r}. \tag{5.165}$$

Finally, we find by substituting Eqs. (5.158) and (5.165) into Eq. (5.157) that the diffracted E field obtained by Eq. (5.157) is written as [116]

$$\begin{aligned}
\text{Re } \mathbf{E}(\mathbf{x}) &= \hat{r} k \omega \frac{[\mu]}{\pi^2} \phi_0(r) \times \mathbf{H}_0 \frac{2\pi}{3} a^3 + \hat{r} \frac{k^2}{2\pi^2} \phi_0(r) \times \left(\frac{2\pi}{3} a^3 \mathbf{E}_0 \times \hat{r} \right) \\
&= \hat{r} \frac{k a^3}{3\pi} \phi_0(r) \times \left[2\omega[\mu] \mathbf{H}_0 + k(\mathbf{E}_0 \times \hat{r}) \right],
\end{aligned} \tag{5.166}$$

which can be written in the unit of Gaussian units (CGS) by replacing ω with $\omega/v = k$ as [116]

$$\text{Re } \mathbf{E}(\mathbf{x}) = \hat{r} \frac{k^2 a^3}{3\pi} \phi_0(r) \times \left[2\mathbf{H}_0 + \mathbf{E}_0 \times \hat{r} \right] \text{ (CGS)}. \tag{5.167}$$

5.3.2.8 Diffracted H field by a small hole

We recall from Eq. (5.70) that the H field induced by the magnetic surface current density and charge density can be obtained by replacing \mathbf{K}_m with $\mathbf{K}_m^{\text{total}}$, giving

$$\mathbf{H}(\mathbf{x}) = \mathbf{H}^{(1)}(\mathbf{x}) + \mathbf{H}^{(2)}(\mathbf{x}), \tag{5.168}$$

²⁵Note that $\cos 2t = \cos^2 t - \sin^2 t = 1 - 2 \sin^2 t$ such that $\sin^2 t = \frac{1 - \cos 2t}{2}$.
Furthermore, we find by subtracting $\sin(a - b)$ from $\sin(a + b)$ that

$$\begin{array}{l}
\sin(a + b) = \sin a \cos b + \sin b \cos a \\
\sin(a - b) = \sin a \cos b - \sin b \cos a \\
\hline
\sin(a + b) - \sin(a - b) = 2 \sin b \cos a
\end{array}$$

which implies that

$$\cos a \sin b = \frac{\sin(a + b) - \sin(a - b)}{2}.$$

where

$$\mathbf{H}^{(1)}(\mathbf{x}) = \left[\frac{\epsilon}{4\pi} \right] \int d^2x' i\omega \mathbf{K}_m^{\text{total}} \phi(\mathbf{x}, \mathbf{x}'), \quad (5.169a)$$

$$\mathbf{H}^{(2)}(\mathbf{x}) = -\frac{1}{[4\pi\mu]} \int d^2x' \eta_m(\mathbf{x}') \nabla \phi(\mathbf{x}, \mathbf{x}'). \quad (5.169b)$$

In the far-field zone (*i.e.* $|\mathbf{r}'| \ll |\mathbf{x}|$), we find by using the same method used in section 5.3.2.7 that

$$\begin{aligned} \mathbf{H}^{(1)}(\mathbf{x}) &= \left[\frac{\epsilon}{4\pi} \right] \int d^2x' i\omega \left(i\omega \frac{[4\pi\mu]}{\pi^2} \sqrt{a^2 - r'^2} \mathbf{H}_0 + \frac{[4\pi]}{2\pi^2} \frac{1}{\sqrt{a^2 - r'^2}} \mathbf{r}' \times \mathbf{E}_0 \right) \phi_0(r) \left[1 - ik \hat{r} \cdot \mathbf{r}' \right] \\ &= \left[\frac{\epsilon}{4\pi} \right] \int d^2x' \left[-\omega^2 \frac{[4\pi\mu]}{\pi^2} \sqrt{a^2 - r'^2} \mathbf{H}_0 \phi_0(r) + i\omega \frac{[4\pi]}{2\pi^2} \frac{1}{\sqrt{a^2 - r'^2}} \mathbf{r}' \times \mathbf{E}_0 \phi_0(r) \right. \\ &\quad \left. + ik\omega^2 \frac{[4\pi\mu]}{\pi^2} \sqrt{a^2 - r'^2} \mathbf{H}_0 (\hat{r} \cdot \mathbf{r}') \phi_0(r) + k\omega \frac{[4\pi]}{2\pi^2} \frac{1}{\sqrt{a^2 - r'^2}} \mathbf{r}' \times \mathbf{E}_0 (\hat{r} \cdot \mathbf{r}') \phi_0(r) \right] \\ &= \left[\frac{\epsilon}{4\pi} \right] \int d^2x' \left[-\omega^2 \frac{[4\pi\mu]}{\pi^2} \sqrt{a^2 - r'^2} \mathbf{H}_0 \phi_0(r) + k\omega \frac{[4\pi]}{2\pi^2} \frac{1}{\sqrt{a^2 - r'^2}} \mathbf{r}' \times \mathbf{E}_0 (\hat{r} \cdot \mathbf{r}') \phi_0(r) \right. \\ &\quad \left. + i \left\{ k\omega^2 \frac{[4\pi\mu]}{\pi^2} \sqrt{a^2 - r'^2} \mathbf{H}_0 (\hat{r} \cdot \mathbf{r}') \phi_0(r) + \omega \frac{[4\pi]}{2\pi^2} \frac{1}{\sqrt{a^2 - r'^2}} \mathbf{r}' \times \mathbf{E}_0 \phi_0(r) \right\} \right], \end{aligned} \quad (5.170a)$$

and

$$\begin{aligned} \mathbf{H}^{(2)}(\mathbf{x}) &= \frac{ik}{\pi^2} \int d^2x' \frac{\mathbf{H}_0 \cdot \mathbf{r}'}{\sqrt{a^2 - r'^2}} \hat{r} \phi_0(r) \left[1 - ik \hat{r} \cdot \mathbf{r}' \right] \\ &= \hat{r} \frac{k^2}{\pi^2} \phi_0(r) \int d^2x' \frac{\mathbf{H}_0 \cdot \mathbf{r}'}{\sqrt{a^2 - r'^2}} (\hat{r} \cdot \mathbf{r}') + i\hat{r} \frac{k}{\pi^2} \phi_0(r) \int d^2x' \frac{\mathbf{H}_0 \cdot \mathbf{r}'}{\sqrt{a^2 - r'^2}}. \end{aligned} \quad (5.170b)$$

By taking the real part of H field, we obtain

$$\begin{aligned} \text{Re } \mathbf{H}^{(1)}(\mathbf{x}) &= \left[\frac{\epsilon}{4\pi} \right] \int d^2x' \left[-\omega^2 \frac{[4\pi\mu]}{\pi^2} \sqrt{a^2 - r'^2} \mathbf{H}_0 \phi_0(r) \right. \\ &\quad \left. + k\omega \frac{[4\pi]}{2\pi^2} \frac{1}{\sqrt{a^2 - r'^2}} \mathbf{r}' \times \mathbf{E}_0 (\hat{r} \cdot \mathbf{r}') \phi_0(r) \right], \end{aligned} \quad (5.171a)$$

$$\text{Re } \mathbf{H}^{(2)}(\mathbf{x}) = \hat{r} \frac{k^2}{\pi^2} \phi_0(r) \int d^2x' \frac{\mathbf{H}_0 \cdot \mathbf{r}'}{\sqrt{a^2 - r'^2}} (\hat{r} \cdot \mathbf{r}'). \quad (5.171b)$$

Here the first and second integrals in Eq. (5.171a) corresponds to Eqs. (5.158) and (5.159) (\rightarrow (5.165)), respectively. So, the expression for $\text{Re } \mathbf{H}^{(1)}$ becomes [116]

$$\begin{aligned} \text{Re } \mathbf{H}^{(1)}(\mathbf{x}) &= -\frac{[\epsilon\mu]}{\pi^2} \omega^2 \mathbf{H}_0 \phi_0(r) \int d^2x' \sqrt{a^2 - r'^2} + k\omega \frac{[\epsilon]}{2\pi^2} \phi_0(r) \int d^2x' \frac{(\hat{r} \cdot \mathbf{r}')}{\sqrt{a^2 - r'^2}} \mathbf{r}' \times \mathbf{E}_0 \\ &= -\frac{[\epsilon\mu]}{3\pi} 2a^3 \omega^2 \phi_0(r) \mathbf{H}_0 - \frac{[\epsilon]}{3\pi} a^3 k\omega \phi_0(r) \mathbf{E}_0 \times \hat{r} \\ &= -\frac{\omega a^3}{3\pi} [\epsilon] \phi_0(r) \left(2\omega[\mu] \mathbf{H}_0 + k \mathbf{E}_0 \times \hat{r} \right). \end{aligned} \quad (5.172)$$

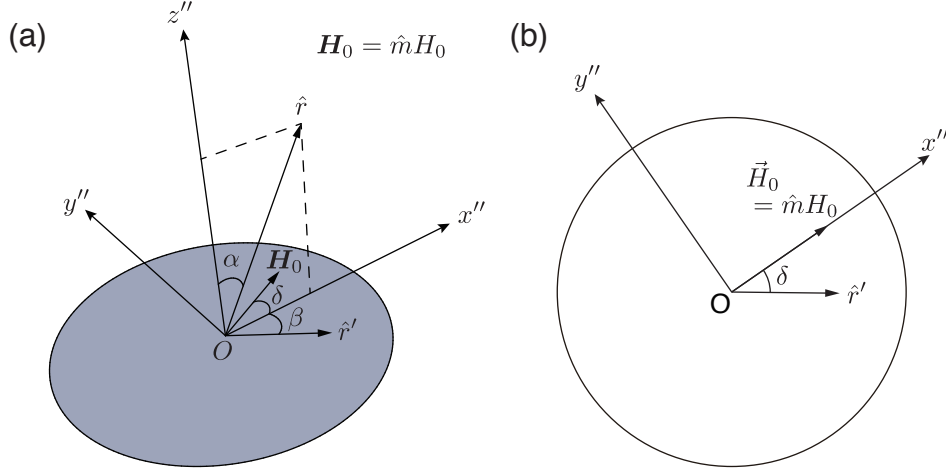


Figure 5.6: Representations for integration in (a) Eq. (5.171b) and (b) Eq. (5.182b). α is an angle defined as $\angle(\hat{r}, \hat{z}'')$ and δ is an angle defined as $\angle(\hat{r}', \mathbf{H}_0)$. A unit vector \hat{m} is parallel to the constant H field vector \mathbf{H}_0 .

Eq. (5.171b) can be rewritten in terms of the polar coordinates as

$$\text{Re } \mathbf{H}^{(2)}(\mathbf{x}) = \hat{r} \frac{k^2}{\pi^2} \phi_0(r) \int_0^a dr' \frac{r'^3}{\sqrt{a^2 - r'^2}} \int_0^{2\pi} d\theta' \mathbf{H}_0 \cdot \hat{r}' (\hat{r} \cdot \hat{r}'), \quad (5.173)$$

where $\mathbf{r}' = \hat{r}' r'$. The integral in Eq. (5.173) cannot be handled before, but can now be solved by using the similar method as in section 5.3.2.7 to calculate the second integration in Eq. (5.157). Figure 5.6(a) shows the schematic representation of the integral with respect to θ' in Eq. (5.173). By analogy with Eq. (5.162a), we find that the integral with respect to θ' in Eq. (5.173) is evaluated as

$$\text{Int } 5 = \int_0^{2\pi} d\theta' \mathbf{H}_0 \cdot \hat{r}' (\hat{r} \cdot \hat{r}') = \mathbf{H}_0 \cdot \int_0^{2\pi} d\theta' \hat{r}' (\hat{r} \cdot \hat{r}') = \mathbf{H}_0 \cdot \hat{x}'' \pi \sin \alpha, \quad (5.174a)$$

which can be expressed in terms of \hat{r} by noting that $\mathbf{H}_0 = \hat{m} H_0$ is in the $x''y''$ plane as

$$\text{Int } 5 = \pi \hat{m} H_0 \cdot (\hat{x}'' \sin \alpha + \hat{z}'' \cos \alpha) = \pi \mathbf{H}_0 \cdot \hat{r}, \quad (5.174b)$$

where $\hat{m} \cdot \hat{z}'' = 0$. By substituting this equation into Eq. (5.173), we obtain

$$\text{Re } \mathbf{H}^{(2)}(\mathbf{x}) = \hat{r} \frac{k^2}{\pi} \phi_0(r) (\mathbf{H}_0 \cdot \hat{r}) \int_0^a dr' \frac{r'^3}{\sqrt{a^2 - r'^2}}. \quad (5.175)$$

We therefore find from Eq. (5.164) that

$$\text{Re } \mathbf{H}^{(2)}(\mathbf{x}) = \hat{r} \frac{2k^2 a^3}{3\pi} \phi_0(r) (\mathbf{H}_0 \cdot \hat{r}). \quad (5.176)$$

Through use of the following relation²⁶

$$\hat{r} \times (\mathbf{H}_0 \times \hat{r}) = (\hat{r} \cdot \hat{r}) \mathbf{H}_0 - \hat{r} (\hat{r} \cdot \mathbf{H}_0), \quad (5.177)$$

²⁶Note that $\mathbf{a} \times (\mathbf{b} \times \mathbf{c}) = \mathbf{b}(\mathbf{a} \cdot \mathbf{c}) - \mathbf{c}(\mathbf{a} \cdot \mathbf{b})$.

the expression for $\text{Re } \mathbf{H}^{(2)}$ becomes

$$\text{Re } \mathbf{H}^{(2)}(\mathbf{x}) = \frac{2k^2 a^3}{3\pi} \phi_0(r) \left(\mathbf{H}_0 - \hat{r} \times (\mathbf{H}_0 \times \hat{r}) \right). \quad (5.178)$$

By combining Eqs. (5.172) and (5.178), we find that the diffracted H field can be expressed as

$$\begin{aligned} \text{Re } \mathbf{H}(\mathbf{x}) &= -\frac{\omega a^3}{3\pi} [\epsilon] \phi_0(r) \left(2\omega [\mu] \mathbf{H}_0 + k \mathbf{E}_0 \times \hat{r} \right) + \frac{2k^2 a^3}{3\pi} \phi_0(r) \left(\mathbf{H}_0 - \hat{r} \times (\mathbf{H}_0 \times \hat{r}) \right) \\ &= -\frac{2\omega^2 a^3}{3\pi} [\mu \epsilon] \phi_0(r) \mathbf{H}_0 - \frac{k\omega a^3}{3\pi} [\epsilon] \phi_0(r) \mathbf{E}_0 \times \hat{r} \\ &\quad + \frac{2k^2 a^3}{3\pi} \phi_0(r) \mathbf{H}_0 - \frac{2k^2 a^3}{3\pi} \phi_0(r) \hat{r} \times (\mathbf{H}_0 \times \hat{r}), \end{aligned} \quad (5.179)$$

which can be written in the Gaussian units (CGS) by replacing ω with $\omega/v = k$ as [116]

$$\begin{aligned} \text{Re } \mathbf{H}(\mathbf{x}) &= -\frac{2k^2 a^3}{3\pi} \phi_0(r) \mathbf{H}_0 - \frac{k^2 a^3}{3\pi} \phi_0(r) \mathbf{E}_0 \times \hat{r} + \frac{2k^2 a^3}{3\pi} \phi_0(r) \mathbf{H}_0 - \frac{2k^2 a^3}{3\pi} \phi_0(r) \hat{r} \times (\mathbf{H}_0 \times \hat{r}) \\ &= -\frac{k^2 a^3}{3\pi} \phi_0(r) \mathbf{E}_0 \times \hat{r} - \frac{2k^2 a^3}{3\pi} \phi_0(r) \hat{r} \times (\mathbf{H}_0 \times \hat{r}) \\ &= -\frac{k^2 a^3}{3\pi} \phi_0(r) \left(2 \hat{r} \times (\mathbf{H}_0 \times \hat{r}) + \mathbf{E}_0 \times \hat{r} \right) = -\frac{k^2 a^3}{3\pi} \phi_0(r) \left(2 \hat{r} \times (\mathbf{H}_0 \times \hat{r}) - \hat{r} \times \mathbf{E}_0 \right) \\ &= -\frac{k^2 a^3}{3\pi} \phi_0(r) \hat{r} \times \left(2\mathbf{H}_0 \times \hat{r} - \mathbf{E}_0 \right) \quad (\text{CGS}). \end{aligned} \quad (5.180)$$

5.3.2.9 Magnetic dipole moment

Analogous to the electric case, the magnetic dipole moment \mathbf{M} can be written in terms of its magnetic charge density as [116]

$$\mathbf{m} = \int d^2 x' \eta_m(\mathbf{r}') \mathbf{r}'. \quad (5.181)$$

From Eq. (5.114), the magnetic dipole moment in the hole can be written as

$$\mathbf{m} = -\frac{[4\pi\mu]}{\pi^2} \int d^2 x' \left(\frac{\mathbf{H}_0 \cdot \mathbf{r}'}{\sqrt{a^2 - r'^2}} \right) \mathbf{r}', \quad (5.182a)$$

which can be rewritten in terms of the polar coordinates as

$$\begin{aligned} \mathbf{m} &= -\frac{[4\pi\mu]}{\pi^2} \int_0^{2\pi} d\theta' \int_0^a dr' r' \frac{\mathbf{H}_0 \cdot \mathbf{r}'}{\sqrt{a^2 - r'^2}} \mathbf{r}' \\ &= -\frac{[4\pi\mu]}{\pi^2} \int_0^a dr' \frac{r'}{\sqrt{a^2 - r'^2}} \int_0^{2\pi} d\theta' \mathbf{H}_0 \cdot \mathbf{r}' \mathbf{r}' \\ &= -\frac{[4\pi\mu]}{\pi^2} \int_0^a dr' \frac{r'^3}{\sqrt{a^2 - r'^2}} \int_0^{2\pi} d\theta' \mathbf{H}_0 \cdot \hat{r}' \hat{r}', \end{aligned} \quad (5.182b)$$

where $\mathbf{r}' = \hat{r}' r'$. The last integral with respect to θ' can be solved by using the similar method used in section 5.3.2.7 to calculate the second integration in Eq. (5.157). Figure 5.6 shows the representation of the integral with respect to θ' in Eq. (5.182b). Using a notation similar to that of Eqs. (5.160a) and (5.160b), we find from Fig. 5.6 that

$$\hat{r}' = \hat{x}'' \cos \delta + \hat{y}'' (-\sin \delta), \quad (5.183a)$$

$$\hat{m} = \hat{x}'', \quad (5.183b)$$

which yield

$$\mathbf{H}_0 \cdot \hat{\mathbf{r}}' = H_0 \hat{m} \cdot \hat{\mathbf{r}}' = H_0 \hat{x}'' \cdot (\hat{x}'' \cos \delta + \hat{y}'' (-\sin \delta)) = H_0 \cos \delta. \quad (5.184)$$

From this equation, the integral with respect to θ' is evaluated as

$$\begin{aligned} \text{Int 6} &= \int_0^{2\pi} d\theta' \mathbf{H}_0 \cdot \hat{\mathbf{r}}' \hat{\mathbf{r}}' = \int_0^{2\pi} d\delta H_0 \cos \delta (\hat{x}'' \cos \delta + \hat{y}'' (-\sin \delta)) \\ &= H_0 \left[\hat{x}'' \int_0^{2\pi} d\delta \cos^2 \delta - \hat{y}'' \int_0^{2\pi} d\delta \cos \delta \sin \delta \right] = H_0 \hat{x}'' \pi = \pi \mathbf{H}_0. \end{aligned} \quad (5.185)$$

By substituting Eq. (5.185) into Eq. (5.182b), we thus find from Eq. (5.164) that the magnetic dipole moment is expressed as [116]

$$\mathbf{m} = -\frac{[4\pi\mu]}{\pi^2} \int_0^a dr' \frac{r'^3}{\sqrt{a^2 - r'^2}} \pi \mathbf{H}_0 = -\frac{[4\pi\mu]}{\pi} \mathbf{H}_0 \int_0^a dr' \frac{r'^3}{\sqrt{a^2 - r'^2}} = -[4\pi\mu] \frac{2}{3\pi} \mathbf{H}_0 a^3. \quad (5.186)$$

5.3.2.10 Electric dipole moment

By introducing Eq. (5.186) into Eq. (5.167), the E field can be expressed as

$$\begin{aligned} \text{Re } \mathbf{E}(\mathbf{x}) &= -\hat{\mathbf{r}} k^2 \phi_0(r) \times \left[-\frac{2}{3\pi} \mathbf{H}_0 a^3 \right] + \hat{\mathbf{r}} k^2 \phi_0(r) \times \left(\frac{1}{3\pi} \mathbf{E}_0 a^3 \times \hat{\mathbf{r}} \right) \\ &= -\hat{\mathbf{r}} k^2 \phi_0(r) \times \mathbf{m} + \hat{\mathbf{r}} k^2 \phi_0(r) \times \left(\frac{1}{3\pi} \mathbf{E}_0 a^3 \times \hat{\mathbf{r}} \right) \quad (\text{CGS}). \end{aligned} \quad (5.187)$$

The electric surface dipole moment is defined as [12]

$$\mathbf{p} = \int d^2x' \sigma(\mathbf{r}') \mathbf{r}', \quad (5.188)$$

where σ is the electric surface charge density defined as

$$\sigma = \mathbf{P} \cdot \hat{\mathbf{n}}, \quad (5.189)$$

where \mathbf{P} is the polarization defined as $\mathbf{P} = \chi \mathbf{E}$ (CGS). We then can easily see from Eq. (5.188) through (5.189) that the electric dipole moment is of the order $E_0 a^3$. We hence conclude from Eq. (5.187) that the electric dipole moment in our case can be deduced as [116]

$$\mathbf{p} = \frac{1}{3\pi} \mathbf{E}_0 a^3. \quad (5.190)$$

The electric dipole moment in Eq. (5.190) is also obtained by expressing Eq. (5.166) in the SI units yielding the same result.

5.3.2.11 Relation between diffracted H field and diffracted E field

The expressions for the H field and E field are

$$\text{Re } \mathbf{H}(\mathbf{x}) = -\frac{k^2 a^3}{3\pi} \phi_0(r) \hat{\mathbf{r}} \times (2\mathbf{H}_0 \times \hat{\mathbf{r}} - \mathbf{E}_0) \quad (\text{CGS}), \quad (5.191)$$

$$\text{Re } \mathbf{E}(\mathbf{x}) = \hat{\mathbf{r}} \frac{k^2 a^3}{3\pi} \phi_0(r) \times (2\mathbf{H}_0 + \mathbf{E}_0 \times \hat{\mathbf{r}}) \quad (\text{CGS}). \quad (5.192)$$

Here it is easily seen that

$$\hat{r} \times (\hat{r} \times \mathbf{H}_0) = (\hat{r} \cdot \mathbf{H}_0) \hat{r} - (\hat{r} \cdot \hat{r}) \mathbf{H}_0 = \hat{r} (\hat{r} \cdot \mathbf{H}_0) - \mathbf{H}_0. \quad (5.193)$$

Using this equation, we obtain

$$\begin{aligned} \hat{r} \times \left[\hat{r} \times (\hat{r} \times \mathbf{H}_0) \right] &= \hat{r} \times \left[\hat{r} (\hat{r} \cdot \mathbf{H}_0) \right] - \hat{r} \times \mathbf{H}_0 \\ &= (\hat{r} \cdot \mathbf{H}_0) \hat{r} - \hat{r} \times \mathbf{H}_0 = -\hat{r} \times \mathbf{H}_0, \end{aligned} \quad (5.194a)$$

which implies that

$$\hat{r} \times \left[\hat{r} \times (\mathbf{H}_0 \times \hat{r}) \right] = \hat{r} \times \mathbf{H}_0. \quad (5.194b)$$

Similarly, it is also easily seen that

$$\hat{r} \times (\hat{r} \times \mathbf{E}_0) = \hat{r} (\hat{r} \cdot \mathbf{E}_0) - \mathbf{E}_0. \quad (5.195)$$

This equation further make

$$\hat{r} \times \left[\hat{r} \times (\hat{r} \times \mathbf{E}_0) \right] = -\hat{r} \times \mathbf{E}_0, \quad (5.196a)$$

which implies that

$$\hat{r} \times \left[\hat{r} \times (\mathbf{E}_0 \times \hat{r}) \right] = \hat{r} \times \mathbf{E}_0. \quad (5.196b)$$

From Eqs. (5.193) through (5.196b), the expression for the H field in Eq. (5.191) becomes [116]

$$\begin{aligned} \hat{r} \times \text{Re } \mathbf{H}(\mathbf{x}) &= -\frac{k^2 a^3}{3\pi} \phi_0(r) \hat{r} \times \left(2\hat{r} \times (\mathbf{H}_0 \times \hat{r}) - \hat{r} \times \mathbf{E}_0 \right) \\ &= -\frac{k^2 a^3}{3\pi} \phi_0(r) \left[2\hat{r} \times (\hat{r} \times (\mathbf{H}_0 \times \hat{r})) - \hat{r} \times (\hat{r} \times \mathbf{E}_0) \right] \\ &= -\frac{k^2 a^3}{3\pi} \phi_0(r) \left[2\hat{r} \times \mathbf{H}_0 - \hat{r} \times (\hat{r} \times \mathbf{E}_0) \right] \\ &= -\hat{r} \frac{k^2 a^3}{3\pi} \phi_0(r) \times \left[2\mathbf{H}_0 + \mathbf{E}_0 \times \hat{r} \right] = -\text{Re } \mathbf{E}(\mathbf{x}) \quad (\text{CGS}). \end{aligned} \quad (5.197)$$

Similarly, we can obtain the expression for the E field in Eq. (5.192) as [116]

$$\begin{aligned} \hat{r} \times \text{Re } \mathbf{E}(\mathbf{x}) &= \frac{k^2 a^3}{3\pi} \phi_0(r) \hat{r} \times \left[2\hat{r} \times \mathbf{H}_0 + \hat{r} \times (\mathbf{E}_0 \times \hat{r}) \right] \\ &= \frac{k^2 a^3}{3\pi} \phi_0(r) \left[2\hat{r} \times (\hat{r} \times \mathbf{H}_0) + \hat{r} \times (\hat{r} \times (\mathbf{E}_0 \times \hat{r})) \right] \\ &= \frac{k^2 a^3}{3\pi} \phi_0(r) \left[2\hat{r} \times (\hat{r} \times \mathbf{H}_0) + \hat{r} \times \mathbf{E}_0 \right] \\ &= \hat{r} \frac{k^2 a^3}{3\pi} \phi_0(r) \times \left[2\hat{r} \times \mathbf{H}_0 + \mathbf{E}_0 \right] \\ &= \hat{r} \frac{k^2 a^3}{3\pi} \phi_0(r) \times \left[-2\mathbf{H}_0 \times \hat{r} + \mathbf{E}_0 \right] = \text{Re } \mathbf{H}(\mathbf{x}) \quad (\text{CGS}). \end{aligned} \quad (5.198)$$

We therefore find that Eqs. (5.197) and (5.198) satisfy Maxwell's equations for plane waves [116].

5.3.2.12 Diffracted waves in the radiation zone

When the incident waves are transverse, the normal component of the E field is zero, which leads to $\mathbf{E}_0 = 0$. For this reason, the expressions for H and E fields in the far-field zone are given in accordance to Eqs. (5.191) and (5.192) by

$$\text{Re } \mathbf{H}(\mathbf{x}) = -\frac{2k^2 a^3}{3\pi} \phi_0(r) \hat{r} \times (\mathbf{H}_0 \times \hat{r}) \quad (\text{CGS}), \quad (5.199)$$

$$\text{Re } \mathbf{E}(\mathbf{x}) = \hat{r} \frac{2k^2 a^3}{3\pi} \phi_0(r) \times \mathbf{H}_0 \quad (\text{CGS}), \quad (5.200)$$

which can be rewritten in the SI units as

$$\text{Re } \mathbf{H}(\mathbf{x}) = -\frac{2k^2 a^3}{3\pi} \phi_0(r) \hat{r} \times (\mathbf{H}_0 \times \hat{r}), \quad (5.201)$$

$$\text{Re } \mathbf{E}(\mathbf{x}) = \hat{r} \frac{2ka^3}{3\pi} \phi_0(r) \times \omega[\mu] \mathbf{H}_0. \quad (5.202)$$

Furthermore, E and H fields are expressed in terms of the magnetic dipole moment as²⁷

$$\begin{aligned} \text{Re } \mathbf{H}(\mathbf{x}) &= \frac{k^2}{[4\pi\mu]} \phi_0(r) \hat{r} \times \left[\left(-[4\pi\mu] \frac{2}{3\pi} \mathbf{H}_0 a^3 \right) \times \hat{r} \right] \\ &= \frac{k^2}{[4\pi\mu]} \hat{r} \times (\mathbf{m} \times \hat{r}) \phi_0(r), \end{aligned} \quad (5.203)$$

$$\begin{aligned} \text{Re } \mathbf{E}(\mathbf{x}) &= -\frac{vk}{[4\pi]} \phi_0(r) \hat{r} \times \frac{\omega}{v} \left(-[4\pi\mu] \frac{2}{3\pi} \mathbf{H}_0 a^3 \right) \\ &= -\frac{vk^2}{[4\pi]} \hat{r} \times \mathbf{m} \phi_0(r). \end{aligned} \quad (5.204)$$

5.3.3 Diffraction by a sub-wavelength slit

According to Bethe [116], Eqs. (5.35) and (5.37) obtained by the boundary conditions are regardless of shape and size of the hole. We can thus apply this condition to the case of a single slit as well as a hole. For this reason, the constant H field is regardless to the slit direction [116, 122, 123]. Recall that we can deduce from the waveguide theory that the electric field perpendicular to the slit direction can propagate through the slit due to the low cutoff frequency. However, the electric field parallel to the slit direction is difficult to propagate according to the same analogy. The E field inside the slit thus exhibits a strong polarization dependence. Therefore, each case of the slit direction perpendicular to either the H field or E field is physically interpreted as E field reducing case [116, 123, 128] or the E field enhancing case [111, 112, 123, 128]. The normal component of the E field in the hole is neglected when the incident field is a transverse field [116].

5.3.3.1 E field parallel to the slit direction: \parallel -case

When the incident H field \mathbf{H}_0 is perpendicular to the slit direction ($\mathbf{H} \perp \mathbf{L}$), the diffracted E field can be thought of as the radiation originating from the magnetic dipole moment at the far field zone as

²⁷Compare these expressions with equations in Jackson [12] p. 411.

a function of wavenumber $k = \omega/c = 2\pi/\lambda$ given as [12, 116]

$$\begin{aligned}\mathbf{H}(\mathbf{r}) &= \frac{k^2}{4\pi\mu_0} \hat{\mathbf{n}} \times (\mathbf{m} \times \hat{\mathbf{n}}) \frac{\exp(ikr)}{r}, \\ \mathbf{E}(\mathbf{r}) &= -\frac{ck^2}{4\pi} \hat{\mathbf{n}} \times \mathbf{m} \frac{\exp(ikr)}{r},\end{aligned}\tag{5.205}$$

where \mathbf{m} and $\hat{\mathbf{n}}$ are the magnetic dipole moment and a unit vector in the direction of the field point \mathbf{r} , respectively. The magnitude of the field point and the speed of light are denoted as r and c , respectively.

5.3.3.1.1 Magnetic surface charge density in a sub-wavelength slit

A constant H field in the slit can be produced by an ellipsoidal magnetic dipole distribution having the same direction of the magnetic field [116]. The magnetic charge distribution from an ellipsoid with a height of h along the z' -axis will be identical to the surface charge distribution provided that h is sufficiently small [116]. The cross section of the ellipsoid in the $x'y'$ plane becomes approximately a rectangular slit with width d on the x' -axis and length L on the y' -axis as shown in Fig. 5.7. Analogous to Eq. (5.96), we find that the equation for the ellipsoid with $d \ll L$ is given by

$$\frac{x'^2}{(d/2)^2} + \frac{y'^2}{(L/2)^2} + \frac{z'^2}{(h/2)^2} = 1,\tag{5.206}$$

which implies that the ordinate of the ellipsoid in Fig. 5.7 can be expressed as

$$z = \frac{h}{2} \sqrt{1 - \frac{x'^2}{(d/2)^2} - \frac{y'^2}{(L/2)^2}} = \frac{h}{d} \sqrt{\frac{d^2}{4} - x'^2 - y'^2 \frac{d^2}{L^2}},\tag{5.207}$$

so that

$$z \simeq \frac{h}{d} \sqrt{\frac{d^2}{4} - x'^2}.\tag{5.208}$$

So, we find from this equation that the ordinate (z -axis) of the ellipsoid for $d \ll L$ is proportional to $\sqrt{d^2/4 - x'^2}$ [123]. In a similar fashion to Eq. (5.99), the magnetic surface charge density η can then be

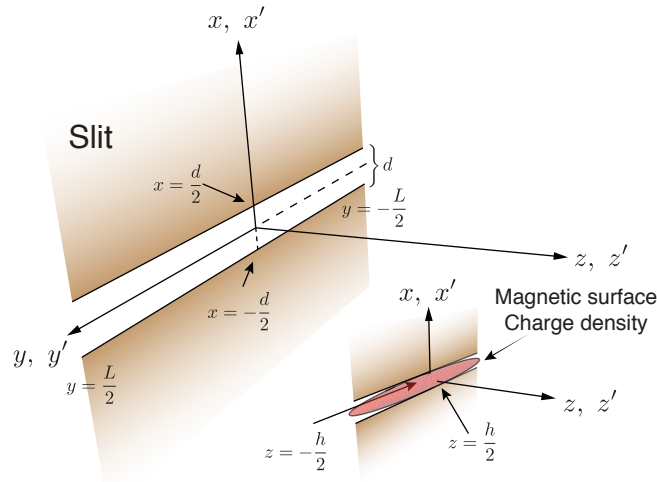


Figure 5.7: The magnetic surface charge density η over the slit.

expressed as²⁸

$$\eta(x', y') = C \mathbf{H}_0 \cdot \nabla' \left[\sqrt{\frac{d^2}{4} - x'^2} \right] = -C \frac{H_0 x'}{\sqrt{\frac{d^2}{4} - x'^2}}, \quad (5.211)$$

where C is a proportional coefficient and $\mathbf{H}_0 = \hat{x}' H_0$ since we assumed that the initial H field is perpendicular to the slit direction [12, 116, 123]. The coefficient was obtained by the following two steps. First, it is need to calculate the infinitesimal H field $\delta \mathbf{H}$ induced from the magnetic volume charge density ρ at the infinitesimal displacement $\delta x'$ located at $(x - x')$ as in Fig. 5.8, giving

$$\nabla \cdot \delta \mathbf{H} = \frac{\rho}{[\mu_0]}, \quad (5.212)$$

where $\rho(\mathbf{x}) = \rho(x') \delta(\mathbf{x} - \mathbf{x}')$. After applying Gauss's law to Eq. (5.212) assuming that the slit is wrapped by a Gaussian cylinder (V) with a closed surface (S) whose a radius is $x - x'$ along the y -axis as shown in Fig. 5.8, we obtain

$$\int_V \nabla \cdot \delta \mathbf{H} d^3x = \frac{1}{[\mu_0]} \int d^3x \rho(\mathbf{x}), \quad (5.213)$$

which becomes

$$\int_S \delta \mathbf{H} \cdot \hat{\mathbf{n}} da = \frac{1}{[\mu_0]} \int d^3x' \rho(\mathbf{x}'), \quad (5.214)$$

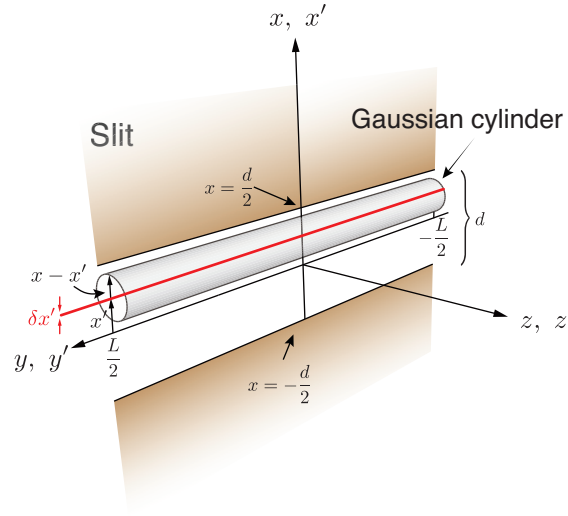


Figure 5.8: The Gaussian cylinder in the slit.

²⁸By taking the divergence of both sides of Eq. (5.208), we obtain

$$\begin{aligned} \nabla' \left[\sqrt{\frac{d^2}{4} - x'^2} \right] &= \left[\hat{x}' \frac{\partial}{\partial x'} + \hat{y}' \frac{\partial}{\partial y'} + \hat{z}' \frac{\partial}{\partial z'} \right] \sqrt{\frac{d^2}{4} - x'^2} \\ &= \hat{x}' \frac{1}{2} \left(\frac{d^2}{4} - x'^2 \right)^{-\frac{1}{2}} (-2x') = -\frac{\hat{x}' x'}{\sqrt{\frac{d^2}{4} - x'^2}}. \end{aligned} \quad (5.209)$$

Since \mathbf{H}_0 is a constant vector perpendicular to the slit direction, *i.e.*, $\mathbf{H} \perp \mathbf{L}$, we find that $\mathbf{H} = \hat{x}' H_0$, which leads to

$$\eta(x', y') \propto \mathbf{H}_0 \cdot \nabla' \left[\sqrt{\frac{d^2}{4} - x'^2} \right] = \hat{x}' H_0 \cdot \frac{(-\hat{x}' x')}{\sqrt{\frac{d^2}{4} - x'^2}} = -\frac{H_0 x'}{\sqrt{\frac{d^2}{4} - x'^2}}. \quad (5.210)$$

where $\rho(\mathbf{x}) = \rho(\mathbf{x}')\delta(\mathbf{x} - \mathbf{x}')$. The volume integral can then be evaluated over the closed surface given by

$$\int_S \delta \mathbf{H} \cdot \hat{\mathbf{n}} da = \frac{1}{[\mu_0]} \int_{-\frac{L}{2}}^{\frac{L}{2}} dy' \int_{-\frac{\delta x'}{2}}^{\frac{\delta x'}{2}} dx' \eta(x', y'), \quad (5.215)$$

where the volume charge density was defined as $\rho(\mathbf{x}') = \eta(x', y') \delta(z')$. η is a constant in $\delta x'$ and the infinitesimal area ($\hat{\mathbf{n}} da$) over the Gaussian surface is $\hat{\mathbf{n}} da = \hat{\mathbf{r}} r d\phi dx = \hat{\mathbf{r}}(x - x') d\phi dx$ in which ϕ is the azimuthal angle of the Gaussian surface. Using this relation, Eq. (5.215) is calculated as²⁹

$$\delta H(x - x') 2\pi L = \frac{1}{\mu_0} L \delta x' \eta. \quad (5.218)$$

Second, the H field induced from the magnetic charge density over the whole x' range is obtained. The H field in the Gaussian surface can be retrieved by integrating Eq. (5.218) over the x' from $-d/2$ to $d/2$ given by [123]

$$H = -\frac{C}{2\pi[\mu_0]} \int_{-\frac{d}{2}}^{\frac{d}{2}} dx' \frac{H_0 x'}{(x - x')\sqrt{\frac{d^2}{4} - x'^2}}, \quad (5.219)$$

where H is $1/2 H_0$ since the H field in the slit is half of the initial H field described in Eq. (5.35). When calculating Eq. (5.219), we conducted integration over the optical axis ($x = 0$) for the sake of simplicity [123]. After some integration, a constant C was determined as μ_0 as follows³⁰

$$\eta(x', y') = -[\mu_0] \frac{H_0 x'}{\sqrt{\frac{d^2}{4} - x'^2}}. \quad (5.224)$$

²⁹The left-hand side of Eq. (5.215) becomes

$$\int_S \delta \mathbf{H} \cdot \hat{\mathbf{n}} da = \int_S \hat{\mathbf{r}} \delta H \cdot \hat{\mathbf{r}}(y - y') d\phi dx = (x - x') \delta H \int_0^{2\pi} d\phi \int_{-L/2}^{L/2} dx = (x - x') \delta H 2\pi L. \quad (5.216)$$

Furthermore, the right-hand side of Eq. (5.215) becomes

$$\frac{1}{[\mu_0]} \int_{-\frac{L}{2}}^{\frac{L}{2}} dy' \int_{-\frac{\delta x'}{2}}^{\frac{\delta x'}{2}} dx' \eta(x', y') = \frac{1}{[\mu_0]} \eta \int_{-\frac{L}{2}}^{\frac{L}{2}} dy' \int_{-\frac{\delta x'}{2}}^{\frac{\delta x'}{2}} dx' = \frac{1}{[\mu_0]} \eta L \delta x'. \quad (5.217)$$

³⁰

$$H = \frac{1}{2} H_0 = -\frac{C}{2\pi[\mu_0]} \int_{-\frac{d}{2}}^{\frac{d}{2}} dx' \frac{H_0 x'}{(x - x')\sqrt{\frac{d^2}{4} - x'^2}}, \quad (5.220)$$

which implies that

$$\frac{1}{2} = -\frac{C}{2\pi[\mu_0]} \int_{-\frac{d}{2}}^{\frac{d}{2}} dx' \frac{x'}{(x - x')\sqrt{\frac{d^2}{4} - x'^2}}, \quad (5.221)$$

where H_0 is a constant. For the optical axis ($x = 0$), this equation becomes

$$\frac{1}{2} = -\frac{C}{2\pi[\mu_0]} \int_{-\frac{d}{2}}^{\frac{d}{2}} dx' \frac{x'}{(x - x')\sqrt{\frac{d^2}{4} - x'^2}} = \frac{C}{2\pi[\mu_0]} \int_{-\frac{d}{2}}^{\frac{d}{2}} dx' \frac{1}{\sqrt{\frac{d^2}{4} - x'^2}}. \quad (5.222)$$

By taking $x' = \frac{d}{2} \sin t$ such that $dx' = \frac{d}{2} \cos t dt$, we find that $t = \pi/2$ for $x' = d/2$ and $t = -\pi/2$ for $x' = -d/2$. The integral in Eq. (5.222) can then be evaluated as

$$\int_{-\frac{d}{2}}^{\frac{d}{2}} dx' \frac{1}{\sqrt{\frac{d^2}{4} - x'^2}} = \int_{-\frac{\pi}{2}}^{\frac{\pi}{2}} \frac{d}{2} \cos t dt \frac{1}{\sqrt{\frac{d^2}{4} - \frac{d^2}{4} \sin^2 t}} = \int_{-\frac{\pi}{2}}^{\frac{\pi}{2}} \frac{d}{2} \cos t dt \frac{1}{\frac{d}{2} \cos t} = \int_{-\frac{\pi}{2}}^{\frac{\pi}{2}} dt = \pi. \quad (5.223)$$

Therefore, we find by comparing both sides of Eq. (5.222) that the constant C equals $[\mu_0]$.

5.3.3.1.2 Magnetic dipole moment in a sub-wavelength slit

We derived the surface magnetic charge density η from the ellipsoidal magnetic dipole distribution. From η , the magnetic dipole moment \mathbf{m} can be calculated as [116, 123]³¹

$$\begin{aligned} m &= \int_S dx' dy' \eta(x', y') x' \\ &= -[\mu_0] \int_{-\frac{d}{2}}^{\frac{d}{2}} dy' \int_{-\frac{d}{2}}^{\frac{d}{2}} dx' \frac{H_0 x'^2}{\sqrt{\frac{d^2}{4} - x'^2}} = -\frac{\pi[\mu_0]}{8} d^2 L H_0, \end{aligned} \quad (5.226)$$

where the magnetic dipole was interpreted in the direction of the x' -axis since we assumed that η is a function of x' with no y' -dependence. We find that the dipole moment m is antiparallel to the initial H field H_0 as expected by Bethe [116].

5.3.3.1.3 Diffracted E field by a sub-wavelength slit when $\mathbf{E}_0 \parallel \mathbf{L}$

Therefore, the diffracted E field with harmonic time dependence $\exp(-i\omega t)$ by a small slit is³²

$$\mathbf{E}(z, t) \equiv \mathbf{E}_{\parallel} = \frac{\pi^2}{8} \left(\frac{d}{\lambda}\right)^2 Z_0 L \hat{\mathbf{n}} \times \mathbf{H}_0 \frac{\exp[i(kz - \omega t)]}{z}, \quad (5.227)$$

where $Z_0 = \sqrt{\mu_0/\epsilon_0}$ is the impedance of free space [12, 116, 123]. The diffracted E field is tangential to the conducting screen. From Eq. (5.227), we concluded that the diffracted E field through a sub-wavelength sized slit is proportional to $(d/\lambda)^2$ [116, 123], which is different with the case when the slit direction is perpendicular to the E field.

5.3.3.2 E field perpendicular to the slit direction: \perp -case

When the incident E field \mathbf{E}_0 is perpendicular to the slit direction, the E field diffracted by a small slit can be thought of as the radiation from the electric dipole moment and by the ordinary diffraction explained by Kirchhoff's diffraction theory [12, 123].

5.3.3.2.1 Diffracted E field by a electric dipole moment

The E field from the radiation by an electric dipole moment is equal to the H field of a magnetic dipole \mathbf{m} in Eq. (5.205) with the substitution $\mathbf{m} \rightarrow \mathbf{p}$ and $\mu_0 \rightarrow \epsilon_0$ given by

$$\mathbf{E}(\mathbf{r}) = \frac{k^2}{4\pi\epsilon_0} \hat{\mathbf{n}} \times (\mathbf{p} \times \hat{\mathbf{n}}) \frac{\exp(ikr)}{r}, \quad (5.228)$$

³¹The integral with respect to x' can be solved by taking $x' = \frac{d}{2} \sin t$ such that $dx' = \frac{d}{2} \cos t dt$, which gives $t = \pi/2$ for $x' = d/2$ and $t = -\pi/2$ for $x' = -d/2$. We thus find that

$$\begin{aligned} \int_{-\frac{d}{2}}^{\frac{d}{2}} dx' \frac{x'^2}{\sqrt{\frac{d^2}{4} - x'^2}} &= \int_{-\frac{\pi}{2}}^{\frac{\pi}{2}} \frac{d}{2} \cos t dt \frac{\frac{d^2}{4} \sin^2 t}{\frac{d}{2} \cos t} \\ &= \frac{d^2}{4} \int_{-\frac{\pi}{2}}^{\frac{\pi}{2}} dt \sin^2 t = \frac{d^2}{4} \frac{\pi}{2} = \frac{\pi d^2}{8}, \end{aligned} \quad (5.225)$$

where the relation in Eq. C.70e is used.

³²Note that $k = 2\pi/\lambda$ and $c\mu_0 = \sqrt{\frac{\mu_0^2}{\epsilon_0\mu_0}} = \sqrt{\frac{\mu_0}{\epsilon_0}} = Z_0$.

where \mathbf{p} and $\hat{\mathbf{n}}$ are the electric dipole moment and a unit vector in the direction of the field point \mathbf{r} , respectively [12, 116]. The continuity equation is defined as

$$\nabla \cdot \mathbf{K}_e(\mathbf{r}') = i\omega\eta_e(\mathbf{r}'), \quad (5.229)$$

where \mathbf{K}_e and η_e are the electric current density and charge density, respectively, and $\mathbf{r}' = (x', y')$ [12]. By multiplying \mathbf{r}' to both sides of Eq. (5.229), we obtain

$$\mathbf{r}' \left[\nabla \cdot \mathbf{K}_e(\mathbf{r}') \right] = i\omega\mathbf{r}'\eta_e(\mathbf{r}'). \quad (5.230)$$

By integrating both sides of this equation with respect to the source points, Eq. (5.230) becomes

$$\int_S \mathbf{r}' (\nabla \cdot \mathbf{K}_e) d^2r' = i\omega\mathbf{p}, \quad (5.231)$$

where

$$\mathbf{p} = \int_S \mathbf{r}'\eta_e(\mathbf{r}') d^2r' \quad (5.232)$$

is the electric dipole moment, S is the boundary surface and r' indicate and the source point [12]. Here the left-hand side of Eq. (5.231) can be evaluated by integration by parts³³

$$\int_S \mathbf{r}' (\nabla \cdot \mathbf{K}_e) d^2r' = \int_S \mathbf{K}_e d^2r', \quad (5.236)$$

yielding

$$\int_S \mathbf{K}_e d^2r' = -i\omega\mathbf{p}. \quad (5.237)$$

Therefore, in terms of the electric surface current \mathbf{K}_e , Eq. (5.228) is slightly changed to³⁴

$$\mathbf{E}(\mathbf{r}) = i \frac{kZ_0 \exp(ikr)}{4\pi r} \hat{\mathbf{n}} \times \left[\int_S \mathbf{K}_e d^2r' \times \hat{\mathbf{n}} \right], \quad (5.238)$$

where $Z_0 = \sqrt{\epsilon_0/\mu_0}$ is the impedance of free space and $\omega = kc$ is used, which implies that the electric field is induced by the current [12, 122, 123]. By the vector identity, the vector terms in Eq. (5.238) becomes

$$\hat{\mathbf{n}} \times \left[\int_S \mathbf{K}_e d^2r' \times \hat{\mathbf{n}} \right] = (\hat{\mathbf{n}} \circ \hat{\mathbf{n}}) \int_S \mathbf{K}_e d^2r' - \hat{\mathbf{n}} \left[\hat{\mathbf{n}} \cdot \int_S \mathbf{K}_e d^2r' \right], \quad (5.239)$$

where \mathbf{K}_e is in the same direction of the incident E field. Within the spherical Gaussian surface at the

³³An integral can be evaluated by integration by parts as

$$\int fg' dx = fg - \int f'g dx. \quad (5.233)$$

For example, if J is an one dimensional current density, we obtain

$$\int J dx = \left[Jx \right] - \int x \left(\frac{dJ}{dx} \right) dx, \quad (5.234)$$

where the first term should be zero due to the physical reality. Similarly, if J is a three dimensional current density, we find that

$$\int \mathbf{J} d^3x = - \int \mathbf{x} (\nabla \cdot \mathbf{J}) d^3x. \quad (5.235)$$

³⁴Note that $k = \omega/c$ and $\frac{1}{\epsilon_0 c} = \sqrt{\frac{\epsilon_0 \mu_0}{\epsilon_0^2}} = \sqrt{\frac{\mu_0}{\epsilon_0}} = Z_0$.

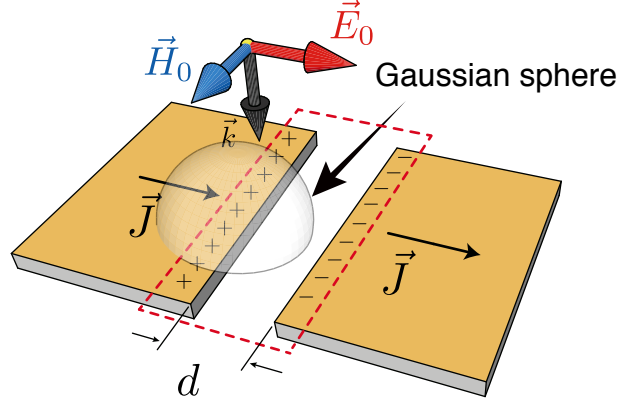


Figure 5.9: Schematic geometry including a Gaussian sphere with a Gaussian surface (S) on the edge of the slit when $\mathbf{E}_0 \perp \mathbf{L}$.

edge of the slit as in Fig. 5.9, \mathbf{K} and the initial E field \mathbf{E}_0 have a relation induced by Gauss's law, giving

$$\oint_S \mathbf{E} \cdot \hat{\mathbf{n}} \, da = \frac{Q}{\epsilon_0}, \quad (5.240)$$

which leads to

$$E_0 A = \frac{Q}{\epsilon_0}, \quad (5.241)$$

where Q is the total electric charge in the closed Gaussian surface ($S=A$). With harmonic time dependence $e^{-i\omega t}$, the E field can be expressed as $E_0(\mathbf{x}, t) = E_0(\mathbf{x})e^{-i\omega t}$. By differentiating Eq. (5.241) with respect to time t , we then obtain

$$A \frac{\partial E_0}{\partial t} = \frac{1}{\epsilon_0} \frac{\partial Q}{\partial t}, \quad (5.242)$$

which further makes

$$\frac{\partial E_0(\mathbf{x}, t)}{\partial t} = -i\omega E_0(\mathbf{x})e^{-i\omega t} = \frac{K_e}{\epsilon_0}, \quad (5.243)$$

where

$$K_e = \frac{1}{A} \frac{\partial Q}{\partial t} \quad (5.244)$$

is the surface current density. So, the surface current density K_e is obtained, yielding

$$\mathbf{K}_e(\mathbf{x}, t) = -i\omega\epsilon_0 \mathbf{E}_0(\mathbf{x})e^{-i\omega t}, \quad (5.245)$$

which implies that

$$\mathbf{K}_e(\mathbf{x}) = -i\omega\epsilon_0 \mathbf{E}_0(\mathbf{x}), \quad (5.246)$$

Therefore, \mathbf{K}_e and the initial E field \mathbf{E}_0 have a relation

$$\frac{\mathbf{K}_e(\mathbf{x})}{|\mathbf{K}_e(\mathbf{x})|} = \frac{-i\omega\epsilon_0 \mathbf{E}_0(\mathbf{x})}{|-i\omega\epsilon_0 \mathbf{E}_0(\mathbf{x})|} = -i \frac{\mathbf{E}_0(\mathbf{x})}{|\mathbf{E}_0(\mathbf{x})|} \quad (5.247)$$

in accordance with Gauss's law [122]. Provided the second term in Eq. (5.239) vanishes when $\hat{\mathbf{n}}$ is normal to the conducting screen³⁵ (*i.e.* the optical axis), we find by substituting Eq. (5.247) into the first term

³⁵Since $\hat{\mathbf{n}}$ is normal to the screen and surface current by \mathbf{K} is in the screen, we find that

$$\hat{\mathbf{n}} \cdot \text{surface current by } \mathbf{K} = 0.$$

in Eq. (5.239) that the E field of Eq. (5.238) with harmonic time dependence $\exp(-i\omega t)$ can be written as [122]

$$\mathbf{E}(\mathbf{r}, t) = \frac{kZ_0}{4\pi} \frac{\exp[i(kr - \omega t)]}{r} \int_S d^2r' \left| \frac{\mathbf{K}_e(\mathbf{r}')}{\mathbf{E}_0(\mathbf{r}')} \right| \mathbf{E}_0(\mathbf{r}'). \quad (5.248)$$

By Ohm's law, the magnitude of \mathbf{K}_e is also proportional to the induced E field \mathbf{E}_i ($\mathbf{K}_e = \sigma \mathbf{E}_i$, $\sigma = c_1$ is the conductivity) since we assumed that the screen is a perfect conductor [12].³⁶ The integral term over the source area (S) can be simplified at the optical axis with substitution $(x, y) = (0, 0)$ and $(x', y') = (0, 0)$. Then the integral becomes just a surface integral over the source area. The E field in the optical axis can be obtained, giving³⁷

$$\mathbf{E}(z, t) = \frac{c_1 Z_0}{2} \left(\frac{d}{\lambda}\right) L \frac{\exp[i(kz - \omega t)]}{z} \left| \frac{\mathbf{E}_i(\mathbf{0})}{\mathbf{E}_0(\mathbf{0})} \right| \mathbf{E}_0(\mathbf{0}), \quad (5.250)$$

where the origin was denoted as $\mathbf{0}$. It is known that the E field perpendicular to the slit direction is strongly enhanced in the slit when the slit width d is small enough compared with the wavelength of λ of the incident E field [111, 112]. The relation between the incident E field \mathbf{E}_0 and the induced E field \mathbf{E}_i was resulted by [111, 112]

$$\left| \frac{\mathbf{E}_i(\mathbf{0})}{\mathbf{E}_0(\mathbf{0})} \right| \propto \frac{\lambda}{d}. \quad (5.251)$$

Therefore, in the optical axis, the E field radiated by the electric dipole has no dependence with d/λ , yielding

$$\mathbf{E}(z, t) = \beta L \mathbf{E}_0(\mathbf{0}) \frac{\exp[i(kz - \omega t)]}{z}, \quad (5.252)$$

where β is a proportional coefficient [123].

5.3.3.2.2 Ordinary transmitted E field

Using the same parameters in Section 5.3.3.1, the E field diffracted by a slit at the far field zone when $\mathbf{E}_0 \perp \mathbf{L}$ can be also explained by Kirchhoff's diffraction theory as

$$\mathbf{E}(\mathbf{r}, t) = -\frac{ik}{2\pi} \frac{\exp[i(kr - \omega t)]}{r} \int_S d^2r' \mathbf{E}_0(x', y', z' = 0) \exp\left[-ik \frac{\mathbf{r} \cdot \mathbf{r}'}{r}\right], \quad (5.253)$$

where the oblique factor is 1 and the theory is also described in section A.10 in detail.³⁸ In the optical axis, the integral term becomes a simple surface integral over the source area. The ordinary diffracted

³⁶Here, the conductivity of the metal is considered as a nearly constant c_1 . See Jackson [12] p. 312.

³⁷In the optical axis, the integral becomes

$$\begin{aligned} \mathbf{E}(\mathbf{r}, t) &= \frac{kZ_0}{4\pi} \frac{\exp[i(kr - \omega t)]}{r} \int_S d^2r' \left| \frac{\mathbf{K}_e(\mathbf{r}')}{\mathbf{E}_0(\mathbf{r}')} \right| \mathbf{E}_0(\mathbf{r}') = \frac{kZ_0}{4\pi} \frac{\exp[i(kr - \omega t)]}{r} \left| \frac{\mathbf{K}_e(\mathbf{0})}{\mathbf{E}_0(\mathbf{0})} \right| \mathbf{E}_0(\mathbf{0}) \int_S d^2r' \\ &= \frac{kZ_0}{4\pi} \frac{\exp[i(kr - \omega t)]}{r} \left| \frac{\mathbf{K}_e(\mathbf{0})}{\mathbf{E}_0(\mathbf{0})} \right| \mathbf{E}_0(\mathbf{0}) \int_{-\frac{d}{2}}^{\frac{d}{2}} dx' \int_{-\frac{L}{2}}^{\frac{L}{2}} dy' \\ &= \frac{kZ_0}{4\pi} \frac{\exp[i(kr - \omega t)]}{r} \left| \frac{\mathbf{K}_e(\mathbf{0})}{\mathbf{E}_0(\mathbf{0})} \right| \mathbf{E}_0(\mathbf{0}) d L, \end{aligned} \quad (5.249)$$

which leads to Eq. (5.250).

³⁸See Jackson [12] p. 482 in which we find that the oblique factor becomes 1 when θ or θ' is zero (*i.e.* in the optical axis).

E field in the optical axis can then be obtained, yielding³⁹

$$\mathbf{E}(z, t) = -i \left(\frac{d}{\lambda} \right) L \mathbf{E}_0(\mathbf{0}) \frac{\exp [i(kz - \omega t)]}{z}. \quad (5.255)$$

From Eq. (5.255), the Kirchhoff's solution gives the E field of the order proportional to (d/λ) .

5.3.3.2.3 Diffracted E field by a sub-wavelength slit when $\mathbf{E}_0 \perp \mathbf{L}$

Therefore, the total diffracted E field in the optical axis can be written by a summation of the terms in Eqs. (5.252) and (5.255) as

$$\mathbf{E}(z, t) \equiv \mathbf{E}_\perp = \left[\beta - i \left(\frac{d}{\lambda} \right) \right] \mathbf{E}_0(\mathbf{0}) L \frac{\exp [i(kz - \omega t)]}{z}. \quad (5.256)$$

5.4 Results and discussion

The polarization dependence of the diffracted E field through a reference sub-wavelength slit can be summarized in such a way that the amplitudes of the diffracted E fields in the \parallel -case and \perp -case have dependence with $(d/\lambda)^2$ and d/λ , respectively. However, the average field amplitude \bar{A} in the slit with respect to the slit width d should be considered in order to compare the amplitude behavior for both cases. If the slit thickness is sufficiently small compared with the slit width d , through use of Eqs. (5.227) and (5.256), \bar{A} for both cases can be represented as

$$\bar{A}(\omega) = \frac{1}{d} |\mathbf{E}(\omega)| \propto \begin{cases} \frac{d}{\lambda^2} & \text{for } \parallel\text{-case,} \\ \frac{1}{d} \sqrt{\beta^2 + \frac{d^2}{\lambda^2}} & \text{for } \perp\text{-case,} \end{cases} \quad (5.257)$$

where dl is the line element along the slit width d . Equation (5.257) is valid for our case since a slit thickness of 500 nm is about ten times smaller than the minimum slit width of 6 μm . Therefore, one can may conclude that the amplitude of the diffracted E field through the reference slit shows different tendencies as a function of the slit width d as below: $\bar{A}_\parallel \propto d$, $\bar{A}_\perp \propto 1/d$ for a given frequency and $\beta \gg 1$.⁴⁰

In the presence of a resonant material confined in a sub-wavelength slit, the E field parallel to the slit orientation does not electrically interact with the resonant material within the slit, which is expected

³⁹The integral in Eq. (5.253) can be evaluated in the optical axis $((x', y') = (x, y) = (0, 0))$ as

$$\begin{aligned} \int_S d^2 r' \mathbf{E}_0(x', y', z' = 0) e^{-ik \frac{\mathbf{r} \cdot \mathbf{r}'}{r}} &= \int_S d^2 r' \mathbf{E}_0(\mathbf{0}) = \mathbf{E}_0(\mathbf{0}) \int_S d^2 r' \\ &= \mathbf{E}_0(\mathbf{0}) \int_{-\frac{d}{2}}^{\frac{d}{2}} dx' \int_{-\frac{L}{2}}^{\frac{L}{2}} dy' = \mathbf{E}_0(\mathbf{0}) d L. \end{aligned} \quad (5.254)$$

⁴⁰For \perp case,

$$\begin{aligned} \frac{1}{d} \sqrt{\beta^2 + \frac{d^2}{\lambda^2}} &= \frac{\beta}{d} \left[1 + \frac{d^2}{\lambda^2} \frac{1}{\beta^2} \right]^{1/2} \simeq \frac{\beta}{d} \left[1 + \frac{1}{2\beta^2} \frac{d^2}{\lambda^2} \right] \\ &= \frac{\beta}{d} + \frac{1}{2\beta} \frac{d}{\lambda^2} \simeq \frac{\beta}{d} \text{ for } \beta \gg 1 \text{ and } d \ll \lambda. \end{aligned} \quad (5.258)$$

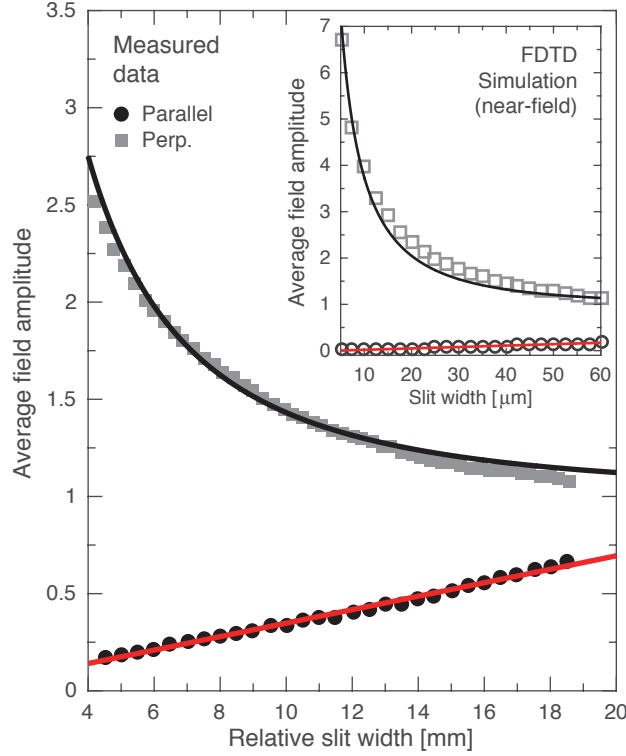


Figure 5.10: Average field amplitude of the measured transmitted THz waves at 0.53 THz through the reference slit with respect to the relative slit thickness of d for \parallel -case (black, closed circles) and \perp -case (gray, closed rectangles). Inset shows average field amplitude in near-field zone for \parallel -case (black, open circles) and \perp -case (gray, open rectangles) confirmed by the FDTD simulation. All the red and black solid lines represent fitting curves described by Eqs. (5.227) and (5.256), respectively. Note that measured average field amplitudes are normalized by a factor with the limitation for the \perp -case.

to result in complete vanishing of the otherwise resonant absorption since the H field does not interact with an electrically resonant material. The theoretical model explained in section 5.3.3 describes the behavior of the E field in the far-field zone using a sub-wavelength slit without a confined sample. In order to understand the origin of this model, the near-field distribution of E field in the sub-wavelength slit should be considered. To verify the field amplitude in the sub-wavelength slit, the numerical study was carried out by two-dimensional finite-difference time-domain (FDTD) analysis over the simulation area of $300 \mu\text{m} \times 1600 \mu\text{m}$ of which the slit thickness was 500 nm and the slit width was in a range from $5 \mu\text{m}$ to $100 \mu\text{m}$.

Figure 5.10 shows the average field amplitude \bar{A} of the measured transmitted THz waves through a reference slit at 0.53 THz as a function of the slit width d for \parallel -case (black, closed circles) and \perp -case (gray, closed rectangles), where the relative slit width corresponds to an actual slit width ranging from $6 \mu\text{m}$ to $60 \mu\text{m}$. Inset shows the average field amplitude in the near-field zone as a function of the slit width for the \parallel -case (black, open circles) and \perp -case (gray, open rectangles) computed by the FDTD simulation. All the red and black solid lines in Fig. 5.10 are obtained by the theoretical model described in Eq. (5.257). The measured average field amplitudes are normalized by a factor with the limitation for the \perp -case. With verification by the FDTD analysis, we find that the behavior of the computed field amplitude illustrated in the inset of Fig. 5.10 is well in accordance with Eq. (5.257), which implies that the diffracted E field through the sub-wavelength slit in the far-field zone comes from the near-field zone.

To verify our expectation for the \parallel -case and \perp -case in the presence of a resonant material in the

slit, the absorbance α is obtained via the measured transmission in the frequency range from 0.1 THz to 2.0 THz as

$$\alpha(\omega) = -\ln \left| \frac{\tilde{E}_s(\omega)}{\tilde{E}_{\text{ref}}(\omega)} \right|, \quad (5.259)$$

where \tilde{E}_s and \tilde{E}_{ref} are the transmitted THz electric fields with and without α -lactose, respectively. The extracted absorbances explained in Eq. (5.259) for the \parallel -case and \perp -case are plotted as a function of the relative slit width in Figs. 5.11(a) and Fig. 5.11(c), respectively. It is noted that α -lactose monohydrate have three distinct resonance points below 2 THz of which profiles are in accordance with Lorentzian line shapes [88, 124] given by

$$\alpha(\omega) = \text{Im} \sum_n \frac{S_n}{\omega_{0,n}^2 - \omega^2 - i\gamma_n\omega} + c, \quad (5.260)$$

where S_n , $\omega_{0,n}$ and γ_n are the oscillator strength, the center frequency and the linewidth for the n -th modes, respectively. The fitting constant is denoted as c . Figure 5.11(b) shows the computed absorbances for the \parallel -case obtained with the help of the parameters in Ref. [124]. The computed absorbance for the \perp -case is also shown in Fig. 5.11(d).

The absorbances at 0.53 THz with a high Q-factor [88] are clearly shown in Figs. 5.11(e) and Fig. 5.11(f) when $d=16.5$ mm and $d=4$ mm, respectively. Furthermore, absorbances at 1.2 THz and 1.37 THz are shown in Fig. 5.11(g) at $d=16.5$ mm and Fig. 5.11(h) at $d=8$ mm, respectively. All the measured data are plotted as closed circles (black) for the \parallel -case and open rectangles (gray) for the \perp -case. The fitting curves obtained by Eq. (5.260) are then represented as red solid lines for the \parallel -case

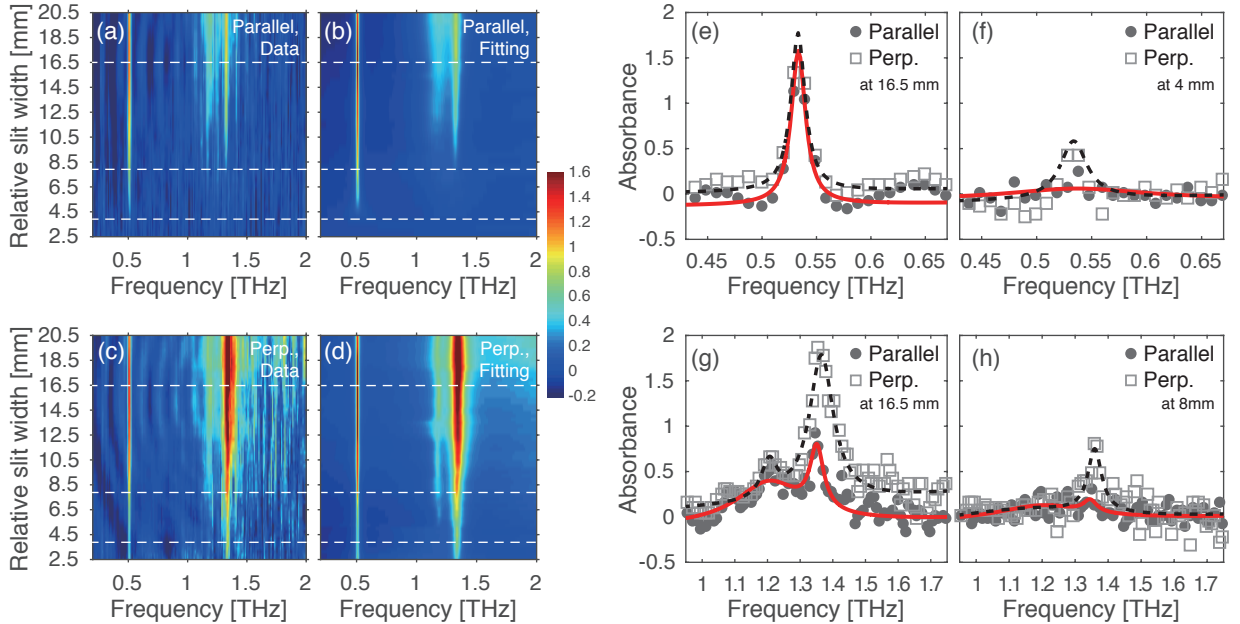


Figure 5.11: The extracted absorbances calculated by Eq. (5.259) for (a) the \parallel -case and (c) the \perp -case as a function of the relative slit width. Corresponding computed absorbances calculated by Eq. (5.260) for (b) the \parallel -case (d) for the \perp -case. Absorbance at 0.53 THz (e) at $d=16.5$ mm or (f) at $d=4$ mm. Absorbances at 1.2 THz and 1.37 THz (g) at $d=16.5$ mm and (h) at $d=8$ mm. All the measured data are plotted with closed circles (black) for the \parallel -case and open rectangles (gray) for the \perp -case. The fitting curves obtained by Eq. (5.260) are represented as red solid lines for the \parallel -case and black dashed lines for the \perp -case.

and black dashed lines for the \perp -case.

5.5 Conclusion

We conducted polarization spectroscopy using the α -lactose monohydrate confined in a wedge-shaped sub-wavelength metal slit using THz-TDS. By Bethe's diffraction theory, the absorption behavior in the far field measurement should vanish in the presence of an electrically resonant material restricted into the sub-wavelength slit. The experimental results obtained by THz-TDS show that absorption vanishes when the size of the aperture is of extreme sub-wavelength.

Chapter 6. Conclusion

THz time-domain spectroscopy (THz-TDS) has played an important role in exploring new properties and phenomena of materials in the THz frequency range. In particular, the direct field measurement carried out by the electro-optic sampling allowed us to obtain simultaneously the phase information as well as the amplitude of the transmitted or reflected waves from the material without resorting to the Kramers-Kronig relationship.

In this dissertation, we studied and demonstrated the possibility of a THz lens using dolomite stone, strong optical phonon observed in seraphinite gemstone and the polarization dependence of α -lactose confined in a sub-wavelength metal slit. Firstly, we presented the possibility of applying natural stones as an optical element material in the THz frequency range. We measured optical constants of various natural stones using THz-TDS. Among the investigated stones, dolomite in particular exhibited a high refractive index of 2.7 and low absorption over the measured THz frequency range. Using these properties, a planoconvex lens was fabricated using dolomite stone by the conventional lens making processes. The measured beam profiles using the 4-f geometry were well explained by Fraunhofer's diffraction theory in the THz frequency range. With the proof-of-principle demonstration of a THz lens made out of dolomite, it was suggested that natural stones have the possibility as THz optical element materials for both scientific and economic aspects.

Secondly, we have reported for the first time a spectral fingerprint of crystal seraphinite, a type of gemstone, in the THz frequency range. It was found from our measurement that seraphinite has the strong IR-active modes at 0.80, 0.96 and 1.20 THz. In particular, the 0.96 THz mode has exhibited a strong and narrow absorption with a quality factor of 8, which is comparable to the well known reported 0.53 THz mode in α -lactose monohydrate. The polarization-dependent THz-TDS measurements with varying the azimuthal angle of seraphinite show that seraphinite has the birefringence originated from its crystalline monoclinic structure with the space group C2/m as well as the $A_u(z')$ -symmetry of the 0.80 and 1.20 THz modes and the $B_u(x', y')$ -symmetry of the 0.96 THz mode. Theoretical interpretation based on the Kurosawa formula has shown an excellent agreement with the observed phonon-polariton dispersion anisotropy. Thus, we concluded that the strong absorption mode at 0.96 THz is expected as an optical phonon mode. It is hoped from the experimental results measured with natural stones and gemstones that THz spectroscopy may become useful for identification and characterization of various mineral compounds.

Finally, we studied the polarization dependence of α -lactose monohydrate confined in a wedge-shaped sub-wavelength metal slit using THz-TDS. The diffraction from an aperture is one of well known physical phenomena. However, the diffraction by a sub-wavelength sized aperture shows anomalous behaviors that can not be explained by classical Kirchhoff's diffraction theory. When the aperture is replaced by a single slit, the diffraction caused by the slit has two distinct situations in which corresponds to the polarization of the incident waves with respect to the slit direction. Although the Kirchhoff's theory fails in the sub-wavelength region, it can be deduced from the waveguide theory that the electric field perpendicular to the slit direction can propagate through the slit due to low cutoff frequency. However, it is difficult for the electric field parallel to the slit direction to propagate through by the same analogy. In contrast to the electric field, since the boundary conditions obtained by Bethe's first-order approximation are regardless of shape and size of the aperture, the magnetic field perpendicular or parallel to the slit

direction is always considered as constant over the slit. Thus, the E field inside the slit exhibits a strong polarization dependence. Using the α -lactose monohydrate with a strong absorption line at 0.53 THz, we measured the temporal and spectral amplitude changes of the transmitted THz wave within a slit with in the range from 6 μm to 60 μm . Experimental results carried out by THz-TDS reveal that the spectral response of the material is strongly coupled with the polarization state of the THz waves, and that the material does not interact at all with the THz waves in the limit of an extreme sub-wavelength-sized slit when the polarization of the incident electric field is parallel to the slit direction. This study would be helpful for research on polarization sensitive investigation using small amounts of materials confined in a sub-wavelength sized slit or aperture using spectroscopic techniques.

Chapter A. Supplements

A.1 The physical units in THz frequency range

A.1.1 The relation between distance and time

Provided the distance and time are denoted as s and t , then $s = c \cdot t$, where c is the speed of light in vacuum. Then the time corresponding 1mm is as follows

$$\begin{aligned} 1 \text{ mm} &= 3 \times 10^8 \text{ m/s} \times t \\ \Leftrightarrow t &= \frac{1 \times 10^{-3}}{3 \times 10^8} \text{ s} = \frac{1}{3} \times 10^{-11} \text{ s} = \frac{1}{3} \times 10^{-12} \times 10 \text{ s} = 3.3 \text{ ps}. \end{aligned} \quad (\text{A.1})$$

According to the above equation, 10000 fs is derived as follows

$$\begin{aligned} 1 \text{ mm} : 3.3 \text{ ps} &= 3 \text{ mm} : X \\ \Leftrightarrow X &= 9.9 \text{ ps} \simeq 10 \text{ ps} = 10000 \text{ fs}. \end{aligned} \quad (\text{A.2})$$

A.1.2 The relation between 1 THz and wavelength

The basic dispersion equation is

$$k = \frac{\omega}{c} n = \frac{2\pi}{\lambda_0} n = \frac{2\pi}{\lambda_m}, \quad (\text{A.3})$$

where λ_0 is the wavelength in vacuum, λ_m is the wavelength in material, and $\omega = 2\pi f$. In vacuum, n is 1, then

$$\begin{aligned} k &= \frac{\omega}{c} = \frac{2\pi f}{c} = \frac{2\pi}{\lambda_m} \\ \Leftrightarrow \frac{f}{c} &= \frac{1 \text{ THz}}{3 \times 10^8 \text{ m/s}} = \frac{1 \times 10^{12} \text{ s}^{-1}}{3 \times 10^8 \text{ m/s}} = \frac{1}{\lambda_m} \\ \Leftrightarrow \lambda_m &= 3 \times 10^{-4} \text{ m} = 3 \times 10^{-4} \times 10^{-2} \times 10^2 \text{ m} \\ &= 3 \times 10^2 \text{ } \mu\text{m} = 300 \text{ } \mu\text{m}. \end{aligned} \quad (\text{A.4})$$

Therefore the wavelength is inversely proportional to the frequency.

A.1.3 The relation between 1 THz and wavenumber

In vacuum, the basic dispersion equation is

$$\begin{aligned} k &= \frac{\omega}{c} = \frac{2\pi f}{c} = \frac{2\pi}{\lambda_m} \\ \Leftrightarrow k &= 2\pi \times \frac{1 \text{ THz}}{3 \times 10^8 \text{ m/s}} = 2\pi \times \frac{10^{12} \text{ s}^{-1}}{3 \times 10^8 \text{ m/s}} = 2\pi \times \left[\frac{1}{3} \times 10^4 \text{ m}^{-1} \right] \\ &= 2\pi \times \left[\frac{1}{3} \times \frac{10^4 \times 10^{-2}}{10^{-2} \text{ m}} \right] = 2\pi \times \left[\frac{1}{3} \times \frac{10^2}{\text{cm}} \right] \simeq 2\pi \times \left[33 \text{ cm}^{-1} \right]. \end{aligned} \quad (\text{A.5})$$

A.1.4 The relation between 1 THz and Energy

Energy corresponding to 1THz is as follows

$$\begin{aligned}
 E &= \hbar\omega = \frac{h}{2\pi} \cdot 2\pi f = h \cdot f \\
 &\simeq (4.1 \times 10^{-15} \text{ eV} \cdot \text{s}) \times (1 \times 10^{12} \text{ s}^{-1}) \\
 &= 4.1 \times 10^{-3} \text{ eV} = 4.1 \text{ meV}.
 \end{aligned} \tag{A.6}$$

A.2 No Pockels effect in the centro-symmetric crystals

In section 2.5.2, we encountered that the linear electro-optic effect vanishes in centro-symmetric crystals [7, 19]. The reason is due to the spatial inversion of the crystal [19].¹ The linear electro-optic coefficient r_{ijk} is defined by Eq. (2.108). For a centro-symmetric crystal, r_{ijk} under the inversion operator denoted as i^{inv} becomes

$$i^{\text{inv}} r_{ijk} = i^{\text{inv}} \left[\frac{\partial \eta_{ij}}{\partial E_k} \Big|_{\mathbf{E}=0} \right] = \frac{\partial \eta_{ij}}{\partial (-E_k)} \Big|_{\mathbf{E}=0} = -\frac{\partial \eta_{ij}}{\partial E_k} \Big|_{\mathbf{E}=0} = -r_{ijk}, \tag{A.7}$$

where the inversion operator i^{inv} represents a symmetry operation with respect to the center of symmetry or center of inversion (*i.e.* a point) [19, 85].² Since any tensor is invariant under the inversion operation in a centro-symmetric system, i^{inv} under the inversion operator can be evaluated as

$$i^{\text{inv}} r_{ijk} = r_{ijk}. \tag{A.8}$$

Eqs. (A.7) and (A.8) are satisfied only if $r_{ijk} = 0$ [19]. Consequently, there is no Pockels effect in centro-symmetric crystals. This fact can be also described using a potential curve of noncentro-symmetric or centro-symmetric crystals, which is explained in Boyd pp. 22-33 [7].

A.3 Estimating the peak intensity of the laser beam

A.3.1 Beam radius at the focus

Suppose that a Gaussian beam with a wavelength of λ propagates in the direction of z . The radius of the beam spot w would be focused when the beam passes through a lens with focal length of f . At the focus, the radius of the beam spot becomes w_0 . Then the beam parameter at the focus is defined as

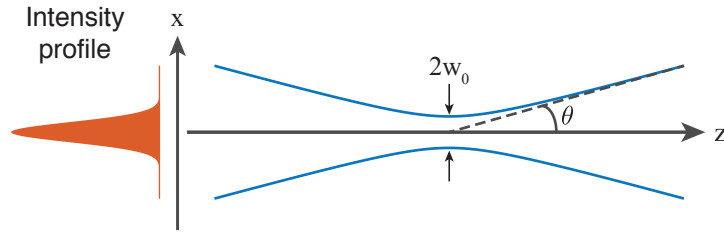


Figure A.1: The spot size w (blue) of a Gaussian beam as a function of propagation direction of z .

¹See Yariv. [19] p. 223.

²See Cotton [85] pp. 22, 35.

$z_0 = \pi w_0^2 n / \lambda$, where n is the refractive index of the space with the beam. Using this beam parameter, the radius of the beam spot w can be written as a function of w_0 and z_0 , giving [19]

$$w^2(z) = w_0^2 \left(1 + \frac{z^2}{z_0^2} \right). \quad (\text{A.9})$$

Fig. A.1 shows a Gaussian beam is focused with a beam radius of w_0 , where the blue line represents w . For large z^3 , Eq. (A.9) becomes [19]

$$w(z) \simeq w_0 \frac{z}{z_0} = \frac{z \lambda}{\pi w_0 n}. \quad (\text{A.11})$$

Equation (A.11) is a well used formula to calculate the beam radius at the focus by substituting the focal length f of the used optical component into z . So, if we know the spot radius w_0 of the incident beam to the lens, then the beam radius at the focus can be estimated as

$$w_0 = \frac{f \lambda}{\pi w n} \propto \frac{f}{w}. \quad (\text{A.12})$$

Provided D is the diameter at the lens position and d is the diameter at the focus, Eq. (A.12) can be modified in terms of the beam diameter as⁴

$$d = \frac{4}{\pi} \frac{\lambda f}{D n} \simeq 1.27 \frac{\lambda f}{D n}, \quad (\text{A.14})$$

where Eq. (A.14) is approximately the same with the diameter of an Airy disk induced by the Fraunhofer's diffraction theory: [11]

$$d \simeq 1.22 \frac{\lambda f}{D}. \quad (\text{A.15})$$

Suppose that a laser beam with wavelength of 840 nm and beam radius 5 mm passes through a lens with focal length 150 mm. Then the beam radius at the focus is computed as

$$w_0 = \frac{f \lambda}{\pi w n} = \frac{840 \text{ nm} \times 150 \text{ mm}}{\pi \times 5 \text{ mm} \times 1} = 8021 \text{ nm} \simeq 8 \mu\text{m}. \quad (\text{A.16})$$

Therefore, the beam diameter of the spot is approximately 20 μm .

A.3.2 Peak intensity (power) at the focus

In this section, calculation of the peak intensity is described. Assume that a laser beam from a mode-locked Ti:Sapphire oscillator with repetition rate of 80 MHz is focused to a beam radius of 5 μm . The measured beam power is 2 W.

First, the energy per a pulse (S_{pulse}) needs to be calculated. Since the beam has a repetition rate (R)

3

$$w^2(z) = w_0^2 \left(1 + \frac{z^2}{z_0^2} \right) = w_0^2 \frac{z^2}{z_0^2} \left(1 + \frac{z_0^2}{z^2} \right) \simeq w_0^2 \frac{z^2}{z_0^2} \text{ for large } z. \quad (\text{A.10})$$

4

$$w_0 = \frac{f \lambda}{\pi w n} = \frac{2 f \lambda}{\pi D n} = \frac{d}{2} \Leftrightarrow d = \frac{4 \lambda f}{\pi D n} \simeq 1.27 \frac{\lambda f}{D n}. \quad (\text{A.13})$$

of 80 MHz, a single pulse energy can be calculated as

$$\begin{aligned} S_{\text{pulse}} &= \frac{P}{R} = \frac{2 \text{ W}}{80 \text{ MHz}} \\ &= \frac{2 \text{ J s}^{-1}}{80 \times 10^6 \text{ s}^{-1}} = 0.025 \text{ } \mu\text{J} = 25 \text{ nJ}, \end{aligned} \quad (\text{A.17})$$

where P is intensity measured by a power meter.

Next, the peak intensity at the focus should be calculated. For the sake of simplicity, assume that the pulse is a square pulse as shown in Fig. A.2 and the FWHM (full width at half maximum) of a pulse is 160 fs. Then the peak intensity can be calculated by a pulse energy divided by FWHM. The beam spot (beam diameter) is given by

$$I_{\text{peak}} = 25 \text{ nJ} \times \frac{1}{160 \text{ fs}} \times \frac{1}{\pi \times (5 \text{ } \mu\text{m})^2} \simeq 190 \text{ GW/cm}^2. \quad (\text{A.18})$$

A.3.3 Estimating the electric field strength and the peak intensity

If a square pulse is replaced by a Gaussian pulse, more accurate peak intensity can be obtained. The electric field with a slowly varying field amplitude in the direction of z -axis can be expressed as

$$E(\mathbf{x}, t) = E_0(\mathbf{x}, t)e^{i(kz-\omega t)} + \text{c.c.}, \quad (\text{A.19})$$

where ω is the carrier frequency and k is the linear part of the wavevector at ω [7]. The slowly varying amplitude E_0 is generally written in terms of the spectral profile F and the phase Φ as

$$E_0(\mathbf{x}, t) = A_0 F(x, y) A(z, t) e^{i\Phi(z, t)}, \quad (\text{A.20})$$

where $F(x, y)$ has a Gaussian distribution with respect to x and y and A_0 is in the units of [V/m]. For sake of simplicity, F is assumed to be unity (1) (*i.e.* The distribution on the xy plane is uniform.). Then, Eq. (A.19) at $\mathbf{x} = 0$ becomes

$$E(\mathbf{x}, t) = A_0 A(z, t) e^{i\Phi(z, t)} e^{i(kz-\omega t)} + \text{c.c.}, \quad (\text{A.21})$$

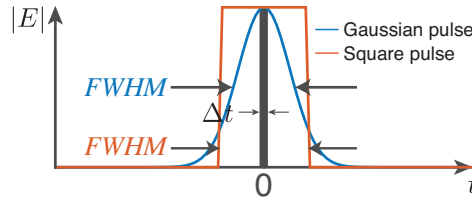


Figure A.2: A Gaussian pulse and a square pulse as a function of time t . FWHM of the Gaussian pulse $|E(t)|$ and square pulse are represented by blue letter and red letters, respectively.

which implies that⁵

$$|E(0, t)| = A_0 \exp \left[-\frac{(t-t_0)^2}{\sigma^2} \right] \quad (\text{A.23})$$

with

$$A(0, t) = \exp \left[-\frac{(t-t_0)^2}{\sigma^2} \right], \quad (\text{A.24})$$

where the deviation σ is defined by $\sigma = \text{FWHM}/(2\sqrt{\ln 2})$.⁶ In order to obtain the field strength A_0 , the energy flow described by the Poynting vector of \mathbf{S} should be considered. For the infinite plane wave, Eq. (A.19) becomes

$$E(\mathbf{x}, t) = E_0 e^{i(kz-\omega t)} + \text{c.c.}, \quad (\text{A.30})$$

where E_0 is the magnitude of the electric field or just simply the electric field strength. In the case of the electric field defined by Eq. (A.30), the time-averaged Poynting vector $\langle \mathbf{S} \rangle$ is [7]⁷

$$\langle \mathbf{S} \rangle = \langle \mathbf{E} \times \mathbf{H} \rangle = \hat{\mathbf{k}} 2n \sqrt{\frac{\epsilon_0}{\mu_0}} |E_0|^2 = \hat{\mathbf{k}} 2n\epsilon_0 c |E_0|^2. \quad (\text{A.31})$$

The magnitude of the time-averaged Poynting vector is called as the intensity I ([W/m²]) given by [12,27]⁸

$$I \equiv |\langle \mathbf{S} \rangle| = 2 \sqrt{\frac{\epsilon}{\mu}} |E_0|^2 = 2n \sqrt{\frac{\epsilon_0}{\mu_0}} |E_0|^2 = 2n\epsilon_0 c |E_0|^2 = \frac{2n}{Z_0} |E_0|^2, \quad (\text{A.33})$$

where $Z_0 = \sqrt{\mu_0/\epsilon_0} = 376.7 \Omega$ is the impedance of free space and n is assumed to be unity. Although the electric field in the system is a pulse, the intensity can be approximately obtained from Eq. (A.33). Equation (A.33) is valid for the electric field described in Eq. (A.30). The conventional description of the electric field is defined by $E(\mathbf{x}, t) = 1/2 \times (E_0 e^{i(kz-\omega t)} + \text{c.c.})$. In this case, the intensity is $|\langle \mathbf{S} \rangle| = (1/2) \sqrt{\epsilon/\mu} |E_0|^2 = (1/2) n \sqrt{\epsilon_0/\mu_0} |E_0|^2 = (1/2) n\epsilon_0 c |E_0|^2 = (n/2Z_0) |E_0|^2$. The unit of the

5

$$|E(\mathbf{x}, t)| = |A_0 A(z, t) e^{i\Phi(z,t)} e^{i(kz-\omega t)} + \text{c.c.}| = |A_0 A(z, t)| \left| \left(e^{i\Phi(z,t)} e^{i(kz-\omega t)} + \text{c.c.} \right) \right| = E_0 |A(z, t)|. \quad (\text{A.22})$$

⁶A function $f(x)$ with Gaussian distribution $N(\mu = 0, \sigma)$ is given by

$$f(x) = a_0 \exp \left[-\frac{x^2}{\sigma^2} \right]. \quad (\text{A.25})$$

Then $f(x)$ has half maximum value at some position denoted by x_p , which can be obtained by

$$\frac{a_0}{2} = a_0 \exp \left[-\frac{x_p^2}{\sigma^2} \right] \quad (\text{A.26})$$

$$\Leftrightarrow \ln(1/2) = -\frac{x_p^2}{\sigma^2} \Leftrightarrow -\ln 2 = -\frac{x_p^2}{\sigma^2} \Leftrightarrow x_p^2 = \sigma^2 \ln 2 \quad (\text{A.27})$$

$$\Leftrightarrow x_p = \sigma \sqrt{\ln 2}. \quad (\text{A.28})$$

Therefore the full width at the half maximum (FWHM) is

$$\text{FWHM} = 2x_p = 2\sigma \sqrt{\ln 2}. \quad (\text{A.29})$$

⁷See Boyd [7] p.p. 592-593.

⁸From Eq. (3.51),

$$\sqrt{\frac{\epsilon}{\mu}} = \sqrt{\frac{\epsilon_0 \epsilon}{\epsilon_0 \mu}} = \sqrt{\frac{\epsilon}{\epsilon_0}} \sqrt{\frac{\epsilon_0}{\mu}} = n \sqrt{\frac{\epsilon_0}{\mu_0}} = \frac{n}{Z_0} \left(= n \sqrt{\frac{\epsilon_0 \epsilon_0}{\epsilon_0 \mu_0}} = n\epsilon_0 c \right). \quad (\text{A.32})$$

See Jackson, *Classical electrodynamics 3 rd edition* [12], p. 298.

intensity is W/m^2 as follows

$$\frac{1}{[\Omega]} \frac{[V^2]}{[m^2]} = \frac{[A]}{[V]} \frac{[V^2]}{[m^2]} = \frac{[A][V]}{m^2} = \frac{[C/s][J/C]}{m^2} = \frac{[J/s]}{m^2} = \frac{W}{m^2}, \quad (\text{A.34})$$

where the units of the impedance, the electric potential and the electric current are Ω , V , and A (Ampere), respectively.

The electromagnetic power can be considered as the flux of the Poynting vector \mathbf{S} over a specific area given by [129]

$$P = \int_{\text{area}} \langle \mathbf{S} \rangle \cdot \hat{n} da, \quad (\text{A.35})$$

where da is the area element and \hat{n} is the normal vector of the area. Since the power is proportional to $\langle \mathbf{S} \rangle$ (*i.e.* $\langle \mathbf{S} \rangle \propto |E_0|^2$), the power can be written as⁹

$$P(t) = P_0 \exp \left[-\frac{2t^2}{\sigma^2} \right], \quad (\text{A.37})$$

where P_0 is in the units of $[W=J/s]$ and t_0 is substituted by zero. A single pulse energy S_{pulse} obtained by Eq. (A.17) can be written as

$$S_{\text{pulse}} \equiv \int_{-\infty}^{\infty} dt P(t) = P_0 \int_{-\infty}^{\infty} \exp \left[-\frac{2t^2}{\sigma^2} \right] dt = \sigma P_0 \sqrt{\frac{\pi}{2}}, \quad (\text{A.38})$$

where Eq. (C.106) is used for the integration. Then, P_0 becomes

$$P_0 = \frac{S_{\text{pulse}}}{\sigma} \sqrt{\frac{2}{\pi}}. \quad (\text{A.39})$$

Since the optical beam has a Gaussian distribution, the intensity in Eq. (A.33) can be considered to have a spectral distribution given by

$$I = I_{\text{peak}} \exp \left[-\frac{x^2}{\sigma_x^2} \right] \exp \left[-\frac{y^2}{\sigma_y^2} \right], \quad (\text{A.40})$$

where I_{peak} is the peak intensity in the units of $[W/m^2]$. Note that the power has a peak value of P_0 at $t = 0$. By substituting Eq. (A.40) into Eq. (A.35), the peak power P_0 can be written by

$$\begin{aligned} P_0 &= \int_{-\infty}^{\infty} dx \int_{-\infty}^{\infty} dy I_{\text{peak}} \exp \left[-\frac{x^2}{\sigma_x^2} \right] \exp \left[-\frac{y^2}{\sigma_y^2} \right] \\ &= I_{\text{peak}} \int_{-\infty}^{\infty} dx \exp \left[-\frac{x^2}{\sigma_x^2} \right] \int_{-\infty}^{\infty} dy \exp \left[-\frac{y^2}{\sigma_y^2} \right] = \sigma_x \sigma_y \pi I_{\text{peak}}, \end{aligned} \quad (\text{A.41})$$

so that

$$I_{\text{peak}} = \frac{P_0}{\sigma_x \sigma_y \pi}. \quad (\text{A.42})$$

⁹Since $E(\mathbf{x}, t)$ can be expressed by separation variables, the power becomes

$$P = \int_{\text{area}} \langle \mathbf{S} \rangle \cdot \hat{n} da \propto \int_{\text{area}} d^2x' |E_0(\mathbf{x}', t)|^2 = \int_{\text{area}} d^2x' |F(t) E_0(\mathbf{x}')|^2 = |F(t)|^2 \int_{\text{area}} d^2x' |E_0(\mathbf{x}')|^2 \propto |F(t)|^2. \quad (\text{A.36})$$

Therefore $|F(t)|$ can be written given by $|F(t)| = \exp[(t - t_0)^2/\sigma^2]$ when $|F(t)|$ has a Gaussian distribution in Eq. (A.24).

A function $f(x)$ with Gaussian distribution $N(\mu = 0, \sigma)$ has a value of $1/e \times f(x = \sigma)$.¹⁰ Then the deviations σ_j for $j \in \{x, y\}$ can be approximated as half of the beam radius given by

$$\sigma_j \simeq \frac{r}{2}, \quad (\text{A.45})$$

where r is the beam radius at the focus. By substituting Eq. (A.45) into Eq. (A.42), we obtain the peak intensity in the form

$$I_{\text{peak}} \simeq \frac{P_0}{\frac{r}{2} \frac{r}{2} \pi} = 4 \frac{P_0}{\pi r^2} = \frac{4}{\pi r^2} \frac{S_{\text{pulse}}}{\sigma} \sqrt{\frac{2}{\pi}}. \quad (\text{A.46})$$

By Eq. (A.33), the field strength in the case of the Gaussian beam can be obtained by

$$\begin{aligned} |E_0| &= \sqrt{\frac{Z_0}{2n}} I_{\text{peak}} \simeq \sqrt{\frac{Z_0}{2n}} \times 4 \frac{P_0}{\pi r^2} \\ &= \sqrt{\frac{Z_0}{2n}} \times \frac{4}{\pi r^2} \times \frac{S_{\text{pulse}}}{\sigma} \sqrt{\frac{2}{\pi}} = \frac{2}{r} (2\pi)^{-1/4} \sqrt{\frac{Z_0}{n}} \frac{S_{\text{pulse}}}{\pi \sigma}, \end{aligned} \quad (\text{A.47})$$

where the deviation σ is defined by $\text{FWHM}/(2\sqrt{\ln 2})$. The unit of the electric field strength is of course V/m as follows

$$\begin{aligned} \sqrt{[\Omega] \frac{[W]}{[m^2]}} &= \sqrt{\frac{[V]}{[A]} \frac{[J/s]}{[m^2]}} = \sqrt{\frac{[V]}{[m^2]} \frac{[J]}{[A] [s]}} \\ &= \sqrt{\frac{[V]}{[m^2]} \frac{[J]}{[C/s] [s]}} = \sqrt{\frac{[V]}{[m^2]} \frac{[J]}{[C]}} = \sqrt{\frac{[V]}{[m^2]} [V]} = [V/m], \end{aligned} \quad (\text{A.48})$$

where the units of the impedance, the electric potential, and the electric current are Ω , V , and A (Ampere), respectively. Note that the SI unit of the electric field is also N/C .

A.4 Estimating the THz electric field strength

By Eq. (2.160), the maximum THz field probed by the method described in section 2.5.6 can be obtained for $\varphi = \pi$ and $\alpha = \pi/2$ in the form (Equation (2.160) has maxima for $\varphi = \alpha + \pi/2$ [21].)

$$\Delta I = I_p \frac{wL}{c} n^3 r_{41} E_{\text{THz}}, \quad (\text{A.49})$$

where the refractive index n of ZnTe at the optical frequency of 800 nm is 2.8 and the electro-optic coefficient r_{41} of ZnTe is 4 pm/V [2, 21]. ω is the optical angular frequency of the probe beam and the maximum THz field can be obtained by just varying the azimuthal angle of ZnTe.

The THz field strength can be roughly calculated by Eq. (A.49) provided that we know all the terms of ΔI and I_p in the same unit. However, this is an indifferent method since the THz waveform is measured in the unit of voltage (V) by a Lock-in amplifier and the intensity of the probe beam I_p has in

¹⁰A function $f(x)$ with the Gaussian distribution $N(\mu = 0, \sigma)$ is given by

$$f(x) = \exp\left[-\frac{x^2}{\sigma^2}\right]. \quad (\text{A.43})$$

At $x = \sigma$, $f(x)$ becomes

$$f(\sigma) = \exp\left[-\frac{\sigma^2}{\sigma^2}\right] = e^{-1} \simeq 0.4. \quad (\text{A.44})$$

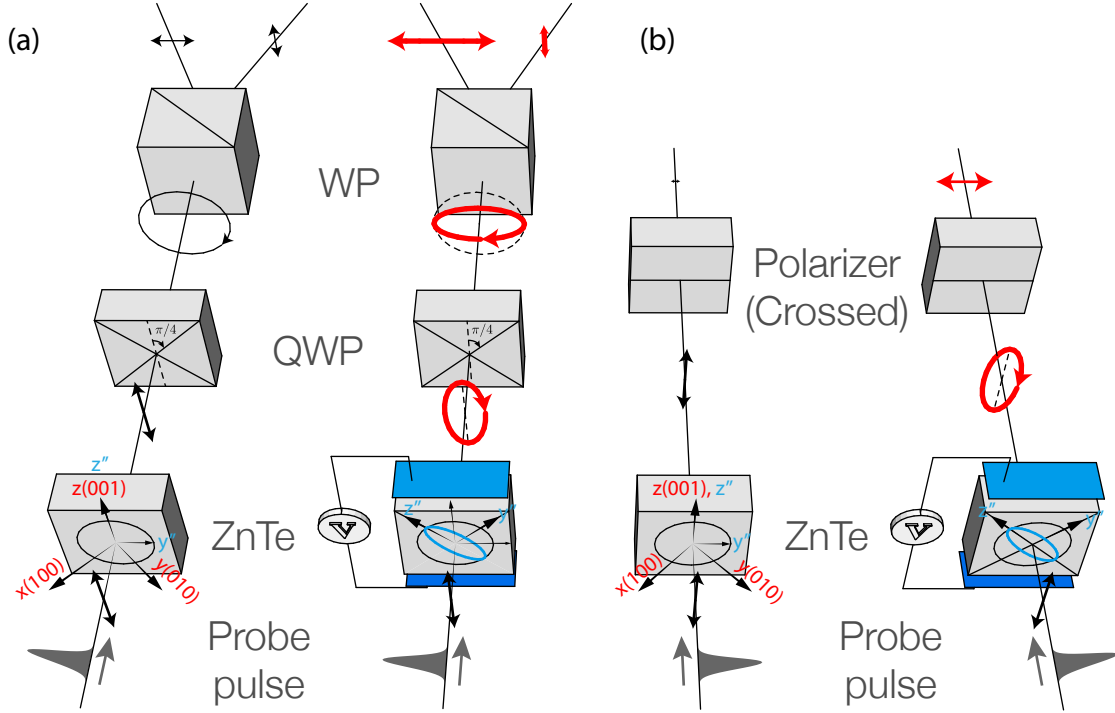


Figure A.3: THz field strength measurement setup in case of probing (a) the elliptically polarized probe beam and (b) the linearly polarized probe beam. The polarizer denoted by P has a slow axis oriented at 90° with respect to the former polarizer (not seen this figure). The experimental components should be the same as THz-TDS except for applying not THz waves but AC bias voltage to the EO material using function generator.

the units of W/m^2 . To obtain the THz electric field strength by Eq. (A.49), ΔI and I_p should be unified into the same unit.

The better way to obtain the THz field strength rather than by using Eq. (A.49) is to directly compare an applied biased voltage in the EO material via a Lock-in voltage signal from an elliptically polarized probe beam through EO material induced by THz field [130–132]. This approach is the same as using an EO light modulator [19]. Let's consider that the EO material has a square shape of thickness l and length d of one side and electrodes are attached on the top and bottom of the EO material across the gap of d . An EO material such as ZnTe has to be mounted in a non-metal holder. Provided the external voltage V_{FG} from a function generator (FG) is biased in the EO material, the external electric field E_{ext} is defined as

$$E_{\text{ext}} = \frac{V_{\text{FG}}}{d}. \quad (\text{A.50})$$

Figure A.3 shows the experimental setup for measuring the THz field strength, which is nearly the same as the setups shown in Fig. 2.11. Since THz waves can be measured by two ways described in section 2.5.6 and 2.5.7, THz field strength can also be measured by probing the elliptically polarized probe beam (Fig. A.3(a)) or the linearly polarized probe beam (Fig. A.3(b)). The experimental components should be the same as THz-TDS except for applying not THz waves but bias voltage to the EO material using a function generator. Recall that the biased electric field is achieved by a step function signal from a 65 kHz function generator with dc voltages of 30 V (TOELLNER TOE 7704). We applied DC bias with step function signal of 65 kHz (AC bias) to EO material since the signal is measured by a Lock-in amplifier to remove noise.

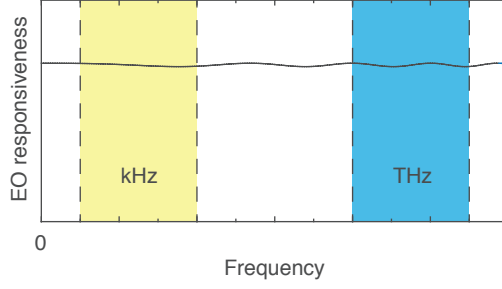


Figure A.4: The described EO responsiveness measured frequency range.

THz field strength measurement described in Fig. A.3 must be accompanied by the assumption that the EO responsivity is nearly the same in the measured frequency range in kHz by the function generator and THz by the THz waves as shown in Fig. A.4. When the AC bias is applied to the EO material, the intensity of the probe beam measured by two photodiodes in Fig. A.3(a) (or a photodiode in Fig. A.3(b)) is different from zero. Then the photocurrents from the photodiodes are measured by a Lock-in amplifier in the units of voltage. Provided E_{ext} is 30 V/cm from $V_{\text{FG}}=30$ V and $d=1$ cm from Eq. (A.50), the measured voltage signal can be calibrated following the procedure by

$$30 \text{ V/cm} \equiv V_{\text{Lock-in}}, \quad (\text{A.51})$$

where $V_{\text{Lock-in}}$ is the Lock-in signal in the unit of valtage.

A.5 Radiated electric field by the nonlinear source in the far-field

Assuming that the nonlinear crystal is assumed to be an isotropic dispersionless material, the nonlinear wave equation in the time domain is [7]

$$\nabla^2 \mathbf{E} - \frac{\epsilon^{(1)}}{c^2} \frac{\partial^2}{\partial t^2} \mathbf{E}(\mathbf{x}, t) = \frac{1}{\epsilon_0 c^2} \frac{\partial^2}{\partial t^2} \mathbf{P}^{\text{NL}}(\mathbf{x}, t), \quad (\text{A.52})$$

where the relative (dimensionless) dielectric constant is denoted as $\epsilon^{(1)} = \epsilon/\epsilon_0$ and the electric field \mathbf{E} represents the radiated field induced by the nonlinear polarization \mathbf{P}^{NL} . The coefficient of the second term can be written as

$$\frac{\epsilon^{(1)}}{c^2} = \frac{\epsilon}{\epsilon_0} \frac{1}{c^2} = \frac{\epsilon}{\epsilon_0} \mu_0 \epsilon_0 = \mu_0 \epsilon = \frac{1}{v^2}, \quad (\text{A.53})$$

where v is the phase velocity. Recall that \mathbf{E} and \mathbf{P}^{NL} in Eq. (A.52) were assumed to be quasi-monochromatic in the beginning of section A.6.1. By Eq. (A.100), \mathbf{E} and \mathbf{P}^{NL} can be written in the form

$$\begin{aligned} \mathbf{E}(\mathbf{x}, t) &= \mathbf{E}(\mathbf{x}) e^{-i\omega t}, \\ \mathbf{P}^{\text{NL}}(\mathbf{x}, t) &= \mathbf{P}^{\text{NL}}(\mathbf{x}) e^{-i\omega t}. \end{aligned} \quad (\text{A.54})$$

According to electromagnetic wave theory [12, 127]¹¹, the scalar potential or any component of an

¹¹See J. D. Jackson [12] pp. 243-246 and J. A. Stratton [127] pp. 424-248.

electric field satisfies the wave equation given by

$$\left[\nabla^2 - \frac{1}{v^2} \frac{\partial^2}{\partial t^2} \right] \Psi(\mathbf{x}, t) = -f(\mathbf{x}, t), \quad (\text{A.55})$$

where g represents a source distribution. The Fourier transforms of $\Psi(\mathbf{x}, t)$ and $f(\mathbf{x}, t)$ are defined by the equations

$$\begin{aligned} \Psi(\mathbf{x}, t) &= \frac{1}{2\pi} \int d\omega \Psi(\mathbf{x}, \omega) e^{-i\omega t}, \\ f(\mathbf{x}, t) &= \frac{1}{2\pi} \int d\omega f(\mathbf{x}, \omega) e^{-i\omega t}. \end{aligned} \quad (\text{A.56})$$

The Green function $G(\mathbf{x}, \mathbf{x}', t, t')$ satisfies the inhomogeneous wave equation in Eq. (A.55), yielding [133]¹²

$$\left[\nabla^2 - \frac{1}{v^2} \frac{\partial^2}{\partial t^2} \right] G(\mathbf{x}, \mathbf{x}', t, t') = -\delta(\mathbf{x} - \mathbf{x}') \delta(t - t'), \quad (\text{A.57})$$

which implies that the solution Ψ of Eq. (A.55) can be written as¹³

$$\Psi(\mathbf{x}, t) = \int d^3x' dt' G(\mathbf{x}, \mathbf{x}', t, t') f(\mathbf{x}', t'), \quad (\text{A.59})$$

where \mathbf{x} and \mathbf{x}' represent the field (observation) point and the source point, respectively. Then the Green function is calculated as¹⁴ [12]

$$G(\mathbf{x}, \mathbf{x}', t, t') = \frac{1}{4\pi R} \delta\left(t' - \left[t - \frac{R}{v}\right]\right), \quad (\text{A.60})$$

where $R = |\mathbf{R}| = |\mathbf{x} - \mathbf{x}'|$ and the retarded time is denoted by $t' = t - R/v$. By using Eqs. (A.59) and (A.60), the explicit solution Ψ of Eq. (A.55) can be obtained by [12, 127]

$$\begin{aligned} \Psi(\mathbf{x}, t) &= \int d^3x' dt' G(\mathbf{x}, \mathbf{x}', t, t') f(\mathbf{x}', t') \\ &= \frac{1}{4\pi} \int d^3x' dt' \frac{f(\mathbf{x}', t')}{R} \delta\left(t' - \left[t - \frac{R}{v}\right]\right) \\ &= \frac{1}{4\pi} \int d^3x' \frac{[f(\mathbf{x}', t')]_{\text{ret}}}{R}, \end{aligned} \quad (\text{A.61})$$

where $[f(\mathbf{x}', t')]_{\text{ret}} = f(\mathbf{x}', t' = t - R/v)$. Since the wave equation for each field component in Cartesian coordinates can be written as Eq. (A.55), the solution \mathbf{E} of Eq. (A.52) can be also obtained by [12]¹⁵

$$\mathbf{E}(\mathbf{x}, t) = -\frac{1}{4\pi\epsilon_0 c^2} \int d^3x' \frac{1}{R} \left[\frac{\partial^2}{\partial t'^2} \mathbf{P}^{\text{NL}}(\mathbf{x}', t') \right]_{\text{ret}}, \quad (\text{A.62})$$

¹²See M. L. Boas [133] pp. 670-674

¹³Since ∇ and t are independent with respect to \mathbf{x}' and t' , Eq. (A.59) can be a solution of Eq. (A.55) given by

$$\begin{aligned} \left[\nabla^2 - \frac{1}{v^2} \frac{\partial^2}{\partial t^2} \right] \Psi(\mathbf{x}, t) &= \left[\nabla^2 - \frac{1}{v^2} \frac{\partial^2}{\partial t^2} \right] \int d^3x' dt' G(\mathbf{x}, \mathbf{x}', t, t') f(\mathbf{x}', t') \\ &= \int d^3x' dt' \left[\nabla^2 - \frac{1}{v^2} \frac{\partial^2}{\partial t^2} \right] G(\mathbf{x}, \mathbf{x}', t, t') f(\mathbf{x}', t') \\ &= - \int d^3x' dt' \delta(\mathbf{x} - \mathbf{x}') \delta(t - t') f(\mathbf{x}', t') = -f(\mathbf{x}, t). \end{aligned} \quad (\text{A.58})$$

¹⁴See Jackson [12] pp.243-245.

¹⁵See J. D. Jackson [12] p. 246.

where the last term containing the time derivative in the integrands can be calculated as [12]¹⁶

$$\left[\frac{\partial^2}{\partial t'^2} \mathbf{P}^{\text{NL}}(\mathbf{x}', t') \right]_{\text{ret}} = \frac{\partial^2}{\partial t^2} [\mathbf{P}^{\text{NL}}(\mathbf{x}', t')]_{\text{ret}} = \frac{\partial^2}{\partial t^2} \mathbf{P}^{\text{NL}}(\mathbf{x}', t' = t - R/v). \quad (\text{A.69})$$

By Fourier transformation, the nonlinear wave equation of Eq. (A.52) in the frequency domain becomes

$$\nabla^2 \mathbf{E} + \frac{\omega^2}{c^2} \epsilon^{(1)} \mathbf{E}(\mathbf{x}, \omega) = -\frac{\omega^2}{\epsilon_0 c^2} \mathbf{P}^{\text{NL}}(\mathbf{x}, \omega), \quad (\text{A.70})$$

which can be written as a wave equation in the frequency domain as in Eq. (A.55) as¹⁷

$$\nabla^2 \Psi(\mathbf{x}, \omega) + \frac{\omega^2}{c^2} \epsilon^{(1)} \Psi(\mathbf{x}, \omega) = -f(\mathbf{x}, \omega), \quad (\text{A.71})$$

where $\omega^2 n^2 / c^2 = \omega^2 / v^2$ and $n^2 = \epsilon^{(1)}$. Analogous to Eq. (A.57), the Green function G satisfying the

¹⁶See R. W. Boyd [7] p. 381. Let A be a function of t and z so that $A(t, z)$. Since the retarded time t' is defined by $t' = t - z/v$, the function A can be written as $A(t, z) = A(t', z')$ in the case when $z = z'$. The total differentials of $A(t', z')$ and $A(t, z)$ become

$$\begin{aligned} dA(z', t') &= \frac{\partial A}{\partial z'} dz' + \frac{\partial A}{\partial t'} dt' \\ &= \frac{\partial A}{\partial z'} dz' + \frac{\partial A}{\partial t'} \left[\frac{\partial t'}{\partial t} dt + \frac{\partial t'}{\partial z'} dz' \right] \end{aligned} \quad (\text{A.63})$$

$$\begin{aligned} &= \left[\frac{\partial A}{\partial z'} + \frac{\partial A}{\partial t'} \frac{\partial t'}{\partial z'} \right] dz' + \frac{\partial A}{\partial t'} \frac{\partial t'}{\partial t} dt, \\ dA(z, t) &= \frac{\partial A}{\partial z} dz + \frac{\partial A}{\partial t} dt = \frac{\partial A}{\partial z} dz' + \frac{\partial A}{\partial t} dt. \end{aligned} \quad (\text{A.64})$$

By comparing Eqs. (A.63) and (A.64), we obtain

$$\left(\frac{dA}{dz} \right)_{dt=0} = \left(\frac{\partial A}{\partial z} \right)_t \equiv \frac{\partial A}{\partial z} = \frac{\partial A}{\partial z'} + \frac{\partial A}{\partial t'} \frac{\partial t'}{\partial z'}, \quad (\text{A.65})$$

$$\left(\frac{dA}{dt} \right)_{dz'=0} = \left(\frac{\partial A}{\partial t} \right)_{z'} \equiv \frac{\partial A}{\partial t} = \frac{\partial A}{\partial t'} \frac{\partial t'}{\partial t}, \quad (\text{A.66})$$

which implies that

$$\frac{\partial}{\partial z} = \frac{\partial}{\partial z'} - \frac{1}{v} \frac{\partial}{\partial t'}, \quad (\text{A.67})$$

$$\frac{\partial}{\partial t} = \frac{\partial}{\partial t'}, \quad (\text{A.68})$$

where $\partial t' / \partial z' = -1/v$ and $\partial t' / \partial t = 1$.

¹⁷By using Eq. (A.56),

$$\begin{aligned} &\nabla^2 \Psi - \frac{1}{v^2} \frac{\partial^2}{\partial t^2} \Psi(\mathbf{x}, t) = -f(\mathbf{x}, t) \\ \Leftrightarrow &\nabla^2 \frac{1}{2\pi} \int d\omega \Psi(\mathbf{x}, \omega) e^{-i\omega t} - \frac{1}{v^2} \frac{\partial^2}{\partial t^2} \frac{1}{2\pi} \int d\omega \Psi(\mathbf{x}, \omega) e^{-i\omega t} = -\frac{1}{2\pi} \int d\omega f(\mathbf{x}, \omega) e^{-i\omega t} \\ \Leftrightarrow &\frac{1}{2\pi} \int d\omega \nabla^2 \Psi(\mathbf{x}, \omega) e^{-i\omega t} - \frac{1}{v^2} \frac{1}{2\pi} \int d\omega \Psi(\mathbf{x}, \omega) \frac{\partial^2}{\partial t^2} e^{-i\omega t} = -\frac{1}{2\pi} \int d\omega f(\mathbf{x}, \omega) e^{-i\omega t} \\ \Leftrightarrow &\frac{1}{2\pi} \int d\omega \nabla^2 \Psi(\mathbf{x}, \omega) e^{-i\omega t} + \frac{1}{v^2} \frac{1}{2\pi} \int d\omega \Psi(\mathbf{x}, \omega) \omega^2 e^{-i\omega t} = -\frac{1}{2\pi} \int d\omega f(\mathbf{x}, \omega) e^{-i\omega t} \\ \Leftrightarrow &\frac{1}{2\pi} \int d\omega \left[\nabla^2 \Psi(\mathbf{x}, \omega) + \frac{\omega^2}{v^2} \Psi(\mathbf{x}, \omega) \right] e^{-i\omega t} = -\frac{1}{2\pi} \int d\omega f(\mathbf{x}, \omega) e^{-i\omega t} \\ \Leftrightarrow &\nabla^2 \Psi(\mathbf{x}, \omega) + \frac{\omega^2}{v^2} \Psi(\mathbf{x}, \omega) = -f(\mathbf{x}, \omega), \end{aligned}$$

where $\omega^2 / v^2 = \omega^2 n^2 / c^2$ and $n^2 = \epsilon^{(1)}$. Eq. (A.52) is also transformed into Eq. (A.70) in the frequency domain by the same analogy.

inhomogeneous wave equation as in Eq. (A.71) can be written as¹⁸

$$\left[\nabla^2 + \frac{\omega^2}{c^2} \epsilon^{(1)} \right] G(\mathbf{x}, \mathbf{x}', \omega) = -\delta(\mathbf{x} - \mathbf{x}'), \quad (\text{A.73})$$

which implies that the solution Ψ of Eq. (A.71) can be written as

$$\Psi(\mathbf{x}, \omega) = \int d^3x' G(\mathbf{x}, \mathbf{x}', \omega) f(\mathbf{x}', \omega). \quad (\text{A.74})$$

$G(\mathbf{x}, \mathbf{x}', \omega)$ is the inverse Fourier transform of $G(\mathbf{x}, \mathbf{x}', t, t')$ given by

$$G(\mathbf{x}, \mathbf{x}', \omega) = \int d\tau G(\mathbf{x}, \mathbf{x}', \tau) e^{i\omega\tau}, \quad (\text{A.75})$$

where $G(\mathbf{x}, \mathbf{x}', t, t') = G(\mathbf{x}, \mathbf{x}', \tau)$ with $\tau = R/v = t - t'$, so that $G(\mathbf{x}, \mathbf{x}', \omega)$ becomes¹⁹

$$G(\mathbf{x}, \mathbf{x}', \omega) = \frac{1}{4\pi R} \exp\left[i\omega \frac{R}{v}\right], \quad (\text{A.77})$$

where $R = |\mathbf{x} - \mathbf{x}'|$. Therefore, the explicit solution Ψ of Eq. (A.71) is [12]

$$\begin{aligned} \Psi(\mathbf{x}, \omega) &= \int d^3x' G(\mathbf{x}, \mathbf{x}', \omega) f(\mathbf{x}', \omega) \\ &= \frac{1}{4\pi} \int d^3x' \frac{f(\mathbf{x}', \omega)}{R} e^{i\omega R/v}. \end{aligned} \quad (\text{A.78})$$

The solution \mathbf{E} of Eq. (A.70) is

$$\mathbf{E}(\mathbf{x}, \omega) = \frac{1}{4\pi\epsilon_0} \frac{\omega^2}{c^2} \int d^3x' \frac{\mathbf{P}^{\text{NL}}(\mathbf{x}', \omega)}{R} e^{i\omega R/v}. \quad (\text{A.79})$$

Now, we need to concentrate on finding the far-field solution of Eqs. (A.62) and (A.79). In the

¹⁸Analogous to Eq. (A.57),

$$\begin{aligned} \left[\nabla^2 + \frac{\omega^2}{c^2} \epsilon^{(1)} \right] \Psi(\mathbf{x}, \mathbf{x}', \omega) &= \left[\nabla^2 + \frac{\omega^2}{c^2} \epsilon^{(1)} \right] \int d^3x' G(\mathbf{x}, \mathbf{x}', \omega) f(\mathbf{x}', \omega) \\ &= \int d^3x' \left[\nabla^2 + \frac{\omega^2}{c^2} \epsilon^{(1)} \right] G(\mathbf{x}, \mathbf{x}', \omega) f(\mathbf{x}', \omega) \\ &= - \int d^3x' \delta(\mathbf{x} - \mathbf{x}') f(\mathbf{x}', \omega) = -f(\mathbf{x}, \omega). \end{aligned} \quad (\text{A.72})$$

¹⁹By Eq. (A.60) and $\tau = R/v = t - t'$,

$$\begin{aligned} G(\mathbf{x}, \mathbf{x}', \omega) &= \int d\tau G(\mathbf{x}, \mathbf{x}', \tau) e^{i\omega\tau} \\ &= \frac{1}{4\pi R} \int d\tau \delta\left(t' - \left[t - \frac{R}{v}\right]\right) e^{i\omega\tau} = \frac{1}{4\pi R} \int d\tau \delta\left(-[t - t'] + \frac{R}{v}\right) e^{i\omega\tau} \\ &= \frac{1}{4\pi R} \int d\tau \delta\left(-\tau + \frac{R}{v}\right) e^{i\omega\tau} = \frac{1}{4\pi R} e^{i\omega \frac{R}{v}}. \end{aligned} \quad (\text{A.76})$$

far-field zone (*i.e.* $|\mathbf{x}'| \ll |\mathbf{x}|$), R in the integrands of Eqs. (A.62) and (A.79) can be expanded as²⁰

$$R \simeq r - \frac{\mathbf{x} \cdot \mathbf{x}'}{r}, \quad \frac{1}{R} \simeq \frac{1}{r} + \frac{\mathbf{x} \cdot \mathbf{x}'}{r^3}, \quad (\text{A.82})$$

where $|\mathbf{x}| = r$ and $|\mathbf{x}'| = r'$. Then the far-field solutions²¹ for time domain and frequency domain become

$$\mathbf{E}(\mathbf{x}, t) = \frac{-1}{4\pi\epsilon_0 c^2} \frac{1}{r} \frac{\partial^2}{\partial t^2} \int d^3x' \mathbf{P}^{\text{NL}} \left(\mathbf{x}', t' = t - \frac{R}{v} \right), \quad (\text{A.83})$$

$$\mathbf{E}(\mathbf{x}, \omega) = \frac{\omega^2}{4\pi\epsilon_0 c^2} \frac{\exp(ikr)}{r} \int d^3x' \mathbf{P}^{\text{NL}}(\mathbf{x}', \omega) \exp \left[-ik \frac{\mathbf{x} \cdot \mathbf{x}'}{r} \right], \quad (\text{A.84})$$

where $\omega/v = \omega n/c \equiv k$. From Eqs. (A.62) and (A.79), we can see that the electric field \mathbf{E} can be calculated provided that we know the nonlinear polarization \mathbf{P}^{NL} . If the nonlinear medium is spatially homogeneous, or in other words, the nonlinear polarization is considered a constant with respect to the source points (*i.e.* independent from the source position), the radiated electric field in the far-field $\mathbf{E}(\mathbf{x}, t)$ is approximately proportional to the nonlinear polarization as follows:

$$\mathbf{E}(\mathbf{x}, t) \simeq \frac{-1}{4\pi\epsilon_0 c^2} \frac{1}{r} \frac{\partial^2}{\partial t^2} [\mathbf{P}^{\text{NL}}(t')]_{\text{ret}} \int d^3x' \propto \frac{\partial^2}{\partial t^2} \mathbf{P}^{\text{NL}}(t). \quad (\text{A.85})$$

By the same analogy, the radiated field $\mathbf{E}(\mathbf{x}, \omega)$ in the far-field becomes

$$\mathbf{E}(\mathbf{x}, \omega) \propto \omega^2 \mathbf{P}^{\text{NL}}(\omega). \quad (\text{A.86})$$

We can say that the radiated electric field in the frequency domain is proportional to the nonlinear polarization.

There is a practical example described in Ref. [5, 6]. For a linearly polarized field, the effective polarization \mathbf{P}^{NL} in the z -axis direction can be expressed by [5–7]

$$P^{(2)}(\mathbf{x}, t) = P^{(2)}(\mathbf{x}, \omega_2) e^{-i\omega_2 t}, \quad (\text{A.87})$$

with

$$P^{(2)}(\mathbf{x}, \omega_2) = \epsilon_0 \chi^{(2)} A_1^*(\mathbf{x}) A_3(\mathbf{x}) e^{ik_2 z} = P^{(2)} e^{ik_2 z}, \quad (\text{A.88})$$

where $k_2 = k_3 - k_1$ and $\chi^{(2)}(\omega_2; -\omega_1, \omega_3)$. With $A_1(\mathbf{x})$ and $A_3(\mathbf{x})$ being constant, the nonlinear polarization becomes

$$P^{(2)}(\mathbf{x}, t) \simeq P^{(2)} e^{i(k_2 z - \omega_2 t)}. \quad (\text{A.89})$$

²⁰Provided the angle between $|\mathbf{x}| = r$ and $|\mathbf{x}'| = r'$ is γ , R for $\mathbf{x}' \ll \mathbf{x}$ can be expressed by the law of cosines given by [13]

$$\begin{aligned} R &= |\mathbf{x} - \mathbf{x}'| = \sqrt{r^2 + r'^2 - 2rr' \cos \gamma} = \sqrt{r^2 + r'^2 - 2\mathbf{x} \cdot \mathbf{x}'} \\ &= \left[r^2 \left(1 + \frac{r'^2}{r^2} - 2 \frac{\mathbf{x} \cdot \mathbf{x}'}{r^2} \right) \right]^{\frac{1}{2}} = r \left[\left(1 - 2 \frac{\mathbf{x} \cdot \mathbf{x}'}{r^2} \right) \right]^{\frac{1}{2}} \simeq r \left[1 - \frac{\mathbf{x} \cdot \mathbf{x}'}{r^2} \right] = r - \frac{\mathbf{x} \cdot \mathbf{x}'}{r}, \end{aligned} \quad (\text{A.80})$$

which implies that

$$\frac{1}{R} = \left[r - \frac{\mathbf{x} \cdot \mathbf{x}'}{r} \right]^{-1} = \left[r \left(1 - \frac{\mathbf{x} \cdot \mathbf{x}'}{r^2} \right) \right]^{-1} \simeq \frac{1}{r} \left[1 + \frac{\mathbf{x} \cdot \mathbf{x}'}{r^2} + \dots \right] = \frac{1}{r} + \frac{\mathbf{x} \cdot \mathbf{x}'}{r^3} + \dots \quad (\text{A.81})$$

²¹The term “far-field” is defined in J. D. Jackson, *Classical electrodynamics 3 rd edition*, p. 408 [12].

The far-field solutions for the time domain and frequency domains in the case of Eq. (A.89) become²²

$$\mathbf{E}(\mathbf{x}, t) = \frac{-1}{4\pi\epsilon_0 c^2} \frac{1}{r} \frac{\partial^2}{\partial t^2} P^{(2)} \exp[i(k_2 r - \omega_2 t)] \int d^3 x' \exp \left[ik_2 \left(z' - \frac{\mathbf{x} \cdot \mathbf{x}'}{r} \right) \right], \quad (\text{A.92})$$

$$\mathbf{E}(\mathbf{x}, \omega) = \frac{1}{4\pi\epsilon_0} \frac{\omega^2}{c^2} \frac{\exp(ikr)}{r} \mathbf{P}^{(2)} \int d^3 x' \exp \left[ik_2 \left(z' - \frac{\mathbf{x} \cdot \mathbf{x}'}{r} \right) \right], \quad (\text{A.93})$$

where $k_2 \equiv \omega_2/v$.

A.6 Generation and detection behavior from zinc-blende crystals with various cut orientation

A.6.1 THz generation via optical rectification

The rectified field radiated by the optical rectification described in section 2.4.1 is THz waves. Assuming that the pump beams are quasi-monochromatic, the optical rectification is described by the difference frequency generation which comes from 2nd-order nonlinear susceptibility in the nonlinear crystal, giving

$$P_i^{(2)}(\Omega) = 2\epsilon_0 \sum_{jk} \chi_{ijk}^{(2)}(\Omega; -\omega + \Omega, \omega) E_j^*(\omega - \Omega) E_k(\omega), \quad (\text{A.94})$$

where Ω and ω represent a THz frequency and an optical frequency, respectively. In the optical rectification, Ω is sufficiently smaller than ω , which implies that Ω can be considered as zero. Then Eq. (A.94) becomes

$$P_i^{(2)}(0) = 2\epsilon_0 \sum_{jk} \chi_{ijk}^{(2)}(0; -\omega, \omega) E_j^*(\omega) E_k(\omega). \quad (\text{A.95})$$

When the frequency of the probe beam is much smaller than the lowest resonance frequency of the nonlinear crystal and the dispersion of the susceptibility for the nonlinear crystal is neglected²³, the

22

$$\begin{aligned} \mathbf{E}(\mathbf{x}, t) &= \frac{-1}{4\pi\epsilon_0 c^2} \frac{1}{r} \frac{\partial^2}{\partial t^2} \int d^3 x' P^{(2)} \exp \left[i \left\{ k_2 z' - \omega_2 \left(t - \frac{R}{v} \right) \right\} \right] \\ &= \frac{-1}{4\pi\epsilon_0 c^2} \frac{1}{r} \frac{\partial^2}{\partial t^2} P^{(2)} \int d^3 x' \exp [i(k_2 z' - \omega_2 t)] \exp \left[i\omega_2 \frac{1}{v} \left(r - \frac{\mathbf{x} \cdot \mathbf{x}'}{r} \right) \right] \\ &= \frac{-1}{4\pi\epsilon_0 c^2} \frac{1}{r} \frac{\partial^2}{\partial t^2} P^{(2)} \exp(ik_2 r) \int d^3 x' \exp [i(k_2 z' - \omega_2 t)] \exp \left[-ik_2 \frac{\mathbf{x} \cdot \mathbf{x}'}{r} \right] \\ &= \frac{-1}{4\pi\epsilon_0 c^2} \frac{1}{r} \frac{\partial^2}{\partial t^2} P^{(2)} \exp[i(k_2 r - \omega_2 t)] \int d^3 x' \exp \left[ik_2 \left(z' - \frac{\mathbf{x} \cdot \mathbf{x}'}{r} \right) \right], \end{aligned} \quad (\text{A.90})$$

$$\begin{aligned} \mathbf{E}(\mathbf{x}, \omega) &= \frac{1}{4\pi\epsilon_0} \frac{\omega^2}{c^2} \frac{\exp(ikr)}{r} \int d^3 x' \mathbf{P}^{(2)} \exp \left[ik_2 \left(z' - \frac{\mathbf{x} \cdot \mathbf{x}'}{r} \right) \right] \\ &= \frac{1}{4\pi\epsilon_0} \frac{\omega^2}{c^2} \frac{\exp(ikr)}{r} \mathbf{P}^{(2)} \int d^3 x' \exp \left[ik_2 \left(z' - \frac{\mathbf{x} \cdot \mathbf{x}'}{r} \right) \right]. \end{aligned} \quad (\text{A.91})$$

²³Each sentence has a meaning as follows [7].

- ✓ The frequency of the probe beam is much smaller than the lowest resonance frequency of the nonlinear crystal.
 - ⇒ There is no resonance in the frequency range measured by the probe beam.
 - ⇒ The nonlinear material can be considered as a lossless material.
- ✓ The dispersion of the susceptibility for the nonlinear crystal is neglected.
 - ⇒ The nonlinear susceptibility χ^{NL} is a constant in frequency domain.
 - ⇒ The response function R in time domain (t) responds instantaneously to the applied electric field.

nonlinear polarization can be obtained by Kleinman's symmetry condition [7]. Under this condition, the 2nd-order susceptibility $\chi_{ijk}^{(2)}$ in a relationship with d_{ijk} given by

$$d_{ijk} = \frac{1}{2} \chi_{ijk}^{(2)} \quad (\text{A.96})$$

can be abbreviated to the 3×6 matrix d_{il} with contracted indices l [7]. In the case of a zinc-blende crystal with the point group $\bar{4}3m$, the contracted matrix d_{il} is simplified as

$$d_{il} = \begin{bmatrix} 0 & 0 & 0 & d_{14} & 0 & 0 \\ 0 & 0 & 0 & 0 & d_{14} & 0 \\ 0 & 0 & 0 & 0 & 0 & d_{14} \end{bmatrix}. \quad (\text{A.97})$$

The ZnTe crystal, a member of the point group $\bar{4}3m$, is a widely used nonlinear crystal for generation as well as detection of THz waves. Provided the polarization of the incident pump beam propagating in the $+z$ direction is given by

$$\mathbf{E} = E_0 \begin{pmatrix} 1 \\ 0 \\ 0 \end{pmatrix} \quad (\text{A.98})$$

in the lab coordinates (x, y, z) as shown in Fig. A.5, the electric field \mathbf{E} on the (110) or (100) plane can be expressed as \mathbf{E}' in the crystallographic coordinates (x', y', z') by using the successive rotation matrices. In crystallographic coordinates, the nonlinear polarization \mathbf{P}' induced by $\chi^{(2)}(0; -\omega, \omega)$ can be written in the form

$$\begin{pmatrix} P_{x'}^{(2)}(0) \\ P_{y'}^{(2)}(0) \\ P_{z'}^{(2)}(0) \end{pmatrix} = 4\epsilon_0 d_{14} \begin{bmatrix} 0 & 0 & 0 & 1 & 0 & 0 \\ 0 & 0 & 0 & 0 & 1 & 0 \\ 0 & 0 & 0 & 0 & 0 & 1 \end{bmatrix} \begin{pmatrix} E_{x'}^*(\omega)E_{x'}(\omega) \\ E_{y'}^*(\omega)E_{y'}(\omega) \\ E_{z'}^*(\omega)E_{z'}(\omega) \\ E_{y'}^*(\omega)E_{z'}(\omega) + E_{z'}^*(\omega)E_{y'}(\omega) \\ E_{x'}^*(\omega)E_{z'}(\omega) + E_{z'}^*(\omega)E_{x'}(\omega) \\ E_{x'}^*(\omega)E_{y'}(\omega) + E_{y'}^*(\omega)E_{x'}(\omega) \end{pmatrix}, \quad (\text{A.99})$$

where $E_{x'}^*(\omega) = E_{x'}(-\omega)$.

Now, it is time to take into account the amplitude terms E_j in Eq. (A.99). The electric field for a quasi-monochromatic wave is generally expressed as a function of amplitude and phase in the form²⁴

$$\mathbf{E}(\mathbf{x}, t) = E_0 \text{Re} \left[e^{i(\mathbf{k} \cdot \mathbf{x} - \omega t)} \right], \quad (\text{A.100})$$

\Leftrightarrow The response function $R(t)$ can be expressed by a delta function $\delta(t)$ given by

$$R(t) = \chi^{(\text{NL})} \delta(t),$$

where $\chi^{(\text{NL})}$ is a constant.

²⁴Eq. (A.101) is explained in detail in Boys [7] pp. 18-19.

which implies²⁵

$$\begin{aligned}
\mathbf{E}(\mathbf{x}, t) &= \frac{E_0}{2} \left[e^{i(\mathbf{k}\cdot\mathbf{x}-\omega t)} + e^{-i(\mathbf{k}\cdot\mathbf{x}-\omega t)} \right] \\
&= \left[\frac{E_0}{2} e^{i(\mathbf{k}\cdot\mathbf{x})} \right] e^{-i\omega t} + \left[\frac{E_0}{2} e^{-i(\mathbf{k}\cdot\mathbf{x})} \right] e^{i\omega t} \\
&= E(\omega) e^{-i\omega t} + E(-\omega) e^{i\omega t},
\end{aligned} \tag{A.101}$$

where $E(\omega) = A(\omega)e^{i(\mathbf{k}\cdot\mathbf{x})}$ and $A(\omega) = E_0/2$. Note that we are interested only in nonlinear behavior in the time domain at a fixed position. So, we obtain $A(\omega) = A(-\omega) = E_0/2$ for the fixed position in the case when $\mathbf{x} = 0$, which implies that $E(\omega) = E(-\omega) = E^*(\omega)$. Then Eq. (A.99) is reduced as

$$\begin{pmatrix} P_{x'}^{(2)}(0) \\ P_{y'}^{(2)}(0) \\ P_{z'}^{(2)}(0) \end{pmatrix} = 4\epsilon_0 d_{14} \begin{bmatrix} 0 & 0 & 0 & 1 & 0 & 0 \\ 0 & 0 & 0 & 0 & 1 & 0 \\ 0 & 0 & 0 & 0 & 0 & 1 \end{bmatrix} \begin{pmatrix} E_{x'}^2(\omega) \\ E_{y'}^2(\omega) \\ E_{z'}^2(\omega) \\ 2E_{y'}(\omega)E_{z'}(\omega) \\ 2E_{x'}(\omega)E_{z'}(\omega) \\ 2E_{x'}(\omega)E_{y'}(\omega) \end{pmatrix}. \tag{A.102}$$

A.6.1.1 THz generation from (110) ZnTe crystal

The electric field on the (110) plane as shown in Fig. A.5(a) can be expressed in crystallographic coordinates (x', y', z') as

$$\mathbf{E}' = M^{(110)} \mathbf{E} = E_0 \begin{pmatrix} -\frac{1}{\sqrt{2}} \sin \theta \\ \frac{1}{\sqrt{2}} \sin \theta \\ \cos \theta \end{pmatrix} \tag{A.103}$$

with

$$M^{(110)} \equiv R_{z_2}^{\text{sys}} \left(\frac{3}{4}\pi \right) R_{x_1}^{\text{sys}}(-\theta) R_y^{\text{sys}} \left(\frac{\pi}{2} \right), \tag{A.104}$$

where the rotations R_j^{sys} are defined by Eq. (C.15). θ represents the angle between the polarization of the optical pump beam and the x -axis as shown in Fig. A.5. By Eq. (A.102), we obtain the 2nd-order polarization in crystallographic coordinates as [134]

$$\mathbf{P}' = 8\epsilon_0 d_{14} E_0^2 \begin{pmatrix} \frac{1}{\sqrt{2}} \cos \theta \sin \theta \\ -\frac{1}{\sqrt{2}} \cos \theta \sin \theta \\ -\frac{1}{2} \sin^2 \theta \end{pmatrix}. \tag{A.105}$$

According to Eq. (C.17), the inverse matrix of $M^{(110)}$ in Eq. (A.104) becomes

$$M_{(110)}^{-1} = \left[R_{z_2}^{\text{sys}} \left(\frac{3}{4}\pi \right) R_{x_1}^{\text{sys}}(-\theta) R_y^{\text{sys}} \left(\frac{\pi}{2} \right) \right]^{-1} = R_y^{\text{sys}} \left(-\frac{\pi}{2} \right) R_{x_1}^{\text{sys}}(\theta) R_{z_2}^{\text{sys}} \left(-\frac{3}{4}\pi \right), \tag{A.106}$$

²⁵ $\mathbf{E}(\mathbf{x}, t)$ for a quasi-monochromatic wave can be also expressed as [7]

$$\mathbf{E}(\mathbf{x}, t) = E(\omega) e^{-i\omega t} + E(-\omega) e^{i\omega t} = E(\mathbf{x}) e^{-i\omega t} + \text{c.c.}$$

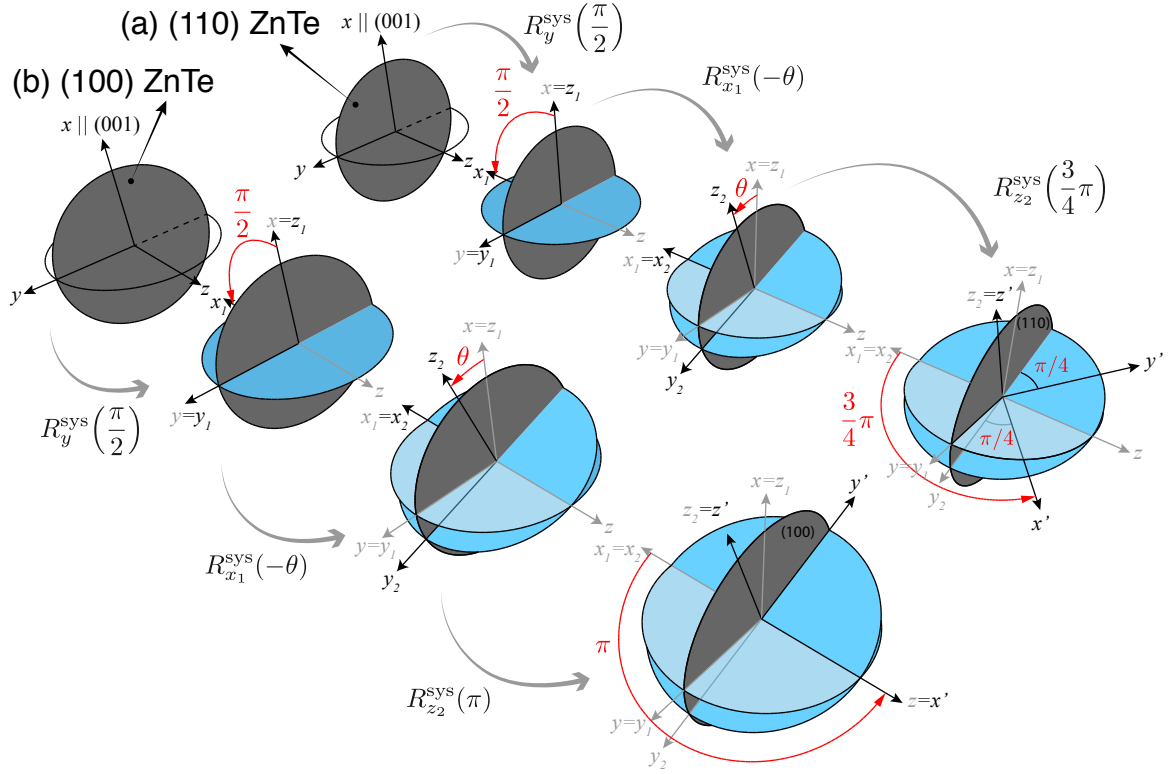


Figure A.5: Lab coordinates and crystallographic coordinates in case of (a) (110) ZnTe (b) (100) ZnTe.

by which \mathbf{P}' can be transformed into lab coordinates as [134]

$$\mathbf{P} = M_{(110)}^{-1} \mathbf{P}' = 8\epsilon_0 d_{14} E_0^2 \begin{pmatrix} -\frac{3}{2} \cos \theta \sin^2 \theta \\ \cos^2 \theta \sin \theta - \frac{1}{2} \sin^3 \theta \\ 0 \end{pmatrix}. \quad (\text{A.107})$$

In order to compute the radiated THz field induced by nonlinear polarization, we should go back to the nonlinear wave equation. From Eq. (A.86), the angular dependence of the magnitude of the THz electric field radiated from (110) ZnTe crystal in the far-field can be expressed as²⁶

$$|\mathbf{E}(\Omega)| \propto |\mathbf{P}(\Omega)| \propto \left| \frac{\sin \theta}{2} [1 + 3 \cos^2 \theta]^{1/2} \right|. \quad (\text{A.112})$$

In a similar fashion, the polarization of the induced THz fields parallel to the x and y axes can be

²⁶By using Matlab,

$$\mathbf{P}(\Omega) \propto \left[\left(-\frac{3}{2} \cos \theta \sin^2 \theta \right)^2 + \left(\cos^2 \theta \sin \theta - \frac{1}{2} \sin^3 \theta \right)^2 \right]^{1/2} = \left[\frac{\sin^6 \theta}{4} + \frac{5 \cos^2 \theta \sin^4 \theta}{4} + \cos^4 \theta \sin^2 \theta \right]^{1/2} \quad (\text{A.108})$$

$$= \frac{\sin \theta}{2} [\sin^4 \theta + 5 \cos^2 \theta \sin^2 \theta + 4 \cos^4 \theta]^{1/2} \quad (\text{A.109})$$

$$= \frac{\sin \theta}{2} [\sin^2 \theta (1 - \cos^2 \theta) + 5 \cos^2 \theta \sin^2 \theta + 4 \cos^2 \theta (1 - \sin^2 \theta)]^{1/2} \quad (\text{A.110})$$

$$= \frac{\sin \theta}{2} [\sin^2 \theta + 4 \cos^2 \theta]^{1/2} = \frac{\sin \theta}{2} [1 + 3 \cos^2 \theta]^{1/2}. \quad (\text{A.111})$$

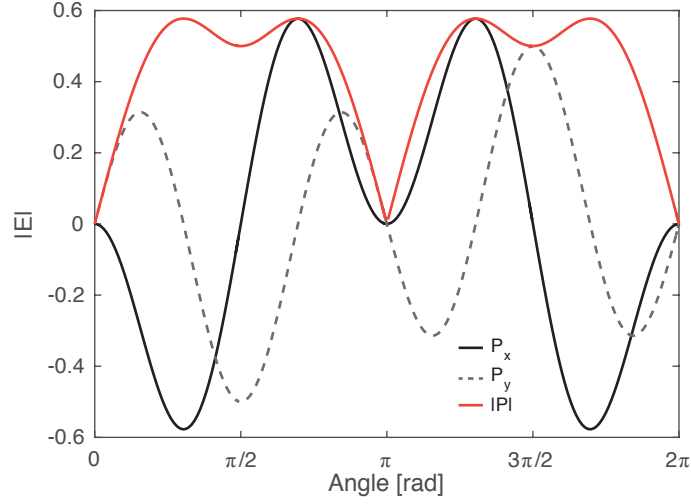


Figure A.6: The angular dependence of the radiated THz field with respect to the azimuthal angle θ of (110) ZnTe crystal.

expressed as²⁷

$$\mathbf{E}_x(\Omega) \propto \mathbf{P}_x(\Omega) = 8\epsilon_0 d_{14} E_0^2 \left[\frac{3}{8} (\cos 3\theta - \cos \theta) \right], \quad (\text{A.117})$$

$$\mathbf{E}_y(\Omega) \propto \mathbf{P}_y(\Omega) = 8\epsilon_0 d_{14} E_0^2 \left[\frac{3}{8} \left(\sin 3\theta - \frac{1}{3} \sin \theta \right) \right]. \quad (\text{A.118})$$

Figure A.6 shows the angular dependence of the radiated THz field. Note that angle θ represents the angle between the polarization of the optical pump beam and the x -axis as shown in Fig. A.5. More simple analysis is done in Ref. [135]. This may also be helpful in studying the radiation from zinc-blend crystals.

27

$$\begin{aligned} \cos 3\theta - \cos \theta &= \cos(\theta + 2\theta) - \cos \theta = \cos \theta \cos 2\theta - \sin \theta \sin 2\theta - \cos \theta \\ &= \cos \theta \cdot (\cos^2 \theta - \sin^2 \theta) - \sin \theta \cdot (2 \sin \theta \cos \theta) - \cos \theta \\ &= \cos^3 \theta - 3 \cos \theta \sin^2 \theta - \cos \theta = \cos^3 \theta - 3 \cos \theta \cdot (1 - \cos^2 \theta) - \cos \theta \\ &= 4(\cos^3 \theta - \cos \theta) = 4 \cos \theta \cdot (\cos^2 \theta - 1) = -4 \cos \theta \sin^2 \theta, \end{aligned} \quad (\text{A.113})$$

which leads to

$$-\frac{3}{2} \cos \theta \sin^2 \theta = \frac{3}{8} (\cos 3\theta - \cos \theta). \quad (\text{A.114})$$

$$\begin{aligned} 2 \sin \theta \cos^2 \theta - \sin^3 \theta &= 2 \cdot \frac{e^{i\theta} - e^{-i\theta}}{2i} \left(\frac{e^{i\theta} + e^{-i\theta}}{2} \right)^2 - \left(\frac{e^{i\theta} - e^{-i\theta}}{2i} \right)^2 \\ &= \frac{1}{8i} [-e^{i\theta} + e^{-i\theta} + 3e^{i3\theta} - 3e^{-i3\theta}] \\ &= \frac{1}{8i} \left[-\left(\frac{e^{i\theta} - e^{-i\theta}}{2i} \right) 2i + 3 \left(\frac{e^{i3\theta} - e^{-i3\theta}}{2i} \right) 2i \right] = \frac{1}{4} (-\sin \theta + 3 \sin 3\theta), \end{aligned} \quad (\text{A.115})$$

so that

$$\cos^2 \theta \sin \theta - \frac{1}{2} \sin^3 \theta = \frac{1}{8} (3 \sin 3\theta - \sin \theta). \quad (\text{A.116})$$

A.6.1.2 No THz generation from (100) ZnTe crystal

If the polarization of the incident pump beam is given by Eq. (A.98), the electric field \mathbf{E} on the (100) plane as shown in Fig. A.5(b) is expressed in the crystallographic coordinates (x', y', z') as

$$\mathbf{E}' = M^{(100)} \mathbf{E} = E_0 \begin{pmatrix} 0 \\ \sin \theta \\ \cos \theta \end{pmatrix} \quad (\text{A.119})$$

with

$$M^{(110)} \equiv R_{z_2}^{\text{sys}}(\pi) R_{x_1}^{\text{sys}}(-\theta) R_y^{\text{sys}}\left(\frac{\pi}{2}\right). \quad (\text{A.120})$$

By Eq. (A.102), the 2nd-order polarization for (100) ZnTe crystal in the crystallographic coordinates is

$$\mathbf{P}' = 8\epsilon_0 d_{14} E_0^2 \begin{pmatrix} \cos \theta \sin \theta \\ 0 \\ 0 \end{pmatrix}. \quad (\text{A.121})$$

\mathbf{P}' can be transformed into the lab coordinates as

$$\mathbf{P} = M_{(100)}^{-1} \mathbf{P}' = 8\epsilon_0 d_{14} E_0^2 \begin{pmatrix} 0 \\ 0 \\ \cos \theta \sin \theta \end{pmatrix}. \quad (\text{A.122})$$

By noting that the incident beam propagates along the z -direction, it is concluded that THz field cannot be radiated from a (100) ZnTe crystal since there is no nonlinear polarization terms on the xy plane (*i.e.* x and y axes) in Eq. (A.122). The content described in this section was confirmed in Ref. [134–136].

A.6.2 THz detection via the Pockels effect

A.6.2.1 Simple representation of the balanced detection scheme

The probe beam transmitted through a quarter-wave plate, a ZnTe and a half-wave plate can be written by the Jones matrix as

$$\mathbf{E} = E_p \underbrace{R\left(-\frac{\pi}{4}\right) J\left(\frac{\pi}{2}\right) R\left(\frac{\pi}{4}\right)}_{\lambda/4 \text{ plate}} \underbrace{\begin{bmatrix} 1 & 0 \\ 0 & e^{i\Gamma} \end{bmatrix}}_{\text{ZnTe}} \underbrace{\frac{1}{\sqrt{2}} \begin{pmatrix} 1 \\ 1 \end{pmatrix}}_{\mathbf{E}_{\text{probe}}}, \quad (\text{A.123})$$

where R and J represent the rotation matrix and the Jones matrix for a retardation plate defined by Eq. (2.120) and Eq. (2.121), respectively. By calculation, this equation becomes²⁸

$$\mathbf{E} = \frac{E_p}{2} \exp\left(i\frac{\pi}{4}\right) \begin{bmatrix} 1 - i \exp(i\Gamma) \\ -i + \exp(i\Gamma) \end{bmatrix}, \quad (\text{A.124})$$

so that²⁹

$$I_x = |E_x|^2 = \frac{E_p^2}{2} (1 + \sin \Gamma), \quad (\text{A.127})$$

$$I_y = |E_y|^2 = \frac{E_p^2}{2} (1 - \sin \Gamma). \quad (\text{A.128})$$

The balanced signal is then obtained as

$$\Delta I = I_x - I_y = I_p \sin \Gamma, \quad (\text{A.129})$$

where $I_p \equiv E_p^2$.

A.6.2.2 THz detection by the (110) ZnTe crystal

The principle for the measurement of THz field by EO sampling is explained in the preceding section 2.5. The processes of the EO detection method with (110) ZnTe are more briefly introduced in this section.

Figure A.7 shows the geometry of a (110) ZnTe crystal used as a THz sensor, where x , y and z are the principal axes of the ZnTe crystal. The z -axis is parallel to (001) of the crystal. α and φ are angles of the polarization of the THz beam and the polarization of the probe beam with respect to z -axis (001), respectively. Note that the two angles are measured on the (110) plane. By the same analogy with Eq. (2.126), the index ellipsoid in the presence of an externally applied THz field can be written as

$$\frac{x^2 + y^2 + z^2}{n^2} + 2r_{41} E_{\text{THz}}^x yz + 2r_{41} E_{\text{THz}}^y xz + 2r_{41} E_{\text{THz}}^z xy = 1, \quad (\text{A.130})$$

where E_{THz}^x , E_{THz}^y and E_{THz}^z are the components of the THz waves applied to ZnTe. As shown in

28

$$\begin{aligned} \mathbf{E} &= \begin{bmatrix} \frac{1}{2} + \frac{1}{2} \exp\left(i\frac{\pi}{2}\right) & \frac{1}{2} - \frac{1}{2} \exp\left(i\frac{\pi}{2}\right) \\ \frac{1}{2} - \frac{1}{2} \exp\left(i\frac{\pi}{2}\right) & \frac{1}{2} + \frac{1}{2} \exp\left(i\frac{\pi}{2}\right) \end{bmatrix} \frac{E_p}{\sqrt{2}} \begin{pmatrix} 1 \\ \exp(i\Gamma) \end{pmatrix} \\ &= \frac{E_p}{2\sqrt{2}} \begin{bmatrix} 1+i & 1-i \\ 1-i & 1+i \end{bmatrix} \begin{pmatrix} 1 \\ \exp(i\Gamma) \end{pmatrix} = \frac{E_p}{2\sqrt{2}} \begin{bmatrix} \sqrt{2} \exp\left(i\frac{\pi}{4}\right) & \sqrt{2} \exp\left(-i\frac{\pi}{4}\right) \\ \sqrt{2} \exp\left(-i\frac{\pi}{4}\right) & \sqrt{2} \exp\left(i\frac{\pi}{4}\right) \end{bmatrix} \begin{pmatrix} 1 \\ \exp(i\Gamma) \end{pmatrix} \\ &= \frac{E_p}{2} \exp\left(i\frac{\pi}{4}\right) \begin{bmatrix} 1 & -i \\ -i & 1 \end{bmatrix} \begin{pmatrix} 1 \\ \exp(i\Gamma) \end{pmatrix} = \frac{E_p}{2} \exp\left(i\frac{\pi}{4}\right) \begin{bmatrix} 1 - i \exp(i\Gamma) \\ -i + \exp(i\Gamma) \end{bmatrix}. \end{aligned}$$

29

$$\begin{aligned} |1 - ie^{i\Gamma}|^2 &= |1 - e^{i(\Gamma+\pi/2)}|^2 = (1 - e^{-i(\Gamma+\pi/2)})(1 - e^{i(\Gamma+\pi/2)}) = 1 - e^{i(\Gamma+\pi/2)} - e^{-i(\Gamma+\pi/2)} + 1 \\ &= 2 - 2 \frac{e^{i(\Gamma+\pi/2)} + e^{-i(\Gamma+\pi/2)}}{2} = 2 - 2 \cos(\Gamma + \pi/2) = 2(1 - \sin \Gamma), \end{aligned} \quad (\text{A.125})$$

$$|-i + e^{i\Gamma}|^2 = (i + e^{-i\Gamma})(-i + e^{i\Gamma}) = 2 + ie^{i\Gamma} - ie^{i\Gamma} = 2 + i \frac{e^{i\Gamma} - e^{-i\Gamma}}{2i} 2i = 2(1 - \sin \Gamma). \quad (\text{A.126})$$

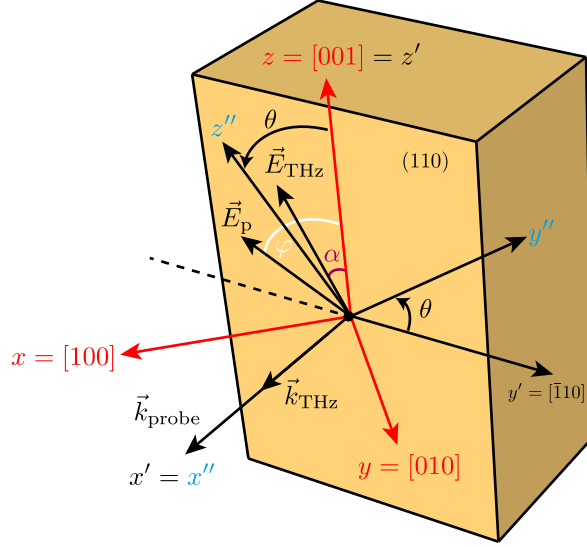


Figure A.7: Geometry of the (110) ZnTe crystal as a THz sensor. x , y and z are the principal axes of the ZnTe crystal, where the z -axis is parallel to [001] of the crystal. α and φ are angles of the polarization of the THz beam and the polarization of the probe beam with respect to the z -axis [001], respectively.

Fig. A.7, the components of the THz waves can be obtained, giving

$$\mathbf{E}_{\text{THz}} = \begin{pmatrix} E_{\text{THz}}^x \\ E_{\text{THz}}^y \\ E_{\text{THz}}^z \end{pmatrix} = E_{\text{THz}} \begin{pmatrix} \sin \alpha \cdot \cos(-45^\circ) \\ \sin \alpha \cdot \sin(-45^\circ) \\ \cos \alpha \end{pmatrix} = E_{\text{THz}} \begin{pmatrix} \frac{1}{\sqrt{2}} \sin \alpha \\ -\frac{1}{\sqrt{2}} \sin \alpha \\ \cos \alpha \end{pmatrix}.$$

Substituting Eq. (A.131) into Eq. (A.130) leads to

$$\frac{x^2 + y^2 + z^2}{n^2} + 2r_{41} \frac{E_{\text{THz}} \sin \alpha}{\sqrt{2}} yz - 2r_{41} \frac{E_{\text{THz}} \sin \alpha}{\sqrt{2}} xz + 2r_{41} E_{\text{THz}} \cos \alpha xy = 1. \quad (\text{A.131})$$

This equation can be simplified by means of a coordinate transformation from crystallographic coordinates (x, y, z) to the lab coordinates (x', y', z') . Through the use of Eq. (2.127), Eq. (A.131) becomes

$$x'^2 \left(\frac{1}{n^2} + r_{41} E_{\text{THz}} \cos \alpha \right) + y'^2 \left(\frac{1}{n^2} - r_{41} E_{\text{THz}} \cos \alpha \right) + \frac{z'^2}{n^2} + 2r_{41} E_{\text{THz}} \sin \alpha y' z' = 1. \quad (\text{A.132})$$

To obtain the index ellipsoid on the (110) plane (*i.e.* $y'z'$ plane), we substitute $x' = 0$ into Eq. (A.132) which becomes [135]

$$y'^2 \left(\frac{1}{n^2} - r_{41} E_{\text{THz}} \cos \alpha \right) + \frac{z'^2}{n^2} + 2r_{41} E_{\text{THz}} \sin \alpha y' z' = 1. \quad (\text{A.133})$$

We next should find the index ellipsoid in the principle coordinates (y'', z'') which is a kind of an

eigenvalue problem. Equation (A.133) can be written in the form

$$\begin{pmatrix} y' & z' \end{pmatrix} \begin{pmatrix} a & c/2 \\ c/2 & b \end{pmatrix} \begin{pmatrix} y' \\ z' \end{pmatrix} = 1, \quad (\text{A.134})$$

where

$$a = \frac{1}{n^2} - r_{41} E_{\text{THz}} \cos \alpha, \quad b = \frac{1}{n^2}, \quad c = 2r_{41} E_{\text{THz}} \sin \alpha. \quad (\text{A.135})$$

To satisfy the eigenvalue equation, the determinant in the following equation should be zero, yielding

$$\left| M - \mu I \right| = 0 \quad (\text{A.136})$$

with

$$M = \begin{pmatrix} a & c/2 \\ c/2 & b \end{pmatrix}, \quad (\text{A.137})$$

where μ and I represent eigenvalues and the identity matrix, respectively. By solving Eq. (A.136), we obtain the eigenvalues of a matrix M given by [135]³⁰

$$\mu = \frac{1}{n^2} + \frac{r_{41}}{2} E_{\text{THz}} \left[-\cos \alpha \pm \sqrt{1 + 3 \sin^2 \alpha} \right]. \quad (\text{A.140})$$

By introducing the lab coordinates

$$X' = \begin{pmatrix} y' \\ z' \end{pmatrix}, \quad (\text{A.141})$$

Eq. (A.134) can be expressed in the form

$$X'^T M X' = 1, \quad (\text{A.142})$$

which implies that

$$X'^T (V D V^T) X' = 1 \quad (\text{A.143})$$

with

$$M = V D V^T \text{ or } (M V = V D), \quad (\text{A.144})$$

where D is a diagonalized matrix of M and V is a square matrix whose columns are eigenvalues of M . Note that $V^{-1} = V^T$ since V is orthogonal. Equation (A.143) then reduces to

$$X''^T D X'' = 1 \text{ with } X'' = V^T X', \quad (\text{A.145})$$

30

$$\begin{aligned} \left| M - \mu I \right| &= \begin{vmatrix} a - \mu & c/2 \\ c/2 & b - \mu \end{vmatrix} = (a - \mu)(b - \mu) - \frac{c^2}{4} \\ &= \mu^2 - (a + b)\mu + ab - \frac{c^2}{4} = 0, \end{aligned} \quad (\text{A.138})$$

which becomes

$$\mu = \frac{a + b}{2} \pm \sqrt{(a - b)^2 + c^2}. \quad (\text{A.139})$$

Substituting Eq. (A.135) into Eq. (A.139) leads to the result

$$\mu = \frac{1}{n^2} + \frac{r_{41}}{2} E_{\text{THz}} \left[-\cos \alpha \pm \sqrt{1 + 3 \sin^2 \alpha} \right].$$

where X'' represents the principle coordinates (y'', z'') . So, we obtain the index ellipsoid in the principle coordinates given by³¹

$$\left[\frac{1}{n^2} + \frac{r_{41}}{2} E_{\text{THz}} \left(-\cos \alpha + \sqrt{1 + 3 \sin^2 \alpha} \right) \right] y''^2 + \left[\frac{1}{n^2} + \frac{r_{41}}{2} E_{\text{THz}} \left(-\cos \alpha - \sqrt{1 + 3 \sin^2 \alpha} \right) \right] z''^2 = 1, \quad (\text{A.147})$$

which implies that³²

$$n''_y = n + \frac{n^3 r_{41}}{4} E_{\text{THz}} \left(\cos \alpha - \sqrt{1 + 3 \sin^2 \alpha} \right), \quad (\text{A.150})$$

$$n''_z = n + \frac{n^3 r_{41}}{4} E_{\text{THz}} \left(\cos \alpha + \sqrt{1 + 3 \sin^2 \alpha} \right), \quad (\text{A.151})$$

so that the induced birefringence in the presence of THz fields becomes

$$\Delta n = n''_z - n''_y = \frac{n^3 r_{41}}{2} E_{\text{THz}} \sqrt{1 + 3 \sin^2 \alpha}. \quad (\text{A.152})$$

Analogous to Eq. (2.150), the phase retardation induced by the birefringence Δn is expressed as

$$\Gamma_{\text{THz}} = \frac{\omega}{c} \Delta n L = \frac{\omega n^3 E_{\text{THz}} r_{41} L}{2c} \sqrt{1 + 3 \sin^2 \alpha}. \quad (\text{A.153})$$

By Eq. (A.129), we find that the balanced signal is proportional to the phase retardation given by [135]

$$\Delta I \propto \frac{E_{\text{THz}}}{2} \sqrt{1 + 3 \sin^2 \alpha}. \quad (\text{A.154})$$

³¹Equation (A.145) leads to the form

$$X''^T D X'' = (y'' \quad z'') \begin{pmatrix} \mu_1 & 0 \\ 0 & \mu_2 \end{pmatrix} \begin{pmatrix} y'' \\ z'' \end{pmatrix} = \mu_1 y''^2 + \mu_2 z''^2 = 1, \quad (\text{A.146})$$

where μ_1 and μ_2 are eigenvalues of M .

$$\begin{aligned} n''_y &= \frac{1}{\sqrt{\mu_1}} = \left[\frac{1}{n^2} + \frac{r_{41}}{2} E_{\text{THz}} \left(-\cos \alpha + \sqrt{1 + 3 \sin^2 \alpha} \right) \right]^{-1/2} \\ &= n \left[1 + \frac{n^2 r_{41}}{2} E_{\text{THz}} \left(-\cos \alpha + \sqrt{1 + 3 \sin^2 \alpha} \right) \right]^{-1/2} \\ &\simeq n \left[1 - \frac{n^2 r_{41}}{4} E_{\text{THz}} \left(-\cos \alpha + \sqrt{1 + 3 \sin^2 \alpha} \right) \right], \end{aligned} \quad (\text{A.148})$$

$$\begin{aligned} n''_z &= \frac{1}{\sqrt{\mu_2}} = \left[\frac{1}{n^2} + \frac{r_{41}}{2} E_{\text{THz}} \left(-\cos \alpha - \sqrt{1 + 3 \sin^2 \alpha} \right) \right]^{-1/2} \\ &= n \left[1 + \frac{n^2 r_{41}}{2} E_{\text{THz}} \left(-\cos \alpha - \sqrt{1 + 3 \sin^2 \alpha} \right) \right]^{-1/2} \\ &\simeq n \left[1 - \frac{n^2 r_{41}}{4} E_{\text{THz}} \left(-\cos \alpha - \sqrt{1 + 3 \sin^2 \alpha} \right) \right]. \end{aligned} \quad (\text{A.149})$$

A.6.2.3 No THz birefringence by (100) ZnTe crystal

The geometry of (100) oriented ZnTe crystal is illustrated in Fig. A.8. The components of THz waves on the (100) ZnTe plane can be then expressed as

$$\mathbf{E}_{\text{THz}} = \begin{pmatrix} E_{\text{THz}}^x \\ E_{\text{THz}}^y \\ E_{\text{THz}}^z \end{pmatrix} = E_{\text{THz}} \begin{pmatrix} 0 \\ -\sin \alpha \\ \cos \alpha \end{pmatrix}. \quad (\text{A.155})$$

In a similar fashion with the preceding section A.6.2.2, we find by substituting Eq. (A.155) into Eq. (A.130) that

$$\frac{x^2 + y^2 + z^2}{n^2} - 2r_{41}E_{\text{THz}} \sin \alpha xz + 2r_{41}E_{\text{THz}} \cos \alpha xy = 1. \quad (\text{A.156})$$

Since the crystallographic coordinates xyz and the lab coordinates $x'y'z'$ coincide, the coordinate transformation from xyz to $x'y'z'$ is not needed. By taking $x = 0$, we obtain the index ellipsoid on the (100) plane, giving

$$\frac{y^2 + z^2}{n^2} = 1, \quad (\text{A.157})$$

which leads to

$$n_y = n, \quad (\text{A.158})$$

$$n_z = n, \quad (\text{A.159})$$

so that the birefringence Δn in (100) ZnTe induced by the applied THz waves becomes

$$\Delta n = n_y - n_z = 0. \quad (\text{A.160})$$

We therefore see that THz waves cannot be measured with (100) ZnTe since there is no birefringence induced by the applied THz waves.

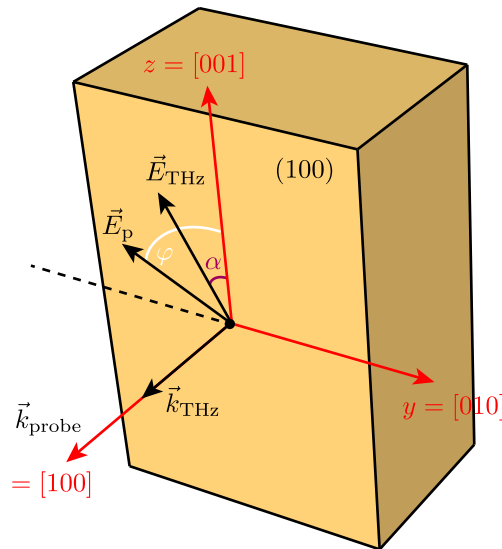


Figure A.8: Geometry of (100) ZnTe crystal as a THz sensor. x , y and z are the principal axes of the ZnTe crystal and z -axis is parallel to [001] of the crystal. α and φ are angles of the polarization of the THz beam and the probe beam with respect to the z -axis [001], respectively.

A.7 EO detection by probing the index ellipse induced from linear polarized probe beam

According to section 2.5.7, we need to take into account the scattering contribution η and the optical bias Γ_{ob} in conventional EO detection using a quarter-wave plate and a prism. From Eqs. (2.153), (2.154) and (2.155), the intensity of the transmitted probe beam through all the optics is simplified as

$$I = I_p \begin{pmatrix} f_1(\Gamma_{\text{THz}}) + g_1 \\ f_2(\Gamma_{\text{THz}}) + g_2 \end{pmatrix}, \quad (\text{A.161})$$

where f_j are functions of Γ_{THz} terms and g_j are functions of other terms except Γ_{THz} terms.

By considering the two terms η and Γ_{ob} , the intensity of the transmitted field can be defined with the substitution $\Gamma_{\text{THz}} \rightarrow \Gamma_{ob} + \Gamma_{\text{THz}}$ as follows

$$I = I_p \begin{pmatrix} \eta + f_1(\Gamma_{ob} + \Gamma_{\text{THz}}) + g_1 \\ \eta + f_2(\Gamma_{ob} + \Gamma_{\text{THz}}) + g_2 \end{pmatrix} = \begin{pmatrix} |E_{x^*}|^2 \\ |E_{y^*}|^2 \end{pmatrix}, \quad (\text{A.162})$$

where we assumed that scattering by the probe beam has the same contribution on each photodiode. Since THz waves can be measured by balance detection as $\Delta I = |E_{x^*}|^2 - |E_{y^*}|^2$, the effect of scattering contribution vanishes. Then we obtain

$$\begin{aligned} I &= I_p \sin\{2(\varphi - \theta)\} \sin(\Gamma_{ob} + \Gamma_{\text{THz}}) \\ &\propto \sin(\Gamma_{ob} + \Gamma_{\text{THz}}) \simeq \Gamma_{ob} + \Gamma_{\text{THz}}, \end{aligned} \quad (\text{A.163})$$

where the optical bias Γ_{ob} is always constant and the THz wave is measured by sweeping via the time-delay. Therefore, the results considering the two terms in this detection process shows the same result as in Eq. (2.160). This is described in section 2.5.7 in detail.

A.8 Finding the optic axis on (110) ZnTe in the presence of THz field

From Maxwell's equation, the wave equation is expressed in terms of the Cartesian coordinates as [19]³³

$$\mathbf{k} \times (\mathbf{k} \times \mathbf{E}) + \omega^2 \mu \epsilon \mathbf{E} = 0, \quad (\text{A.164})$$

which leads to

$$k^2 \mathbf{E} - (\mathbf{k} \cdot \mathbf{E}) \mathbf{k} = k_0^2 \frac{\epsilon}{\epsilon_0} \mathbf{E}, \quad (\text{A.165})$$

where \mathbf{k} is the wave vector, \mathbf{E} is the electric field and $k_0^2 = \omega^2 \mu \epsilon_0$. The permeability for a orthorhombic crystal is defined by [7, 137]

$$\epsilon = \epsilon_0 \begin{bmatrix} n_x^2 & 0 & 0 \\ 0 & n_y^2 & 0 \\ 0 & 0 & n_z^2 \end{bmatrix}, \quad (\text{A.166})$$

³³See Yariv [19] pp. 72-73.

where $n_x < n_y < n_z$. By substituting Eq. (A.166) into Eq. (A.165), we obtain

$$\begin{bmatrix} k_0^2 n_x^2 - k_y^2 - k_z^2 & k_x k_y & k_x k_z \\ k_x k_y & k_0^2 n_y^2 - k_x^2 - k_z^2 & k_y k_z \\ k_x k_z & -k_y k_z & k_0^2 n_z^2 - k_x^2 - k_y^2 \end{bmatrix} \begin{pmatrix} E_x \\ E_y \\ E_z \end{pmatrix} = 0. \quad (\text{A.167})$$

For non-trivial solutions to exist, the determinant of Eq. (A.167) should be zero. When k_z is zero, Eq. (A.167) becomes

$$\begin{bmatrix} k_0^2 n_x^2 - k_y^2 & k_x k_y & 0 \\ k_x k_y & k_0^2 n_y^2 - k_x^2 & 0 \\ 0 & 0 & k_0^2 n_z^2 - k_x^2 - k_y^2 \end{bmatrix} \begin{pmatrix} E_x \\ E_y \\ E_z \end{pmatrix} = 0, \quad (\text{A.168})$$

which leads to the determinant, giving

$$\det M = (-1)^{3+3} (k_0^2 n_z^2 - k_x^2 - k_y^2) [(k_0^2 n_x^2 - k_y^2)(k_0^2 n_y^2 - k_x^2) - k_x^2 k_y^2] = 0. \quad (\text{A.169})$$

We then find that the equation for the normal surface can be factorized according to

$$\left(\frac{k_x^2}{n_y^2} + \frac{k_y^2}{n_x^2} - \frac{\omega^2}{c^2} \right) \left(\frac{k_x^2}{n_z^2} + \frac{k_y^2}{n_z^2} - \frac{\omega^2}{c^2} \right) = 0. \quad (\text{A.170})$$

When k_y is zero, Eq. (A.167) becomes

$$\begin{bmatrix} k_0^2 n_x^2 - k_z^2 & 0 & k_x k_z \\ 0 & k_0^2 n_y^2 - k_x^2 - k_z^2 & 0 \\ k_x k_z & 0 & k_0^2 n_z^2 - k_x^2 \end{bmatrix} \begin{pmatrix} E_x \\ E_y \\ E_z \end{pmatrix} = 0, \quad (\text{A.171})$$

The determinant can be obtained, giving

$$(-1)^{2+2} (k_0^2 n_y^2 - k_x^2 - k_z^2) [(k_0^2 n_x^2 - k_z^2)(k_0^2 n_z^2 - k_x^2) - k_x^2 k_z^2] = 0, \quad (\text{A.172})$$

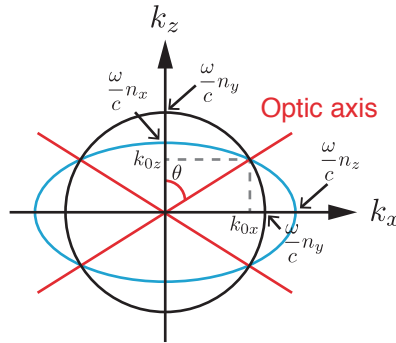


Figure A.9: Intersection of the normal surface of a biaxial crystal in xz plane. θ is the angle between the optic axis and k_z .

which yields

$$\left(\frac{k_x^2}{n_z^2} + \frac{k_z^2}{n_x^2} - \frac{\omega^2}{c^2}\right) \left(\frac{k_x^2}{n_y^2} + \frac{k_z^2}{n_y^2} - \frac{\omega^2}{c^2}\right) = 0. \quad (\text{A.173})$$

In contrast to Eq. (A.170), we can see that there are intersections of the ellipse and the circle in the xz plane illustrated in Fig. A.9.³⁴ From the second term in Eq. (A.173), we find that k_x is expressed as

$$k_x^2 = \frac{\omega^2}{c^2} n_y^2 - k_z^2. \quad (\text{A.174})$$

By substituting Eq. (A.174) into the first term in Eq. (A.173), we obtain

$$\frac{1}{n_z^2} \left(\frac{\omega^2}{c^2} n_y^2 - k_z^2\right) + \frac{k_z^2}{n_x^2} = \frac{\omega^2}{c^2}, \quad (\text{A.175})$$

which leads to

$$k_z \equiv k_{0z} = \pm \frac{\omega}{c} n_x \sqrt{\frac{n_z^2 - n_y^2}{n_z^2 - n_x^2}}. \quad (\text{A.176})$$

Similarly, the expression for k_x can be also obtained, giving

$$k_x \equiv k_{0x} = \pm \frac{\omega}{c} n_z \sqrt{\frac{n_x^2 - n_y^2}{n_x^2 - n_z^2}} = \pm \frac{\omega}{c} n_z \sqrt{\frac{n_y^2 - n_x^2}{n_z^2 - n_x^2}}. \quad (\text{A.177})$$

Therefore, the angle ϕ between one of the optic axes and the z axis (k_z) is expressed in terms of refractive indices as

$$\tan \theta = \frac{k_{0x}}{k_{0z}} = \frac{n_z}{n_x} \sqrt{\frac{n_y^2 - n_x^2}{n_z^2 - n_y^2}}, \quad (\text{A.178})$$

which implies that

$$\theta = \tan^{-1} \left[\frac{n_z}{n_x} \sqrt{\frac{n_y^2 - n_x^2}{n_z^2 - n_y^2}} \right], \quad (\text{A.179})$$

where $n_x < n_y < n_z$.

We now recall from Eq. (2.143) the index ellipsoid of ZnTe for $\alpha = \pi/2$ in the presence of THz field, giving³⁵

$$\frac{x''^2}{n^2} + y''^2 \left\{ \frac{1}{n^2} + r_{41} E_{\text{THz}} \sin 2\theta \right\} + z''^2 \left\{ \frac{1}{n^2} - r_{41} E_{\text{THz}} \sin 2\theta \right\} = 1. \quad (\text{A.180})$$

For a small external electric field, the refractive indices can be evaluated to obtain

$$n_{y''} = \left[\frac{1}{n^2} + r_{41} E_{\text{THz}} \sin 2\theta \right]^{-1/2} \simeq n \left(1 - \frac{1}{2} r_{41} n^2 E_{\text{THz}} \sin 2\theta \right), \quad (\text{A.181})$$

$$n_{z''} = \left[\frac{1}{n^2} - r_{41} E_{\text{THz}} \sin 2\theta \right]^{-1/2} \simeq n \left(1 + \frac{1}{2} r_{41} n^2 E_{\text{THz}} \sin 2\theta \right), \quad (\text{A.182})$$

which lead to the index ellipsoid

$$\frac{x''^2}{n^2} + \frac{y''^2}{(n - \beta)^2} + \frac{z''^2}{(n + \beta)^2} = 1, \quad (\text{A.183})$$

³⁴See Yariv [19] p. 74.

³⁵ZnTe is a cubic crystal when the external electric field is zero. However, the structure of ZnTe is changed into an orthorhombic crystal when the external electric field is different from zero [137]. So, the optical symmetry of ZnTe becomes biaxial.

where $\beta = \frac{1}{2}r_{41}n^3E_{\text{THz}}\sin 2\theta$. When $n_x < n_y < n_z$, it is deduced from Eq. (A.173) that the optic axes are on the xz plane. In a similar fashion, we thus find that there are optic axes on the $y''z''$ plane when $n_{y''} < n_{x''} < n_{z''}$. Hence, the angle θ_{Optic} between one of the optic axes and the z'' axis ($k_{z''}$) is thereby obtained from Eq. (A.178), yielding

$$\tan \theta_{\text{Optic}} = \frac{n + \beta}{n - \beta} \sqrt{\frac{n^2 - n^2(1 - r_{41}E_{\text{THz}}\sin 2\theta)}{n^2(1 + r_{41}E_{\text{THz}}\sin 2\theta) - n^2}}, \quad (\text{A.184})$$

where $n_x = n - \beta = n_{y''}$, $n_y = n = n_{x''}$ and $n_z = n + \beta = n_{z''}$ are substituted into Eq. (A.178). Since the electro-optic coefficient r_{41} of ZnTe is the order of 10^{-12} m/V [138], we conclude that

$$\tan \theta_{\text{Optic}} = \frac{n + \beta}{n - \beta} \simeq \frac{n}{n} = 1, \quad (\text{A.185})$$

so that θ_{Optic} is $\pi/4$ with respect to the z'' axis ($k_{z''}$).

A.9 THz pulse train shown in the measured THz field

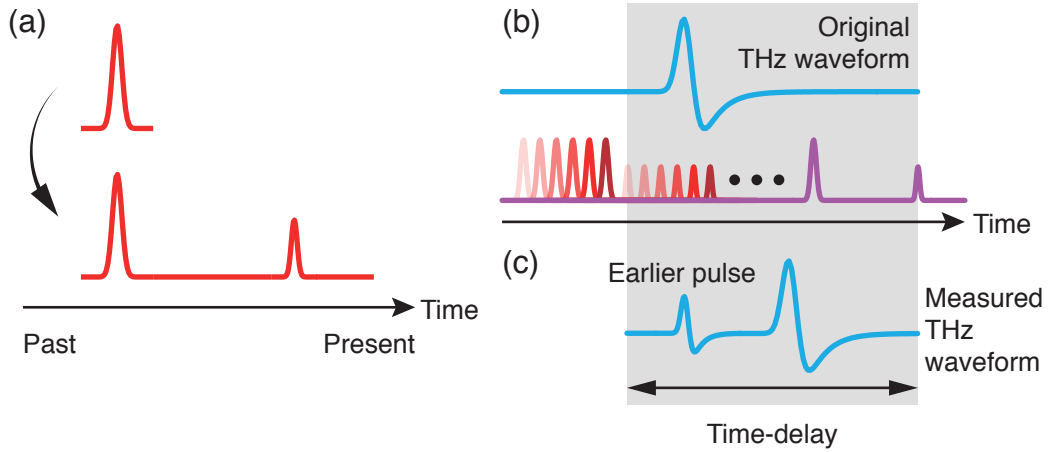


Figure A.10: Schematic diagram of measuring THz waveform using a probe pulse. (a) The optical probe beam is reflected by some optical elements. (b) When THz waveform is measured by the probe beam by varying the time-delay between the THz signal and the probe beam in a range depicted by a gray color, the THz waveform is measured as a shape with an earlier THz pulse illustrated in (c).

From the measured data in Fig. 3.3(a), we can see that there is an earlier pulse than the main THz waveform through the sample (red solid line) near 55 ps. The reason why there is an earlier pulse than the main THz signal is that the optical probe beam is reflected by optical elements involved in the measurement.

The schematic diagram for understanding is illustrated in Fig. A.10. First, the optical probe beam is reflected by some optical elements as shown in Fig. A.10(a). When THz waveform is measured by the probe beam by varying the time-delay between the THz signal and the probe beam in a range depicted by a gray color in Fig. A.10(b), THz waveform in the time-domain is measured as a shape with an earlier THz pulse illustrated in Fig. A.10(c).

A.10 Why the directionality of light becomes better for higher frequency light?

The directionality of light can be described by the diffraction of which physical interpretation is explained by Kirchhoff's diffraction theory given by [11, 12, 27]³⁶

$$E(\mathbf{x}, t) = -\frac{ik e^{-i\omega t}}{2\pi} \int_S d^2x' E_0(x', y', z' = 0) \frac{e^{ikR}}{R} \Theta(\theta_0, \theta), \quad (\text{A.186})$$

where $E(\mathbf{x}, t)$ is the electric wave at a field point \mathbf{x} with $r = \sqrt{x^2 + y^2 + z^2}$. $R = |\mathbf{x} - \mathbf{x}'|$ is the distance between the field point and the source point in the aperture plane S, which is the closed surface on the $(x', y', z' = 0)$ plane. $E_0(x', y', z' = 0)$ is the incident wave on S.³⁷ Θ is the oblique factor given as a function of $\theta_0 = \angle(\hat{n}, \mathbf{x}')$ and $\theta = \angle(\hat{n}, \mathbf{x})$ in which \hat{n} is the normal vector of S. Kirchhoff's diffraction theory is valid when the width of the slit is large enough compared with the wavelength λ of the incident electric field.

When both the incident and diffracted waves are effective plane waves, Kirchhoff diffraction is called as the Fraunhofer diffraction. Effective plane waves means that the distance from the aperture to the observation plane is large enough compared to the distance from the aperture to the source, *i.e.*, $r' \ll r$. By substituting Eq. (A.82) into R , Eq. (A.186) for the far-field zone ($r' \ll r$) becomes

$$E(\mathbf{x}, t) = -\frac{ik}{2\pi} \frac{\exp[i(kr - \omega t)]}{r} \int_S d^2x' E_0(x', y', z' = 0) \exp\left[-ik \frac{\mathbf{x} \cdot \mathbf{x}'}{r}\right], \quad (\text{A.187})$$

where $k = 2\pi/\lambda$ in air and $\Theta(\theta_0, \theta) \simeq 1$ since r is sufficiently large compared to the aperture size.

A.10.1 Fraunhofer diffraction in the rectangular aperture

Provided that the incident field on the aperture plane with $x' \in [-a/2, a/2]$ and $y' \in [-b/2, b/2]$ is assumed to be constant over the entire aperture, Eq. (A.187) in the case of an rectangular aperture can be obtained, yielding [11, 27]³⁸

$$E(\mathbf{x}, t) = CE_0ab \frac{\exp[i(kr - \omega t)]}{r} \frac{\sin X}{X} \frac{\sin Y}{Y}, \quad (\text{A.191})$$

³⁶Eq. (A.186) is called as "Kirchhoff's diffraction formula".

³⁷In general, $E_0(x', y', z' = 0)$ is defined as $E_0 \exp(ik\rho')/\rho'$ with $\rho' = \sqrt{x'^2 + y'^2}$ for a spherical wave.

³⁸See Hecht [11] pp. 464-470 and Fowles [27] pp. 106-117.

$$E(\mathbf{x}, t) = C \frac{\exp[i(kr - \omega t)]}{r} E_0 \int_{-a/2}^{a/2} dx' \exp\left[-ik \frac{xx'}{r}\right] \int_{-b/2}^{b/2} dy' \exp\left[-ik \frac{yy'}{r}\right], \quad (\text{A.188})$$

where $C = -ik/2\pi$. With $kx/r = \alpha'$, the integral with respect to x' containing an exponential function is calculated as

$$\begin{aligned} \int_{-a/2}^{a/2} dx' \exp\left[-ik \frac{xx'}{r}\right] &= \int_{-a/2}^{a/2} dx' e^{-i\alpha'x'} = \frac{-1}{i\alpha'} \left[e^{-i\alpha'x'} \right]_{x'=-a/2}^{x'=a/2} = \frac{-1}{i\alpha'} \left[e^{-i\alpha'a/2} - e^{i\alpha'a/2} \right] \\ &= \frac{1}{i\alpha'} \left[e^{i\alpha'a/2} - e^{-i\alpha'a/2} \right] = \frac{2}{\alpha'} \frac{\left[e^{i\alpha'a/2} - e^{-i\alpha'a/2} \right]}{2i} \\ &= \frac{2}{\alpha'} \sin\left(\alpha' \frac{a}{2}\right) = \frac{a}{\alpha' a/2} \sin\left(\alpha' \frac{a}{2}\right) = a \frac{\sin X}{X}, \end{aligned} \quad (\text{A.189})$$

where $X = kax/2r$. Similarly, the integral with respect to y' is also calculated as

$$\int_{-b/2}^{b/2} dy' \exp\left[-ik \frac{yy'}{r}\right] = b \frac{\sin Y}{Y}, \quad (\text{A.190})$$

where $Y = kby/2r$.

where $C = -ik/2\pi$, $X = kax/2r$ and $Y = kby/2r$. The corresponding irradiance is expressed as

$$I = \langle (\text{Re } E)^2 \rangle = \frac{1}{2} |E(\mathbf{x}, t)|^2 = I_0 \left(\frac{\sin X}{X} \right)^2 \left(\frac{\sin Y}{Y} \right)^2, \quad (\text{A.192})$$

where I_0 is merely another constant.

In order to answer the question of this section, we need to focus when the irradiance is zero. Zero values occur at $X = m\pi$ and $Y = n\pi$ for $m, n \in \mathbb{Z}$ given by

$$X = \frac{kax}{2r} = m\pi, \quad Y = \frac{kby}{2r} = n\pi. \quad (\text{A.193})$$

With $k = \omega/c = 2\pi/\lambda$, the above equations can be written as

$$X = \frac{2\pi}{\lambda} \frac{ax}{2r} = m\pi, \quad (\text{A.194})$$

$$Y = \frac{2\pi}{\lambda} \frac{by}{2r} = n\pi. \quad (\text{A.195})$$

From these equations, we find that the positions of the minima for Eqs. (A.194) and (A.195) are proportional to λ , which implies that the positions of the minima are proportional to $1/f$, where f is the frequency of the incident field. Therefore, the positions of the minima on the observation plane are closed to the optical axis when the frequency of the incident field is higher; *i.e.*, the directionality of light with higher frequency is much better than light with lower frequency.

This question can also be solved by using the Gaussian beam at a focus described as in the section A.3.1. Although the paraxial approximation is used, we can find the tendency of diffraction for a light with a specific frequency. From Eq. (A.11), the angular beam spread for $\theta \ll \pi$ as shown in Fig. A.1 is defined by [19]³⁹

$$\theta = \tan^{-1} \left(\frac{\lambda}{\pi w_0 n} \right) \simeq \frac{\lambda}{\pi w_0 n}, \quad (\text{A.197})$$

which implies that λ of the incident wave is proportional to θ . In other words, the frequency f is proportional to $1/\theta$; *i.e.*, the light with higher frequency is diffracted less than the light with lower frequency. This result is the same as that induced by the diffraction theory.

A.10.2 Fraunhofer diffraction in the circular aperture

Provided that the incident field on the aperture plane with radius of a is assumed to be constant over the entire aperture, Eq. (A.187) in the case of an circular aperture can be expressed by a change of variables as

$$\begin{aligned} E(\mathbf{x}, t) &= -\frac{ik}{2\pi} \frac{\exp[i(kr - \omega t)]}{r} E_0 \int_S d^2x' \exp \left[-ik \frac{\mathbf{x} \cdot \mathbf{x}'}{r} \right] \\ &= -\frac{ik}{2\pi} \frac{\exp[i(kr - \omega t)]}{r} E_0 \int_S d^2x' \exp \left[-ik \frac{qr' \cos \theta \cos \theta' + qr' \sin \theta \sin \theta'}{r} \right] \\ &= -\frac{ik}{2\pi} \frac{\exp[i(kr - \omega t)]}{r} E_0 \int_S d^2x' \exp \left[-ik \frac{qr'}{r} \cos(\theta - \theta') \right], \end{aligned} \quad (\text{A.198})$$

39

$$\tan \theta = \frac{z\lambda}{\pi w_0 n} = \frac{\lambda}{\pi w_0 n}. \quad (\text{A.196})$$

where

$$x' = r' \cos \theta', \quad x = q \cos \theta, \quad (\text{A.199})$$

$$y' = r' \sin \theta', \quad y = q \sin \theta. \quad (\text{A.200})$$

For sake of simplicity, we just consider the situation in the case of $\theta = 0$. We then find that the integral in Eq. (A.208) becomes

$$\text{Int} = \int_{\mathbb{S}} d^2 x' \exp \left[-ik \frac{qr'}{r} \cos \theta' \right] = \int_0^a dr' r' \int_0^{2\pi} \exp \left[-ik \frac{qr'}{r} \cos \theta' \right]. \quad (\text{A.201})$$

By using the first kind Bessel function of the order of zero given by [11, 133]

$$J_0(x) = \frac{1}{2\pi} \int_0^{2\pi} dy e^{ix \cos y}, \quad (\text{A.202})$$

the integral can be evaluated as

$$\text{Int} = \int_0^a dr' r' \int_0^{2\pi} \exp \left[i \left(-\frac{kqr'}{r} \right) \cos \theta' \right] = 2\pi \int_0^a dr' r' J_0 \left(-\frac{kqr'}{r} \right). \quad (\text{A.203})$$

With a relation $J_n(-x) = (-1)^n J_n(x)$, this equation becomes

$$\text{Int} = 2\pi \int_0^a dr' r' J_0 \left(\frac{kqr'}{r} \right). \quad (\text{A.204})$$

By taking $kqr'/r = \xi$ such that $kq dr'/r = d\xi$, the integral can be evaluated as

$$\text{Int} = 2\pi \int_0^{kqa/r} \frac{r}{kq} d\xi \frac{r}{kq} \xi J_0(\xi) = 2\pi \left(\frac{r}{kq} \right)^2 \int_0^{kqa/r} d\xi \xi J_0(\xi). \quad (\text{A.205})$$

The well used property of Bessel function is

$$\int_0^y dx x J_0(x) = y J_1(y), \quad (\text{A.206})$$

which leads to

$$\text{Int} = 2\pi \left(\frac{r}{kq} \right)^2 \frac{kqa}{r} J_1 \left(\frac{kqa}{r} \right) = 2\pi \frac{ra}{kq} J_1 \left(\frac{kqa}{r} \right). \quad (\text{A.207})$$

Therefore, the E field diffracted by a circular aperture is written as

$$E(\mathbf{x}, t) = -ik \frac{\exp[i(kr - \omega t)]}{r} E_0 \frac{2\pi a^2}{\left(\frac{kqa}{r} \right)} J_1 \left(\frac{kqa}{r} \right) = -ik E_0 \frac{\exp[i(kr - \omega t)]}{r} 2\pi a^2 \frac{J_1(kqa/r)}{kqa/r}, \quad (\text{A.208})$$

which implies that the irradiance is given by

$$I = \langle (\text{Re}E)^2 \rangle = \frac{1}{2} |E(\mathbf{x}, t)|^2 = \frac{1}{2} \left(\frac{kE_0 \pi a^2}{r} \right)^2 \left| \frac{2J_1(kqa/r)}{kqa/r} \right|^2. \quad (\text{A.209})$$

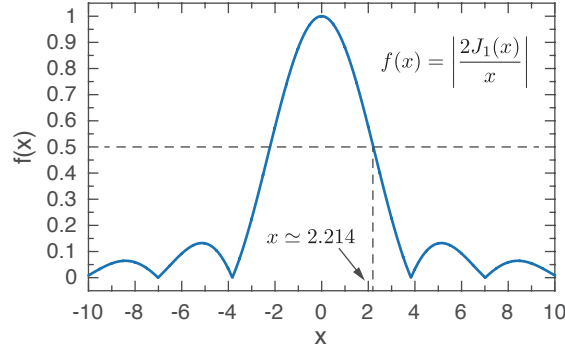


Figure A.11: Graph of a function of $f(x)$.

Furthermore, we find from Eq. (A.208) that the magnitude of the E field is written as

$$|E(\mathbf{x}, t)| = |E_{\text{initial}}| \left| \frac{2J_1(kqa/r)}{kqa/r} \right|, \quad (\text{A.210})$$

where the last term including the Bessel function is illustrated in Fig. A.11 and

$$|E_{\text{initial}}| = \left| \frac{kE_0}{r} \pi a^2 \right|. \quad (\text{A.211})$$

Eq. A.210 straightforwardly indicates Eq. (4.7) in chapter 4. In order to obtain the representation of FWHM, we need to find x corresponding to the half maximum of Eq. (A.210), which can be obtained by taking Eq. (A.210) to have the form

$$\left| \frac{2J_1(x)}{x} \right| = 0.5, \quad (\text{A.212})$$

so that $x \simeq 2.214$. It should be noted that a plane wave by using a focusing lens exhibits the same physical phenomenon that takes place in the diffraction by a circular aperture [11].⁴⁰ When an incident plane wave with a wavelength of λ and a beam radius of $W_0/2$ is focused by a lens with a focal length of f , the beam radius $W/2$ in the plane of observation can be obtained, yielding

$$\frac{kqa}{r} \equiv \frac{k(W/2)(W_0/2)}{f} = 2.214, \quad (\text{A.213})$$

which leads to Eq. (4.7) given by

$$W = \frac{4.43f}{\pi W_0} \lambda, \quad (\text{A.214})$$

where $k = 2\pi/\lambda$.

⁴⁰See Hecht [11] p. 467.

A.11 Different intensity of optical beam with 45° pol. by two optical components

Through a polarizer	Through a half-wave plate
$M_{\text{pol}} = R(-\varphi) \begin{bmatrix} 1 & 0 \\ 0 & 0 \end{bmatrix} R(\varphi)$	$M_{\lambda/2} = R(-\varphi) \begin{bmatrix} 1 & 0 \\ 0 & e^{i\pi} = -1 \end{bmatrix} R(\varphi)$
$E = M_{\text{pol}}(\varphi = 45^\circ) E_i = E_p \frac{1}{2} \begin{pmatrix} 1 \\ 1 \end{pmatrix}$	$E = M_{\lambda/2} \left(\varphi = \frac{\pi}{8} \right) E_i = E_p \frac{1}{\sqrt{2}} \begin{pmatrix} 1 \\ 1 \end{pmatrix}$
$\rightarrow E = \sqrt{\left(\frac{1}{2}\right)^2 + \left(\frac{1}{2}\right)^2} = \frac{1}{\sqrt{2}}$	$\rightarrow E = 1$

Table A.1: Transmitted intensities from an optical beam with 45° polarization through different optical elements. $R(\varphi)$ is the rotation matrix defined in Eq. (2.120).

It is easily seen from table A.1 that the transmitted intensity through a polarizer is different from that of a half-wave plate.

Matlab code

Matlab code for calculating Eqs. (2.153) and (2.157).

```
clear all;
%%
syms x y z n r41 ex ey ez;
ff=(x/n)^2 + (y/n)^2+ (z/n)^2 + 2*r41*(ex*y*z + ey*x*z + ez*x*y);
rot3x=@(x) [1 0 0;0 cos(x) -sin(x) ; 0 sin(x) cos(x)];
rot3z=@(x) [cos(x) -sin(x) 0 ; sin(x) cos(x) 0 ; 0 0 1];
syms theta xp yp zp
xx=rot3x(theta)* [xp; yp; zp];

return;
%%
syms theta gamma phi
w.znte=...
[cos(theta)^2+sin(theta)^2*exp(i*gamma) cos(theta)*sin(theta)-cos(theta)*sin(theta)*exp(i*gamma);
cos(theta)*sin(theta)-cos(theta)*sin(theta)*exp(i*gamma) sin(theta)^2+cos(theta)^2*exp(i*gamma)];

ei=[cos(phi);sin(phi)];
rot=@(x) [ cos(x) sin(x) ; -sin(x) cos(x)];
w.quarter=rot(-pi/4)*[1 0; 0 exp(i*pi/2)]*rot(pi/4);
```

```

%%
et=w_quarter*w_znte*ei;
% ( cos(gamma)+i*sin(gamma))
return;
%%
et1 =cos(phi)*(cos(theta)*sin(theta)*(1/2 - i/2) + cos(theta)^2*(1/2 + i/2) +...
( cos(gamma)+i*sin(gamma))*sin(theta)^2*(1/2 + i/2) +...
( cos(gamma)+i*sin(gamma))*cos(theta)*sin(theta)*(- 1/2 + i/2)) +...
sin(phi)*(cos(theta)*sin(theta)*(1/2 + i/2) + sin(theta)^2*(1/2 - i/2) +...
( cos(gamma)+i*sin(gamma))*cos(theta)^2*(1/2 - i/2) + ( cos(gamma)+...
i*sin(gamma))*cos(theta)*sin(theta)*(- 1/2 - i/2));

cet1=cos(phi)*(cos(theta)*sin(theta)*(1/2 + i/2) + cos(theta)^2*(1/2 -i/2) +...
( cos(gamma)-i*sin(gamma))*sin(theta)^2*(1/2 - i/2) +...
( cos(gamma)-i*sin(gamma))*cos(theta)*sin(theta)*(- 1/2- i/2)) +...
sin(phi)*(cos(theta)*sin(theta)*(1/2 - i/2) + sin(theta)^2*(1/2 + i/2) +...
( cos(gamma)-i*sin(gamma))*cos(theta)^2*(1/2 + i/2) +...
( cos(gamma)-i*sin(gamma))*cos(theta)*sin(theta)*(- 1/2 + i/2));
% cet1= conjugate of et1.
%%
et2 =cos(phi)*(cos(theta)*sin(theta)*(1/2 + i/2) + cos(theta)^2*(1/2 - i/2) ...
+ ( cos(gamma)+i*sin(gamma))*sin(theta)^2*(1/2 - i/2) ...
+ ( cos(gamma)+i*sin(gamma))*cos(theta)*sin(theta)*(- 1/2 - i/2)) + ...
sin(phi)*(cos(theta)*sin(theta)*(1/2 - i/2) + sin(theta)^2*(1/2 + i/2) +...
( cos(gamma)+i*sin(gamma))*cos(theta)^2*(1/2 + i/2) +...
( cos(gamma)+i*sin(gamma))*cos(theta)*sin(theta)*(- 1/2 + i/2));

cet2=cos(phi)*(cos(theta)*sin(theta)*(1/2 - i/2) + cos(theta)^2*(1/2 + i/2) ...
+ ( cos(gamma)-i*sin(gamma))*sin(theta)^2*(1/2 + i/2) ...
+ ( cos(gamma)-i*sin(gamma))*cos(theta)*sin(theta)*(- 1/2 + i/2)) + ...
sin(phi)*(cos(theta)*sin(theta)*(1/2 + i/2) + sin(theta)^2*(1/2 - i/2) ...
+ ( cos(gamma)-i*sin(gamma))*cos(theta)^2*(1/2 - i/2) ...
+ ( cos(gamma)-i*sin(gamma))*cos(theta)*sin(theta)*(- 1/2 - i/2));
% cet2= conjugate of et2.
%%
finalet=expand(et1*cet1-et2*cet2)
% ans=2*cos(phi)*cos(theta)^4*sin(gamma)*sin(phi) ...
% - 2*cos(phi)*sin(gamma)*sin(phi)*sin(theta)^4 ...
% - 2*cos(phi)^2*cos(theta)*sin(gamma)*sin(theta)^3 ...
% - 2*cos(phi)^2*cos(theta)^3*sin(gamma)*sin(theta) ...
% + 2*cos(theta)*sin(gamma)*sin(phi)^2*sin(theta)^3 ...
% + 2*cos(theta)^3*sin(gamma)*sin(phi)^2*sin(theta);

```

Chapter B. Experiment equipment

B.1 Lock-in amplifier

The Lock-in amplifier is an experimental equipment used to remove noise in the measured signal. If the frequency of the reference signal is ω_r , the noise in the measured signal can be removed by the lock-in amplifier as [139]

$$V_{\text{out}}(t) = \frac{1}{T} \int_{t-T}^t \sin(\omega_r t + \theta) V_{\text{in}}(t), \quad (\text{B.1})$$

where

$$V_{\text{in}}(t) = V_0 \sum_j \sin(\omega_j t) \quad (\text{B.2})$$

is the input signal, V_0 is the magnitude of the measured signal, T is the averaging time, θ is a phase that can be modified using the lock-in amplifier.

Note that the original signal has only one frequency component, however, the signal is changed into the measured signal with noise comprised of each frequency component. We find from Eq. (B.1) that the noise in the input signal can be removed due to the orthogonality of sine function.

B.2 Laser system

The used laser system is a femtosecond Ti:Sapphire pulsed laser with a repetition rate of 80 MHz. To understand the oscillator system, we need to know about concepts of spontaneous emission, stimulated emission, Brewster angle and etc. References [2, 140] would be help to understand.

Chapter C. Useful mathematical formulas

C.1 Unit vector calculation

C.1.1 Unit vectors in the spherical coordinates

All the vectors in a n -th dimensional space can be described using a number of linearly independent unit vectors. In three-dimensional (3D) space, Cartesian coordinate system is often used in the vector space to represent the direction of an arbitrary vector. In this coordinate system, the unit vectors are defined by

$$\hat{x}, \hat{y}, \hat{z}. \quad (\text{C.1})$$

The Cartesian coordinate system is, however, sometimes confusing for one who wants to know its the physical meaning in relationship to a problem. Therefore, alternative coordinate systems such as spherical coordinate and cylindrical coordinate systems are required.

In the spherical coordinate system, the unit vectors in the Cartesian coordinates must be changed. In this section, it is briefly explained that unit vectors in Cartesian coordinates are changed into spherical unit vectors. In Cartesian coordinates, a position vector at point P is defined by

$$\vec{r} = \hat{x}x + \hat{y}y + \hat{z}z. \quad (\text{C.2})$$

If r is the norm of the position vector, each axis can be defined by three parameters given by

$$x = r \sin \theta \cos \phi, \quad y = r \sin \theta \sin \phi, \quad z = r \cos \theta. \quad (\text{C.3})$$

Then the position vector described in Eq. (C.2) becomes

$$\vec{r} = \hat{x} r \sin \theta \cos \phi + \hat{y} r \sin \theta \sin \phi + \hat{z} r \cos \theta = \hat{r} r, \quad (\text{C.4})$$

where \hat{r} is the unit vector in the radial direction. From Eq. (C.4), we obtain the radial unit vector \hat{r} given by

$$\hat{r} = \frac{\vec{r}}{r} = \hat{x} \sin \theta \cos \phi + \hat{y} \sin \theta \sin \phi + \hat{z} \cos \theta. \quad (\text{C.5})$$

By total differentiation of both sides of Eq. (C.5), the derivative of \hat{r} is

$$\begin{aligned} d\hat{r} &= \hat{x} (\cos \phi \cos \theta d\theta - \sin \theta \sin \phi d\phi) + \hat{y} (\cos \theta \sin \phi d\theta + \sin \theta \cos \phi d\phi) - \hat{z} \sin \theta d\theta \\ &= \left[\hat{x} \cos \theta \cos \phi + \hat{y} \cos \theta \sin \phi - \hat{z} \sin \theta \right] d\theta + \left[-\hat{x} \sin \theta \sin \phi + \hat{y} \sin \theta \cos \phi \right] d\phi \end{aligned} \quad (\text{C.6})$$

where $d\hat{x}$, $d\hat{y}$ and $d\hat{z}$ are zero¹. Recall that the derivative of the position vector \vec{r} is described as

$$\vec{r} = \hat{r} dr + \hat{\theta} r d\theta + \hat{\phi} r \sin \theta d\phi, \quad (\text{C.8})$$

¹

$$d(\hat{x} \sin \theta \cos \phi) = \underbrace{d\hat{x}}_{=0} \sin \theta \cos \phi + \hat{x} d(\sin \theta) \cos \phi + \hat{x} \sin \theta d(\cos \phi). \quad (\text{C.7})$$

where Eq. (C.8) is further explained in section C. Therefore, from Eqs. (C.6) and Eq. (C.8), an unit vector in the polar angle $\hat{\theta}$ and another unit vector in the azimuthal angle $\hat{\phi}$ can be obtained, giving

$$\begin{aligned} \frac{1}{r} \left(\frac{d\vec{r}}{d\theta} \right)_{d\phi=0} &= \left(\frac{d\hat{r}}{d\theta} \right)_{d\phi=0} = \left(\frac{\partial \hat{r}}{\partial \theta} \right)_{\phi} \\ &= \hat{x} \cos \theta \cos \phi + \hat{y} \cos \theta \sin \phi - \hat{z} \sin \theta = \hat{\theta} \end{aligned} \quad (\text{C.9})$$

$$\begin{aligned} \frac{1}{r \sin \theta} \left(\frac{d\vec{r}}{d\phi} \right)_{d\theta=0} &= \frac{1}{\sin \theta} \left(\frac{d\hat{r}}{d\phi} \right)_{d\theta=0} = \frac{1}{\sin \theta} \left(\frac{\partial \hat{r}}{\partial \theta} \right)_{\theta} \\ &= -\hat{x} \sin \phi + \hat{y} \cos \phi = \hat{\phi}. \end{aligned} \quad (\text{C.10})$$

C.1.2 Cross product using spherical unit vectors

In Cartesian coordinates, the cross product of any two vectors can be easily calculated by the Laplace development. If there are \hat{x} and \hat{y} , then the cross product of the vectors becomes

$$\hat{x} \times \hat{y} = \begin{vmatrix} \hat{x} & \hat{y} & \hat{z} \\ 1 & 0 & 0 \\ 0 & 1 & 0 \end{vmatrix} = (-1)^{1+1} \hat{x} \begin{vmatrix} 0 & 0 \\ 1 & 0 \end{vmatrix} + (-1)^{1+2} \hat{y} \begin{vmatrix} 1 & 0 \\ 0 & 0 \end{vmatrix} + (-1)^{1+3} \hat{z} \begin{vmatrix} 1 & 0 \\ 0 & 1 \end{vmatrix} = \hat{z}. \quad (\text{C.11})$$

How can the cross product of two vectors be obtained when any of the two vectors are in the spherical coordinates? Let's consider that there are two unit vectors in the spherical coordinates given by \hat{r} and $\hat{\theta}$. Then the cross product of \hat{r} and $\hat{\theta}$ can be calculated by spherical coordinate elements or Cartesian coordinates elements. The cross product can be evaluated as

$$\begin{aligned} \hat{r} \times \hat{\theta} &= \frac{1}{r^2 \sin \theta} \begin{vmatrix} \hat{r} & r \hat{\theta} & r \sin \theta \hat{\phi} \\ 1 & 0 & 0 \\ 0 & r & 0 \end{vmatrix} \\ &= \frac{1}{r^2 \sin \theta} \left[(-1)^{1+1} \hat{r} \begin{vmatrix} 0 & 0 \\ r & 0 \end{vmatrix} + (-1)^{1+2} r \hat{\theta} \begin{vmatrix} 1 & 0 \\ 0 & 0 \end{vmatrix} + (-1)^{1+3} r \sin \theta \hat{\phi} \begin{vmatrix} 1 & 0 \\ 0 & r \end{vmatrix} \right] \\ &= \frac{1}{r^2 \sin \theta} r^2 \sin \theta \hat{\phi} = \hat{\phi}. \end{aligned} \quad (\text{C.12})$$

The cross product can be also obtained by Cartesian coordinate elements as in Eqs (C.5), (C.9) and (C.10) as follows

$$\begin{aligned} \hat{r} \times \hat{\theta} &= \begin{vmatrix} \hat{x} & \hat{y} & \hat{z} \\ \sin \theta \cos \phi & \sin \theta \sin \phi & \cos \theta \\ \cos \theta \cos \phi & \cos \theta \sin \phi & -\sin \theta \end{vmatrix} \\ &= \hat{x} \begin{vmatrix} \sin \theta \sin \phi & \cos \theta \end{vmatrix} - \hat{y} \begin{vmatrix} \sin \theta \cos \phi & \cos \theta \end{vmatrix} + \hat{z} \begin{vmatrix} \sin \theta \cos \phi & \sin \theta \sin \phi \\ \cos \theta \cos \phi & \cos \theta \sin \phi \end{vmatrix} \\ &= \hat{x}(-\sin \phi) + \hat{y} \cos \phi = \hat{\phi}. \end{aligned} \quad (\text{C.13})$$

The cross product of $\hat{r} \times \hat{\phi}$ becomes

$$\begin{aligned}
\hat{r} \times \hat{\phi} &= \frac{1}{r^2 \sin \theta} \begin{vmatrix} \hat{r} & r \hat{\theta} & r \sin \theta \hat{\phi} \\ 1 & 0 & 0 \\ 0 & 0 & r \sin \theta \end{vmatrix} \\
&= \frac{1}{r^2 \sin \theta} \left[(-1)^{1+1} \hat{r} \begin{vmatrix} 0 & 0 \\ 0 & r \sin \theta \end{vmatrix} + (-1)^{1+2} r \hat{\theta} \begin{vmatrix} 1 & 0 \\ 0 & r \sin \theta \end{vmatrix} + (-1)^{1+3} r \sin \theta \hat{\phi} \begin{vmatrix} 1 & 0 \\ 0 & 0 \end{vmatrix} \right] \\
&= \frac{-1}{r^2 \sin \theta} r^2 \sin \theta \hat{\theta} = -\hat{\theta}. \tag{C.14}
\end{aligned}$$

C.2 The rotation matrix

There are two ways to describe the rotation matrix. One is the intrinsic rotation and the other is the extrinsic rotation. These expressions may not be familiar to somebody. However, we have learned about the matrix rotating the system coordinates or the vector in many text books [133]. The coordinate system rotation matrix is one that rotates the coordinate system about a given axis in a counterclockwise direction [141]. On the other hand, the vector rotation matrix represents a matrix that rotates a given vector about the global axis in a counterclockwise direction [141]. These rotations can be categorized into the intrinsic or extrinsic rotations [142]. In other words, the coordinate system rotation and the vector (or point) rotation can be understood as intrinsic and the extrinsic rotations, respectively.

The system coordinate rotation R_j^{sys} about the j -axis and the vector rotation matrices R_j^{vec} about the j -axis are defined as [133, 141]

$$R_x^{\text{sys}}(\theta) = \begin{bmatrix} 1 & 0 & 0 \\ 0 & \cos \theta & \sin \theta \\ 0 & -\sin \theta & \cos \theta \end{bmatrix}, \quad R_y^{\text{sys}}(\theta) = \begin{bmatrix} \cos \theta & 0 & -\sin \theta \\ 0 & 1 & 0 \\ \sin \theta & 0 & \cos \theta \end{bmatrix}, \quad R_z^{\text{sys}}(\theta) = \begin{bmatrix} \cos \theta & \sin \theta & 0 \\ -\sin \theta & \cos \theta & 0 \\ 0 & 0 & 1 \end{bmatrix}, \tag{C.15}$$

$$R_x^{\text{vec}}(\theta) = \begin{bmatrix} 1 & 0 & 0 \\ 0 & \cos \theta & -\sin \theta \\ 0 & \sin \theta & \cos \theta \end{bmatrix}, \quad R_y^{\text{vec}}(\theta) = \begin{bmatrix} \cos \theta & 0 & \sin \theta \\ 0 & 1 & 0 \\ -\sin \theta & 0 & \cos \theta \end{bmatrix}, \quad R_z^{\text{vec}}(\theta) = \begin{bmatrix} \cos \theta & -\sin \theta & 0 \\ \sin \theta & \cos \theta & 0 \\ 0 & 0 & 1 \end{bmatrix}. \tag{C.16}$$

Since the rotation matrix is orthogonal, R_j^{sys} is related to R_j^{vec} as

$$R_{j,\text{sys}}^{-1}(\theta) = R_{j,\text{sys}}^{\text{T}}(\theta) = R_j^{\text{vec}}(\theta) = R_j^{\text{sys}}(-\theta), \tag{C.17}$$

$$R_{j,\text{vec}}^{-1}(\theta) = R_j^{\text{vec}}(-\theta), \tag{C.18}$$

where T represents the transpose matrix.

C.3 Vector derivatives

Table C.1: Vector derivatives in each coordinate system.

	Cartesian coordinates	Spherical coordinates	Cylindrical coordinates
The (differential) line element	$d\vec{r} = \hat{x} dx + \hat{y} dy + \hat{z} dz$	$d\vec{r} = \hat{r} dr + \hat{\theta} r d\theta + \hat{\phi} r \sin\theta d\phi$	$d\vec{r} = \hat{r} dr + \hat{\phi} r d\phi + \hat{z} dz$
The (differential) area element	$d\vec{\sigma}_x = \hat{x} dy dz$ $d\vec{\sigma}_y = \hat{y} dx dz$ $d\vec{\sigma}_z = \hat{z} dx dy$	$d\vec{\sigma}_r = \hat{r} r^2 \sin\theta d\theta d\phi$ $d\vec{\sigma}_\theta = \hat{\theta} r \sin\theta dr d\phi$ $d\vec{\sigma}_\phi = \hat{\phi} r dr d\theta$	$d\vec{\sigma}_r = \hat{r} r d\phi dz$ $d\vec{\sigma}_\phi = \hat{\phi} dr dz$ $d\vec{\sigma}_z = \hat{z} r dr d\phi$
The (differential) volume element	$d\tau = dx dy dz$	$d\tau = r^2 \sin\theta dr d\theta d\phi$	$d\tau = r dr d\phi dz$
Gradient	$\nabla = \hat{x} \frac{\partial}{\partial x} + \hat{y} \frac{\partial}{\partial y} + \hat{z} \frac{\partial}{\partial z}$	$\nabla = \hat{r} \frac{\partial}{\partial r} + \hat{\theta} \frac{1}{r} \frac{\partial}{\partial \theta} + \hat{\phi} \frac{1}{r \sin\theta} \frac{\partial}{\partial \phi}$	$\nabla = \hat{r} \frac{\partial}{\partial r} + \hat{\phi} \frac{1}{r} \frac{\partial}{\partial \phi} + \hat{z} \frac{\partial}{\partial z}$
Divergence (=div)	$\nabla \cdot \vec{V} = \left(\frac{\partial}{\partial x}, \frac{\partial}{\partial y}, \frac{\partial}{\partial z} \right) \cdot \begin{pmatrix} V_x \\ V_y \\ V_z \end{pmatrix}$	$\nabla \cdot \vec{V} = \frac{1}{r^2 \sin\theta} \left(\frac{\partial}{\partial r}, \frac{\partial}{\partial \theta}, \frac{\partial}{\partial \phi} \right) \cdot \begin{pmatrix} r^2 \sin\theta V_r \\ r \sin\theta V_\theta \\ r V_\phi \end{pmatrix}^a$	$\nabla \cdot \vec{V} = \frac{1}{r} \left(\frac{\partial}{\partial r}, \frac{\partial}{\partial \phi}, \frac{\partial}{\partial z} \right) \cdot \begin{pmatrix} r V_r \\ V_\phi \\ V_z \end{pmatrix}$
Curl	$\nabla \times \vec{V} = \begin{pmatrix} \hat{x} & \hat{y} & \hat{z} \\ \frac{\partial}{\partial x} & \frac{\partial}{\partial y} & \frac{\partial}{\partial z} \\ V_x & V_y & V_z \end{pmatrix}$	$\nabla \times \vec{V} = \begin{pmatrix} \hat{r} & r \hat{\theta} & r \sin\theta \hat{\phi} \\ \frac{\partial}{\partial r} & \frac{\partial}{\partial \theta} & \frac{\partial}{\partial \phi} \\ V_r & r V_\theta & r \sin\theta V_\phi \end{pmatrix}$	$\nabla \times \vec{V} = \frac{1}{r} \begin{pmatrix} \hat{r} & r \hat{\phi} & \hat{z} \\ \frac{\partial}{\partial r} & \frac{\partial}{\partial \phi} & \frac{\partial}{\partial z} \\ V_r & r V_\phi & V_z \end{pmatrix}$
Laplacian (=∇ ²)	$\nabla^2 = \left(\frac{\partial}{\partial x}, \frac{\partial}{\partial y}, \frac{\partial}{\partial z} \right) \cdot \begin{pmatrix} \frac{\partial}{\partial x} \\ \frac{\partial}{\partial y} \\ \frac{\partial}{\partial z} \end{pmatrix}$	$\nabla^2 = \frac{1}{r^2 \sin\theta} \left(\frac{\partial}{\partial r}, \frac{\partial}{\partial \theta}, \frac{\partial}{\partial \phi} \right) \cdot \begin{pmatrix} r^2 \sin\theta \frac{\partial}{\partial r} \\ r \sin\theta \left(\frac{\partial}{\partial \theta} \right) \\ r \left(\frac{\partial}{\partial \phi} \right) \end{pmatrix}^b$	$\nabla^2 = \frac{1}{r} \left(\frac{\partial}{\partial r}, \frac{\partial}{\partial \phi}, \frac{\partial}{\partial z} \right) \cdot \begin{pmatrix} r \frac{\partial}{\partial r} \\ \frac{\partial}{\partial \phi} \\ r \frac{\partial}{\partial z} \end{pmatrix}$

^a

$$r^2 \sin\theta \begin{pmatrix} V_r \\ \frac{1}{r} V_\theta \\ \frac{1}{r \sin\theta} V_\phi \end{pmatrix} = \begin{pmatrix} r^2 \sin\theta V_r \\ r \sin\theta V_\theta \\ r V_\phi \end{pmatrix}. \quad (\text{C.19})$$

^b

$$\nabla^2 = \frac{1}{r^2 \sin\theta} \left(\hat{r} \frac{\partial}{\partial r} + \hat{\theta} \frac{1}{r} \frac{\partial}{\partial \theta} + \hat{\phi} \frac{1}{r \sin\theta} \frac{\partial}{\partial \phi} \right) \cdot r^2 \sin\theta \left(\hat{r} \frac{\partial}{\partial r} + \hat{\theta} \frac{1}{r} \frac{\partial}{\partial \theta} + \hat{\phi} \frac{1}{r \sin\theta} \frac{\partial}{\partial \phi} \right) = \frac{1}{r^2 \sin\theta} \left(\frac{\partial}{\partial r}, \frac{\partial}{\partial \theta}, \frac{\partial}{\partial \phi} \right) \cdot \begin{pmatrix} r^2 \sin\theta \frac{\partial}{\partial r} \\ r \sin\theta \left(\frac{\partial}{\partial \theta} \right) \\ r \left(\frac{\partial}{\partial \phi} \right) \end{pmatrix}. \quad (\text{C.20})$$

C.4 Taylor expansion

The one-dimensional (1D) Taylor series for $f(x)$ about a point $x=a$ is given by [133]

$$\begin{aligned} f(x) &= f(a) + (x-a) f'(a) + \frac{(x-a)^2}{2!} f''(a) + \dots + \frac{(x-a)^n}{n!} f^{(n)}(a) + \dots \\ &= \sum_{n=0}^{\infty} \left[(x-a) \frac{d}{dx} \right]^n \frac{f(x)}{n!} \Big|_{x=a}, \end{aligned} \quad (\text{C.21})$$

where

$$\left[(x-a) \frac{d}{dx} \right]^n \equiv (x-a)^n \left(\frac{d}{dx} \right)^n. \quad (\text{C.22})$$

The relation in Eq. (C.22) is invalid in the general calculation cases.

The Taylor series can also be generalized to any function of more than one variables. A function of two variables, $f(x, y)$, can be expanded about a point $x = a$ and $y = b$ given by

$$\begin{aligned} f(x, y) &= \sum_{n=0}^{\infty} \left[(x-a) \frac{\partial}{\partial x} + (y-b) \frac{\partial}{\partial y} \right]^n \frac{f(x, y)}{n!} \Big|_{x=a, y=b} \\ &= f(a, b) + (x-a) \frac{\partial}{\partial x} f(x, y) \Big|_{(a, b)} + (y-b) \frac{\partial}{\partial y} f(x, y) \Big|_{(a, b)} \\ &\quad + \left[(x-a)^2 \frac{\partial^2}{\partial^2 x} + (x-a)(y-b) \frac{\partial^2}{\partial x \partial y} + (y-b)^2 \frac{\partial^2}{\partial^2 y} \right] \frac{f(x, y)}{2!} \Big|_{(a, b)} + \dots \end{aligned} \quad (\text{C.23})$$

A function of three variables, $f(x, y, z)$, can also be expanded about a point (a, b, c) given by

$$f(x, y, z) = \sum_{n=0}^{\infty} \left[(x-a) \frac{\partial}{\partial x} + (y-b) \frac{\partial}{\partial y} + (z-c) \frac{\partial}{\partial z} \right]^n \frac{f(x, y, z)}{n!} \Big|_{x=a, y=b, z=c}. \quad (\text{C.24})$$

The Taylor series for a function of three variables can be treated in many physical problems since any vector consists of three elements. Then the Maclaurin series² for $f(x, y, z)$ is defined by

$$\begin{aligned} f(x, y, z) &= \sum_{n=0}^{\infty} \left[x \frac{\partial}{\partial x} + y \frac{\partial}{\partial y} + z \frac{\partial}{\partial z} \right]^n \frac{f(x, y, z)}{n!} \Big|_{(0, 0, 0)} \\ &= f(0, 0, 0) + \left[x \frac{\partial}{\partial x} + y \frac{\partial}{\partial y} + z \frac{\partial}{\partial z} \right] f(x, y, z) \Big|_{(0, 0, 0)} + \dots \\ &= f(0, 0, 0) + (\hat{x} x + \hat{y} y + \hat{z} z) \cdot \left(\hat{x} \frac{\partial}{\partial x} + \hat{y} \frac{\partial}{\partial y} + \hat{z} \frac{\partial}{\partial z} \right) f(x, y, z) \Big|_{(0, 0, 0)} + \dots \\ &= f(0, 0, 0) + \vec{x} \cdot \nabla f(x, y, z) \Big|_{(0, 0, 0)} + \dots \end{aligned} \quad (\text{C.25})$$

Here, the third term can be simplified as

$$\left[x \frac{\partial}{\partial x} + y \frac{\partial}{\partial y} + z \frac{\partial}{\partial z} \right]^2 = \left[(\hat{x} x + \hat{y} y + \hat{z} z) \cdot \left(\hat{x} \frac{\partial}{\partial x} + \hat{y} \frac{\partial}{\partial y} + \hat{z} \frac{\partial}{\partial z} \right) \right]^2 = [\vec{x} \cdot \nabla]^2, \quad (\text{C.26})$$

²The Maclaurin series is the Taylor series about the origin [133].

where $\vec{x} \cdot \nabla$ can be represented by its elements in the form

$$\vec{x} \cdot \nabla = \left(\sum_{i=1}^3 \hat{e}_i x_i \right) \cdot \left(\sum_{j=1}^3 \hat{e}_j \frac{\partial}{\partial x_j} \right) = \sum_{i,j} (\hat{e}_i \cdot \hat{e}_j) x_i \frac{\partial}{\partial x_j} = \sum_{i,j} \delta_{ij} x_i \frac{\partial}{\partial x_j} = \sum_i x_i \frac{\partial}{\partial x_i}. \quad (\text{C.27})$$

From Eq. (C.22), the square of $\vec{x} \cdot \nabla$ becomes

$$[\vec{x} \cdot \nabla]^2 \equiv \sum_i x_i \frac{\partial}{\partial x_i} \sum_j x_j \frac{\partial}{\partial x_j} = \sum_{i,j} x_i x_j \frac{\partial^2}{\partial x_i \partial x_j}. \quad (\text{C.28})$$

The above equation is in general invalid when the relation in Eq. (C.22) is not defined. Therefore, the Maclaurin series for $f(x, y, z)$ about $\vec{0} = (0, 0, 0)$ is

$$f(x, y, z) = f(0, 0, 0) + \vec{x} \cdot \nabla f(x, y, z) \Big|_{\vec{0}} + \frac{1}{2!} \sum_{i,j=1}^3 x_i x_j \frac{\partial^2}{\partial x_i \partial x_j} f(x, y, z) \Big|_{\vec{0}} + \dots \quad (\text{C.29})$$

The Maclaurin series for well used functions are as follows

$$e^x = 1 + x + \frac{x^2}{2!} + \frac{x^3}{3!} + \dots = \sum_{j=0}^{\infty} \frac{x^j}{j!} \text{ for all } x, \quad (\text{C.30a})$$

$$\cos x = 1 - \frac{x^2}{2!} + \frac{x^4}{4!} - \frac{x^6}{6!} + \dots \text{ for all } x, \quad (\text{C.30b})$$

$$\sin x = x - \frac{x^3}{3!} + \frac{x^5}{5!} - \frac{x^7}{7!} + \dots \text{ for all } x, \quad (\text{C.30c})$$

$$\tan x = x + \frac{x^3}{3} + \frac{2}{15}x^5 + \frac{17}{315}x^7 \dots \text{ for } -1 < x < 1, \quad (\text{C.30d})$$

$$\tan^{-1} x = x - \frac{x^3}{3} + \frac{x^5}{5} - \frac{x^7}{7} + \dots \text{ for all } x, \quad (\text{C.30e})$$

$$\ln(1+x) = x - \frac{x^2}{2} + \frac{x^3}{3} - \frac{x^4}{4} + \dots \text{ for } -1 < x \leq 1, \quad (\text{C.30f})$$

$$\sinh x = x + \frac{x^3}{3!} + \frac{x^5}{5!} + \frac{x^7}{7!} + \dots \text{ for all } x, \quad (\text{C.30g})$$

$$\frac{1}{1-x} = 1 + x + x^2 + x^3 + \dots \text{ for } -1 < x < 1. \quad (\text{C.30h})$$

C.5 Binomial expansion

The binomial series is often used to solve enormous physical problems. For a variable x much less than 1, the binomial series of the function defined by $(1+x)^s$ for $s \in \mathbb{C}$ is

$$(1+x)^s = 1 + s x + \frac{s(s-1)}{2!} x^2 + \frac{s(s-1)(s-2)}{3!} x^3 + \frac{s(s-1)(s-2)(s-3)}{4!} x^4 + \dots \text{ for } |x| \ll 1. \quad (\text{C.31})$$

The binomial theorem is generally expressed as

$$(a+b)^n = \sum_{r=0}^n \binom{n}{r} a^r b^{n-r}, \quad (\text{C.32})$$

where the matrix form represents the r-combinations of n elements in the form

$$\binom{n}{r} = {}_n C_r = \frac{n!}{r!(n-r)!}. \quad (\text{C.33})$$

C.6 Leibniz's rule

Leibniz's rule is a convenient integral formula defined by [133]

$$\frac{d}{dx} \int_{u(x)}^{v(x)} f(x,t) dt = f(x,v) \frac{dv}{dx} - f(x,u) \frac{du}{dx} + \int_u^v \frac{\partial}{\partial x} f(x,t) dt. \quad (\text{C.34})$$

C.7 Flux

$$\Phi = \int_A \mathbf{V} \cdot \hat{n} d\sigma, \quad (\text{C.35})$$

where \hat{n} is the unit normal vector to the closed surface A , which is pointing out of the surface. $d\sigma$ represents an area element on the surface A [133].

C.8 Gauss theorem (Green's theorem, Divergence theorem)

If \mathbf{A} is a vector function and S is a closed surface bounding a three-dimensional volume V , then

$$\int_V \nabla \cdot \mathbf{A} d^3x = \oint_S \mathbf{A} \cdot \hat{n} da, \quad (\text{C.36})$$

where \hat{n} is the unit normal vector to the closed surface A .

If S is a surface in a plane with boundary ∂S , Eq. (C.36) can be written as

$$\int_S \nabla \cdot \mathbf{A} d^2x = \oint_{\partial S} \mathbf{A} \cdot \hat{n} dl. \quad (\text{C.37})$$

With the substitution $\mathbf{A} \rightarrow \phi \mathbf{C}$,

$$\int_V \nabla \phi d^3x = \oint_S \phi \hat{n} da, \quad (\text{C.38})$$

where \mathbf{C} is any constant vector.

With the substitution $\mathbf{A} \rightarrow \mathbf{A} \times \mathbf{C}$,

$$\int_V \nabla \times \mathbf{A} d^3x = \oint_S \hat{n} \times \mathbf{A} da, \quad (\text{C.39})$$

where \mathbf{C} is any constant vector.

C.9 Stoke's theorem

If \mathbf{A} is a vector function and C is a closed contour bounding an open surface S , then

$$\int_S (\nabla \times \mathbf{A}) \cdot \hat{n} da = \oint_C \mathbf{A} \cdot d\mathbf{l}, \quad (\text{C.40})$$

where $d\mathbf{l}$ is the line element of the contour. Problem 17 on p. 293 in Boyd [7] would be a help to understand.

C.10 Fourier transformation

The Fourier transform is defined as [7, 12]

$$\tilde{E}(t) = \frac{1}{2\pi} \int_{-\infty}^{\infty} d\omega \tilde{F}(\omega) e^{-i\omega t} \equiv \mathcal{F}[\tilde{F}(\omega)], \quad (\text{C.41a})$$

$$\tilde{F}(\omega) = \int_{-\infty}^{\infty} dt \tilde{E}(t) e^{i\omega t} \equiv \mathcal{F}^{-1}[\tilde{E}(t)]. \quad (\text{C.41b})$$

By replacing t by k and ω by x , the Fourier transform can also be written as

$$\tilde{E}(k) = \frac{1}{2\pi} \int_{-\infty}^{\infty} dx \tilde{F}(x) e^{-ikx}, \quad (\text{C.42a})$$

$$\tilde{F}(x) = \int_{-\infty}^{\infty} dk \tilde{E}(k) e^{ikx}. \quad (\text{C.42b})$$

C.11 Planckerel's theorem

$$\delta(x) = \frac{1}{2\pi} \int_{-\infty}^{\infty} dk e^{ikx}. \quad (\text{C.43})$$

Proof. The Fourier transform can be written as

$$g(k) = \frac{1}{2\pi} \int_{-\infty}^{\infty} dx f(x) e^{-ikx}, \quad (\text{C.44a})$$

$$f(x) = \int_{-\infty}^{\infty} dk g(k) e^{ikx}. \quad (\text{C.44b})$$

By substituting $f(x) = \delta(x)$ into Eq. (C.44a), it follows that

$$g(k) = \frac{1}{2\pi} \int_{-\infty}^{\infty} dx \delta(x) e^{-ikx} = \frac{1}{2\pi}, \quad (\text{C.45})$$

which leads to

$$f(x) = \int_{-\infty}^{\infty} dk g(k) e^{ikx} = \frac{1}{2\pi} \int_{-\infty}^{\infty} dk e^{ikx}. \quad (\text{C.46})$$

We therefore obtain the relation in Eq. (C.43). \square

C.12 Differentiation and inverse functions

Definition C.12.1. Natural number

$$\lim_{x \rightarrow 0} (1+x)^{\frac{1}{x}} = \lim_{x \rightarrow 0} (1+\frac{1}{x})^x = e \simeq 2.7182818. \quad (\text{C.47})$$

Derivative C.12.1. A logarithmic function and an exponential function

$$\frac{d}{dx}(\log_a x) = \frac{1}{x \ln a} \quad \text{for } a > 0, a \neq 1, x > 0. \quad (\text{C.48a})$$

$$\frac{d}{dx}(a^x) = a^x \ln a \quad \text{for } a > 0, a \neq 1. \quad (\text{C.48b})$$

Formula C.12.1. Euler's formula

$$e^{ix} = \cos x + i \sin x. \quad (\text{C.49})$$

This can be proved by the Taylor expansion.

Note C.12.1.

$$\cos x = \frac{e^{ix} + e^{-ix}}{2}, \quad \sin x = \frac{e^{ix} - e^{-ix}}{2i} \quad (\text{C.50})$$

Definition C.12.2.

$$\text{If } z = a + ib = re^{i\theta}, \quad \ln z = \ln |z| + i \arg z, \quad \text{where } |z| = r \text{ and } \arg(z) = \theta. \quad (\text{C.51})$$

Derivative C.12.2. Total derivative

$$df(x, y, z) = \frac{\partial f}{\partial x} dx + \frac{\partial f}{\partial y} dy + \frac{\partial f}{\partial z} dz \quad (\text{C.52})$$

$$= \left(\frac{\partial f}{\partial x}, \frac{\partial f}{\partial y}, \frac{\partial f}{\partial z} \right) \cdot (dx, dy, dz)$$

$$= \nabla f \cdot dr, \quad (\text{C.53})$$

where ∇f is a gradient of f .

C.12.1 Trigonometric functions

Definition C.12.3. Trigonometric functions.

$$\cos x = \frac{e^{ix} + e^{-ix}}{2} \quad \sin x = \frac{e^{ix} - e^{-ix}}{2i} \quad \tan x = \frac{\sin x}{\cos x} \quad (\text{C.54a})$$

$$\cot x = \frac{\cos x}{\sin x} \quad \sec x = \frac{1}{\cos x} \quad \csc x = \frac{1}{\sin x} \quad (\text{C.54b})$$

$$\cos^2 x + \sin^2 x = 1 \quad 1 + \tan^2 x = \sec^2 x \quad 1 + \cot^2 x = \csc^2 x. \quad (\text{C.54c})$$

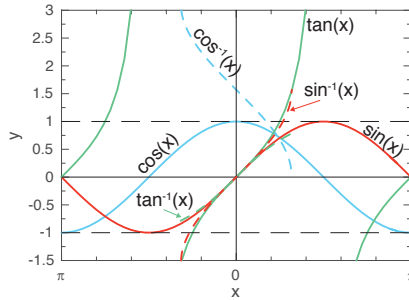


Figure C.1: Trigonometric functions.

Definition C.12.4. Addition of trigonometric functions.

$$\sin(a \pm b) = \sin a \cos b \pm \cos a \sin b \quad (\text{C.55a})$$

$$\cos(a \pm b) = \cos a \cos b \mp \sin a \sin b \quad (\text{C.55b})$$

$$\tan(a \pm b) = \frac{\tan a \pm \tan b}{1 \mp \tan a \tan b}. \quad (\text{C.55c})$$

Note C.12.2. The law of cosines

$$a^2 = b^2 + c^2 - 2bc \cos A, \quad (\text{C.56a})$$

$$b^2 = a^2 + c^2 - 2ac \cos B, \quad (\text{C.56b})$$

$$c^2 = a^2 + b^2 - 2ab \cos C. \quad (\text{C.56c})$$

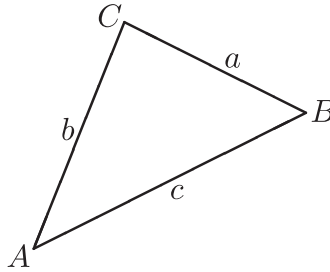


Figure C.2: Triangle

Proof. From the above figure, we find that

$$a = b \cos C + c \cos B, \quad (\text{C.57a})$$

$$b = c \cos A + a \cos C, \quad (\text{C.57b})$$

$$c = a \cos B + b \cos A, \quad (\text{C.57c})$$

which further make

$$a^2 = ab \cos C + ac \cos B, \quad (\text{C.58a})$$

$$b^2 = bc \cos A + ab \cos C, \quad (\text{C.58b})$$

$$c^2 = ac \cos B + bc \cos A. \quad (\text{C.58c})$$

By combining Eqs. (C.58b) through (C.58c), we obtain

$$b^2 + c^2 = bc \cos A + ab \cos C + ac \cos B + bc \cos A. \quad (\text{C.59})$$

We then find by subtracting this equation from Eq. (C.58a) that

$$a^2 - (b^2 + c^2) = ab \cos C + ac \cos B - (bc \cos A + ab \cos C + ac \cos B + bc \cos A), \quad (\text{C.60})$$

which implies that

$$a^2 - (b^2 + c^2) = -2bc \cos A, \quad (\text{C.61})$$

so that

$$a^2 = b^2 + c^2 - 2bc \cos A. \quad (\text{C.62a})$$

Similarly, we find that

$$b^2 = a^2 + c^2 - 2ac \cos B, \quad (\text{C.62b})$$

$$c^2 = a^2 + b^2 - 2ab \cos C. \quad (\text{C.62c})$$

□

Note C.12.3.

$$\cos 2a = \cos^2 a - \sin^2 a = \begin{cases} 2 \cos^2 a - 1 & \rightarrow \cos^2 a = (1 + \cos 2a)/2 \\ 1 - 2 \sin^2 a & \rightarrow \sin^2 a = (1 - \cos 2a)/2. \end{cases} \quad (\text{C.63})$$

Derivative C.12.3. Trigonometric functions.

$$\frac{d}{dx} \sin x = \cos x \qquad \frac{d}{dx} \cos x = -\sin x \quad (\text{C.64a})$$

$$\frac{d}{dx} \tan x = \sec^2 x \qquad \frac{d}{dx} \cot x = -\csc^2 x \quad (\text{C.64b})$$

$$\frac{d}{dx} \sec x = \sec x \tan x \qquad \frac{d}{dx} \csc x = -\csc x \cot x \quad (\text{C.64c})$$

Derivative C.12.4. Inverse trigonometric functions.

$$\frac{d}{dx} \sin^{-1} x = \frac{1}{\sqrt{1-x^2}} \text{ for } -1 < x < 1 \qquad \frac{d}{dx} \cos^{-1} x = \frac{-1}{\sqrt{1-x^2}} \text{ for } -1 < x < 1 \quad (\text{C.65a})$$

$$\frac{d}{dx} \tan^{-1} x = \frac{1}{1+x^2} \qquad \frac{d}{dx} \cot^{-1} x = \frac{-1}{1+x^2} \quad (\text{C.65b})$$

$$\frac{d}{dx} \sec^{-1} x = \frac{1}{x\sqrt{x^2-1}}, \quad x \in (-\infty, -1] \cup [1, \infty) \qquad \frac{d}{dx} \csc^{-1} x = \frac{-1}{x\sqrt{x^2-1}}, \quad x \in (-\infty, -1] \cup [1, \infty). \quad (\text{C.65c})$$

Proof.

$$\begin{aligned} \sin^{-1} x = y &\Leftrightarrow x = \sin y \\ \Leftrightarrow \frac{d}{dx} x &= \frac{d}{dx} \sin y, \quad \Leftrightarrow 1 = \frac{dy}{dx} \frac{d}{dy} \sin y = \cos y \, y' \\ \Leftrightarrow y' &= \frac{1}{\cos y} = \frac{1}{\sqrt{1-\sin^2 y}} = \frac{1}{\sqrt{1-x^2}} \quad \therefore y' = \frac{d}{dx} \sin^{-1} x = \frac{1}{\sqrt{1-x^2}}. \end{aligned}$$

□

Derivative C.12.5.

$$\cos^{-1} w = \frac{1}{i} \ln(w \pm \sqrt{w^2 - 1}), \quad w \pm \sqrt{w^2 - 1} > 0 \text{ for } w \in \mathbb{R}. \quad (\text{C.66})$$

Proof.

$$\begin{aligned}
\cos z = \frac{e^{iz} + e^{-iz}}{2} = w &\Leftrightarrow \frac{(e^{iz})^2 + 1}{2} = w e^{iz} \quad \text{by multiplying } e^{iz} \text{ in both sides.} \\
\Leftrightarrow (e^{iz})^2 - 2w(e^{iz}) + 1 &= (e^{iz})^2 - 2w(e^{iz}) + w^2 - w^2 + 1 = 0 \\
\Leftrightarrow (e^{iz} - w)^2 = w^2 - 1 &\Leftrightarrow e^{iz} = w \pm \sqrt{w^2 - 1} \\
\Leftrightarrow \ln e^{iz} = iz = \ln(w \pm \sqrt{w^2 - 1}) &\quad \therefore z = \cos^{-1} w = \frac{1}{i} \ln(w \pm \sqrt{w^2 - 1}) \text{ for } w \in \mathbb{C}.
\end{aligned}$$

□

Variable x must be bigger than zero when the function is defined as $\ln x$. Since $\ln(w \pm \sqrt{w^2 - 1})$ can not be defined when $w \pm \sqrt{w^2 - 1} < 0$, we obtain the result for real numbers as follows

$$z = \cos^{-1} w = \frac{1}{i} \ln(w \pm \sqrt{w^2 - 1}), \quad w \pm \sqrt{w^2 - 1} > 0 \text{ for } w \in \mathbb{R}. \quad (\text{C.67})$$

Derivative C.12.6.

$$\sin^{-1} w = \frac{1}{i} \ln(iw \pm \sqrt{1 - w^2}) \text{ for } w \in \mathbb{C}. \quad (\text{C.68})$$

Proof.

$$\begin{aligned}
\sin z = \frac{e^{iz} - e^{-iz}}{2i} = w &\Leftrightarrow \frac{(e^{iz})^2 - 1}{2i} = w e^{iz} \quad \text{by multiplying } e^{iz} \text{ to both sides.} \\
\Leftrightarrow (e^{iz})^2 - 2iw(e^{iz}) - 1 &= (e^{iz})^2 - 2iw(e^{iz}) + (iw)^2 + w^2 - 1 = 0 \\
\Leftrightarrow (e^{iz} - iw)^2 = 1 - w^2 &\Leftrightarrow e^{iz} = iw \pm \sqrt{1 - w^2} \\
\Leftrightarrow \ln e^{iz} = iz = \ln(iw \pm \sqrt{1 - w^2}) &\quad \therefore z = \sin^{-1} w = \frac{1}{i} \ln(iw \pm \sqrt{1 - w^2}) \text{ for } w \in \mathbb{C}.
\end{aligned}$$

□

Derivative C.12.7.

$$\tan^{-1} w = \frac{1}{2i} \ln \left(\frac{1 + iw}{1 - iw} \right) \text{ for } w \in \mathbb{C}. \quad (\text{C.69})$$

Proof.

$$\tan z = \frac{\sin z}{\cos z} = \frac{1}{\left(\frac{e^{iz} + e^{-iz}}{2} \right)} \frac{e^{iz} - e^{-iz}}{2i} = \frac{e^{iz} - e^{-iz}}{i(e^{iz} + e^{-iz})} = w,$$

which implies that

$$e^{iz} - e^{-iz} = iw(e^{iz} + e^{-iz}).$$

By multiplying e^{iz} to both sides, we obtain

$$(e^{iz})^2 - 1 = iw \left[(e^{iz})^2 + 1 \right],$$

which leads to

$$(1 - iw)(e^{iz})^2 = 1 + iw \Leftrightarrow (e^{iz})^2 = \frac{1 + iw}{1 - iw},$$

so that

$$\ln(e^{iz})^2 = 2 \ln(e^{iz}) = 2iz = \ln \left(\frac{1+iw}{1-iw} \right).$$

We therefore find that

$$z = \tan^{-1} w = \frac{1}{2i} \ln \left(\frac{1+iw}{1-iw} \right) \text{ for } w \in \mathbb{C}.$$

□

Note C.12.4. Orthogonality of trigonometric functions

$$\int_0^{2\pi} \cos mx \cos nx = \int_{-\pi}^{\pi} \cos mx \cos nx = \begin{cases} 0 & \text{for } m \neq n \\ \pi & \text{for } m = n \\ 2\pi & \text{for } m = n = 0 \end{cases}, \quad (\text{C.70a})$$

$$\int_0^{2\pi} \sin mx \sin nx = \int_{-\pi}^{\pi} \sin mx \sin nx = \begin{cases} 0 & \text{for } m \neq n \\ \pi & \text{for } m = n \end{cases}, \quad (\text{C.70b})$$

$$\int_0^{2\pi} \cos mx \sin nx = \int_{-\pi}^{\pi} \cos mx \sin nx = 0, \quad (\text{C.70c})$$

$$\int_0^{\pi} \cos mx \cos nx = \int_{-\pi/2}^{\pi/2} \cos mx \cos nx = \begin{cases} 0 & \text{for } m \neq n \\ \frac{\pi}{2} & \text{for } m = n \\ \pi & \text{for } m = n = 0 \end{cases}, \quad (\text{C.70d})$$

$$\int_0^{\pi} \sin mx \sin nx = \int_{-\pi/2}^{\pi/2} \sin mx \sin nx = \begin{cases} 0 & \text{for } m \neq n \\ \frac{\pi}{2} & \text{for } m = n \end{cases} \quad (\text{C.70e})$$

$$\int_0^{\pi} \cos mx \sin nx = \int_{-\pi/2}^{\pi/2} \cos mx \sin nx = 0. \quad (\text{C.70f})$$

C.12.2 Hyperbolic functions

Definition C.12.5. Hyperbolic functions.

$$\cosh x = \frac{e^x + e^{-x}}{2} \quad \sinh x = \frac{e^x - e^{-x}}{2} \quad \tanh x = \frac{\sinh x}{\cosh x} \quad (\text{C.71a})$$

$$\coth x = \frac{\cosh x}{\sinh x} \quad \operatorname{sech} x = \frac{1}{\cosh x} \quad \operatorname{csch} x = \frac{1}{\sinh x} \quad (\text{C.71b})$$

$$\cosh^2 x - \sinh^2 x = 1 \quad 1 - \tanh^2 x = \operatorname{sech}^2 x \quad \coth^2 x - 1 = \operatorname{csch}^2 x. \quad (\text{C.71c})$$

Derivative C.12.8. Hyperbolic functions.

$$\frac{d}{dx} \sinh x = \cosh x \quad \frac{d}{dx} \cosh x = \sinh x \quad (\text{C.72a})$$

$$\frac{d}{dx} \tanh x = \operatorname{sech}^2 x \quad \frac{d}{dx} \coth x = -\operatorname{csch}^2 x \quad (\text{C.72b})$$

$$\frac{d}{dx} \operatorname{sech} x = -\operatorname{sech} x \tanh x \quad \frac{d}{dx} \operatorname{csch} x = -\operatorname{csch} x \coth x \quad (\text{C.72c})$$

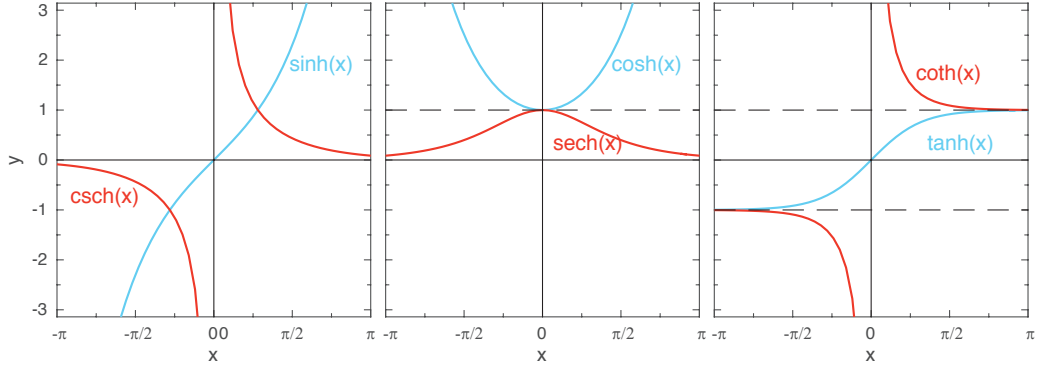


Figure C.3: Hyperbolic functions.

Derivative C.12.9. Inverse hyperbolic functions.

$$\frac{d}{dx} \sinh^{-1} x = \frac{1}{\sqrt{x^2 + 1}} \text{ for } x \in \mathbb{R} \quad \frac{d}{dx} \cosh^{-1} x = \frac{1}{\sqrt{x^2 - 1}} \text{ for } 1 < x \quad (\text{C.73a})$$

$$\frac{d}{dx} \tanh^{-1} x = \frac{1}{1 - x^2} \text{ for } |x| < 1 \quad \frac{d}{dx} \coth^{-1} x = \frac{1}{1 - x^2} \text{ for } |x| > 1 \quad (\text{C.73b})$$

$$\frac{d}{dx} \operatorname{sech}^{-1} x = \frac{-1}{x\sqrt{1 - x^2}} \text{ for } 0 < x < 1 \quad \frac{d}{dx} \operatorname{csch}^{-1} x = \frac{-1}{|x|\sqrt{1 + x^2}} \text{ for } x \neq 0 \quad (\text{C.73c})$$

Derivative C.12.10.

$$\cosh^{-1} w = \ln(w \pm \sqrt{w^2 - 1}) \text{ for } w \in \mathbb{C}. \quad (\text{C.74})$$

Proof.

$$\begin{aligned} \cosh z = \frac{e^z + e^{-z}}{2} = w &\Leftrightarrow \frac{(e^z)^2 + 1}{2} = w e^z \text{ by multiplying } e^z \text{ to both sides.} \\ \Leftrightarrow (e^z)^2 - 2 w (e^z) + 1 = (e^z)^2 - 2 w (e^z) + w^2 - w^2 + 1 = 0 \\ \Leftrightarrow (e^z - w)^2 = w^2 - 1 &\Leftrightarrow e^z = w \pm \sqrt{w^2 - 1} \\ \Leftrightarrow \ln e^z = z = \ln(w \pm \sqrt{w^2 - 1}) &\therefore z = \cosh^{-1} w = \ln(w \pm \sqrt{w^2 - 1}) \text{ for } w \in \mathbb{C}. \end{aligned}$$

□

Derivative C.12.11.

$$\sinh^{-1} w = \ln(w + \sqrt{w^2 + 1}) \text{ for } w \in \mathbb{R}. \quad (\text{C.75})$$

Proof.

$$\begin{aligned} \sinh z = \frac{e^z - e^{-z}}{2} = w &\Leftrightarrow \frac{(e^z)^2 - 1}{2} = w e^z \text{ by multiplying } e^z \text{ to both sides.} \\ \Leftrightarrow (e^z)^2 - 2 w (e^z) - 1 = (e^z)^2 - 2 w (e^z) + w^2 - w^2 - 1 = 0 \\ \Leftrightarrow (e^z - w)^2 = w^2 + 1 &\Leftrightarrow e^z = w \pm \sqrt{w^2 + 1} \\ \Leftrightarrow \ln e^z = z = \ln(w \pm \sqrt{w^2 + 1}) &\therefore z = \sinh^{-1} w = \ln(w \pm \sqrt{w^2 + 1}) \text{ for } w \in \mathbb{C}. \end{aligned}$$

□

Recall that the variable x should be bigger than zero when the function is defined as $\ln x$. For $w \in \mathbb{R}$, $\ln(w - \sqrt{w^2 + 1})$ can not be defined since $w - \sqrt{w^2 + 1} < 0$. Thus we obtain the result for real number as follows

$$z = \sinh^{-1} w = \ln(w + \sqrt{w^2 + 1}) \text{ for } w \in \mathbb{R}.$$

Derivative C.12.12.

$$\tanh^{-1} w = \frac{1}{2} \ln \left(\frac{1+w}{1-w} \right) \text{ for } w \in \mathbb{C}. \quad (\text{C.76})$$

Proof.

$$\begin{aligned} \tanh z &= \frac{\sinh z}{\cosh z} = \frac{1}{\left(\frac{e^z + e^{-z}}{2} \right)} \frac{e^z - e^{-z}}{2} = \frac{e^z - e^{-z}}{e^z + e^{-z}} = w \\ \Leftrightarrow e^z - e^{-z} &= w (e^z + e^{-z}) \\ \Leftrightarrow (e^z)^2 - 1 &= w [(e^z)^2 + 1] \quad \text{by multiplying } e^z \text{ to both sides.} \\ \Leftrightarrow (1-w)(e^z)^2 &= 1+w \Leftrightarrow (e^z)^2 = \frac{1+w}{1-w} \\ \Leftrightarrow \ln(e^z)^2 &= 2 \ln(e^z) = 2z = \ln \left(\frac{1+w}{1-w} \right) \quad \therefore z = \tanh^{-1} w = \frac{1}{2} \ln \left(\frac{1+w}{1-w} \right) \text{ for } w \in \mathbb{C}. \end{aligned}$$

□

C.13 Well used integral calculus

Integral C.13.1.

$$\int dx \frac{1}{\cos x} = \ln(\sec x + \tan x). \quad (\text{C.77})$$

Proof. By taking $t = \sin x$ such that $\cos x \, dx = dt$, we obtain

$$\text{Int} = \int dx \frac{1}{\cos x} = \int dx \frac{\cos x}{\cos^2 x} = \int dx \frac{\cos x}{1 - \sin^2 x} = \int dt \frac{1}{1 - t^2}.$$

Here, the integrand can be written as

$$\frac{1}{1 - t^2} = \frac{a}{1 + t} + \frac{b}{1 - t},$$

which implies that $a = b = 1/2$. Using this relation, the integral becomes

$$\begin{aligned} \text{Int} &= \frac{1}{2} \int dt \left[\frac{1}{1+t} + \frac{1}{1-t} \right] = \frac{1}{2} \left[\ln(1+t) + \ln(1-t) \right] \\ &= \frac{1}{2} \ln \left(\frac{1+t}{1-t} \right) = \frac{1}{2} \ln \left(\frac{1 + \sin x}{1 - \sin x} \right) = \frac{1}{2} \ln \left(\frac{(1 + \sin x)^2}{(1 - \sin x)(1 + \sin x)} \right) \\ &= \ln \left(\frac{1 + \sin x}{\sqrt{1 - \sin^2 x}} \right) = \ln \left(\frac{1 + \sin x}{\cos x} \right) = \ln(\sec x + \tan x). \end{aligned}$$

□

Integral C.13.2.

$$\int dx \frac{1}{\sin x} = \ln \left(\tan \frac{x}{2} \right). \quad (\text{C.78})$$

Proof. By taking $\tan \frac{x}{2} = t$, we find that

$$\frac{1}{2} \sec^2 \frac{x}{2} dx = dt. \quad (\text{C.79})$$

Using a relation

$$1 + \tan^2 \frac{x}{2} = \sec^2 \frac{x}{2},$$

Eq. (C.79) becomes

$$dt = \frac{1}{2} (1 + t^2) dx. \quad (\text{C.80})$$

Furthermore, the integrand can be written as

$$\begin{aligned} \sin x &= \sin \left(\frac{x}{2} + \frac{x}{2} \right) = 2 \sin \frac{x}{2} \cos \frac{x}{2} \\ &= \frac{2 \sin \frac{x}{2} \cos \frac{x}{2}}{\cos^2 \frac{x}{2} + \sin^2 \frac{x}{2}} = \frac{2 \sin \frac{x}{2} \cos \frac{x}{2} \frac{1}{\cos^2 \frac{x}{2}}}{\frac{1}{\cos^2 \frac{x}{2}} + \frac{\sin^2 \frac{x}{2}}{\cos^2 \frac{x}{2}}} = \frac{2 \tan \frac{x}{2}}{1 + \tan^2 \frac{x}{2}} = \frac{2t}{1 + t^2}. \end{aligned} \quad (\text{C.81})$$

We then find from Eqs. (C.80) and (C.81) that

$$\int dx \frac{1}{\sin x} = \int dt \frac{2}{1 + t^2} \frac{1 + t^2}{2t} = \int dt \frac{1}{t} = \ln t = \ln \left(\tan \frac{x}{2} \right).$$

□

Integral C.13.3.

$$\int dx \frac{1}{\tan x} = \ln(\sin x). \quad (\text{C.82})$$

Proof. By taking $t = \sin x$ such that $dt = \cos x dx$, we obtain

$$\int dx \frac{1}{\tan x} = \int dx \frac{\cos x}{\sin x} = \int dt \frac{1}{\cos x} \frac{\cos x}{t} = \ln t = \ln(\sin x).$$

□

Integral C.13.4.

$$\int dx \frac{1}{a^2 + x^2} = \frac{1}{i2a} \ln \left(\frac{1 + i\frac{x}{a}}{1 - i\frac{x}{a}} \right). \quad (\text{C.83})$$

Proof. By taking $x = a \tan t$ such that $dx = a \sec^2 t dt$, we obtain

$$\begin{aligned} \text{Int} &= \int dx \frac{1}{a^2 + x^2} = \int dt \frac{a \sec^2 t}{a^2 + a^2 \tan^2 t} \\ &= \frac{1}{a} \int dt = \frac{1}{a} \tan^{-1} \left(\frac{x}{a} \right). \end{aligned}$$

We then find from Eq. (C.69) that

$$\text{Int} = \frac{1}{i2a} \ln \left(\frac{1 + i\frac{x}{a}}{1 - i\frac{x}{a}} \right). \quad (\text{C.84})$$

□

Integral C.13.5.

$$\int dx \frac{1}{\sqrt{a^2 - x^2}} = \sin^{-1} \left(\frac{x}{a} \right) = \frac{1}{i} \ln \left(i \frac{x}{a} \pm \sqrt{1 - \frac{x^2}{a^2}} \right). \quad (\text{C.85})$$

See Eq. (5.107).

Integral C.13.6.

$$\int dx \frac{1}{\sqrt{x^2 - a^2}} = \ln \left(\frac{x}{a} \pm \sqrt{\frac{x^2}{a^2} - 1} \right). \quad (\text{C.86})$$

Proof. By taking $x = a \cosh t$ such that $dx = a \sinh t dt$, we obtain

$$\begin{aligned} \text{Int} &= \int dx \frac{1}{\sqrt{x^2 - a^2}} = \int dt \frac{a \sinh t}{\sqrt{a^2 \cosh^2 t - a^2}} \\ &= \int dt \frac{a \sinh t}{\sqrt{a^2 \sinh^2 t}} = \int dt = t = \cosh^{-1} \left(\frac{x}{a} \right), \end{aligned}$$

where $\cosh^2 t - \sinh^2 t = 1$. We then find from Eq. (C.74) that

$$\text{Int} = \ln \left(\frac{x}{a} \pm \sqrt{\frac{x^2}{a^2} - 1} \right).$$

□

Integral C.13.7.

$$\int dx \frac{1}{\sqrt{x^2 + a^2}} = \ln \left(\frac{x}{a} + \sqrt{\frac{x^2}{a^2} + 1} \right). \quad (\text{C.87})$$

Proof. By taking $x = a \sinh t$ such that $dx = a \cosh t dt$, we obtain

$$\begin{aligned} \text{Int} &= \int dx \frac{1}{\sqrt{x^2 + a^2}} = \int dt \frac{a \cosh t}{\sqrt{a^2 \sinh^2 t + a^2}} \\ &= \int dt = t = \sinh^{-1} \left(\frac{x}{a} \right). \end{aligned}$$

From Eq. (C.75), we find that

$$\text{Int} = \ln \left(\frac{x}{a} + \sqrt{\frac{x^2}{a^2} + 1} \right).$$

□

Integral C.13.8.

$$\int dx \frac{1}{a^2 - x^2} = \frac{1}{2a} \ln \left(\frac{1 + \frac{x}{a}}{1 - \frac{x}{a}} \right). \quad (\text{C.88})$$

Proof. By taking $x = a \tanh t$ such that $dx = a \text{sech}^2 t dt$, we obtain

$$\begin{aligned} \text{Int} &= \int dx \frac{1}{a^2 - x^2} = \int dt \frac{a \text{sech}^2 t}{a^2 - a^2 \tanh^2 t} = \frac{1}{a} \int dt \frac{\text{sech}^2 t}{\text{sech}^2 t} \\ &= \frac{1}{a} \int dt = \frac{1}{a} t = \frac{1}{a} \tanh^{-1} \left(\frac{x}{a} \right), \end{aligned}$$

where $1 - \tanh^2 t = \operatorname{sech}^2 t$. We thus find from Eq. (C.76) that

$$\operatorname{Int} = \frac{1}{2a} \ln \left(\frac{1 + \frac{x}{a}}{1 - \frac{x}{a}} \right). \quad (\text{C.89})$$

□

Definition C.13.1. Γ function (Gamma function, fractional function)

$$p! = \int_0^\infty dx e^{-x} x^p \equiv \Gamma(p+1), \text{ for } p > -1, p \in \mathbb{R}. \quad (\text{C.90})$$

$$\left(\Gamma(p) = \int_0^\infty dx e^{-x} x^{p-1} = (p-1)!, \text{ for } \operatorname{Re}(p) > 0, p \in \mathbb{C}. \right) \quad (\text{C.91})$$

Proof. For $a > 0$,

$$f(a, x) \equiv \int_0^\infty dx e^{-ax} = -\frac{1}{a} e^{-ax} \Big|_{x=0}^\infty = \frac{1}{a}. \quad (\text{C.92})$$

By differentiation with respect to a , the right-hand side (RHS) and the left-hand side (LHS) of Eq. (C.92) become

$$\begin{aligned} \text{RHS} &= \frac{d}{da} \int_0^\infty dx e^{-ax} = \int_0^\infty dx \frac{\partial}{\partial a} e^{-ax} = \int_0^\infty dx (-x) e^{-ax}, \\ \text{LHS} &= \frac{d}{da} a^{-1} = -a^{-2}. \end{aligned}$$

Therefore we obtain the 1st-order derivative of a function $f(a, x)$ with respect to a given by

$$\int_0^\infty dx x e^{-ax} = a^{-2}. \quad (\text{C.93})$$

Next, by differentiating Eq. (C.93) with respect to a , the 2nd-order derivative is

$$\begin{aligned} \text{RHS} &= \frac{d}{da} \int_0^\infty dx x e^{-ax} = \int_0^\infty dx x \frac{\partial}{\partial a} e^{-ax} = - \int_0^\infty dx x^2 e^{-ax}, \\ \text{LHS} &= \frac{d}{da} a^{-2} = -2a^{-3}, \end{aligned}$$

which becomes

$$\int_0^\infty dx x^2 e^{-ax} = 2a^{-3}.$$

By the same analogy, the 3rd-order derivative of a function $f(a, x)$ with respect to a is

$$\int_0^\infty dx x^3 e^{-ax} = 3! a^{-4}.$$

Therefore, the n -th-order derivative of a function $f(a, x)$ with respect to a can be expressed by

$$\int_0^\infty dx x^n e^{-ax} = n! a^{n+1} = \frac{n!}{a^{n+1}}. \quad (\text{C.94})$$

By substituting a by 1 in Eq. (C.94), one obtain the Gamma function given by

$$\int_0^\infty dx e^{-x} x^n = n!.$$

□

Definition C.13.2. Properties of Γ function

$$\begin{aligned} p! = p(p-1)! &\Leftrightarrow \Gamma(p+1) = p \Gamma(p) \\ &\Leftrightarrow \Gamma(p) = \frac{\Gamma(p+1)}{p}, \text{ where } p < 0, \text{ or } \operatorname{Re}(p) > 0, \end{aligned} \quad (\text{C.95})$$

$$\Gamma(p)\Gamma(1-p) = \frac{\pi}{\sin \pi p} \Leftrightarrow p!(-p)! = \frac{\pi p}{\sin \pi p}. \quad (\text{C.96})$$

Integral C.13.9.

$$\int_0^\infty dx \exp(-x^n) = \left(\frac{1}{n}\right)! \quad (\text{C.97})$$

Proof. Let $x = t^n$ such that (s.t.) $dx = nt^{n-1}dt$. Then the Gamma function Eq.(C.90) is modified by

$$p! = \int_0^\infty dx e^{-x} x^p = \int_0^\infty dt nt^{n-1} e^{-t^n} t^{np} = n \int_0^\infty dt e^{-t^n} t^{np+n-1}. \quad (\text{C.98})$$

In order to eliminate the last term, $np + n - 1$ should be substituted with zero given by

$$np + n - 1 = 0 \Leftrightarrow p = \frac{1-n}{n} = \frac{1}{n} - 1.$$

With this relation, Eq. (C.98) becomes

$$\left(\frac{1}{n} - 1\right)! = n \int_0^\infty dt e^{-t^n},$$

which can be expressed in terms of $(1/n)!$ as

$$\int_0^\infty dt e^{-t^n} = \frac{1}{n} \left(\frac{1}{n} - 1\right)! = \left(\frac{1}{n}\right)!.$$

□

Integral C.13.10.

$$\left(\frac{1}{2}\right)! = \frac{\sqrt{\pi}}{2}. \quad (\text{C.99})$$

Proof. By Eq. (C.97), $(1/2)!$ becomes

$$\left(\frac{1}{2}\right)! = \int_0^\infty dx e^{-x^2} = \frac{1}{2} \int_{-\infty}^\infty dx e^{-x^2}.$$

Since x is a dummy index, the square of $(1/2)!$ can be expressed as

$$\left(\frac{1}{2}\right)! \left(\frac{1}{2}\right)! = \frac{1}{4} \int_{-\infty}^\infty dx e^{-x^2} \int_{-\infty}^\infty dy e^{-y^2} = \frac{1}{4} \int_{-\infty}^\infty dx \int_{-\infty}^\infty dy e^{-(x^2+y^2)}. \quad (\text{C.100})$$

By the spherical coordinates, x and y are transformed in terms of the radial coordinate r and the polar coordinate θ given by

$$x = r \cos \theta, \quad y = r \sin \theta,$$

such that $r^2 = x^2 + y^2$. From Table. C.1, the infinitesimal differential area element is

$$da = dx dy = r dr d\theta.$$

Then Eq. (C.100) becomes

$$\left(\frac{1}{2}\right)!\left(\frac{1}{2}\right)! = \frac{1}{4} \int_{-\infty}^{\infty} dx \int_{-\infty}^{\infty} dy e^{-(x^2+y^2)} = \frac{1}{4} \int_0^{2\pi} d\theta \int_0^{\infty} dr r e^{-r^2},$$

where the integral with respect to r can be solved by integration by substitution ($r^2 = u$ s.t. $2rdr = du$) in the form

$$\int_0^{\infty} dr r e^{-r^2} = \frac{1}{2} \int_0^{\infty} du e^{-u} = -\frac{1}{2} e^{-u} \Big|_0^{\infty} = \frac{1}{2}. \quad (\text{C.101})$$

Therefore Eq. (C.100) is calculated as follows

$$\left(\frac{1}{2}\right)!\left(\frac{1}{2}\right)! = \frac{1}{4} \int_0^{2\pi} d\theta \int_0^{\infty} dr r e^{-r^2} = \frac{1}{4} \times 2\pi \times \frac{1}{2} = \frac{\pi}{4},$$

which implies that

$$\left(\frac{1}{2}\right)! = \frac{\sqrt{\pi}}{2}.$$

□

Integral C.13.11.

$$\int_0^{\infty} dx \exp(-ax^2) = \frac{1}{2} \sqrt{\frac{\pi}{a}}. \quad (\text{C.102})$$

Proof. Let $x = at^2$ s.t. $dx = 2at dt$. Then the Gamma function Eq.(C.90) is modified as

$$p! = \int_0^{\infty} dx e^{-x} x^p = \int_0^{\infty} dt 2at e^{-at^2} (at^2)^p = 2a^{p+1} \int_0^{\infty} dt e^{-at^2} t^{2p+1}. \quad (\text{C.103})$$

In order to eliminate the last term, $2p + 1$ should be substituted with zero given by

$$2p + 1 = 0 \Leftrightarrow p = -\frac{1}{2}.$$

With this relation, Eq. (C.103) becomes

$$\left(-\frac{1}{2}\right)! = 2\sqrt{a} \int_0^{\infty} dt e^{-at^2}. \quad (\text{C.104})$$

From Eq. (C.99), $(-1/2)!$ can be obtained by

$$\left(\frac{1}{2}\right)! = \frac{1}{2} \left(-\frac{1}{2}\right)! = \frac{\sqrt{\pi}}{2},$$

which implies that

$$\left(-\frac{1}{2}\right)! = \sqrt{\pi}. \quad (\text{C.105})$$

Therefore Eq. (C.104) is calculated by

$$\int_0^{\infty} dt e^{-at^2} = \frac{1}{2} \sqrt{\frac{\pi}{a}}.$$

Since e^{-at^2} is an even function, Eq. (C.102) can be written in the form

$$\int_{-\infty}^{\infty} dt e^{-at^2} = \sqrt{\frac{\pi}{a}}. \quad (\text{C.106})$$

□

Integral C.13.12.

$$\int_{-\infty}^{\infty} dx \exp(-ax^2 + bx) = \exp\left[\frac{b^2}{4a}\right] \sqrt{\frac{\pi}{a}}. \quad (\text{C.107})$$

Proof. Provided a and b are any constants, the integral with respect to x becomes

$$\begin{aligned} \int_{-\infty}^{\infty} dx \exp(-ax^2 + bx) &= \int_{-\infty}^{\infty} dx \exp\left[-a\left(x^2 - \frac{b}{a}x + \frac{b^2}{4a^2} - \frac{b^2}{4a^2}\right)\right] \\ &= \exp\left[\frac{b^2}{4a}\right] \int_{-\infty}^{\infty} dx \exp\left[-a\left(x - \frac{b}{2a}\right)^2\right]. \end{aligned}$$

Let $x - b/2a = t$ s.t. $dx = dt$. From Eq. (C.106), the last integral term can be calculated as follows

$$\int_{-\infty}^{\infty} dx \exp\left[-a\left(x - \frac{b}{2a}\right)^2\right] = \int_{-\infty}^{\infty} dt \exp\left[-at^2\right] = \sqrt{\frac{\pi}{a}}.$$

Thus one obtain

$$\int_{-\infty}^{\infty} dx \exp(-ax^2 + bx) = \exp\left[\frac{b^2}{4a}\right] \sqrt{\frac{\pi}{a}}.$$

□

Integral C.13.13.

$$\int_{-\infty}^{\infty} dx \exp(-x^2) \cos ax = \sqrt{\pi} e^{-\frac{1}{4}a^2} \quad (\text{C.108})$$

Proof. Assume that a function f is defined by

$$f(a, x) = \int_{-\infty}^{\infty} dx e^{-x^2} \cos ax.$$

By integration by parts, $f(a, x)$ becomes

$$\begin{aligned} f(a, x) &= \int_{-\infty}^{\infty} dx e^{-x^2} \cos ax = \int_{-\infty}^{\infty} dx e^{-x^2} \frac{d}{dx} \left[\frac{1}{a} \sin ax \right] \\ &= \frac{1}{a} e^{-x^2} \sin ax \Big|_{x=-\infty}^{\infty} - \int_{-\infty}^{\infty} dx (-2xe^{-x^2}) \frac{1}{a} \sin ax \\ &= \frac{2}{a} \int_{-\infty}^{\infty} dx xe^{-x^2} \sin ax. \end{aligned} \quad (\text{C.109})$$

Next, by differentiation with respect to a , one find that

$$\begin{aligned} \frac{d}{da} f(a, x) &= \frac{d}{da} \int_{-\infty}^{\infty} dx e^{-x^2} \cos ax = \int_{-\infty}^{\infty} dx e^{-x^2} \frac{\partial}{\partial a} \left[\cos ax \right] \\ &= - \int_{-\infty}^{\infty} dx xe^{-x^2} \sin ax \equiv -\frac{a}{2} f(a, x), \end{aligned}$$

which becomes the differential equation given by

$$\frac{d}{da} f(a, x) + \frac{a}{2} f(a, x) = 0. \quad (\text{C.110})$$

The 1st-order differential equation can be solved by

$$\frac{d}{da}f(a, x) = -\frac{a}{2}f(a, x) \Leftrightarrow \frac{df}{f} = -\frac{a}{2}da. \quad (\text{C.111})$$

By integration, both sides of Eq. (C.111) are calculated as follows

$$\begin{aligned} \text{RHS} &= \int \frac{df}{f} = \ln f, \\ \text{LHS} &= -\int \frac{a}{2}da = -\frac{1}{4}a^2 + C, \end{aligned}$$

where C is a integral constant. Therefore the solution of Eq. (C.110) is

$$f(a, x) = e^{-\frac{1}{4}a^2+C} \equiv C_1 e^{-\frac{1}{4}a^2},$$

where C_1 is another integral constant. By the initial definition of $f(a, x)$, one obtain

$$f(a, x) = \int_{-\infty}^{\infty} dx e^{-x^2} \cos ax = C_1 e^{-\frac{1}{4}a^2}.$$

By substituting a by 0,

$$f(0, x) = \int_{-\infty}^{\infty} dx e^{-x^2} = \sqrt{\pi} = C_1.$$

Thus a function $f(a, x)$ can be integrated to give

$$\int_{-\infty}^{\infty} dx e^{-x^2} \cos ax = \sqrt{\pi} e^{-\frac{1}{4}a^2}.$$

□

Integral C.13.14.

$$\int_0^{\infty} dx x^2 \exp(-ax^2) = \frac{1}{4} \sqrt{\frac{\pi}{a^3}}. \quad (\text{C.112})$$

Proof. By taking $x = at^2$ such that $dx = 2at dt$, the Gamma function in Eq. (C.90) is expressed as

$$p! = \int_0^{\infty} dx e^{-x} x^p = 2a \int_0^{\infty} dt t e^{-at^2} (at^2)^p = 2a^{p+1} \int_0^{\infty} dt e^{-at^2} t^{2p+1}. \quad (\text{C.113})$$

We find by taking $2p + 1 = 2$ that $p = 1/2$. Equation (C.113) can then be evaluated as

$$\left(\frac{1}{2}\right)! = 2a^{\frac{1}{2}+1} \int_0^{\infty} dt e^{-at^2} t^2.$$

From Eq. (C.99), the integral becomes

$$\int_0^{\infty} dt e^{-at^2} t^2 = \frac{\sqrt{\pi}}{4a^{\frac{3}{2}}} = \frac{1}{4} \sqrt{\frac{\pi}{a^3}}. \quad (\text{C.114})$$

□

Integral C.13.15.

$$\int_{-\infty}^{\infty} dx \frac{\sin^2 x}{x^2} = \pi. \quad (\text{C.115})$$

Proof. Since $\cos 2x = \cos^2 x - \sin^2 x = 1 - 2 \sin^2 x$, the integral can be expressed as [143]

$$\int_{-\infty}^{\infty} dx \frac{\sin^2 x}{x^2} = \frac{1}{2} \int_{-\infty}^{\infty} dx \frac{1 - \cos 2x}{x^2} = \operatorname{Re} \frac{1}{2} \int_{-\infty}^{\infty} dx \frac{1 - e^{i2x}}{x^2}. \quad (\text{C.116})$$

Here, the exponential term in the numerator of the integrand can be expanded by Taylor expansion as

$$e^{i2x} = 1 + i2x + \frac{(i2x)^2}{2!} + \frac{(i2x)^3}{3!} + \dots$$

To eliminate the pole of $(1 - e^{i2x})/x^2$, the integral in Eq. (C.116) needs to be modified as [143]

$$\text{Int} = \int_{-\infty}^{\infty} dx \frac{1 - \cos 2x}{x^2} = \operatorname{Re} \int_{-\infty}^{\infty} dx \frac{1 - e^{i2x} + i2x}{x^2}, \quad (\text{C.117})$$

which further makes

$$\text{Int} = \operatorname{Re} \int_{-\infty}^{\infty} dx \frac{1 + i2x - (1 + i2x + \dots)}{x^2} = -\operatorname{Re} \int_{-\infty}^{\infty} dx \frac{1}{x^2} \left[\frac{(i2x)^2}{2!} + \frac{(i2x)^3}{3!} + \dots \right]. \quad (\text{C.118})$$

We can see from this equation that Eq. (C.117) has no poles due to the term of $i2x$. The integral over the contour C illustrated in Fig. C.4(a) is then obtained according to Cuchy integral theorem [133]

$$\oint_C dz f(z) = \oint_C dz \frac{1 - e^{i2z} + i2z}{z^2} = 0, \quad (\text{C.119})$$

since the integrand $f(z)$ has no poles. Equation (C.119) becomes

$$\oint_C dz f(z) = \int_{C_1} dx \frac{1 - e^{i2x} + i2x}{x^2} + \int_{C_2} dz \frac{1 - e^{i2z} + i2z}{z^2} = 0, \quad (\text{C.120})$$

which yields

$$\begin{aligned} \int_{-R}^R dx \frac{1 - e^{i2x} + i2x}{x^2} &= - \int_{C_2} dz \frac{1 - e^{i2z} + i2z}{z^2} \\ &= -i2 \int_{C_2} dz \frac{1}{z} - \int_{C_2} dz \frac{1 - e^{i2z}}{z^2}. \end{aligned} \quad (\text{C.121})$$

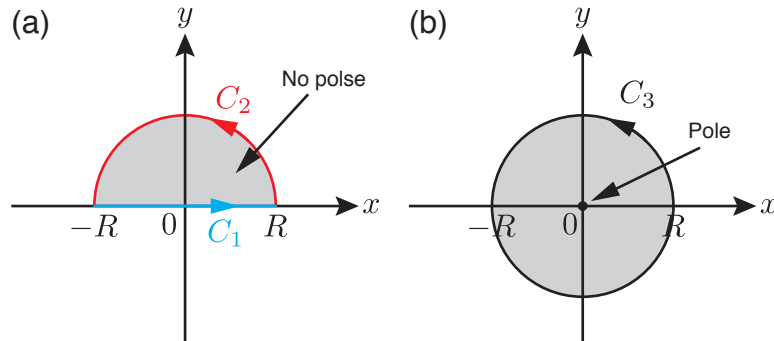


Figure C.4: (a) A contour $C = C_1 + C_2$ on the complex plane $z = x + iy$. (b) There is singular pole at $z = 0$ in a contour C_3 .

The first integral in Eq. (C.121) can be solved to obtain

$$\int_{C_2} dz \frac{1}{z} = \frac{1}{2} \oint_{C_3} dz \frac{1}{z}, \quad (\text{C.122})$$

where the integral over the contour C_3 is obtained according to Residue theorem. When a function f is analytic and f has a pole of the order of m at $z = a$, the residue can be obtained, giving [133]

$$\text{Res}[f(z) : a] = \frac{1}{(m-1)!} \lim_{z \rightarrow a} \left(\frac{d}{dz} \right)^{m-1} (z-a)^m f(z). \quad (\text{C.123})$$

According to Residue theorem, the Cauchy integral can be evaluated as [133]

$$\oint_C dz f(z) = 2\pi i \sum_{k=1}^n \text{Res}[f(z) : z_k]. \quad (\text{C.124})$$

Let us consider that a function $f(z) = p(z)/q(z)$ is analytic at $z = z_0$, $p(z_0) \neq 0$ and $q(z)$ has a simple pole at $z = z_0$. The Residue is then obtained, yielding [133]

$$\text{Res}[f(z) : z_0] = \frac{p(z_0)}{q'(z_0)} = \left. \frac{p(z)}{q'(z)} \right|_{z=z_0} = \lim_{z \rightarrow z_0} \frac{p(z)}{q'(z)}. \quad (\text{C.125})$$

From the Residue theorem, the right-hand side in Eq. (C.122) can be evaluated over the contour C_3 in Fig. C.4(b) as

$$\oint_{C_3} dz \frac{1}{z} = 2\pi i \text{Res} \left[\frac{1}{z} : z = 0 \right] = 2\pi i \times 1 = 2\pi i, \quad (\text{C.126})$$

which leads to

$$\int_{C_2} dz \frac{1}{z} = \frac{1}{2} 2\pi i = i\pi. \quad (\text{C.127})$$

We also find by taking $z = Re^{i\theta}$ that the second term in Eq. (C.121) tends to 0 as $R \rightarrow \infty$, yielding

$$\lim_{R \rightarrow \infty} \int_{C_2} dz \frac{1 - e^{i2z}}{z^2} = \lim_{R \rightarrow \infty} \int_{-R}^R dz \frac{1 - e^{i2Re^{i\theta}}}{R^2 e^{i2\theta}} = 0. \quad (\text{C.128})$$

By substituting Eqs. (C.127) and (C.128) into Eq. (C.121), we thus find that Eq. (C.117) can be evaluated as

$$\lim_{R \rightarrow \infty} \int_{-R}^R dx \frac{1 - e^{i2x} + i2x}{x^2} = -i2 \times i\pi - \int_{C_2} dz \frac{1 - e^{i2z}}{z^2} = 2\pi, \quad (\text{C.129})$$

which leads to the result

$$\int_{-\infty}^{\infty} dx \frac{\sin^2 x}{x^2} = \text{Re} \frac{1}{2} \int_{-\infty}^{\infty} dx \frac{1 - e^{i2x} + i2x}{x^2} = \pi. \quad (\text{C.130})$$

□

Bibliography

- [1] M. Yi and J. Ahn, *Convergence of Terahertz Sciences in Biomedical Systems*, pp. 163-179 (Springer, 2012).
- [2] Y.-S. Lee, *Principles of Terahertz Science and Technology* (Springer, 2009).
- [3] M. Tonouchi, "Cutting-edge terahertz technology," *Nat. Photonics* **1** (2), 97 (2007).
- [4] Y. R. Shen, "Reflections on the early days of THz spectroscopy," 40th International Conference on Infrared, Millimeter, and Terahertz waves (IRMMW-THz), pp. 1-2 (2015).
- [5] Y. R. Shen, *The principles of nonlinear optics* (Wiley-Interscience publication, 1984).
- [6] J. R. Morris and Y. R. Shen, "Far-infrared generation by picosecond pulses in electro-optical materials", *Opt. Commun.* **3**, 81, (1971).
- [7] R. W. Boyd, *Nonlinear Optics 3rd edition* (Academic Press, 2008).
- [8] C. Yim, J. Hong, Y. Parc, S. Jung, D. Han, J. Ryu, J. Park, H.-S. Kang, and I. S. Ko, "Note: Recent achievements at the 60-MeV Linac for sub-picosecond terahertz radiation at the Pohang Accelerator Laboratory," *Review of Scientific Instruments* **82**, 106104 (2011).
- [9] C. Yim, J. Ko, S. Jung, D. Han, C. Kim, J. Park, H.-S. Kang, and I. S. Ko, "Observation of coherent transition radiation in the prewave zone," *Phys. Rev. ST Accel. Beams* **15**, 030706 (2012).
- [10] X. Lu, X. -C. Zhang, "Investigation of ultra-broadband terahertz time-domain spectroscopy with terahertz wave gas photonics," *Front. Optoelectron.* **7**, 121 (2014).
- [11] E. Hecht, *Optics 4 th edition* (Addison Wesley, 2002).
- [12] J. D. Jackson, *Classical electrodynamics 3rd edition* (Wiley, New York, 1999).
- [13] D. Griffiths, *Introduction to Electrodynamics 2nd edition* (Prentice Hall, 1989).
- [14] http://en.wikipedia.org/wiki/Li%C3%A9nard%E2%80%93Wiechert_potential.
- [15] Z. Piao, M. Tani, and K. Sakai, "Carrier Dynamics and Terahertz Radiation in Photoconductive Antennas," *Jpn. J. Appl. Phys.* **39**, 96 (2000).
- [16] J. Faure, J. Van Tilborg, R. A. Kaindl and W . P . Leemans, "Modelling laser-based table-top THz sources: Optical rectification, propagation and electro-optic sampling," *Opt. Quant. Electron.* **36**, 681 (2004).
- [17] M. C. Beard, G. M. Turner, and C. A. Schmuttenmaer, "Terahertz Spectroscopy," *J. Phys. Chem. B* **2002**, 106, 7146-7159 (2002).
- [18] A. Nahata, A. S. Weling, and T. F. Heinz, "A wideband coherent terahertz spectroscopy system using optical rectification and electrooptic sampling," *Appl. Phys. Lett.* **69**, 2321 (1996).

- [19] A. Yariv and P. Yeh, *Optical Waves in Crystals Propagation and Control of Laser Radiation* (Wiley Classic Library, 2003).
- [20] D. J. Cook and R. M. Hochstrasser, “Intense terahertz pulses by four-wave rectification in air,” *Opt. Lett.* **25**, 1210–1212 (2000).
- [21] P. C. M. Planken, H.-K. Nienhuys, H. J. Bakker and T. Wenckebach, “Measurement and calculation of the orientation dependence of terahertz pulse detection in ZnTe,” *J. Opt. Soc. Am. B* **18**, 313 (2001).
- [22] B. E. A. Saleh and M. C. Teich, *Fundamentals of Photonics* edited by J.W. Goodman (Wiley, New York, 1991).
- [23] C. Kittel, *Introduction to solid state physics* (Wiley, Hoboken, NJ, 2005).
- [24] https://en.wikipedia.org/wiki/Miller_index.
- [25] Z. Jiang, F. G. Sun, and Q. Chen, “Electro-optic sampling near zero optical transmission point,” *Appl. Phys. Lett.* **74**, 1191 (1999).
- [26] X. Chen, S. He, Z. Shen, F. L. Zhao, K. Y. Xu, G. Wang, R. Wang, and N. Dai, “Influence of nonlinear effects in ZnTe on generation and detection of terahertz waves,” *J. Appl. Phys.* **105**, 023106 (2009).
- [27] G. R. Fowles, *Introduction to modern optics 2nd edition* (Dover publications, New York, 1975).
- [28] E. Parrott, J. Zeitler, L. Gladden, S. Taraskin, and S. Elliott, “Extracting accurate optical parameters from glasses using terahertz time-domain spectroscopy,” *J. Non-Cryst. Solids* **355**, 1824-1827 (2009).
- [29] W. Withayachumnankul, B. Ferguson, T. Rainsford *et al.*, “Material parameter extraction for terahertz time-domain spectroscopy using fixed-point iteration,” *Proc. SPIE* **5840**, 221–231 (2005).
- [30] W. Withayachumnankul, B. Ferguson, T. Rainsford *et al.*, “Simple material parameter estimation via terahertz time-domain spectroscopy,” *Electron. Lett.* **41** (14), 800 (2005).
- [31] D. Han, K. Lee, J. Lim, S. S. Hong, Y. K. Kim, and J. Ahn, “Terahertz lens made out of natural stone,” *Appl. Optics*, **52**, 8670, (2013).
- [32] T. D. Dorney, R. G. Baraniuk, and D. M. Mittleman, “Material parameter estimation with terahertz time-domain spectroscopy,” *J. Opt. Soc. A* **18**, 1562-1571 (2001).
- [33] P. U. Jepsen and B. M. Fischer, “Dynamic range in terahertz time-domain transmission and reflection spectroscopy,” *Opt. Lett.* **30**, 29-31 (2005).
- [34] W. L. Chan, J. Deibel, and D. M. Mittleman, “Imaging with terahertz radiation,” *Rep. Prog. Phys.* **70**, 1325–1379 (2007).
- [35] Y.-S. Jin, G.-J. Kim, and S.-G. Jeon, “Terahertz Dielectric Properties of Polymers,” *J. Kor. Phys. Soc.* **49** (2), 513–517 (2006).
- [36] J. Chen, Y. Chen, H. Zhao *et al.*, “Absorption coefficients of selected explosives and related compounds in the range of 0.1-2.8 THz,” *Opt. Express* **15** (19), 12060–12067 (2007).

- [37] Y. Kim, J. Ahn, B. G. Kim, and D.-S. Yee, “Terahertz Birefringence in Zinc Oxide,” *Jap. J. Appl. Phys.* **50**, 030203 (2011).
- [38] M. Naftaly and R.E. Miles, “Terahertz time-domain spectroscopy: A new tool for the study of glasses in the far infrared,” *J. Non-Crys. Sol.* **351**, 3341–3346 (2005).
- [39] D. S. Venables and C. A. Schmuttenmaer, “Far-infrared spectra and associated dynamics in acetonitrile–water mixtures measured with femtosecond THz pulse spectroscopy,” *J. Chem. Phys.* **108** (12), 4935–4944 (1998).
- [40] K. J. Tielrooij, N. Garcia-Araez, M. Bonn, H. J. Bakker, “Cooperativity in Ion Hydration,” *Science* **328**, 1006 (2010)
- [41] J.-H. Son, “Terahertz electromagnetic interactions with biological matter and their applications,” *J. Appl. Phys.* **105**, 102033 (2009).
- [42] S. Wietzke, C. Jansen, T. Jung *et al.*, “Terahertz time-domain spectroscopy as a tool to monitor the glass transition in polymers,” *Opt. Express* **17** (21), 19006–19014 (2009).
- [43] N. Krumbholz, T. Hochreina, N. Viewega *et al.*, “Monitoring polymeric compounding processes inline with THz time-domain spectroscopy,” *Polym. Test.* **28** (1), 30–35 (2009).
- [44] S. Gorenflo, “A Comprehensive Study of Macromolecules in Composites using Broadband Terahertz Spectroscopy,” Ph. D. Thesis, (University of Freiburg, 2006).
- [45] B. M. Fischer, “Broadband THz time-domain spectroscopy of biomolecules: a comprehensive study of the dielectric properties of biomaterials in the far-infrared,” Ph. D. Thesis, (University of Freiburg, 2005).
- [46] P. D. Cunningham, N. N. Valdes, F. A. Vallejo *et al.*, “Broadband terahertz characterization of the refractive index and absorption of some important polymeric and organic electro-optic materials,” *J. Appl. Phys.* **109**, 043505 (2011)
- [47] P. E. Powers, R.A. Alkuwari, J. W. Haus *et al.*, “Terahertz generation with tandem seeded optical parametric generators,” *Opt. Lett.* **30** (6), 640–642 (2005).
- [48] D. Grbovic and G. Karunasiri, “Fabrication of Bi-material MEMS detector arrays for THz imaging,” *Proc. SPIE* **7311**, 731108-1–731108-7 (2009).
- [49] B. Scherger, M. Scheller, C. Jansen *et al.*, “Terahertz lenses made by compression molding of micropowders,” *Appl. Opt.* **50** (15), 2256–2262 (2011).
- [50] M. Wichmann, A. S. Mondol, N. Kocic *et al.*, “Terahertz plastic compound lenses,” *Appl. Opt.* **52**(18) 4186–4191 (2013)
- [51] A. Siemion, A. Siemion, M. Makowski *et al.*, “Off-axis metallic diffractive lens for terahertz beams,” *Opt. Lett.* **36**(11), 1960–1962 (2011).
- [52] A. Siemion, A. Siemion, M. Makowski *et al.*, “Diffractive paper lens for terahertz optics,” *Opt. Lett.* **37** (20), 4320–4322 (2012).
- [53] B. Scherger, C. Jördens, and M. Koch, “Variable-focus terahertz lens,” *Opt. Exp.* **19** (5), 4528–4535 (2011).

- [54] M. Wichmann, B. Scherger, S. Schumann *et al*, “Terahertz Brewster lenses,” *Opt. Exp.* **19** (25), 25151–25160 (2011).
- [55] M. Janek, I. Bugár, D. Lorenc *et al*, “Terahertz time-domain spectroscopy of selected layered silicates,” *Clays and Clay Minerals* **57** (4), 416–424 (2009).
- [56] M. Mizuno, K. Fukunaga, S. Saito, and I. Hosako, “Analysis of calcium carbonate for differentiating between pigments using terahertz spectroscopy,” *J. Euro. Opt. Soc.-Rapid Publications* **4**, 09044 (2009).
- [57] M. Schwerdtfeger, E. Castro-Camus, K. Krügener *et al*, “Beating the wavelength limit: three-dimensional imaging of buried subwavelength fractures in sculpture and construction materials by terahertz time-domain reflection spectroscopy,” *Appl. Opt.* **52**(3) 375–380 (2013).
- [58] A. Dreyhaupt, S. Winner, T. Dekorsy, and M. Helm, “High-intensity terahertz radiation from a microstructured large-area photoconductor,” *Appl. Phys. Lett.* **86**, 121114 (2005).
- [59] G. Gallot and D. Grischkowsky, “Electro-optic detection of terahertz radiation,” *J. Opt. Soc. Am. B* **16** (8), 1204–1212 (1999).
- [60] Y. Kim, D.-S. Yee, M. Yi, and J. Ahn, “High-speed High-resolution Terahertz Spectrometers,” *J. Kor. Phys. Soc.* **56** (1), 255–261 (2010).
- [61] B. B. Hu and M. C. Nuss, “Imaging with terahertz waves,” *Opt. Lett.* **20** (16), 1716–1718 (1995).
- [62] A.C. Tennissen, *Nature of earth materials* (Prentice Hall, 1974).
- [63] B.K. Johnson, *Optics and optical instruments: An introduction with special reference to practical applications* (Dover publications, New York, 1960).
- [64] F. A. Jenkins and H. E. White, *Fundamentals of optics* (Tata McGraw-Hill Education, 1957).
- [65] D. Grischkowsky, S. Keiding, M. Vanexter, and C. Fattinger, “Far-infrared time-domain spectroscopy with terahertz beams of dielectrics and semiconductors,” *J. Opt. Soc. Am. B*, **7**, 2006, (1990).
- [66] B. Ferguson and X. C. Zhang, “Materials for terahertz science and technology,” *Nat. Mater.*, **1**, 26, (2002).
- [67] Y. H. K. G.-S. Park, H. Han, J. K. Han, J. Ahn, J.-H. Son, W.-Y. Park, and Y. U. Jeong, *Convergence of terahertz sciences in biomedical systems* (New York: Springer, 2012).
- [68] J. Chen, Y. Q. Chen, H. W. Zhao, G. J. Bastiaans, and X. C. Zhang, “Absorption coefficients of selected explosives and related compounds in the range of 0.1-2.8 THz,” *Opt. Express*, **15**, 12060, (2007).
- [69] H. T. Chen, W. J. Padilla, J. M. O. Zide, A. C. Gossard, A. J. Taylor, and R. D. Averitt, “Active terahertz metamaterial devices,” *Nature*, **444**, 597, (2006).
- [70] M. Naftaly and R. E. Miles, “Terahertz time-domain spectroscopy of silicate glasses and the relationship to material properties,” *J. Appl. Phys.* **102**, 043517, (2007).

- [71] M. Janek, I. Bugár, D. Lorenc, V. Szöcs, D. Velič, and D. Chorvát, “Terahertz time-domain spectroscopy of selected layered silicates,” *Clays and Clay Miner.*, **57**, 416, (2009).
- [72] G. Acbas, K. A. Niessen, E. H. Snell, and A. G. Markelz, “Optical measurements of long-range protein vibrations,” *Nat. Commun.*, **5**, 3076, (2014).
- [73] J. Kröll, J. Darmo, and K. Unterrainer, “Terahertz optical activity of sucrose single-crystals,” *Vib. spectrosc.*, **43**, 324, (2007).
- [74] O. Ostroverkhova, D. Cooke, F. Hegmann, R. Tykwinski, S. Parkin, and J. Anthony, “Anisotropy of transient photoconductivity in functionalized pentacene single crystals,” *Appl. Phys. Lett.*, **89**, 192113, (2006).
- [75] D. J. Aschaffenburg, M. R. C. Williams, D. Talbayev, D. F. Santavicca, D. E. Prober, and C. A. Schmuttenmaer, “Efficient measurement of broadband terahertz optical activity,” *Appl. Phys. Lett.*, **100**, 241114, (2012).
- [76] A. M. Shuvaev, G. V. Astakhov, A. Pimenov, C. Brune, H. Buhmann, and L. W. Molenkamp, “Giant magneto-optical Faraday effect in HgTe thin films in the terahertz spectral range,” *Phys. Rev. Lett.*, **106**, 107404, (2011).
- [77] H. Kim, M. Yi, X. Y. Wang, S. W. Cheong, and J. Ahn, “Ultrafast terahertz transmission ellipsometry of YMn₂O₅ electromagnons,” *Appl. Phys. Lett.*, **101**, 242911, (2012).
- [78] G. Xuejiao, X. Wei, and S. Jingling, “THz Spectroscopy and Polarization of Jade,” *Proceedings of SPIE*, **7854**, 78542H, (2010).
- [79] J. W. Anthony, *Handbook of mineralogy* (Ariz.: Mineral Data Pub., 1990).
- [80] M. D. Welch and W. G. Marshall, “High-pressure behavior of clinocllore,” *Am. Mineral.*, **86**, 1380, (2001).
- [81] A. C. Rule and S. W. Bailey, “Refinement of the crystal-structure of a monoclinic ferroan clinocllore,” *Clays and Clay Miner.*, **35**, 129, (1987).
- [82] C. K. Kohut and C. J. Warren, “Chlorites,” in *Soil Mineralogy with Environmental Applications* edited by J. B. Dizon and D. G. Schulze, (USA: Soil Science Society of America, 2002).
- [83] G. E. Spinnler, P. G. Self, S. Iijima, and P. R. Buseck, “Stacking disorder in clinocllore chlorite,” *Am. Mineral.*, **69**, 252, (1984).
- [84] S. Kojima, N. Tsumura, M. W. Takeda, and S. Nishizawa, “Far-infrared phonon-polariton dispersion probed by terahertz time-domain spectroscopy,” *Phys. Rev. B*, **67**, 035102, (2003).
- [85] N. B. Colthup, L. H. Daly, and S. E. Wiberley, *Introduction to infrared and Raman spectroscopy 3rd edition* (Boston: Academic Press, 1990).
- [86] F. A. Cotton, *Chemical applications of group theory 3rd edition* (New York: Wiley, 1990).
- [87] W. G. Fateley, *Infrared and Raman selection rules for molecular and lattice vibrations: the correlation method* (New York,: Wiley-Interscience, 1972).

- [88] E. R. Brown, J. E. Bjarnason, A. M. Fedor, and T. M. Korter, “On the strong and narrow absorption signature in lactose at 0.53 THz,” *Appl. Phys. Lett.*, **90**, 061908, (2007).
- [89] A. M. Hofmeister, E. Keppel, and A. K. Speck, “Absorption and reflection infrared spectra of MgO and other diatomic compounds,” *Mon. Not. R. Astron. Soc.*, **345**, 16, (2003).
- [90] A. B. Kuzmenko, E. A. Tishchenko, and V. G. Orlov, “Transverse optic modes in monoclinic α - Bi_2O_3 ,” *J. Phys.: Condens. Mat.*, **8**, 6199, (1996).
- [91] T. Moller, P. Becker, L. Bohaty, J. Hemberger, and M. Gruninger, “Infrared-active phonon modes in monoclinic multiferroic MnWO_4 ,” *Phys. Rev. B*, **90**, 155105, (2014).
- [92] J. R. Aronson, A. G. Emslie, E. V. Miseso, E. M. Smith, and P. F. Strong, “Optical-constants of monoclinic anisotropic crystals - gypsum,” *Appl. Optics*, **22**, 4093, (1983).
- [93] S. A. Fitzgerald and A. J. Sievers, “Lattice phonon modes in solid C-60 studied by far-Infrared spectroscopy - Comment,” *Phys. Rev. Lett.*, **70**, 3175, (1993).
- [94] C. Koike, H. Hasegawa, and T. Hattori, “Mid-infrared and far-infrared extinction coefficients of hydrous silicate minerals,” *Astrophys. Space Sci.*, **88**, 89, (1982).
- [95] D. R. Collins, W. G. Stirling, C. R. A. Catlow, and G. Rowbotham, “Determination of acoustic phonon-dispersion curves in layer silicates by inelastic neutron-scattering and computer-simulation techniques,” *Phys. Chem. Miner.*, **19**, 520, (1993).
- [96] K. R. Rao, S. L. Chaplot, N. Choudhury, S. Ghose, and D. L. Price, “Phonon density of states and specific-heat of forsterite, Mg_2SiO_4 ,” *Science*, **236**, 64, (1987).
- [97] K. R. Rao, S. L. Chaplot, N. Choudhury, S. Ghose, J. M. Hastings, L. M. Corliss, et al., “Lattice-dynamics and inelastic neutron-scattering from forsterite, Mg_2SiO_4 : phonon-dispersion relation, density of states and specific-heat,” *Phys. Chem. Miner.*, **16**, 83, (1988).
- [98] F. Gervais and B. Piriou, “Temperature-dependence of transverse-optic and longitudinal-optic modes in TiO_2 (rutile),” *Phys. Rev. B*, **10**, 1642, (1974).
- [99] M. Schubert, T. Tiwald, and C. Herzinger, “Infrared dielectric anisotropy and phonon modes of sapphire,” *Phys. Rev. B*, **61**, 8187, (2000).
- [100] D. W. Berreman and F. C. Unterwald, “Adjusting poles and zeros of dielectric dispersion to fit reststrahlen of PrCl_3 , and LaCl_3 ,” *Phys. Rev.*, **174**, 791, (1968).
- [101] A. S. Barker, “Transverse and longitudinal optic mode study in MgF_2 , and ZnF_2 ,” *Phys. Rev.*, **136**, A1290, (1964).
- [102] T. Kurosawa, “Polarization waves in solids,” *J. Phys. Soc. Jpn.*, **16**, 1298, (1961).
- [103] R. P. Lowndes, “Influence of Lattice Anharmonicity on the Longitudinal Optic Modes of Cubic Ionic Solids,” *Phys. Rev. B*, **1**, 2754, (1970).
- [104] X.-L. Yang and S.-W. Xie. “Expression of third-order effective nonlinear susceptibility for third-harmonic generation in crystals,” *Appl. Optics* **34**, 6130, (1995).

- [105] I. Brener, D. Dykaar, A. Frommer, L. N. Pfeiffer, J. Lopata, J. Wynn, K. West, and M. C. Nuss, “Terahertz emission from electric field singularities in biased semiconductors,” *Opt. Lett.* **21**, 1924-1926 (1996).
- [106] M. Tonouchi, M. Yamashita, and M. Hangyo, “Terahertz radiation imaging of supercurrent distribution in vortex-penetrated $\text{YBa}_2\text{Cu}_3\text{O}_{7-\delta}$ thin film strips,” *J. Appl. Phys.* **87**, 7366-7375 (2000).
- [107] M. Yi, K. Lee, J.-D. Song, and J. Ahn, “Terahertz phase microscopy in the sub-wavelength regime,” *Appl. Phys. Lett.* **100**, 161110 (2012).
- [108] J. Knab, A. Adam, M. Nagel, E. Shaner, M. Seo, D. Kim, and P. Planken, “Terahertz near-field vectorial imaging of subwavelength apertures and aperture arrays,” *Opt. Express* **17**, 15072-15086 (2009).
- [109] J. Knab, A. Adam, E. Shaner, H. Starmans, and P. Planken, “Terahertz near-field spectroscopy of filled subwavelength sized apertures in thin metal films,” *Opt. Express* **21**, 1101-1112 (2013).
- [110] H.-R. Park, K. J. Ahn, S. Han, Y.-M. Bahk, N. Park, and D.-S. Kim, “Colossal Absorption of Molecules Inside Single Terahertz Nanoantennas,” *Nano Lett.* **13**, 1782-1786 (2013).
- [111] M. Seo, H. Park, S. Koo, D. Park, J. Kang, O. Suwal, S. Choi, P. Planken, G. Park, and N. Park, “Terahertz field enhancement by a metallic nano slit operating beyond the skin-depth limit,” *Nat. Photonics* **3**, 152-156 (2009).
- [112] J.-H. Kang, D. Kim, and Q.-H. Park, “Local capacitor model for plasmonic electric field enhancement,” *Phys. Rev. Lett.* **102**, 093906 (2009).
- [113] C. Genet and T. Ebbesen, “Light in tiny holes,” *Nature* **445**, 39-46 (2007).
- [114] E. H. Khoo, E. P. Li, and K. B. Crozier, “Plasmonic wave plate based on subwavelength nanoslits,” *Opt. Lett.* **36**, 2498-2500 (2011).
- [115] P. F. Chimento, N. V. Kuzmin, J. Bosman, P. F. Alkemade, G. W. t Hooft, and E. R. Eliel, “A subwavelength slit as a quarter-wave retarder,” *Opt. Express* **19**, 24219-24227 (2011).
- [116] H. A. Bethe, “Theory of diffraction by small holes,” *Phys. Rev.* **66**, 163 (1944).
- [117] C. J. Bouwkamp, “On Bethe’s theory of diffraction by small holes,” *Philips Res. Rep* **5**, 321-332 (1950).
- [118] F. J. García-Vidal, H. J. Lezec, T. W. Ebbesen, and L. Martín-Moreno, “Multiple paths to enhance optical transmission through a single subwavelength slit,” *Phys. Rev. Lett.* **90**, 213901 (2003).
- [119] C. Wang, C. Du, and X. Luo, “Refining the model of light diffraction from a subwavelength slit surrounded by grooves on a metallic film,” *Physical Review B* **74**, 245403 (2006).
- [120] Y. Takakura, “Optical resonance in a narrow slit in a thick metallic screen,” *Phys. Rev. Lett.* **86**, 5601 (2001).
- [121] F. Yang and J. R. Sambles, “Resonant transmission of microwaves through a narrow metallic slit,” *Phys. Rev. Lett.* **89**, 063901 (2002).

- [122] K. Lee, M. Yi, S. E. Park, and J. Ahn, “Phase-shift anomaly caused by subwavelength-scale metal slit or aperture diffraction,” *Opt. Lett.* **38**, 166-168 (2013).
- [123] K. Lee, J. Lim, and J. Ahn, “Young’s experiment with a double slit of sub-wavelength dimensions,” *Opt. Express* **21**, 18805-18811 (2013).
- [124] A. Roggenbuck, H. Schmitz, A. Deninger, I. Cámara Mayorga, J. Hemberger, R. Güsten, and M. Grüninger, “Coherent broadband continuous-wave terahertz spectroscopy on solid-state samples,” *New J. Phys.* **12**, 043017 (2010).
- [125] I. Pupeza, R. Wilk, and M. Koch, “Highly accurate optical material parameter determination with THz time-domain spectroscopy,” *Opt. Express* **15**, 4335-4350 (2007).
- [126] Y. Kim, D.-S. Yee, M. Yi, and J. Ahn, “High-speed high-resolution terahertz spectrometers,” *J. Korean Phys. Soc* **56**, 255-261 (2010).
- [127] J. A Stratton, *Electromagnetic Theory* (Wiley-IEEE Press, 2007).
- [128] K. Lee, “Fourier optical phenomena and applications using ultra broadband terahertz waves,” Ph. D. Thesis, (Korea Advanced Institute of Science and Technology, 2013).
- [129] <https://en.wikipedia.org/wiki/Flux>.
- [130] C. Winnewisser, P. Uhd Jepsen, M. Schall, V. Schyja, and H. Helm, “Electro-optic detection of THz radiation in LiTaO₃, LiNbO₃ and ZnTe,” *Appl. Phys. Lett.* **70**, 3069 (1997).
- [131] A. Garzarella, S. B. Qadri, Terence J. Wieting, and Dong Ho Wu, “The effects of photorefraction on electro-optic field sensors,” *J. Appl. Phys.* **97**, 113108, (2005).
- [132] A. Garzarella, S. B. Qadri, Terence J. Wieting, Dong Ho Wu, and R. J. Hinton, “Dielectrically induced sensitivity enhancements in electro-optic field sensors,” *Opt. Lett.* **32**, 964, (2007).
- [133] M. L. Boas, *Mathematical methods in the physical sciences 2nd edition*, (John Wiley & Sons, 1983).
- [134] A. Rice, Y. Jin, X. F. Ma, and X.-C. Zhang, “Terahertz optical rectification from ⟨110⟩ zinc-blende crystals”, *Appl. Phys. Lett.* **64**, 1324, (1993).
- [135] Q. Chen, M. Tani, Z. Jiang, and X.-C. Zhang, “Electro-optic transceivers for terahertz-wave applications,” *J. Opt. Soc. Am. B*, **18**, 823, (2001).
- [136] X.-C. Zhang, Y. Jin, and X. F. Ma, “Coherent measurement of THz optical rectification from electro-optic crystals,” *Appl. Phys. Lett.* **23**, 2764, (1992).
- [137] C. A. Valagiannopoulos, N. L. Tsitsas, A. Lakhtakia, and A. Burger, “Pockels cover for switchable control of the reflection from a grounded, isotropic, lossy dielectric slab,” *J. Appl. Phys.* **117**, 083105, (2015).
- [138] S. Casalbuoni, H. Schlarb, B. Schmidt, P. Schmüser, B. Steffen, and A. Winter, “Numerical studies on the electro-optic detection of femtosecond electron bunches,” *Phys. Rev. ST Accel. Beams* **11**, 072802 (2008).
- [139] J. H. Scofield, “A Frequency-Domain Description of a Lock-in Amplifier,” *Am. J. Phys.* **62**, 129 (1994).

- [140] “Construction of a femtosecond mode-locked laser,” Report, University of Pisa, <http://www.df.unipi.it/~fisapp/Gruppi/Metrologia/spiegazioni/boris.pdf>.
- [141] <http://mathworld.wolfram.com/RotationMatrix.html>.
- [142] https://en.wikipedia.org/wiki/Euler_angles.
- [143] J. Bak and D. J. Newman, *Complex analysis* (Springer-Verlag, New York, 1997).

Acknowledgments in Korean

돌아가신 어머니께서는 제가 다른 사람들보다 1년에서 2년 정도 성숙이 느리다는 말을 평소 때 많이 하셨습니다. 그래서 그런지 8년 만의 졸업이 저한테 있어서 많이 느리다는 느낌이 별로 들지 않는 것은 다행이라고 여겨집니다. 이런 저를 뒤에서 지원해주고 학위가 무사히 마쳐질 때까지 기다려준 아버지, 동생 아람이, 그리고 하늘에 계신 어머니께 고맙다는 말을 먼저 전하고 싶습니다.

논문을 완성하기까지 많은 분으로부터 도움을 받았습니다. 먼저, 많이 부족한 저를 8년 동안 이 자리까지 이끌어주시고 무사히 학위과정이 마무리될 수 있도록 지도해주신 안재욱 교수님께 감사와 존경을 표현하고 싶습니다. 또한, 바쁘신 와중에 논문 심사를 맡아주시고 관심을 보여주신 공홍진 교수님, 박재현 박사님, 강명수 교수님, 양찬호 교수님께 감사의 인사를 드립니다. 제가 대학원 과정 중 2년 동안 포항에 있었을 때, 저를 지도해주신 박재현 박사님과 정성훈 박사님께 이 자리를 빌려 감사의 말씀을 다시 한 번 더 전하고 싶습니다. 연구실에서 같이 토론해주고 연구를 도와준 연구실 선배들과 후배들에게도 고맙다는 이야기를 전하고 싶습니다. 연구실 선배로 뿐만 아니라 상담자로서 저를 도와준 민우 형과 영찬이 형, 종석이 형, 그리고 강희 덕분에 연구를 무사히 마칠 수 있었다고 생각합니다. 그리고 같이 저와 함께 연구에 대해 생각해주고 토론해준 한결이, 효섭이, 우준이, 한래, 경태, 윤희, 민혁이한테 고맙다는 말을 하고 싶고, 모두 무사히 박사과정이 마칠기를 진심으로 응원하도록 하겠습니다. 더불어 본 학위논문의 영어 교정을 맡아준 장보선 박사님께도 고맙다는 말을 전하고 싶습니다.

논문심사를 준비할 때에도 제 주변에 있는 많은 분께 도움을 받았습니다. 먼저, 제 발표 자료를 봐준 연주, 경승이 형, 태선이 형, 정한이, 윤정이 누나, 채윤이한테 너무나도 고맙다는 말을 전하고 싶습니다. 특히 예비심사를 보기 며칠 전에 새벽까지 발표자료에 대해 조언을 해준 연주랑 태선이 형에게는 정말 다시 한 번 더 고맙다는 이야기를 하고 싶습니다.

저는 2008년 가을에 카이스트로 입학한 이후 8년 동안 여러 많은 사람과 인연을 맺었습니다. 대학원 입학 후 잘 적응이 안 되었던 대학원 생활은 경승이 형, 태선이 형, 연주, 세현이 덕분에 잘 버틸 수 있었습니다. 이들 모두가 박사과정 내내 저의 든든한 버팀목이 되어주었다는 점 이 자리를 빌어서 말씀드립니다. 또한, 룸메이트였던 경승이 형과 태선이 형한테는 정말 여러 많은 도움을 받았고, 너무나도 고맙습니다. 제가 포항가속기연구소로 2년 동안 파견가 있을 때, 타지에서 저의 든든한 버팀목이 되어준 황호, 세갑이, 경재 형, 준호에게도 고맙다는 말을 하고 싶습니다. 포항에서 대전으로 다시 돌아온 이후 시작한 “수달”이라는 수영 동호회 활동으로, 무한히 반복되는 연구 생활 속에서 하나의 큰 빛이 되어 제가 운동도 하고 연구에 더욱더 집중할 수 있도록 해준 분들에게도 이 자리를 빌려서 고맙다는 말을 하고 싶습니다. 우선 친누나와 같이 저를 챙겨준 윤정이 누나, 제 눈높이 기준으로 이야기해주면서도 잘 챙겨준 성현이, 수영할 때 항상 저를 끝까지 수영하도록 만들어준 기환이, 보선이, 수현이, 영근이, 태효, 만수, 준홍이, 민트, 철규, 혁진이, 용기 형, 호, 선동이, 상근이에게 고맙다는 말을 전하고 싶습니다. 특히, 두 번의 바다 수영대회 때마다 항상 뒤에서 같이 가준 민준이 형에게도 감사를 전합니다. 수달 분들 이외에도 저를 진심으로 걱정해주고 힘내도록 북돋워 주었던 주달방 소속 민준이와 성은이에게도 고맙다는 말을 꼭 전하고 싶습니다.

대학원에 들어오기 전부터 알고 지냈던 제 오래된 분들에게도 고맙다는 말을 전하고 싶습니다. 오랜 대학원 생활 속에서도 매년 한 번씩 계곡이나 바다로 같이 놀러 가서 잠시나마 연구실 생활을 잊게 해준 한대회 소속 형철이 부부와 남선이 부부에게 감사의 인사를 드립니다. 그리고 고등학교 때부터 알고 지내서인지 오랜간만에 만나도 옛그제 만난 것처럼 느껴지는 길백이와 원석이, 태환이에게도 고맙다는 말을 전하고 싶습니다. 같이 대학교 생활은 못 했지만 저와 이야기가 잘 통했던 후배 수현이와 홍신대법장 소속 홍철이형, 법현이, 찬섭이에게도 대학원 생활하면서 힘들 때 저의 고충을 잘 들어주고 같이 웃고 울어주었던 이분들에게도 고맙다는 이야기 전하고 싶습니다.

Curriculum Vitae in Korean

이 름: 한 대 훈
생 년 월 일: 1984년 1월 26일
주 소: 대전광역시 유성구 대학로 291 한국과학기술원 자연과학동 물리학과 3317호
전 자 주 소: handaemilk@kaist.ac.kr

학 력

1999. 3. – 2002. 2. 분당중앙고등학교
2002. 3. – 2008. 2. 동국대학교 물리학과 학사 (B.S.)
2008. 9. – 2016. 8. 한국과학기술원 물리학과 박사 (Ph.D.)

경 력

2009. 9. – 2009. 12. 한국과학기술원 물리학과 일반 물리학 2 조교
2012. 2. – 2012. 5. 한국과학기술원 물리학과 응용 파동 광학 조교
2013. 3. – 2014. 6. 한국과학기술원 물리학과 응용 물리학 실험 조교

연구 업 적

1. **Daehoon Han**, Heejae Jeong, Yunheung Song, Jai Seok Ahn, and Jaewook Ahn, “Lattice vibrations of natural seraphinite gemstone probed by terahertz time-domain spectroscopy,” *IEEE T. THz. Sci. Tec.* **5**, 1021-1027 (2015).
2. Sang-Gil Park, Kanghee Lee, **Daehoon Han**, Jaewook Ahn, and Ki-Hun Jeong, “Subwavelength silicon through-hole arrays as an all-dielectric broadband terahertz gradient index metamaterial,” *Appl. Phys. Lett.* **105**, 091101 (2014).
3. **Daehoon Han**, Kanghee Lee, Jongseok Lim, Sei Sun Hong, Young Kie Kim, and Jaewook Ahn, “Terahertz lens made out of natural stone,” *Appl. Opt.* **52**, 8670-8675 (2013).
4. Dong-Yeun Koh, Hyery Kang, Juwoon Park, Seonghoon Jung, **Daehoon Han**, Jaehun Park, and Huen Lee, “Guest molecule dynamics and guest-specific degassing phenomenon of binary gas hydrate investigated by terahertz time-domain spectroscopy,” *Rsc. Adv.* **3**, 8857-8863 (2013).
5. Changmook Yim, Junho Ko, Seonghoon Jung, **Daehoon Han**, Changbum Kim, Jaehun Park, Heung-Sik Kang, and In Soo Ko, “Observation of coherent transition radiation in the prewave zone,” *Phys. Rev. Spec. Top.-Ac.* **15**, 030706 (2012).

6. Changmook Yim, Juho Hong, Yongwoon Parc, Seonghoon Jung, **Daehoon Han**³, Jaehyun Ryu, Jaehun Park, Heung-Sik Kang, and In Soo Ko, “Note: Recent achievements at the 60-MeV Linac for sub-picosecond terahertz radiation at the Pohang Accelerator Laboratory,” *Rev. Sci. Instrum.* **82**, 106104 (2011).
7. Changmook Yim, Junho Ko, In Soo Ko, Seonghoon Jung, Jaehun Park, Yong-Jung Park, Heung-Sik Kang, and **Daehoon Han**⁴, “Design Study and High-power Beam Test of the 60-MeV Linac for Femtosecond THz Radiation at the PAL,” *J. Korean. Phys. Soc.* **59**, 2702-2708 (2011).

학 회 활 동

1. **Daehoon Han**, Hanlae Jo, Yunheung Song, Minhyuk Kim, Kanghee Lee, and Jaewook Ahn, “Terahertz time-domain spectroscopy of the polarization response of the resonant material confined in a sub-wavelength slit,” *The 10th Asia-Pacific Laser Symposium (APLS 2016)*, Thu-P-70, 서귀포 KAL 호텔, 제주도, 5/10-14, (2016).
2. **Daehoon Han**, Heejae Jeong, Yunheung Song, Jai Seok Ahn, and Jaewook Ahn, “Strong optical phonon mode of natural seraphinite probed by terahertz time-domain spectroscopy”, *40 th International Conference on Infrared, Millimeter, and Terahertz waves (IRMMW-THz)*, MS-15, The Chinese University of Hong Kong, China, 8/23-28, (2015).
3. **Daehoon Han**, Sungmin Kwon, Hanlae Jo, Yunheung Song, Kanghee Lee, and Jaewook Ahn, “Terahertz polarization spectroscopy of resonant materials confined in sub-wavelength metal slits”, *제14회 첨단 레이저 및 레이저 응용 워크샵 (ALTA 2015)*, Fri-P-97, 서귀포 KAL 호텔, 제주도, 5/6-9, (2015) (Poster Award).
4. **한대훈**, 정희재, 우창수, 양찬호, 안재욱, 안재석, “테라헤르츠 시분해 분광기술로 측정된 아염소산염의 포논-플라리톤 공명모드”, *한국광학회 제 26회 정기총회 및 2015년도 동계학술발표회*, T1H-I2, 대전컨벤션센터, 1/28-30, (2015).
5. **한대훈**, 권성민, 조한래, 이강희, 안재욱, “파장보다 작은 금속 슬릿에 속박된 공명 물질의 테라헤르츠 편광 분광 실험”, *한국광학회 제 26회 정기총회 및 2015년도 동계학술발표회*, T2H-I2, 대전컨벤션센터, 1/28-30, (2015).
6. **Daehoon Han**, Hanlae Jo, and Jaewook Ahn, “Terahertz spectroscopy of natural stone materials”, *39 th International Conference on Infrared, Millimeter, and Terahertz waves (IRMMW-THz)*, T5-P14.8, The University of Arizona, USA, 9/14-19, (2014).
7. Heejae Cheong, **Daehoon Han**, Jaewook Ahn, “Terahertz optical properties of gemstones”, *한국광학회 2014년도 하계학술 발표회*, WP-I1, 제주 국제 컨벤션 센터, 제주도, 8/25-27, (2014).
8. Hanlae Jo, **Daehoon Han**, Kanghee Lee, and Jaewook Ahn, “Terahertz polarization dependent spectroscopy in a subwavelength metal slit”, *제13회 첨단 레이저 및 레이저 응용 워크샵 (ALTA 2014)*, Fri-P-26, 서귀포 KAL 호텔, 제주도, 5/7-10, (2014).
9. **Daehoon Han**, Hanlae Jo, and Jaewook Ahn, “Terahertz Conoscopic Spectroscopy of Birefringent Materials”, *제13회 첨단 레이저 및 레이저 응용 워크샵 (ALTA 2014)*, Fri-P-24, 서귀포 KAL 호텔, 제주도, 5/7-10, (2014).

³The author name is written by “Daehun Han” in the paper.

⁴The author name is written by “Daehun Han” in the paper.

10. Hanlae Jo, Kanghee Lee, **Daehoon Han**, and Jaewook Ahn, "Terahertz polarization spectroscopy of an organic material in a sub-wavelength-scale metal slit", 한국물리학회 봄학술논문발표회 및 임시총회, IG-09, 대전 컨벤션 센터, 4/23-25, (2014).
11. **Daehoon Han**, Hanlae Jo, Jongseok Lim, and Jaewook Ahn, "Terahertz conoscopic detection of interference figure of R-cut sapphire", 2014 봄 학술논문발표회 및 제 90회 정기총회, P1-I007, 대전 컨벤션 센터, 4/23-25, (2014).
12. 조한래, 이강희, **한대훈**, 안재욱, "Sub-wavelength terahertz spectroscopy of organic materials in micrometer-size metal slits", 한국물리학회 가을학술논문발표회 및 임시총회, P3-I039, 창원 컨벤션 센터, 10/30-11/1, (2013).
13. **Daehoon Han**, Kanghee Lee, Jongseok Lim, and Jaewook Ahn, "Terahertz optical properties of Minerals and Mineral compounds", 한국물리학회 봄학술논문발표회 및 임시총회, P3-I012, 대전 컨벤션 센터, 4/25, (2013).
14. **Daehoon Han**, Jongseok Lim, Jaehun Park, and Jaewook Ahn, "Terahertz 2D Imaging as a tool for Paleontology", 6th BK21 Young Physicists Workshop, KAIST, 12/27-28, (2012) (Poster Award).
15. **Daehoon Han**, Jongseok Lim, and Jaewook Ahn, "Terahertz two-dimensional imaging as a tool for Paleontology", The 3th World Class Institute Symposium, 서울 KIST, 11/14-16, (2012).
16. Jaehun Park, Seonghoon Jung, Hyun Hwi Lee, and **Daehoon Han**, "Study of ZnO nanorod and nanotube by Terahertz spectroscopy", 37 th International Conference on Infrared, Millimeter, and Terahertz Waves (IRMMW-THz), Mon-Pos-30, University of Wollongong, Australia, 9/13-28, (2012).
17. **Daehoon Han**, Seonghoon Jung, Jaewook Ahn, and a Jaehun Park, "Low temperature study of nucleotide in ice using THz-TDS", 제11회 첨단 레이저 및 레이저 응용 워크숍 (ALTA 2012), Fri-P, 서귀포 KAL 호텔, 제주도, 5/17-19 (2012).
18. **Daehoon Han**, Seonghoon Jung, Jaewook Ahn, and a Jaehun Park, "Low temperature study of Sodium chloride ice in THz", 3th THz-Bio Workshop, 서울대학교, 2/7-8, (2012).
19. **Daehoon Han**, Seonghoon Jung, Jaewook Ahn, and a Jaehun Park, "The low temperature study on the structure and dynamics of ion or DNA in aqueous solution", 5th BK21 Young Physicists Workshop, 포항공과대학교, 1/12-13, (2012) (Poster Award).
20. **Daehoon Han**, Seonghoon Jung, Jaewook Ahn, and Jaehun Park, "Low temperature study of Ice Ih and Sodium chloride in THz range", 한국물리학회 가을학술논문발표회 및 임시총회, P1-I028, 부산 벡스코, 10/19-21, (2011).
21. **Daehoon Han**, Seonghoon Jung, Jaewook Ahn, and Jaehun Park, "Single shot electro optic detection of THz with Chirped pulse", 제10회 첨단 레이저 및 레이저 응용 워크숍 (ALTA 2011), Thu-P-64, 서귀포 KAL 호텔, 제주도, 5/11-14 (2011).
22. Minwoo Yi, **Daehoon Han**, Yong-Je Choi, Ki-Hun Jeong, and Jaewook Ahn, "Tailored Terahertz Pulses by Changing Shapes of Planar Metamaterials," 한국물리학회 가을학술논문발표회 및 임시총회, Ip-II-059, 보광휘닉스파크, 10/20-22, (2010).
23. Minwoo Yi, **Daehoon Han**, Yong-Je Choi, Ki-Hun Jeong, Jaewook Ahn, "Terahertz inductive coupling transparency induced by double asymmetric split resonator," The 7th Asia-Pacific Laser Symposium (APLS 2010), Th-P-67, 서귀포 KAL 호텔, 제주도, 5/11-15, (2010).